Mechanics of Liquid Crystals in Soft Matrices

Yifei Bai

St Edmund Hall

University of Oxford

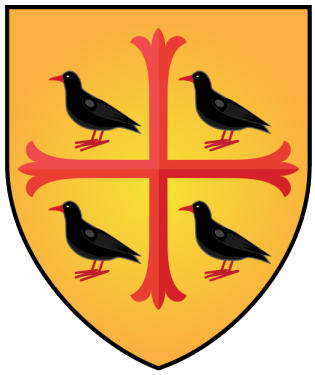

A thesis presented for the degree of

Doctor of Philosophy

Trinity 2025

Dedicated to my family.

Acknowledgements

First, I would like to express my sincere gratitude to my supervisor, Professor Laurence Brassart, for your guidance and support throughout my DPhil. Your expertise in solid mechanics, high standards, and work ethic have been a constant source of inspiration. You taught me how to approach difficult theory with curiosity and courage, and just as importantly, when to step back and refocus. It has been a privilege to be supervised by you over the past four years.

I would also like to thank my lab mates, Professor Zhouzhou, Dr. Gordon, Dr. Lucas, soon-to-be Dr. Thales, Jie, and Yuquan, for the many discussions—useful and useless—and for the friendship that made day-to-day research far more enjoyable. I am especially grateful for the good coffee at Keble and for Lucas's terrible jokes.

To my friends Dr. Xintong and Wilf, Peining and Emma, Dr. Shixiong, Weishen and Alice, thank you for the laughter, the companionship, and for making Oxford feel like home.

To Dr. Lin Cheng, thank you for always believing in me. The time we shared, the formal dinners and pubs, and the places we travelled to are the most beautiful memories of Oxford.

Finally, I would like to thank my parents, Haiying and Rihua, for your unconditional love and support. Your example in how you work, learn, and live has shaped me more than I can say. Thank you for every "be careful", every "take your time", and for everything else you have done for me.

Abstract

Soft polymer materials that contain liquid-crystal inclusions are used in many responsive devices, including polymer-dispersed liquid crystals, where the final performance depends strongly on the inclusion shape and the director field. This thesis develops models to describe how liquid-crystal inclusions in soft matrices deform and how their directors reorient under mechanical loading and external electric fields. It also studies how polymerisation-induced phase separation (PIPS) can create the inclusion microstructures that later control the reference state.

The work is primarily based on a variational modelling approach in which the governing equations follow from a total free energy description, taking into account the elasticity of the matrix, the spatial variation of liquid crystal order parameter, and the anchoring effect at the inclusion-matrix interface. These models are implemented with finite element method in FEniCSx and used in parametric studies. The results show how the elastocapillary number, anchoring strength, and a dimensionless inclusion volume control whether the composite becomes effectively stiffer or softer, and when stress can strongly reorient the director field.

The model is then extended to include electric fields and effects of spontaneous polarisation. Predictions are compared against experimental measurements of droplet elongation under electric fields. The simulations show how matrix stiffness and interfacial constraints control actuation sensitivity, and how electrically driven inclusion deformation in thin films can generate surface wrinkling with micron-scale amplitudes.

Finally, to link processing to microstructure, a chemo-mechanical phase-field model is developed for PIPS in liquid-crystal containing reactive mixtures. The model couples polymerisation kinetics, diffusion-driven demixing, and the appearance of network elasticity through entanglement. The results identify the Damkohler number and an elasticity ratio as key controls of when phase separation starts and how coarsening proceeds or stops. Overall, the thesis provides a modelling route that links microstructure formation, anisotropic interfacial elasticity and electromechanical response in liquid-crystal polymer composites.

Table of Contents

List of Figures

1 | Introduction

Liquid crystals are states of matter that can flow like liquids but possess a certain degree of orientational order due to the geometric anisotropy of their constituent molecules (de Gennes and Prost, 1993). Depending on the microscopic arrangement of the mesogens, liquid crystals can be classified into different categories such as nematics, cholesterics and smectics. Figure 1.1 shows sketches of several typical liquid crystal phases. The simplest type is the nematic phase, which exhibits long-range orientational order but no long-range positional order of the molecules (Figure 1.1, left). When the mesogens also exhibit positional ordering in space, the material is termed a smectic liquid crystal (Figure 1.1, middle). When the orientational order is preserved locally but varies periodically in space, the phase is referred to as a chiral nematic, or cholesteric, liquid crystal (Figure 1.1, right).

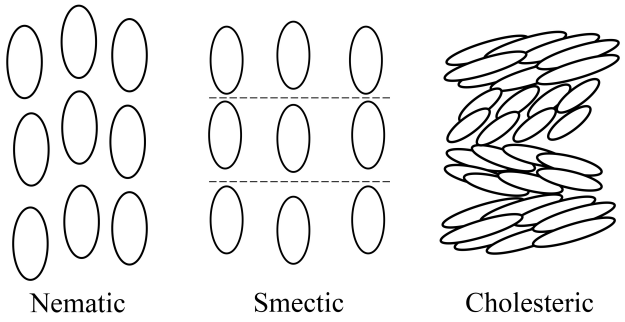

Figure 1.1: Sketches of the nematic, smectic, and cholesteric liquid crystals.

Benefitting from the crystalline ordering of the mesogens, liquid crystals exhibit anisotropic optical properties, which give rise to many colourful patterns under polarised microscopy. These colourful patterns are termed 'textures', and some examples are presented in Figure 1.2. Figure 1.2(a) shows a nematic liquid crystal with a randomly varying orientation in space, where local orientational order is still observed. Similarly, smectics (Figure 1.2(b)) exhibit local orientational order as well as a lay-

ered positional structure. Distortions of smectics therefore not only introduce spatial disorientation of the molecules, but also bending of the layers. For cholesterics (Figure 1.2(c)), a fingerprint-like texture is often observed as a result of the helical molecular field (Andrienko, 2018). On the other hand, the liquid-like behaviour gives the mesogens mobility in space, making them very sensitive to external stimuli such as electric and magnetic fields (Tefelska et al., 2015; Oh-e and Zheng, 2022; Xiao et al., 2022), interfacial effects (Ma et al., 2019; Khan et al., 2021; Loudet et al., 2022), and mechanical stresses (Filip et al., 2006; Bagnani et al., 2019; Novikov and Makarov, 2019). In particular, liquid crystal materials have been used in displays for decades (Schadt, 1997; Huang et al., 2020; He et al., 2022), because an applied electric field can be used to control the orientation of the mesogens and thereby modulate the optical properties in space.

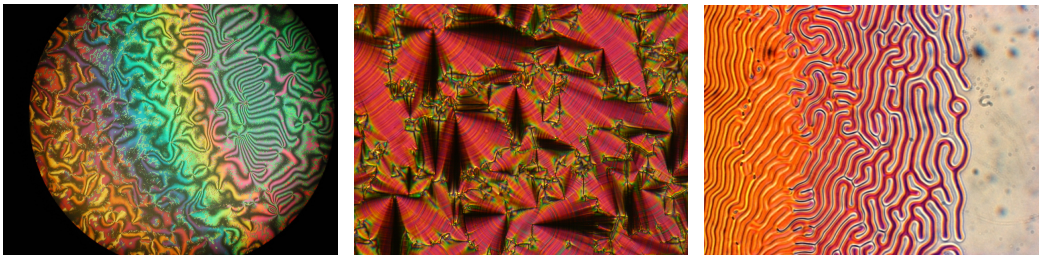

(a) (b) (c)

Figure 1.2: Polarised microphotographs of different types of LCs. (a) Nematic liquid crystal with varying orientation in space (Source:Charles Rosenblatt's Group); (b) Smectic liquid crystal (Source: Wikimedia Common; (c) Cholesteric liquid crystal with its unique 'fingerprint'-like shape (Source: Benjamin Outram).

Despite the advantages conferred by the mobility of the mesogens, liquid crystals themselves have poor mechanical properties. It is therefore essential to combine them with other materials, such as polymers, to exploit their unique responsive behaviour while ensuring sufficient mechanical strength. Polymer-dispersed liquid crystal (PDLC) is a typical example of a liquid-crystal composite, in which liquid-crystal microdroplets are trapped in a polymer matrix. PDLCs have been widely used commercially, for

example in liquid-crystal displays (Bertocchi et al., 2018) and in smart windows and screens (Hakemi, 2019; Oh et al., 2022; Meng et al., 2022), since their invention about thirty years ago. To date, the encapsulation of liquid-crystal inclusions has largely been limited to stiff matrices, which significantly constrains the potential of liquid-crystal composites. Recent studies on embedding liquid-crystal inclusions within more flexible matrices have demonstrated the possibility of designing functional soft materials (Miller et al., 2014; Bertocchi et al., 2018; Zhu et al., 2014). When liquid-crystal microdroplets are embedded in a softer matrix, the composite can be used in wearable devices (Guan et al., 2019; Sang et al., 2022). Similar liquid-crystal droplet-matrix systems are also found in living cells, bacteria and tissues (Tarafder et al., 2020; Wang et al., 2021; Liu et al., 2022; Wei et al., 2022), where the polymeric matrices are very soft hydrogels.

To design engineering material with desired material response and describe the biological system from fundamentals, it is necessary to understand the underpinning physics of these systems. The complex yet intriguing behaviour is due to the coupling of different physics. There are in general three main characters in this multiphysics interplay: the liquid crystal droplet, the matrix, and the interface. The elastic matrix resists any deformation, and when the elastic matrix is deformed, the inclusion's interface will change its shape according to the displacement field. This shape change of the interface in turn reorient the liquid crystal molecules in the inclusions due to the anisotropic surface tension. This phenomenon is known as the anchoring effect, which refers to the tendency of liquid crystal molecules to align at a specific angle relative to the interface. On the other hand, in the bulk, liquid crystal molecules prefer an aligned state. In the presence of an external electric field, the molecules will then be prone to be reorient along the direction of the electric field.

The multiphysics aspects outlined above have largely been investigated separately. Problems involving the interaction between elastic deformation and surface energy are usually referred to as elastocapillary problems, which have been extensively studied

since the groundbreaking work of Gurtin and Murdoch (Gurtin and Murdoch, 1975), and subsequently in a number of theoretical and numerical studies (Duan et al., 2005a,b; Henann and Bertoldi, 2014; Wang and Henann, 2016; Ghosh and Lopez-Pamies, 2022; Steinmann, 2008; Javili and Steinmann, 2010).

The problem of determining the orientational ordering of liquid crystals has also been studied for decades. Two major problems related to our work are the shape-optimisation problem of liquid-crystal droplets in a liquid and the reorientation of liquid-crystal molecules under an external electric field. The first problem considers the competition between the anisotropic surface tension induced by anchoring and the distortional elasticity of the liquid-crystal molecules. Classical textbooks like de Gennes and Prost (1993) and Stewart (2021) presented detailed theories about distortional elasticity and the anchoring effect as individual problems. In particular, Virga (2019) proposed variational theories on the coupling of these physics. The second sub-problem has been investigated extensively in the context of the electro-optical properties of liquid crystals, including the voltage-transmittance relation and the threshold voltage required for device actuation. The underlying physics in these problems is the balance between the tendency of liquid-crystal molecules to align with each other and the applied field (Frisken and Palffy-Muhoray, 1989; Schadt, 1997; Mema et al., 2017).

Although these related problems have been studied in different contexts, the coupling between the elasticity of the matrix and the liquid-crystal field has not yet been investigated in detail. In this thesis, we aim to address the following gaps in the field by developing continuum-mechanics models:

Gap 1: Lack of a model describing the mechanical behaviour of liquid-crystal inclusions in soft matrices When liquid-crystal inclusions are embedded in soft matrices, the mechanical response of the system under external loading depends on the coupling between the liquid-crystal field, the elasticity of the matrix, and the interface

between the two materials. In this thesis, we develop a continuum-mechanics-based theoretical model together with a numerical implementation using the finite element method. The model is based on the assumption that both the inclusion and the matrix are incompressible hyperelastic materials. We validate the model by comparing simulation results with existing theoretical and experimental studies of the shape-optimisation problems mentioned above, which can be recovered as a special case of our formulation. We then perform a parametric study on the material parameters to gain further insight into the underlying physics of the coupling behaviour.

Gap 2: Unexplored coupling between matrix elasticity and an external electric field acting on liquid-crystal inclusions In traditional PDLCs, the polymer matrix is much stiffer than the liquid-crystal phase, and the inclusions are typically approximately spherical, so they do not undergo pronounced shape changes. As a result, when an electric field is applied, the reorientation of the liquid-crystal molecules mainly modifies the optical response and does not induce significant deformation of the surrounding matrix. However, when the inclusions are no longer spherical, or when the stiffness contrast between the liquid crystal and the matrix is reduced, the molecular reorientation can become coupled to the elasticity of the matrix and lead to a measurable electro-mechanical response. In this thesis, we investigate this electro-mechanical response by extending the proposed model and analysing the electrostatic properties of the composite for varying matrix stiffness. A finite element model and a corresponding parametric study are presented.

Gap 3: Unclear role of polymerisation-induced phase separation coupled with elasticity in PDLC manufacturing By addressing the first two gaps, we obtain a better understanding of how elasticity affects the behaviour of the composite in its final, functional state. However, it remains unclear whether, and in what way, elasticity affects the fabrication of such composites. Typical PDLC devices are manufactured via

polymerisation-induced phase separation, during which liquid-crystal inclusions nucleate and are encapsulated in the elastic matrix. The nucleation, growth and coalescence of the liquid-crystal droplets are influenced by the elastic matrix, leading to different morphologies of the resulting microstructure. This issue is not limited to liquid-crystal systems but represents a fundamental problem of phase separation in soft materials. We aim to investigate this chemo-mechanical behaviour by proposing a general theory that describes the coupling between reaction-diffusion processes, interfacial energy and the presence of an elastic polymeric matrix.

In the rest of the thesis, a detailed literature review including fundamental theories will be first introduced in Chapter 2. In Chapter 3, we present the variational theory of liquid crystal inclusions along with a finite element analysis. The coupling between electric field and director field of liquid crystal droplets embedded in soft matrices is illustrated in Chapter 4. In Chapter 5, we propose the chemo-mechanical modelling of the polymerisation induced phase separation behaviour. In Chapter 6, we summarise the main findings of this thesis and discuss their implications and limitations. We also highlight directions for future research and possible extensions of the present modelling framework.

2 | Background

In this chapter, fundamental continuum mechanics theories are discussed, along with a review of the state of the art in the field. Specifically, finite deformation continuum mechanics is briefly introduced in Section 2.1. Liquid crystal theories, including phase transition, distortion elasticity and electrostatic response, are discussed in Section 2.2. Theory regarding surface elasticity is introduced in Section 2.3. In addition, a pedagogical section introducing classical theories of phase separation is presented in Section 2.4.

Notations and conventions We follow standard notation and conventions throughout this chapter and the thesis. Einstein's summation convention is adopted, with indices ranging from 1 to 3 unless otherwise indicated, so that

$$a_i b_i = \sum_{i=1}^{3} a_i b_i. \tag{2.1}$$

Bold letters (such as $\boldsymbol{a}$ and $\boldsymbol{A}$) represent vectors and tensors. With $\boldsymbol{e}_i$ as a set of basis vectors in a Cartesian coordinate system, common tensor operations can be expressed as

$$\begin{aligned} &\boldsymbol{a}\cdot\boldsymbol{b} = a_i b_i, \quad \boldsymbol{A}\cdot\boldsymbol{b} = A_{ij}b_j\boldsymbol{e}_i, \quad \boldsymbol{A}:\boldsymbol{B} = A_{ij}B_{ij}, \\ &\boldsymbol{a}\otimes\boldsymbol{b} = a_i b_j \boldsymbol{e}_i\otimes\boldsymbol{e}_j, \quad \boldsymbol{a}\times\boldsymbol{b} = \epsilon_{ijk}a_i b_j \boldsymbol{e}_k, \\ &\boldsymbol{C}\vdots\boldsymbol{D} = C_{ijk}D_{ijk} \quad (\boldsymbol{C} \text{ and } \boldsymbol{D} \text{ are third order tensors}). \end{aligned} \tag{2.2}$$

Here ϵ_{ijk} is the Levi-Civita symbol (or permutation symbol), defined such that

$$\epsilon_{ijk} = \begin{cases} +1, & \text{if } (i,j,k) = (1,2,3), (2,3,1) \text{ or } (3,1,2), \\ -1, & \text{if } (i,j,k) = (3,2,1), (1,3,2) \text{ or } (2,1,3), \\ 0, & \text{if } i=j,\ j=k, \text{ or } k=i. \end{cases} \tag{2.3}$$

The second order identity tensor is denoted by $\boldsymbol{I}$ and is given by

$$\boldsymbol{I} = \delta_{ij} \boldsymbol{e}_i \otimes \boldsymbol{e}_j, \tag{2.4}$$

where δ_{ij} is the Kronecker delta symbol: $\delta_{ij} = 1$ if $i = j$, and $\delta_{ij} = 0$ otherwise.

2.1 Fundamentals of continuum mechanics

In this section, we summarise the basic concepts of continuum mechanics that are required in the subsequent chapters. The presentation follows standard treatments in the literature and is restricted to those notions that will be used later, such as kinematics of finite deformation, balance laws and standard measures of stress and strain. For a more comprehensive and rigorous theory of continuum mechanics, the reader is referred to classical textbooks such as Gurtin (1982) and Holzapfel (2002).

2.1.1 Kinematics

Consider a body made of a continuous distribution of matter in space and time. We denote by $\mathcal{B}_0$ the region of space that the body occupies at time $t = 0$, referred to as the reference configuration. A point in the reference configuration is described by its position vector $\boldsymbol{X}$. For $t > 0$, the body evolves in space and occupies a new region, called the current configuration, $\mathcal{B}_t$. A material point in the current configuration is described by the position vector $\boldsymbol{x}$. The deformation of the body is described by the mapping $\boldsymbol{x} = \boldsymbol{\varphi}(\boldsymbol{X})$. The associated deformation gradient, which maps line elements from the initial configuration to the current configuration, is defined as

$$\boldsymbol{F} = \operatorname{Grad} \boldsymbol{\varphi}(\boldsymbol{X}), \tag{2.5}$$

where

$$\text{Grad}\,(\cdot) = \frac{\partial(\cdot)}{\partial \boldsymbol{X}} \tag{2.6}$$

is the gradient operator with respect to the reference configuration. Correspondingly,

$$\text{grad}\,(\cdot) = \frac{\partial(\cdot)}{\partial \boldsymbol{x}} \tag{2.7}$$

is the gradient operator with respect to the current configuration. The inverse of the deformation gradient, denoted by $\boldsymbol{f}$, maps vectors in the current configuration to the reference configuration and can be written as

$$\boldsymbol{f} = \frac{\partial \boldsymbol{X}}{\partial \boldsymbol{x}}. \tag{2.8}$$

For an infinitesimal volume element dV in the reference configuration, its relation to the corresponding infinitesimal volume element dv in the current configuration can be written as

$$dv = J\,dV, \tag{2.9}$$

where

$$J = \det \boldsymbol{F} \tag{2.10}$$

is the determinant of the deformation gradient. To transform an infinitesimal area element in the reference configuration to the current configuration, the mapping can be written as

$$da\,\boldsymbol{n} = J\,\boldsymbol{F}^{-T} \cdot \boldsymbol{N}\,dA, \tag{2.11}$$

where $\boldsymbol{n}$ and $\boldsymbol{N}$ are the outward unit normals to the area elements in the current and reference configurations, respectively. This relation is usually referred to as Nanson's formula.

The deformation gradient can be decomposed into an orthogonal tensor and a posi-

tive definite symmetric tensor by the polar decomposition theorem, and can be written as

$$\boldsymbol{F} = \boldsymbol{R}\boldsymbol{U} = \boldsymbol{V}\,\boldsymbol{R}, \tag{2.12}$$

where $\boldsymbol{R}$ is a proper orthogonal tensor, i.e. $\boldsymbol{R}^{-1} = \boldsymbol{R}^T$ and $\det \boldsymbol{R} = 1$. The tensors $\boldsymbol{U}$ and $\boldsymbol{V}$ are the right and left stretch tensors, respectively. The terms "left" and "right" refer to the fact that these tensors appear on the left or right of $\boldsymbol{R}$ in the decomposition. This decomposition clearly distinguishes the stretch and rotation of the deformation gradient; that is, a deformation described by $\boldsymbol{F}$ can be regarded as a stretch $\boldsymbol{U}$ followed by a rigid body rotation $\boldsymbol{R}$, or as a rotation $\boldsymbol{R}$ followed by a stretch $\boldsymbol{V}$. Although the deformation gradient has an intuitive physical interpretation, it is mathematically inconvenient because it maps between the reference and current configurations, which are expressed in different coordinate bases ($\boldsymbol{F} = F_{iJ}\,\boldsymbol{e}_i \otimes \boldsymbol{E}_J$). In contrast, the stretch tensors $\boldsymbol{U}$ and $\boldsymbol{V}$ act within the reference and current configurations, respectively, and can be written as

$$\boldsymbol{U} = U_{IJ}\,\boldsymbol{E}_I \otimes \boldsymbol{E}_J, \quad \boldsymbol{V} = V_{ij}\,\boldsymbol{e}_i \otimes \boldsymbol{e}_j. \tag{2.13}$$

As a result, the stretch tensors admit conventional spectral decompositions and can be written as

$$\boldsymbol{U} = \sum_{i=1}^{3} \lambda_i\,\boldsymbol{M}_i \otimes \boldsymbol{M}_i, \quad \boldsymbol{V} = \sum_{i=1}^{3} \lambda_i\,\boldsymbol{m}_i \otimes \boldsymbol{m}_i, \tag{2.14}$$

where λ_1, λ_2 and λ_3 are the principal stretches of $\boldsymbol{U}$ and $\boldsymbol{V}$, and $\boldsymbol{M}_i$ and $\boldsymbol{m}_i$ are the corresponding principal directions in the reference and current configurations, respectively, with $\boldsymbol{m}_i = \boldsymbol{R}\boldsymbol{M}_i$.

It is convenient to introduce the right Cauchy-Green deformation tensor

$$\boldsymbol{C} = \boldsymbol{U}^2 = \boldsymbol{F}^T\boldsymbol{F}, \tag{2.15}$$

which gives the square of the local change in distances due to deformation, i.e.

$$|d\boldsymbol{x}|^2 = d\boldsymbol{X} \cdot \boldsymbol{C} \cdot d\boldsymbol{X}. \tag{2.16}$$

The eigenvalues of $\boldsymbol{C}$ are the squares of the principal stretches, $\lambda_1^2, \lambda_2^2, \lambda_3^2$. The invariants of $\boldsymbol{C}$ are

$$\begin{aligned} I_1^C &= \operatorname{tr} \boldsymbol{C} = \lambda_1^2 + \lambda_2^2 + \lambda_3^2, \\ I_2^C &= \frac{1}{2}\left[(\operatorname{tr} \boldsymbol{C})^2 - \operatorname{tr}\left(\boldsymbol{C}^2\right)\right], \\ I_3^C &= \det \boldsymbol{C} = \lambda_1^2 \lambda_2^2 \lambda_3^2. \end{aligned} \tag{2.17}$$

Alternatively, the left Cauchy-Green deformation tensor is defined as

$$\boldsymbol{b} = \boldsymbol{V}^2 = \boldsymbol{F}\boldsymbol{F}^T. \tag{2.18}$$

This describes the change in distances through

$$|d\boldsymbol{X}|^2 = d\boldsymbol{x} \cdot \boldsymbol{b}^{-1} \cdot d\boldsymbol{x}. \tag{2.19}$$

The strain tensors can be written in spectral form as

$$\boldsymbol{C} = \sum_{i=1}^{3} \lambda_i^2 \, \boldsymbol{M}_i \otimes \boldsymbol{M}_i, \quad \boldsymbol{b} = \sum_{i=1}^{3} \lambda_i^2 \, \boldsymbol{m}_i \otimes \boldsymbol{m}_i. \tag{2.20}$$

2.1.2 Stress

Consider a surface element of area dA in the reference configuration, with outward unit normal $\boldsymbol{N}$, subjected to a surface traction $\boldsymbol{T}$. The corresponding surface element in the current configuration is denoted by da, with outward unit normal $\boldsymbol{n}$, and the traction is

$\boldsymbol{t}$. The resultant force on this surface is

$$d\boldsymbol{f} = \boldsymbol{t}\, da = \boldsymbol{T}\, dA. \tag{2.21}$$

From Cauchy's theorem, in the absence of a prescribed couple on the surface, there exist second order tensor fields $\boldsymbol{P}$ and $\boldsymbol{\sigma}$ such that

$$\boldsymbol{T} = \boldsymbol{P}\boldsymbol{N}, \quad \boldsymbol{t} = \boldsymbol{\sigma}\boldsymbol{n}. \tag{2.22}$$

Therefore,

$$\boldsymbol{\sigma}\boldsymbol{n}\, da = \boldsymbol{P}\boldsymbol{N}\, dA. \tag{2.23}$$

Using Nanson's formula, $\boldsymbol{P}$ can be written as

$$\boldsymbol{P} = J\, \boldsymbol{\sigma}\boldsymbol{F}^{-T}. \tag{2.24}$$

The tensor $\boldsymbol{\sigma}$ is usually referred to as the true stress or Cauchy stress, and $\boldsymbol{P}$ is termed the nominal stress or first Piola-Kirchhoff stress[1]. In the classical theory of non-polar continua, where body couples and couple stresses are neglected, the balance of angular momentum implies that $\boldsymbol{\sigma}$ is symmetric and that $\boldsymbol{P}$ satisfies $\boldsymbol{P}\boldsymbol{F}^T = \boldsymbol{F}\boldsymbol{P}^T$.

2.1.3 Balance equations

We present the classical balance equations for a non-polar continuum. Let $V_t \subset \mathcal{B}_t$ be any material control volume with boundary ∂V_t and outward unit normal $\boldsymbol{n}$. Denote by $\rho(\boldsymbol{x}, t)$ the mass density in the current configuration, by $\boldsymbol{v}(\boldsymbol{x}, t)$ the spatial velocity, and by $\boldsymbol{b}(\boldsymbol{x}, t)$ the body force per unit current volume. Their referential counterparts

[1] This terminology is not universal. For example, Ogden defines the nominal stress tensor $\boldsymbol{S}$ such that the first Piola-Kirchhoff stress tensor is $\boldsymbol{P} = \boldsymbol{S}^T$ (Ogden, 2001). In this thesis, we adopt the terminology defined by Holzapfel (2002).

are denoted by $\boldsymbol{v}_0(\boldsymbol{X}, t)$ and $\boldsymbol{B}(\boldsymbol{X}, t)$, representing the velocity and the body force per unit reference volume in the reference configuration, respectively. The two pairs are related in different ways: the referential velocity is simply the pull-back of the spatial velocity, $\boldsymbol{v}_0(\boldsymbol{X}, t) = \boldsymbol{v}(\boldsymbol{\varphi}(\boldsymbol{X}, t), t)$, whereas the referential body force is transformed by the volume change, $\boldsymbol{B}(\boldsymbol{X}, t) = J(\boldsymbol{X}, t)\boldsymbol{b}(\boldsymbol{\varphi}(\boldsymbol{X}, t), t)$.

2.1.3.1 Balance of mass

The balance of mass requires that the total mass of any material volume remains constant in time,

$$\frac{d}{dt}\int_{V_t} \rho \, dv \;=\; 0. \tag{2.25}$$

2.1.3.2 Balance of linear momentum

The balance of linear momentum states that the rate of change of total momentum of any material region V_t equals the sum of the external body forces and surface tractions acting on it,

$$\frac{d}{dt}\int_{V_t} \rho \, \boldsymbol{v} \, dv \;=\; \int_{V_t} \boldsymbol{b} \, dv \;+\; \int_{\partial V_t} \boldsymbol{t} \, da \;=\; \int_{V_t} \boldsymbol{b} \, dv \;+\; \int_{\partial V_t} \boldsymbol{\sigma} \cdot \boldsymbol{n} \, da. \tag{2.26}$$

Assuming that the density of the material remains constant throughout the deformation, and using the divergence theorem, we obtain

$$\int_{V_t} \rho \, \dot{\boldsymbol{v}} \, dv = \int_{V_t} (\boldsymbol{b} + \operatorname{div} \boldsymbol{\sigma}) \, dv. \tag{2.27}$$

Alternatively, expressing the balance in the reference configuration, we can write

$$\int_{V_0} \rho \, \dot{\boldsymbol{v}}_0 \, dV = \int_{V_0} (\boldsymbol{B} + \operatorname{Div} \boldsymbol{P}) \, dV. \tag{2.28}$$

When the system is at equilibrium, the inertia term vanishes and the strong form of the problem becomes

$$\boldsymbol{b} + \operatorname{div} \boldsymbol{\sigma} = \mathbf{0}, \qquad \boldsymbol{B} + \operatorname{Div} \boldsymbol{P} = \mathbf{0}. \tag{2.29}$$

2.1.3.3 Balance of angular momentum

The balance of angular momentum states that the rate of change of the total angular momentum of any material region V_t about a fixed point $\boldsymbol{x}_0$ equals the sum of the moments of the external body forces and surface tractions about that point. It can be written as

$$\frac{d}{dt} \int_{V_t} \boldsymbol{r} \times \rho \boldsymbol{v} \, dv = \int_{\partial V_t} \boldsymbol{r} \times \boldsymbol{t} \, da + \int_{V_t} \boldsymbol{r} \times \boldsymbol{b} \, dv, \tag{2.30}$$

where $\boldsymbol{r} = \boldsymbol{x} - \boldsymbol{x}_0$. Using Cauchy's relation $\boldsymbol{t} = \boldsymbol{\sigma n}$ and the divergence theorem, the right-hand side can be expressed as

$$\int_{\partial V_t} \boldsymbol{r} \times \boldsymbol{t} \, da + \int_{V_t} \boldsymbol{r} \times \boldsymbol{b} \, dv = \int_{V_t} \left(\boldsymbol{r} \times \operatorname{div} \boldsymbol{\sigma} + \boldsymbol{\mathcal{E}} : \boldsymbol{\sigma}^T + \boldsymbol{r} \times \boldsymbol{b} \right) dv, \tag{2.31}$$

where $\boldsymbol{\mathcal{E}}$ is the third order alternating tensor with components ϵ_{ijk}, such that

$$(\boldsymbol{\mathcal{E}} : \boldsymbol{\sigma}^T)_i = \epsilon_{ijk} \sigma_{jk}. \tag{2.32}$$

Reorganising the terms and using the balance of linear momentum $\rho \dot{\boldsymbol{v}} = \boldsymbol{b} + \operatorname{div} \boldsymbol{\sigma}$, we obtain

$$\int_{V_t} \boldsymbol{r} \times (\rho \dot{\boldsymbol{v}} - \boldsymbol{b} - \operatorname{div} \boldsymbol{\sigma}) \, dv = \int_{V_t} \epsilon_{ijk} \sigma_{jk} \, dv. \tag{2.33}$$

Since the above relation must hold for all V_t, it follows that

$$\epsilon_{ijk} \sigma_{jk} = 0. \tag{2.34}$$

This relation is satisfied if and only if the Cauchy stress tensor is symmetric. Equivalently, expressing the balance of angular momentum in the reference configuration and using the relation between $\boldsymbol{P}$ and $\boldsymbol{\sigma}$ yields the nominal condition

$$\boldsymbol{P}\boldsymbol{F}^T = \boldsymbol{F}\boldsymbol{P}^T, \tag{2.35}$$

which is consistent with the symmetry of $\boldsymbol{\sigma}$.

2.2 Continuum theory of liquid crystal

2.2.1 Continuum description

In the present study, we focus only on nematic liquid crystals, which are the simplest form of liquid crystal. Figure 2.1 shows a nematic liquid crystal in a Cartesian coordinate system. The ellipsoids represent liquid crystal mesogens; $\boldsymbol{m}^{(a)}$ is the unit vector along the central axis of mesogen a, and $\boldsymbol{d}$ represents the preferred direction of the nematic. This vector is termed the director $\boldsymbol{d}$.

Common liquid crystal molecules are non-polar, meaning that the molecules possess central symmetry. As a consequence, the state of the material is unchanged if all the vectors $\boldsymbol{m}^{(a)}$ are replaced by $-\boldsymbol{m}^{(a)}$, and a simple vector average of the mesogen orientations $\boldsymbol{m}^{(a)}$ is zero. Instead, the orientational ordering is described by the second-order alignment tensor (or $\boldsymbol{Q}$-tensor)

$$\boldsymbol{Q} = \frac{1}{N}\sum_a \left(\boldsymbol{m}^{(a)} \otimes \boldsymbol{m}^{(a)} - \frac{\boldsymbol{I}}{3}\right), \tag{2.36}$$

where the summation is performed over N molecules in a representative volume element of the liquid crystal phase. Note that this expression can be applied to other types of liquid crystals to describe their orientational ordering, although additional order pa-

rameters may be required (e.g. a translational order parameter for smectic liquid crystals (de Gennes and Prost, 1993)).

Let α_i ($i = 1, 2, 3$) be the principal values of the $\boldsymbol{Q}$-tensor, with $\alpha_1 + \alpha_2 + \alpha_3 = 0$, and let $\boldsymbol{d}_i$ denote the corresponding principal directions. Due to its traceless property, the $\boldsymbol{Q}$-tensor can be expressed as

$$\boldsymbol{Q} = S_1(\boldsymbol{d}_1 \otimes \boldsymbol{d}_1) + S_2(\boldsymbol{d}_2 \otimes \boldsymbol{d}_2) - \frac{S_1 + S_2}{3}\boldsymbol{I}, \tag{2.37}$$

where the parameters S_1 and S_2 are related to the principal values by

$$S_1 = 2\alpha_1 + \alpha_2, \quad S_2 = 2\alpha_2 + \alpha_1. \tag{2.38}$$

For uniaxial nematic liquid crystals, the $\boldsymbol{Q}$-tensor is transversely isotropic, which implies that two of its eigenvalues coincide. Without loss of generality, let $\boldsymbol{d}_1$ be the direction of transverse isotropy, so that $\alpha_2 = \alpha_3$ and $S_2 = 0$. The $\boldsymbol{Q}$-tensor (2.36) then simplifies to

$$\boldsymbol{Q} = S\left(\boldsymbol{d} \otimes \boldsymbol{d} - \frac{\boldsymbol{I}}{3}\right), \tag{2.39}$$

where $\boldsymbol{d} \equiv \boldsymbol{d}_1$ and $S \equiv S_1$. When all the molecules are perfectly aligned, it is easily seen from Eqn. (2.37) that $S = 1$. The case where all molecules are randomly oriented corresponds to $S = 0$. Finally, the case where all molecules are isotropically distributed in a plane perpendicular to $\boldsymbol{d}$ corresponds to $S = -\frac{1}{2}$. Thus, the parameter S describes the degree of alignment of the molecules relative to the director. In general, $-\frac{1}{2} \leq S \leq 1$ (Andrienko, 2018). Figure 2.2 shows the two extreme cases where $S = 1$ and $S = -0.5$, representing scenarios where the major and minor axes are perfectly aligned , respectively. The director $\boldsymbol{d}$ and scalar order parameter S together describe the average orientation and degree of disorder of the molecules at a point in the nematic liquid crystal phase.

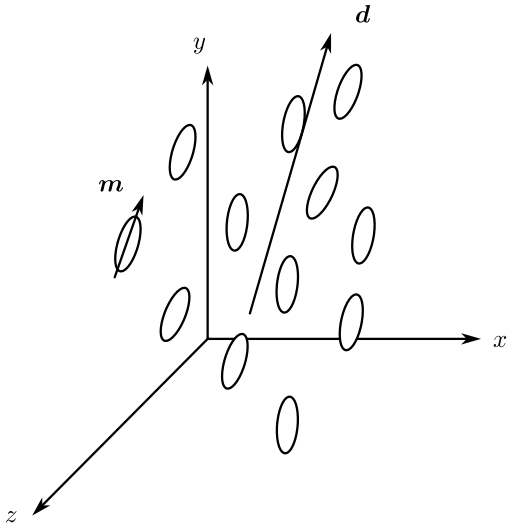

Figure 2.1: Orientation of mesogens in a nematic mesophase. $m^{(a)}$ is the unit vector representing the direction of mesogen i. The director vector d corresponds to the average molecular alignment.

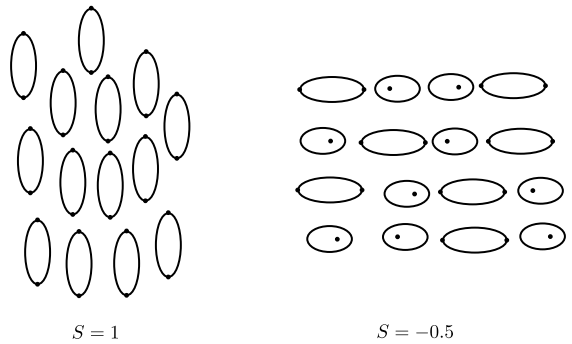

Figure 2.2: Schematic of nematic systems with scalar order parameter $S = 1$ (left) and $S = -0.5$ (right). The black dots represent ends of the major axes of liquid crystal molecules.

2.2.2 Phase transition theories

The orientational ordering of liquid crystals is highly dependent on the environment, such as temperature and concentration. Under certain conditions, liquid crystals can undergo an isotropic-nematic (I-N) phase transition. Depending on the control parameter that drives the I-N transition, liquid crystals can be categorised as thermotropic or lyotropic. Thermotropic liquid crystals exhibit an I-N transition primarily as a function of temperature and are widely used in commercial liquid crystal devices such as screens and polymer dispersed liquid crystal (PDLC) films (Lu et al., 2024b; Ghosh, 2023; Kamal et al., 2022; Khalid et al., 2021; Ren et al., 2005; Zhang et al., 2020), as well as in some biomedical applications (Lockwood et al., 2006; Popov et al., 2017). Lyotropic liquid crystals, on the other hand, exhibit an I-N transition that is mainly controlled by concentration (or composition) and are more commonly seen in biomedical applications and natural systems, such as drug delivery (Boyd et al., 2006; Liu et al., 2021), antioxidants (Gangal et al., 2025), and biofilms (Tarafder et al., 2020).

The isotropic-nematic phase transition for thermotropic liquid crystals is driven by attractive forces between liquid crystal mesogens. Maier and Saupe (Maier and Saupe, 1959) proposed a microscopic mean-field model that describes this behaviour by balancing orientational entropy against anisotropic attractive interactions. As temperature decreases, liquid crystal molecules align in order to reduce the anisotropic interaction energy. The concentration-mediated I-N phase transition in lyotropic liquid crystals is driven by repulsive forces between liquid crystal mesogens. Onsager (Onsager, 1949) proposed a microscopic model that takes into account the effect of excluded volume between two rigid rod-like mesogens. The excluded volume is the region of space that one molecule cannot enter due to the presence of other molecules. For a pair of mesogens, the excluded volume is minimised when the mesogens are aligned with each other and maximised when they are perpendicular. The mesogens can translate in the system

only within the space that is not occupied by the excluded volume. As a result, a smaller excluded volume provides more freedom for translational motion and hence more translational entropy. When the concentration of mesogens increases, the excluded volume increases, reducing the free space available for each molecule to explore; therefore, the mesogens tend to rotate towards alignment in order to gain translational entropy. Details of the Maier-Saupe and Onsager theories can be found in classical textbooks (de Gennes and Prost, 1993; Doi, 2013).

Alternatively, a phenomenological macroscopic model was proposed by de Gennes (de Gennes and Prost, 1993), originally used to describe thermotropic liquid crystals. In the spirit of Landau theory of phase transitions, given an order parameter that is zero in the isotropic state and non-zero in the nematic state, we assume that the associated free energy density is an analytic function of the order parameter tensor $\boldsymbol{Q}$. This free energy can be expanded in terms of the invariants of $\boldsymbol{Q}$ near the transition temperature. A natural choice of such a function is [2]

$$\psi_{IN}(\boldsymbol{Q}) = A\,\mathrm{tr}\big(\boldsymbol{Q}^2\big) + \frac{2B}{3}\,\mathrm{tr}\big(\boldsymbol{Q}^3\big) + \frac{C}{2}\left[\mathrm{tr}\big(\boldsymbol{Q}^2\big)\right]^2, \tag{2.40}$$

where A, B, and C are material parameters depending on temperature. For simplicity, we assume that the dependence on external stimuli enters only through A, so that B and C are treated as constants. Although the model is more commonly used for thermotropic liquid crystals (de Gennes and Prost, 1993; Doi, 2013), it has also been applied to lyotropic liquid crystals by making A a function of concentration (Moldovan and Puică, 2001). For simplicity, we use temperature here as the external stimulus; as a result, A can be expressed as

$$A = \alpha(T - T^*), \tag{2.41}$$

where $\alpha > 0$ is a material parameter independent of temperature, and T^* is the reference

[2] For a three-dimensional symmetric traceless tensor $\boldsymbol{Q}$, the invariant $\mathrm{tr}(\boldsymbol{Q}^4)$ is not independent, since $\mathrm{tr}(\boldsymbol{Q}^4) = \frac{1}{2}[\mathrm{tr}(\boldsymbol{Q}^2)]^2$. Hence the fourth-order term is commonly written as $[\mathrm{tr}(\boldsymbol{Q}^2)]^2$.

temperature. Note that T^* is not the temperature where the phase transition occurs, which will be illustrated later. It can further be shown that the invariants of $\boldsymbol{Q}$ depend only on the scalar order parameter S:

$$\mathrm{tr}\big(\boldsymbol{Q}^2\big) = \frac{2}{3}S^2, \qquad \mathrm{tr}\big(\boldsymbol{Q}^3\big) = \frac{2}{9}S^3, \qquad \big[\mathrm{tr}\big(\boldsymbol{Q}^2\big)\big]^2 = \frac{4}{9}S^4. \tag{2.42}$$

We can thus obtain the equilibrium values of the scalar order parameter S by minimising the bulk free energy ψ_{IN} with respect to S. This yields three stationary solutions:

$$\begin{aligned} S_{\mathrm{eq}}^0 &= 0, \\ S_{\mathrm{eq}}^+ &= \frac{1}{4C}\left(-B + \sqrt{B^2 - 24AC}\right), \\ S_{\mathrm{eq}}^- &= \frac{1}{4C}\left(-B - \sqrt{B^2 - 24AC}\right). \end{aligned} \tag{2.43}$$

The underlying physics of these stationary points can be interpreted by evaluating $d^2\psi_{IN}/dS^2$ and comparing the corresponding free-energy values. As discussed above, we assume that the temperature dependence of the Landau-de Gennes free energy enters only through the linear relation in A. There are three critical values of A that distinguish different phase behaviours. The first corresponds to the limit at which non-trivial nematic solutions cease to exist. This occurs when $B^2 - 24AC = 0$, which defines the nematic spinodal value

$$A_{\mathrm{ns}} = \frac{B^2}{24C}.$$

For $A > A_{\mathrm{ns}}$ the discriminant $B^2 - 24AC$ is negative, so no non-isotropic stationary points exist and the isotropic state is the only stationary solution. The second critical value A_{IN} is obtained by requiring the nematic stationary point to have the same free energy as the isotropic state. Since $\psi_{IN}(0) = 0$, this condition is $\psi_{IN}(S) = 0$ for $S \neq 0$.

Combining this condition with the stationarity condition $3A + BS + 2CS^2 = 0$ gives

$$S_{\mathrm{IN}} = -\frac{B}{3C}, \qquad A_{\mathrm{IN}} = \frac{B^2}{27C}. \tag{2.44}$$

Thus, A_{IN} is the value at which the isotropic and nematic states have equal bulk free energy. This is the first-order transition point because the equilibrium scalar order parameter jumps discontinuously from $S = 0$ to S_{IN}.The third critical value is $A = 0$: when $A < 0$, the stationary point $S^0_{\mathrm{eq}} = 0$ is a local maximum, and therefore the isotropic state becomes unstable and the only stable state is the nematic state.

Let $\alpha = 0.05$, $B = -1$, $C = 0.6$, and $\Delta T = T - T^*$. The material parameters here are dimensionless and are only selected to illustrate the theory. With these material parameters, the critical values are $A_{\mathrm{ns}} \approx 0.0694$ and $A_{\mathrm{IN}} = 0.0617$. From these critical values of A, we obtain the corresponding temperature offsets $\Delta T_{\mathrm{ns}} = A_{\mathrm{ns}}/\alpha \approx 1.389$ and $\Delta T_{\mathrm{IN}} = A_{\mathrm{IN}}/\alpha \approx 1.235$. Figure 2.3(a) shows the relation between the Landau-de Gennes free energy and the scalar order parameter S. When $\Delta T < 0$ (brown), the isotropic phase is unstable and $S^-_{\mathrm{eq}} < 0$ corresponds to an oblate nematic branch. For rod-like systems such as 5CB, this branch is always of higher free energy than the prolate nematic solution ($S^+_{\mathrm{eq}} > 0$), is not realised experimentally, and will not be considered further in this thesis. When $0 < \Delta T < \Delta T_{\mathrm{IN}}$ (red), the isotropic state S^0_{eq} is metastable and S^+_{eq} is the stable nematic state. When $\Delta T = \Delta T_{\mathrm{IN}}$ (green), the free energies of the isotropic and nematic phases are identical, indicating coexistence. The corresponding transition temperature is then

$$T_{\mathrm{IN}} = T^* + \Delta T_{\mathrm{IN}}. \tag{2.45}$$

In the narrow region where $\Delta T_{\mathrm{IN}} < \Delta T < \Delta T_{\mathrm{ns}}$ (orange), S^0_{eq} is stable and S^+_{eq} is metastable. When $\Delta T > \Delta T_{\mathrm{ns}}$, $S^\pm_{\mathrm{eq}}$ are undefined and S^0_{eq} is the only stable phase.

For a uniaxial nematic, $\boldsymbol{Q} = S\,(\boldsymbol{d} \otimes \boldsymbol{d} - \boldsymbol{I}/3)$, so ψ_{IN} depends on S but not on

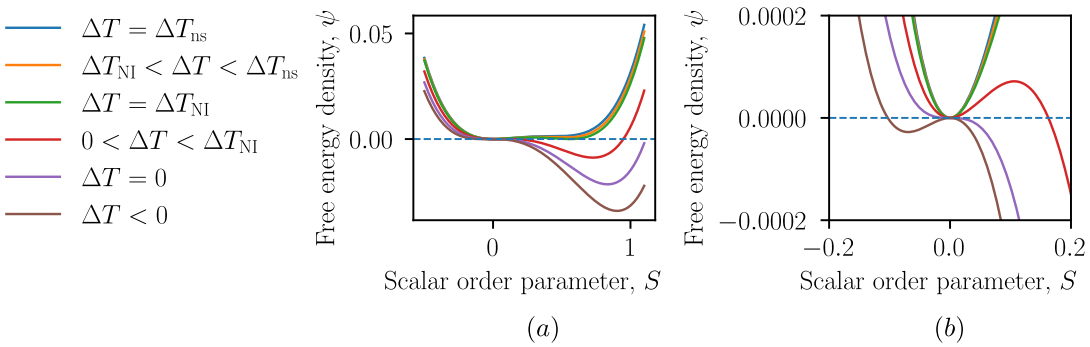

Figure 2.3: (a) Relation between Landau-de Gennes free energy and the scalar order parameter at different temperatures. Parameters: $\alpha = 0.05$, $B = -1$, $C = 0.6$; (b) a zoom-in near $S = 0$.

the orientation of the director $\boldsymbol{d}$. This is not necessarily true in more complex cases such as smectic and cholesteric liquid crystals. Specific models are required to model such materials and is beyond the scope of this thesis.Minimisation with respect to $\boldsymbol{d}$ is therefore trivial: any uniform unit vector $\boldsymbol{d}$ yields the same bulk free energy, and the preferred direction is determined only when elastic terms and boundary conditions are taken into account.

The spinodal behaviour of this phase transition is illustrated in Figure 2.4. The figure shows the equilibrium scalar order parameter S_{eq} as a function of the temperature offset $\Delta T = T - T^*$. At ΔT_{IN}, the stable state changes discontinuously from the isotropic branch to the nematic branch, while ΔT_{ns} and $\Delta T = 0$ mark the spinodal limits of the nematic and isotropic states, respectively.

2.2.3 Distortional elasticity theories

In an unbounded nematic and in the absence of external fields, the thermodynamically preferred state is spatially uniform: the director is everywhere aligned and the scalar order parameter takes its equilibrium value. Confinement, surfaces, and external fields in general induce spatial variation of orientation and degree of order. This spatial vari-

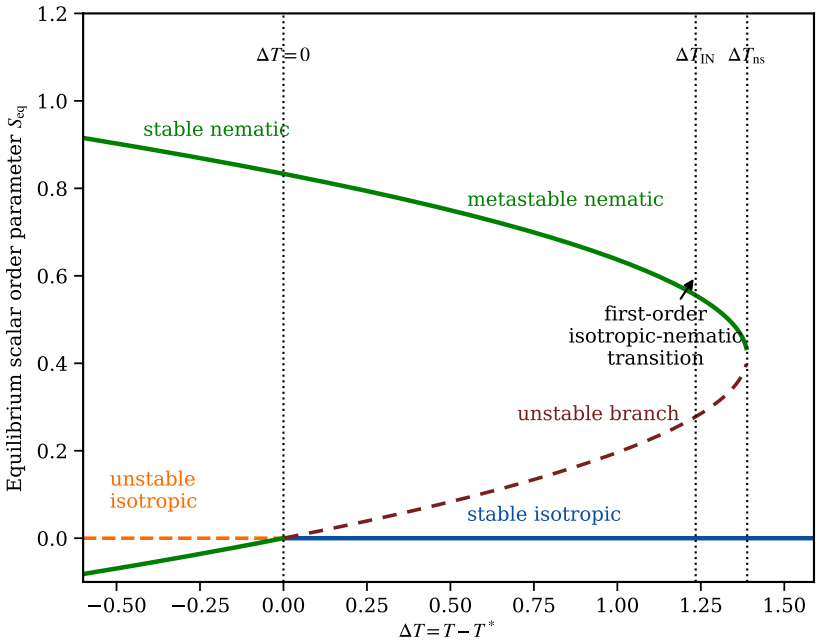

Figure 2.4: Diagram of the equilibrium scalar order parameter S_{eq} as a function of the temperature offset $\Delta T = T - T^*$. The isotropic-nematic transition occurs at ΔT_{IN}, where the isotropic and nematic minima have equal free energy, while ΔT_{ns} and $\Delta T = 0$ mark the spinodal limits of the nematic and isotropic states, respectively.

ation introduces an excess free energy to the system, which is usually referred to as the distortional elastic energy. The distortional elastic energy can be defined based on the director field and the order parameter, corresponding to director theories and $\boldsymbol{Q}$ tensor theories, respectively. Here, we make the constitutive assumption that the liquid-crystal free energy depends on spatial gradients of the orientational order. This gradient dependence represents the elastic cost of director or order-parameter distortions. As a result, there exists a stress-like power conjugate to grad $\boldsymbol{Q}$ and grad $\boldsymbol{d}$. This stress like term plays an important role in coupling problems of liquid crystals.

2.2.3.1 Director theories

A number of classical continuum theories of nematic liquid crystals are formulated in terms of the director field $\boldsymbol{d}(\boldsymbol{x})$. The earliest phenomenological description of elastic distortions in the director field was developed by Oseen and later refined by Frank, leading to the Oseen-Frank theory of nematic elasticity (Oseen, 1933; Frank, 1958). Building on this, Ericksen and Leslie extended the framework to include balance laws and viscous effects, giving rise to the Ericksen and Leslie-Ericksen theories for the statics and dynamics of nematic liquid crystals (Ericksen, 1961; Leslie, 1979). Modern presentations and refinements of these director-based theories can be found in standard textbooks such as de Gennes and Prost (de Gennes and Prost, 1993), Virga (Virga, 2019), Sonnet and Virga (Sonnet and Virga, 2012), and Stewart (Stewart, 2021), as well as in review articles such as Andrienko (2018). The theories presented here are mainly drawn from these references, with the notation adapted for consistency with this thesis. In these theories, liquid crystal is considered as incompressible fluid, therefore, the volumetric ratio is $J = 1$ throughout these theoretical models.

We postulate that the excess free energy due to distortion of the director field per unit current volume is

$$\psi_d = \psi_d(\boldsymbol{d}, \operatorname{grad} \boldsymbol{d}). \tag{2.46}$$

This free energy must satisfy the symmetry of a nematic liquid crystal:

$$\psi_d(\boldsymbol{d}, \text{grad}\, \boldsymbol{d}) = \psi_d(-\boldsymbol{d}, -\text{grad}\, \boldsymbol{d}). \tag{2.47}$$

In addition, since it only describes how distorted the director field is, it should not depend on the actual orientation of the director:

$$\psi_d(\boldsymbol{d}, \text{grad}\, \boldsymbol{d}) = \psi_d(\boldsymbol{R}\boldsymbol{d}, \boldsymbol{R} \cdot \text{grad}\, \boldsymbol{d} \cdot \boldsymbol{R}^T), \tag{2.48}$$

where $\boldsymbol{R}$ is an arbitrary proper orthogonal tensor. To ensure this, we follow Ericksen (1961) and impose conditions on the free energy density so that it satisfies the above requirement of objectivity. Let the rigid body rotation $\boldsymbol{R} = \boldsymbol{R}(t)$ be a function of time, with $\boldsymbol{R}(0) = \boldsymbol{I}$, we obtain

$$\dot{\boldsymbol{R}}(0) + \dot{\boldsymbol{R}}^T(0) = 0. \tag{2.49}$$

The statement above can be written as

$$\begin{aligned} \dot{\psi}_d(0) &= \frac{\partial \psi_d}{\partial \boldsymbol{d}} \cdot \dot{\boldsymbol{R}}(0)\boldsymbol{d} + \frac{\partial \psi_d}{\partial \text{grad}\, \boldsymbol{d}} \cdot \left[\dot{\boldsymbol{R}}(0)\boldsymbol{d} - \boldsymbol{d}\dot{\boldsymbol{R}}(0)\right] \\ &= \dot{\boldsymbol{R}}(0) : \left[\frac{\partial \psi_d}{\partial \boldsymbol{d}} \otimes \boldsymbol{d} + \frac{\partial \psi_d}{\partial \text{grad}\, \boldsymbol{d}} (\text{grad}\, \boldsymbol{d})^T + \left(\frac{\partial \psi_d}{\partial \text{grad}\, \boldsymbol{d}}\right)^T \text{grad}\, \boldsymbol{d}\right] = 0. \end{aligned} \tag{2.50}$$

Since $\boldsymbol{R}$ is proper orthogonal, $\boldsymbol{R}(t)\boldsymbol{R}^T(t) = \boldsymbol{I}$, differentiating this with respect to t gives

$$\dot{\boldsymbol{R}}\boldsymbol{R}^T + \boldsymbol{R}^T\dot{\boldsymbol{R}} = 0. \tag{2.51}$$

Therefore, $\dot{\boldsymbol{R}}(0)$ is a skew-symmetric tensor. Eqn (2.50) must hold for any arbitrary $\boldsymbol{R}$, and hence the term in square brackets must be symmetric, or equivalently,

$$\epsilon_{ijk}\left(d_j \frac{\partial \psi_d}{\partial d_k} + d_{j,l}\frac{\partial \psi_d}{\partial d_{k,l}} + d_{l,j}\frac{\partial \psi_d}{\partial d_{l,k}}\right) = 0. \tag{2.52}$$

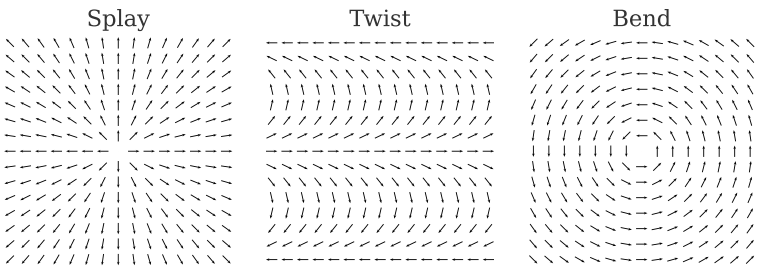

Figure 2.5: Splay, twist and bend distortion modes of liquid crystal

This relation is known as Ericksen's identity. If a free energy function satisfies this condition, the torque arising from the director field is exactly balanced by the antisymmetric part of the force stress, so that the net couple on any material sub-body vanishes. In this sense the continuum is resultant-couple free: only force tractions are needed, and no independent surface or body couples are present in the theory.

The most widely used constitutive model of director distortional elasticity was proposed by Oseen and Frank. Oseen (Oseen, 1933) first proposed the phenomenological model that quantifies this excess energy, and later in 1958, Frank (Frank, 1958) completed the theory. They considered that there are in general four modes of distortion: splay, twist, bend and saddle-splay, as shown in Figure 2.5 (except the saddle-splay mode, which cannot be visualised). The Frank-Oseen elastic free energy density is derived by taking into account all four modes of distortion:

$$\begin{aligned}\psi_{OF} = &\frac{1}{2}K_{11}(\text{div } \boldsymbol{d})^2 + \frac{1}{2}K_{22}[\boldsymbol{d}\cdot(\text{curl } \boldsymbol{d})]^2 + \frac{1}{2}K_{33}[\boldsymbol{d}\times(\text{curl } \boldsymbol{d})]^2 \\ &+ K_{24}\left[\text{tr } (\text{grad } \boldsymbol{d})^2 - (\text{div } \boldsymbol{d})^2\right],\end{aligned} \tag{2.53}$$

where $K_{11}, K_{22}, K_{33}, K_{24}$ are material constants corresponding to splay, twist, bend, and saddle-splay, respectively. We omit the derivation of this free energy density function, interested readers are referred to the original papers mentioned above or classical textbooks like de Gennes and Prost (1993); Virga (2019); Stewart (2021), or this very pedagogical review paper Andrienko (2018). For this free energy to be positive semidef-

inite, Ericksen (1966) determined the following conditions:

$$K_{11} \geq K_{24}, \quad K_{22} \geq K_{24} \geq 0, \quad K_{33} \geq 0. \tag{2.54}$$

While the Frank-Oseen free energy quantifies the energetic cost of distortions, a continuum model is required to clearly state the balance equations and state laws for the static problem of liquid crystal distortional elasticity. Ericksen (Ericksen, 1962) proposed a variational theory on the hydrostatic problems of liquid crystal. Here we adopt the general ideas and assumptions and rederive the variational formulation with the notations consistent with the thesis. We assume a body subjected to a field of body force $\boldsymbol{B}$ in $\mathcal{B}_0$ (force per unit volume in the reference configuration) and to a field of external tractions $\boldsymbol{T}$ applied on its external boundary $\partial\mathcal{B}_0$. The total potential energy of the body is given by:

$$\begin{aligned} I(\boldsymbol{\varphi}, \boldsymbol{d}, \beta, p) = &\int_{\mathcal{B}_0} \Psi(\boldsymbol{F}, \boldsymbol{d}, \operatorname{grad} \boldsymbol{d})\, dV - \int_{\mathcal{B}_0} \boldsymbol{B} \cdot \boldsymbol{\varphi}\, dV - \int_{\partial\mathcal{B}_0} \boldsymbol{T} \cdot \boldsymbol{\varphi}\, dS \\ &+ \int_{\mathcal{B}_0} \frac{1}{2}\beta J(\boldsymbol{d} \cdot \boldsymbol{d} - 1)\, dV + \int_{\mathcal{B}_0} p(J-1)\, dV, \end{aligned} \tag{2.55}$$

where $\boldsymbol{\varphi}$ is the displacement field, $\boldsymbol{F}$ is the deformation gradient, β is the Lagrange multiplier constraining the unity of directors, and p is the Lagrange multiplier applying the incompressibility constraint. In the absence of any elastic strain energy associated with deformation, the free energy can be written as:

$$\Psi(\boldsymbol{F}, \boldsymbol{d}, \operatorname{grad} \boldsymbol{d}) = J\psi_{OF}(\boldsymbol{d}, \operatorname{grad} \boldsymbol{d}). \tag{2.56}$$

We seek to minimise the total potential energy with respect to all admissible fields $\boldsymbol{\varphi}$ and $\boldsymbol{d}$ with $|\boldsymbol{d}| = 1$ and $J = 1$.

Variation $\delta\boldsymbol{\varphi}$ Consider the first variation $\boldsymbol{\varphi} \rightarrow \boldsymbol{\varphi} + \varepsilon\delta\boldsymbol{\varphi}$ around the true solution $(\boldsymbol{\varphi}, \boldsymbol{d}, \beta, p)$, and define the corresponding variation of the potential energy as:

$$\delta_{\boldsymbol{\varphi}} I = \frac{d}{d\varepsilon}[I(\boldsymbol{\varphi} + \varepsilon\delta\boldsymbol{\varphi}, \boldsymbol{d}, \beta, p)]|_{\varepsilon=0}. \tag{2.57}$$

The variation of Ψ writes:

$$\delta_{\boldsymbol{\varphi}}\Psi = \psi_{OF}\delta_{\boldsymbol{\varphi}}J + J\frac{\partial\psi_{OF}}{\partial \text{grad } \boldsymbol{d}} : \delta_{\boldsymbol{\varphi}}\text{grad } \boldsymbol{d}. \tag{2.58}$$

Here we list a few useful results derived from Eqn. 5.2, 2.8 and 2.10:

$$\begin{aligned} \delta_{\boldsymbol{\varphi}}\boldsymbol{F} &= \text{Grad } \delta_{\boldsymbol{\varphi}}\boldsymbol{\varphi}, \\ \delta_{\boldsymbol{\varphi}}\boldsymbol{f} &= -\boldsymbol{f} \cdot \delta_{\boldsymbol{\varphi}}\boldsymbol{F} \cdot \boldsymbol{f}, \\ \delta_{\boldsymbol{\varphi}}J &= J\boldsymbol{f}^T : \delta_{\boldsymbol{\varphi}}\boldsymbol{F}, \\ \delta_{\boldsymbol{\varphi}}\text{grad } \boldsymbol{d} &= \text{Grad } \boldsymbol{d} \cdot \delta_{\boldsymbol{\varphi}}\boldsymbol{f}. \end{aligned} \tag{2.59}$$

Inserting the results 2.58 - 2.59 back into Eqn. 2.57, we obtain:

$$\int_{\mathcal{B}_0} \boldsymbol{P} : \text{Grad } \delta\boldsymbol{\varphi}\, dV - \int_{\mathcal{B}_0} \boldsymbol{B} \cdot \delta\boldsymbol{\varphi}\, dV - \int_{\partial\mathcal{B}_0} \boldsymbol{T} \cdot \delta\boldsymbol{\varphi}\, dS = 0, \tag{2.60}$$

where $\boldsymbol{P}$ represents the first Piola-Kirchhoff stress, given by:

$$\boldsymbol{P} = J\psi_{OF}\boldsymbol{f}^T + J\boldsymbol{\sigma}^E \cdot \boldsymbol{f}^T + J\psi_d^C\boldsymbol{f}^T + pJ\boldsymbol{f}^T, \tag{2.61}$$

where we have also included the contribution from the constraint:

$$\psi_d^C = \frac{1}{2}\beta(\boldsymbol{d} \cdot \boldsymbol{d} - 1). \tag{2.62}$$

$\boldsymbol{\sigma}^E$ denotes the Ericksen stress:

$$\boldsymbol{\sigma}^E = -(\text{grad } \boldsymbol{d})^T \cdot \frac{\partial \psi_{OF}}{\partial \text{grad } \boldsymbol{d}}. \tag{2.63}$$

It describes the contribution to the mechanical stress arising solely from distortions of the director field. In other words, gradients of the director $\boldsymbol{d}$ store distortional elastic energy through the density $\psi_{OF}(\boldsymbol{d}, \text{grad } \boldsymbol{d})$, and the associated internal forces are transmitted mechanically via $\boldsymbol{\sigma}^E$.

From Eqn. 2.60, using integration by parts and the divergence theorem, we obtain the following strong form:

$$\begin{aligned} &\text{Div } \boldsymbol{P} + \boldsymbol{B} = 0 \quad \text{in } \mathcal{B}_0, \\ &\boldsymbol{P} \cdot \boldsymbol{N} = \boldsymbol{T} \quad \text{on } \partial\mathcal{B}_0. \end{aligned} \tag{2.64}$$

This is the balance of linear momentum written in the reference configuration: the divergence of the first Piola–Kirchhoff stress $\boldsymbol{P}$ balances the body force density $\boldsymbol{B}$ (per unit reference volume), and the boundary condition states that the nominal traction transmitted across the boundary equals the prescribed traction $\boldsymbol{T}$.

Variation $\delta \boldsymbol{d}$ Consider next variation $\boldsymbol{d} \rightarrow \boldsymbol{d} + \eta\delta\boldsymbol{d}$, around the true solution $(\boldsymbol{\varphi}, \boldsymbol{d}, \beta, p)$. We define the corresponding variation of the potential energy as:

$$\delta_d I = \frac{d}{d\eta} \left[I(\boldsymbol{\varphi}, \boldsymbol{d} + \eta\delta\boldsymbol{d}, \beta, p) \right] |_{\eta=0}. \tag{2.65}$$

The true solution $(\boldsymbol{\varphi}, \boldsymbol{d}, \beta, p)$ must satisfy $\delta_{\boldsymbol{d}} I = 0$. This condition yields the following weak form:

$$\int_{\mathcal{B}_0} J \left[(\boldsymbol{r} + \beta\boldsymbol{d}) \cdot \delta\boldsymbol{d} + \boldsymbol{s} : \text{grad } \delta\boldsymbol{d} \right] \, dV = 0, \tag{2.66}$$

where $\boldsymbol{s}$ represents the torque stress:

$$\boldsymbol{s} = \frac{\partial \psi_{OF}}{\partial \text{grad}\, \boldsymbol{d}}, \tag{2.67}$$

and $\boldsymbol{r}$ represents the intrinsic body force:

$$\boldsymbol{r} = \frac{\partial \psi_{OF}}{\partial \boldsymbol{d}}. \tag{2.68}$$

The quantities $\boldsymbol{s}$ and $\boldsymbol{r}$ play the same role for the director as the stress and body force do for the deformation in standard continuum mechanics. The torque stress is energetically conjugate to the director gradient grad $\boldsymbol{d}$. Physically, $\boldsymbol{s}$ represents the internal moment per unit area transmitted across an oriented surface due to spatial variations of the director. It tends to rotate the director and therefore accounts for the orientational torque. The vector $\boldsymbol{r}$ acts on the director and is conjugate to $\boldsymbol{d}$. It represents a distributed tendency to rotate the director arising from the local dependence of the free energy on $\boldsymbol{d}$ itself, for example due to external electric or magnetic field energies. The corresponding strong form is easily obtained using the divergence theorem:

$$\text{div}\boldsymbol{s} - \boldsymbol{r} = \beta \boldsymbol{d} \quad \text{in } \mathcal{B}_t, \tag{2.69}$$

$$\boldsymbol{s} \cdot \boldsymbol{n} = 0 \quad \text{on } \partial\mathcal{B}_t. \tag{2.70}$$

These equations express the balance of torques acting on the director: the divergence of the microstress $\boldsymbol{s}$ combining with the intrinsic body force $\boldsymbol{r}$ present as a field that provides a preferred direction for the director. As an analogy, the classical deformational stress $\boldsymbol{\sigma}$ is conjugated to the gradient of displacement $\boldsymbol{\varphi}$. Its divergence combined with body force present as a field that provides a preferred direction for the displacement. Note that the traction-free boundary condition in Eqn. 2.70 is not a universal requirement, but follows from our assumption that no external surface microtraction acts on

the director field. If surface anchoring, electric or magnetic boundary interactions, or other interfacial energetic effects are included, the natural boundary condition must be modified accordingly and specified from the associated boundary contribution to the free energy.

Variation $\delta\beta$ In addition, we consider the variation on the Lagrange multiplier $\delta\beta \rightarrow \beta + \xi\delta\beta$, around the true solution $(\boldsymbol{\varphi}, \boldsymbol{d}, \beta, p)$. We define the corresponding variation of potential energy as:

$$\delta_\beta I = \frac{d}{d\xi}[I(\boldsymbol{\varphi}, \boldsymbol{d}, \beta + \xi\delta\beta, p)]|_{\xi=0}. \tag{2.71}$$

The true solution must satisfy $\delta_\beta I = 0$, which leads to:

$$\int_{\mathcal{B}_0} \frac{J}{2}(\boldsymbol{d}\cdot\boldsymbol{d} - 1)\, dV = 0, \tag{2.72}$$

or alternatively in the strong form:

$$|\boldsymbol{d}| = 1 \quad \text{in } \mathcal{B}_0. \tag{2.73}$$

Variation δp Finally, we consider the variation on the Lagrange multiplier $\delta p \rightarrow p + \zeta\delta p$, around the true solution $(\boldsymbol{\varphi}, \boldsymbol{d}, \beta, p)$. We define the corresponding variation of potential energy as:

$$\delta_p I = \frac{d}{d\zeta}[I(\boldsymbol{\varphi}, \boldsymbol{d}, \beta, p + \zeta\delta p)]|_{\zeta=0}, \tag{2.74}$$

The true solution must satisfy $\delta_p I = 0$, which leads to:

$$\int_{\mathcal{B}_0} (J - 1)\, dV = 0, \tag{2.75}$$

or alternatively in the strong form:

$$J = 1 \quad \text{in } \mathcal{B}_0. \tag{2.76}$$

The governing equations obtained above, though with a different method, are identical to classical equations obtained by Ericksen and can be found in textbooks (Sonnet and Virga, 2012; Stewart, 2021).

Physical interpretation of Ericksen stress To better understand the physical meaning of Ericksen's stress, we introduce a simple example. Consider the one-constant approximation of the Oseen–Frank energy (Eqn. 2.53),

$$\psi_{OF} = \frac{K}{2}|\text{grad}\,\boldsymbol{d}|^2, \tag{2.77}$$

where K is a constant. With this choice,

$$\frac{\partial \psi_{OF}}{\partial(\text{grad}\,\boldsymbol{d})} = K\,\text{grad}\,\boldsymbol{d}, \qquad \Rightarrow \qquad \boldsymbol{\sigma}^E = -K\,(\text{grad}\,\boldsymbol{d})^T(\text{grad}\,\boldsymbol{d}). \tag{2.78}$$

If the director field is uniform, e.g. $\boldsymbol{d} = (1, 0, 0)$, then $\text{grad}\,\boldsymbol{d} = \mathbf{0}$, and therefore $\psi_{OF} = 0$ and $\boldsymbol{\sigma}^E = \mathbf{0}$. Consider a layer of liquid crystal $0 < z < h$ between two rigid plates. We impose Dirichlet boundary conditions on the top and bottom planes,

$$\boldsymbol{d}(0) = (1, 0, 0), \qquad \boldsymbol{d}(h) = (\cos\theta_0, 0, \sin\theta_0), \tag{2.79}$$

so that the director must bend through the thickness. This simple setting is illustrated in Figure 2.6. The imposed mismatch between the director orientations at the two plates creates a spatial variation of $\boldsymbol{d}$ through the layer. When the plate separation is reduced while the boundary orientations are kept fixed, the same change in director orientation must occur over a smaller distance. The director gradient therefore becomes larger, which increases the Oseen–Frank elastic energy and produces a corresponding elastic stress contribution.

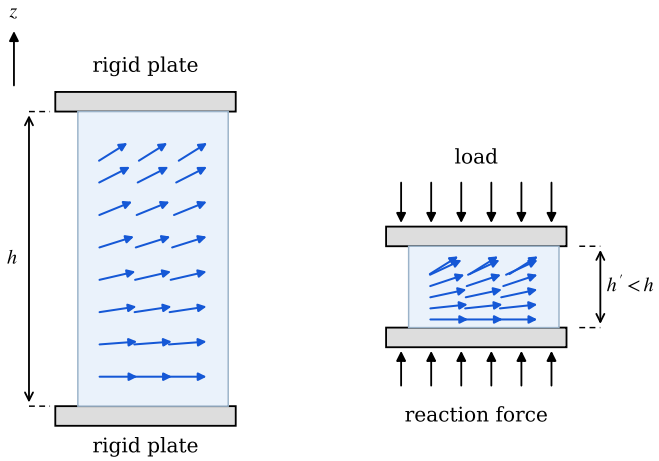

Figure 2.6: Schematic illustration of the physical interpretation of Ericksen stress. A liquid crystal layer confined between two rigid plates develops a director distortion due to the imposed anchoring mismatch. Reducing the plate separation increases the director gradient, leading to a larger orientational elastic stress contribution.

Introduce the parametrisation

$$\boldsymbol{d}(z) = (\cos\theta(z),\, 0,\, \sin\theta(z)). \tag{2.80}$$

Under the one-constant approximation (2.77),

$$\psi_{OF} = \frac{K}{2}|\mathrm{grad}\,\boldsymbol{d}|^2 = \frac{K}{2}\left(\frac{d\theta}{dz}\right)^2, \tag{2.81}$$

since $|d\boldsymbol{d}/dz|^2 = (\theta')^2$. Minimising the Oseen–Frank energy subject to the boundary conditions yields the linear profile

$$\theta(z) = \frac{\theta_0}{h}\,z, \qquad \Rightarrow \qquad \theta' = \frac{\theta_0}{h}. \tag{2.82}$$

The Oseen–Frank energy per unit area is

$$\frac{E}{A} = \int_0^h \psi_{OF}\, dz = \int_0^h \frac{K}{2}\left(\frac{\theta_0}{h}\right)^2 dz = \frac{K\,\theta_0^2}{2h}. \tag{2.83}$$

Suppose a normal load is applied by changing the plate separation h while keeping θ_0 fixed. The nominal normal traction conjugate to h obtained from the Oseen–Frank energy is

$$T_n^{\text{el}} \;=\; -\frac{d}{dh}\left(\frac{E}{A}\right) \;=\; \frac{K\,\theta_0^2}{2h^2}, \tag{2.84}$$

which is nonzero. For the present one-dimensional distortion, $(\operatorname{grad}\boldsymbol{d})^T(\operatorname{grad}\boldsymbol{d}) = (\theta')^2\,\boldsymbol{e}_z\otimes\boldsymbol{e}_z$, and therefore Ericksen's stress is

$$\boldsymbol{\sigma}^E = -K\left(\frac{\theta_0}{h}\right)^2 \boldsymbol{e}_z\otimes\boldsymbol{e}_z. \tag{2.85}$$

The corresponding traction contribution on the plates is the vector

$$\boldsymbol{t}_E = \boldsymbol{\sigma}^E\boldsymbol{n} = -K\left(\frac{\theta_0}{h}\right)^2 \boldsymbol{e}_z. \tag{2.86}$$

Including the isotropic contribution associated with the $J\psi_{OF}\boldsymbol{f}^T$ term (cf. Eqn. 2.61), the Oseen–Frank elastic Cauchy stress may be written as

$$\boldsymbol{\sigma}^{\text{el}} = \psi_{OF}\boldsymbol{I} - (\operatorname{grad}\boldsymbol{d})^T\cdot\frac{\partial\psi_{OF}}{\partial(\operatorname{grad}\boldsymbol{d})} = \psi_{OF}\boldsymbol{I} + \boldsymbol{\sigma}^E. \tag{2.87}$$

In this example,

$$\sigma_{zz}^{\text{el}} = \psi_{OF} + \sigma_{zz}^E = \frac{K}{2}(\theta')^2 - K(\theta')^2 = -\frac{K}{2}\left(\frac{\theta_0}{h}\right)^2, \tag{2.88}$$

which is consistent with $T_n^{\text{el}} = \frac{K\theta_0^2}{2h^2}$. In addition, if incompressibility is enforced via a

Lagrange multiplier p, the total Cauchy stress is

$$\boldsymbol{\sigma} = p\,\boldsymbol{I} + \boldsymbol{\sigma}^{\mathrm{el}}, \tag{2.89}$$

and p is determined from the mechanical boundary conditions. For traction-free lateral sides, one requires $\boldsymbol{\sigma n} = \mathbf{0}$ on surfaces with $\boldsymbol{n} = \boldsymbol{e}_x$ and $\boldsymbol{n} = \boldsymbol{e}_y$, which yields

$$p + \sigma^{\mathrm{el}}_{xx} = 0 \qquad \Rightarrow \qquad p = -\psi_{OF} = -\frac{K}{2}\left(\frac{\theta_0}{h}\right)^2. \tag{2.90}$$

The resulting normal stress on the plates is then

$$\sigma_{zz} = p + \sigma^{\mathrm{el}}_{zz} = -K\left(\frac{\theta_0}{h}\right)^2, \tag{2.91}$$

so that the total normal traction magnitude on the plates scales as $|t_n| = K(\theta_0/h)^2$ when the lateral sides are traction-free.

2.2.3.2 Q-tensor theories

Alternatively, the $\boldsymbol{Q}$-tensor theory, originally proposed by de Gennes (de Gennes and Prost, 1993), uses spatial variations of $\boldsymbol{Q}$ to describe the excess elastic free energy. The scalar free energy must be a function of invariants constructed from $\boldsymbol{Q}$ and its spatial derivatives. Up to second order in gradients, four independent invariants can be formed:

$$\begin{aligned}
I_1^Q &= \operatorname{grad}\boldsymbol{Q} \vdots \operatorname{grad}\boldsymbol{Q} = Q_{ij,k}Q_{ij,k},\\
I_2^Q &= \operatorname{div}\boldsymbol{Q} \cdot \operatorname{div}\boldsymbol{Q} = Q_{ij,j}Q_{ik,k},\\
I_3^Q &= Q_{ij,k}Q_{ik,j},\\
I_4^Q &= \epsilon_{ikl}\,Q_{ij}\,Q_{lj,k}.
\end{aligned} \tag{2.92}$$

The last invariant I_4^Q is only relevant for chiral (cholesteric) liquid crystals and gives rise to a linear gradient term in the free energy. For achiral nematics, it is usually neglected. In that case, the $\boldsymbol{Q}$-tensor-based elastic energy density can be written as

$$\psi_Q = \frac{L_1}{2} I_1^Q + \frac{L_2}{2} I_2^Q + \frac{L_3}{2} I_3^Q, \tag{2.93}$$

where L_1, L_2, and L_3 are elastic constants. The governing equations can be obtained by a variational procedure analogous to that used for the director theory; the derivation is not presented here. A detailed variational formulation of the $\boldsymbol{Q}$-tensor theory, and its relation to the director-based description, will be given in Chapter 3.

The director and $\boldsymbol{Q}$-tensor theories each have advantages and limitations. Director-based models such as the Oseen-Frank theory are conceptually simple and computationally inexpensive: the state of the nematic is described by a unit vector field $\boldsymbol{d}$, and the elastic energy involves only a few material constants. They are very effective when the nematic is strongly ordered, essentially uniaxial, and away from defects or phase boundaries, which explains their widespread use in classical liquid-crystal device modelling. However, director theories cannot describe variations of the scalar order parameter, isotropic-nematic interfaces, or the internal structure and finite core energy of topological defects; they also struggle when biaxiality becomes important. By contrast, the $\boldsymbol{Q}$-tensor theory provides a more general continuum description: the symmetric traceless tensor $\boldsymbol{Q}$ can accommodate changes in the degree of order, biaxial states, and the isotropic-nematic phase transition within a single framework. In particular, it avoids singularity close to topological defects, which may arise numerical difficulties using director thories. The drawback is a larger number of degrees of freedom and elastic coefficients, and consequently a higher computational cost. In contemporary work, director theories remain popular for macroscopic device-scale modelling with smooth textures, while $\boldsymbol{Q}$-tensor models are increasingly preferred for problems involving defects, phase

transitions, strong confinement, or coupling to additional fields, which is the regime of interest in this thesis.

2.3 Theories of interfacial effects in elasticity and liquid crystal

In a heterogeneous system, there naturally exist interfaces separating different media. The interfacial effects on the overall behaviour of the system cannot be neglected when the surface area/volume ratio is large, such as small droplets and inclusions in a surrounding medium. Depending on the system, the competition between interfacial behaviour and other physics leads to many coupled problems (Style et al., 2013; Sharma et al., 2003; Jamali et al., 2015; Koizumi et al., 2023; Schimming and Viñals, 2022). In particular, there are two types of problems that are very close to what we are interested in: elastocapillary problems and shape optimisation problems of liquid crystal droplets. The former corresponds to the competition between surface and elasticity, and the latter describes the balance between surface and the director field of liquid crystal.

2.3.1 Theories of elastocapillarity

The term elastocapillarity refers to problems in which bulk elasticity competes with capillary forces. Classically, capillarity describes the rise or fall of liquids in narrow tubes in the absence of external forces. The first and most well-known quantitative descriptions of capillarity were developed by Young (Young, 1805), who introduced the concept of the contact angle, and by Laplace (de Laplace, 1808), who derived the pressure jump across a curved interface; their results are now combined and known as the Young-Laplace equation. Building on this work, Gibbs established a general variational thermodynamic framework for interfaces and surface tension (Gibbs, 1878). In

the spirit of Gibbs' formulation, Gurtin and Murdoch (Gurtin and Murdoch, 1975) proposed a phenomenological continuum model for surface stress and extended the theory to non-liquid interfaces, such as solid-fluid and solid-solid interfaces. Interfacial energy is often negligible at macroscopic scales and was therefore traditionally ignored in engineering mechanics, but it becomes crucial in soft materials and small-scale systems, which are the focus of elastocapillarity.

For example, in classical composite material models, the size of the inclusions/fibres is not relevant to the overall material properties. This is because the interfacial energy can be neglected compared to the elastic strain energy in the bulk material. However, in certain cases where the inhomogeneities are small and/or the elastic matrix is soft, the interfacial energy can be comparable to the bulk energy. The first case is common in nanomaterials and has been studied extensively for decades (Sharma et al., 2003; Duan et al., 2005a,b). More recently, surface elasticity theories have been extended to soft materials containing liquid inclusions (Henann and Bertoldi, 2014; Style et al., 2015a,b; Wang and Henann, 2016; Ghosh and Lopez-Pamies, 2022). Intuitively, or following classical composite theories, when a liquid inclusion is placed in an elastic matrix, it should reduce the overall stiffness of the composite, as the shear modulus of the liquid is negligible. However, Style et al. (2015a) found that when liquid inclusions are small and the matrix is soft, the composite can be stiffened by the addition of liquid inclusions. This counter-intuitive behaviour is a result of surface elasticity and can be characterised through the non-dimensional elastocapillary number, $\xi = \gamma/(GR)$. During deformation, the inclusion changes shape, which increases the interfacial area and generates excess surface energy. This excess surface energy provides resistance to the deformation and leads to the stiffening effect. Numerous models have been developed to describe surface elasticity theoretically and numerically. Among these theories, Steinmann (2008) proposed a general framework based on variational theories for boundary potentials including not only surfaces, but also lines. The framework was further illus-

trated through finite element modelling (Javili and Steinmann, 2009, 2010). In particular, Javili and Steinmann (2010) showed the effect of anisotropic surface energy on the capillary-induced deformation of soft materials. Although anisotropic surface energy is uncommon for liquid inclusions, it plays a key role at liquid crystal interfaces, as illustrated in the next subsection.

2.3.2 Shape optimisation problem of liquid crystal droplets

For heterogeneous systems consisting of liquid crystals, the interface is no longer isotropic like that of simple liquids. Liquid crystal directors near the interface tend to orient along the surface with a specific angle, where this direction is usually called the easy axis. This behaviour is termed the anchoring effect. Anchoring effects can be categorised into homeotropic and planar, where the easy axis for these cases is the surface normal and the tangent vector, respectively. For rod-like molecules near a structureless interface, the anchoring effect is usually planar. Microscopically, this is because when the rod-like molecules are normal to the interface, there is only one possible placement option for the molecules, which is entropically unfavourable. The orientational entropy is maximised when the rod-like molecules are parallel to the interface, so that they can spin freely within the tangential plane of the interface (Tjipto-Margo and Sullivan, 1988). In addition, when the interaction between the liquid crystal molecules and the molecules across the interface is attractive (negative interaction potential), it will also result in planar anchoring, as the interaction energy is minimised when the contact area between the interface and the liquid crystal is maximised. On the other hand, when the interaction is repulsive, homeotropic anchoring is expected. In practical applications, interfaces can be modified through rubbing or grooving, through which the easy axis can be designed to meet the desired properties.

Due to the anchoring effect, the interfacial energy is anisotropic. A number of mathematical models have been proposed to describe different interfacial behaviours.

The simplest form of anisotropic surface energy was proposed by Rapini and Papoular (1969), and reads

$$\psi_{RP} = \frac{1}{2}\,\gamma\,\omega\sin^2\alpha, \tag{2.94}$$

where ω is the dimensionless anchoring strength and α is the angle between the director $\boldsymbol{d}$ and the easy axis. Taking into account the isotropic surface tension, this can alternatively be written as

$$\psi_{RP} = \gamma\left[1 + \omega(\boldsymbol{d}\cdot\boldsymbol{n})^2\right]. \tag{2.95}$$

If $\boldsymbol{n}$ is the outer normal vector of the interface, directors prefer to stay aligned with the interface when $\omega > 0$ and perpendicular to the interface when $\omega < 0$. A large number of experimental and theoretical studies have been carried out using this expression (Stelzer et al., 1997; Dozov et al., 2000; Yang et al., 2001; Andrienko and Allen, 2002; Teixeira de Souza et al., 2009; Willman et al., 2014; Safdari et al., 2021).

One typical problem of interest is finding the shape and director field of a liquid crystal droplet. This problem was first reported by Zocher (Zocher, 1925), who found that colloids in solution aggregate and form microdroplets that present optical anisotropy and textures like liquid crystals. These microdroplets are prolate ellipsoids with pointy ends at their major axes. This shape was later found in other types of liquids such as tobacco mosaic viruses (Bawden et al., 1936), polypeptides (Robinson, 1956), and bacterial phages (Tarafder et al., 2020). From experimental observations (Kaznacheev et al., 2002), liquid crystal droplets with smaller volume tend to be more elongated, while larger droplets are more spherical.

The first and most classical attempt to describe this phenomenon is through the Wulff construction for crystalline surfaces (Wulff, 1901). This method was adapted to solve liquid crystal droplet problems by assuming that the directors are all fixed and aligned (see Figure 2.7) (Virga, 2019). This model showed that liquid crystal droplets

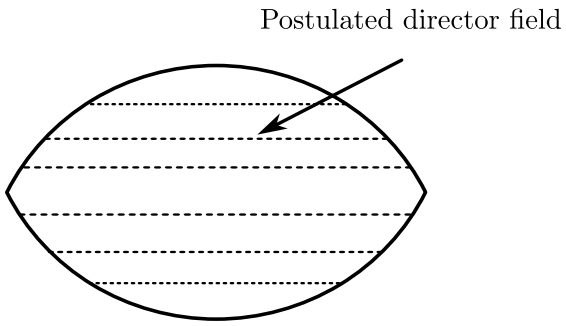

Figure 2.7: Sketch of a liquid crystal droplet with postulated fixed directors in a fluid environment based on Wulff's construction.

with a homogeneous director field and anisotropic surface tension adopt elongated shapes with pointed tips. Although the method is qualitatively reasonable for small droplets, it fails to predict the shapes of larger droplets (Prinsen and van der Schoot, 2003). Prinsen and van der Schoot (2003) and Kaznacheev et al. (2002) proposed a variational method that prescribes the director field as a set of revolving circular arcs that meet at the pointed ends of the droplet, defined in terms of the geometrical parameters of the droplet. The equilibrium shape and director field are obtained by minimising the free energy based on this postulated director field. These models improve the predictions and are able to describe the volume dependence of the droplet shape and director field, but they remain constrained by the strong assumption underlying the prescribed director field. In subsequent work, Prinsen and van der Schoot (2004) extended the theory to less restrictive assumptions by introducing an additional parameter in the director field. These models are very convenient because the director fields are given in explicit form and can readily yield theoretical solutions without complex numerical methods. However, they are fundamentally limited by the assumed ansatz for the director field. Therefore, to obtain more realistic predictions, numerical simulations offer a more direct and detailed description of such a system. For example, Tsige et al. (Tsige et al., 1999) used atomistic simulations for nanoscopic liquid crystal droplets composed of assemblies of 26 and 50 5CB molecules, and demonstrated how nematic ordering and

droplet shape vary with temperature. Bates (Bates, 2003) used Monte Carlo simulations to model a larger system consisting of 112,000 molecules. While these methods are versatile, they are computationally expensive and often require strong assumptions. More recently, finite element models have been developed to address this problem. DeBenedictis and Atherton (2016) used a staggered approach to model the shape and director field in turn and obtained the equilibrium shapes of liquid crystal droplets with different material parameters in 2D. Adler et al. (2023) developed a similar finite element model that determines the shape and director field simultaneously and extended it to 3D predictions. These finite element models are particularly useful for macroscopic liquid crystal droplets, as they offer realistic descriptions at relatively low computational cost.

2.4 Theory of phase separation

The preceding sections have established the mechanical framework for liquid crystal droplets: continuum mechanics to describe deformation, liquid-crystal theories to model the director field, and elastocapillary theory to capture the coupling between elasticity and interfacial tension. Up to this point, droplets have been treated as pre-formed inclusions. In polymer-dispersed liquid crystal (PDLC) materials, however, the droplets emerge dynamically through phase separation of a LC-polymer mixture. We therefore now turn to the thermodynamics of phase separation, and in particular polymerisation-induced phase separation, which sets the size, morphology and distribution of the LC droplets that the previous theories act upon.

2.4.1 Thermodynamics of phase separation

We describe a binary incompressible mixture of A and B by a single composition variable $\phi \in (0, 1)$, taken as the volume fraction of component A (so that $\phi_B = 1 - \phi$). At fixed temperature T, we postulate a homogeneous Helmholtz free energy density

$\psi(\phi, T)$, so that the total Helmholtz free energy of a uniform state occupying volume V is

$$\Psi = V\,\psi(\phi, T). \tag{2.96}$$

Phase separation is driven by non-convexity of $\psi(\phi, T)$: if $\psi(\phi, T)$ develops a double-well shape, the system can lower its total free energy by decomposing into two phases of different compositions.

Local stability (spinodal). Consider small composition fluctuations about a homogeneous state ϕ at a fixed temperature T. For each value of T, we define the composition-dependent free-energy density

$$\psi_T(\phi) := \psi(\phi, T). \tag{2.97}$$

The relevant stability criterion is then determined by the curvature of this function with respect to ϕ:

$$\psi_T''(\phi) := \frac{\mathrm{d}^2\psi_T}{\mathrm{d}\phi^2} = \left.\frac{\partial^2\psi}{\partial\phi^2}\right|_T. \tag{2.98}$$

A homogeneous state is locally stable if

$$\psi_T''(\phi) > 0, \tag{2.99}$$

whereas it is unstable to infinitesimal composition fluctuations if

$$\psi_T''(\phi) < 0. \tag{2.100}$$

The spinodal curve is therefore defined by

$$\psi_T''(\phi) = 0. \tag{2.101}$$

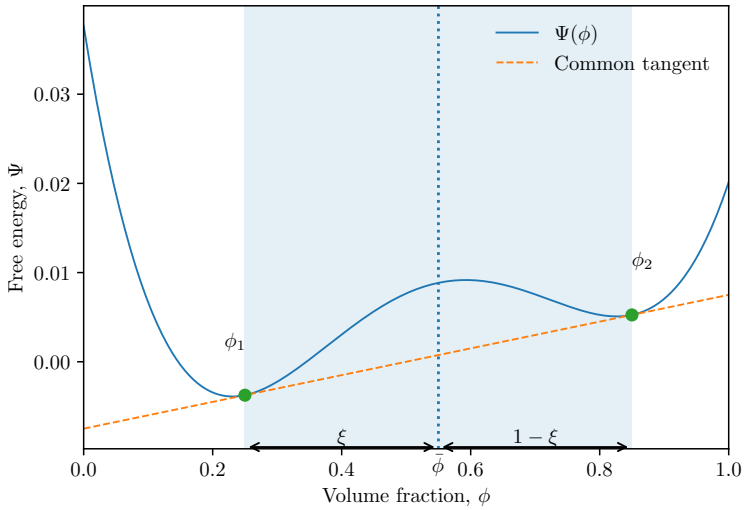

Figure 2.8: Schematic free energy $\Psi(\phi)$ of a binary mixture (solid) and its convex envelope given by the common tangent (dashed). For an overall composition $\bar{\phi} \in (\phi_1, \phi_2)$, the homogeneous state is not globally stable: the system lowers its free energy by separating into two phases of compositions ϕ_1 and ϕ_2.

Phase coexistence (binodal / common tangent). When $\psi'' < 0$, a homogeneous state may still reduce its free energy by separating into two phases with compositions ϕ_1 and ϕ_2. Let $\xi \in (0, 1)$ be the volume fraction of phase 1. Mass conservation gives the lever rule

$$\bar{\phi} = \xi\,\phi_1 + (1-\xi)\,\phi_2, \tag{2.102}$$

where $\bar{\phi}$ is the overall composition. The separated state has free energy density

$$\psi_{\text{sep}}(\bar{\phi}, T) = \xi\,\psi(\phi_1, T) + (1-\xi)\,\psi(\phi_2, T), \tag{2.103}$$

which is the straight line joining $(\phi_1, \psi(\phi_1, T))$ and $(\phi_2, \psi(\phi_2, T))$. The equilibrium coexistence pair (ϕ_1, ϕ_2) minimises the free energy and is given by the common-tangent construction (Fig. 2.8). Equivalently, defining the chemical potential

$$\mu(\phi, T) = \frac{\partial \psi}{\partial \phi}(\phi, T), \tag{2.104}$$

coexistence requires

$$\mu(\phi_1, T) = \mu(\phi_2, T), \tag{2.105}$$

$$\psi(\phi_2, T) - \psi(\phi_1, T) = \mu(\phi_1, T)\,(\phi_2 - \phi_1, T), \tag{2.106}$$

i.e. the tangent line to $\psi(\phi, T)$ has the same slope at ϕ_1 and ϕ_2 and passes through both points. We perform this commen-tangent construction for different values of T, at each temperature we obtain two equilibrium compositions $\phi_1(T)$ and $\phi_2(T)$. Plotting these points in the (ϕ, T) plane results in the binodal curve, which marks the boundary between the single-phase and two-phase regions.

2.4.2 Free energy of mixing

We consider an incompressible binary mixture composed of n_A molecules of species A and n_B molecules of species B, with molecular volumes v_A and v_B, respectively. The total volume is

$$V = n_A v_A + n_B v_B, \tag{2.107}$$

and the volume fractions are

$$\phi_A = \frac{n_A v_A}{V}, \qquad \phi_B = \frac{n_B v_B}{V} = 1 - \phi_A. \tag{2.108}$$

We follow (Brassart et al., 2016) to write the free energy of mixing as the sum of an entropic and an interaction contribution.

Entropy of mixing. Before mixing, A and B molecules occupy volumes $n_A v_A$ and $n_B v_B$, respectively. The numbers of configurations in the isolated pure states and in the

mixed state are

$$W_{\text{iso}} = (n_A v_A)^{n_A} (n_B v_B)^{n_B}, \qquad W_{\text{mix}} = (n_A v_A + n_B v_B)^{n_A+n_B} = V^{n_A+n_B}. \quad (2.109)$$

The entropy change upon mixing is $\Delta S_{\text{mix}} = k_B \ln(W_{\text{mix}}/W_{\text{iso}})$, giving

$$\begin{aligned} \Delta S_{\text{mix}} &= k_B \left[n_A \ln\left(\frac{V}{n_A v_A}\right) + n_B \ln\left(\frac{V}{n_B v_B}\right) \right] \\ &= -k_B \left(n_A \ln \phi_A + n_B \ln \phi_B \right). \end{aligned} \quad (2.110)$$

Dividing by V and using $n_A/V = \phi_A/v_A$ and $n_B/V = \phi_B/v_B$, the entropic free energy density becomes

$$\psi_{\text{ent}}(\phi_A, T) = -T\frac{\Delta S_{\text{mix}}}{V} = k_B T \left(\frac{\phi_A}{v_A} \ln \phi_A + \frac{\phi_B}{v_B} \ln \phi_B \right). \quad (2.111)$$

Interaction energy contribution Interactions between molecules with different volumes can be captured in a mean-field Flory-Huggins form (Flory, 1942; Huggins, 1942), which can also be found in classical textbooks (Rubinstein and Colby, 2003; Doi, 2013). We write the interaction free energy density as

$$\psi_{\text{int}}(\phi_A, T) = \frac{k_B T}{v_0} \chi \, \phi_A \phi_B, \quad (2.112)$$

where v_0 is a chosen reference molecular volume (commonly taken as the solvent molecular volume in polymer solutions) and χ is the dimensionless interaction parameter.

Free energy of mixing. Combining (2.111) and (2.112), we obtain

$$\psi_{\text{mix}}(\phi_A, T) = k_B T \left(\frac{\phi_A}{v_A} \ln \phi_A + \frac{\phi_B}{v_B} \ln \phi_B \right) + \frac{k_B T}{v_0} \chi \, \phi_A \phi_B. \quad (2.113)$$

2.4.3 Mixing of molecules of equal size

Equal-size limit of the general free energy. Starting from the general mixing free energy (Eqn. 2.113), we consider the special case of molecules of equal size, $v_A = v_B = v_0 = v$, and define $\phi := \phi_A$ (so that $\phi_B = 1 - \phi$). The free energy of mixing reduces to the classical symmetric Flory–Huggins form

$$\psi_{\mathrm{mix}}(\phi, T) = \frac{k_B T}{v}\Big[\phi \ln \phi + (1-\phi)\ln(1-\phi) + \chi\,\phi(1-\phi)\Big]. \tag{2.114}$$

Local stability of a homogeneous state is governed by the curvature $\psi'' = \partial^2 \psi_{\mathrm{mix}}/\partial\phi^2$. From Eqn. (2.114),

$$\psi''(\phi, T) = \frac{k_B T}{v}\left(\frac{1}{\phi} + \frac{1}{1-\phi} - 2\chi\right). \tag{2.115}$$

The critical value of χ corresponding to the spinodal condition is defined by $\psi'' = 0$, i.e.

$$\chi_{\mathrm{sp}}(\phi) = \frac{1}{2\phi(1-\phi)}. \tag{2.116}$$

For $\chi < 2$, $\psi''(\phi, T) > 0$ for all $\phi \in (0, 1)$, and the free energy is convex (stable, single phase). At the critical point

$$\phi_c = \frac{1}{2}, \qquad \chi_c = 2, \tag{2.117}$$

the curvature first vanishes. For $\chi > 2$, there exists an interval (ϕ_a, ϕ_b) (with $\phi_a < 1/2 < \phi_b$) in which $\psi'' < 0$ and the homogeneous mixture is unstable (spinodal decomposition).

Equilibrium coexistence compositions are determined by the common-tangent construction. Equivalently, defining the chemical potential

$$\mu(\phi, T) = \frac{\partial \psi_{\mathrm{mix}}}{\partial \phi} = \frac{k_B T}{v}\left[\ln\left(\frac{\phi}{1-\phi}\right) + \chi(1-2\phi)\right], \tag{2.118}$$

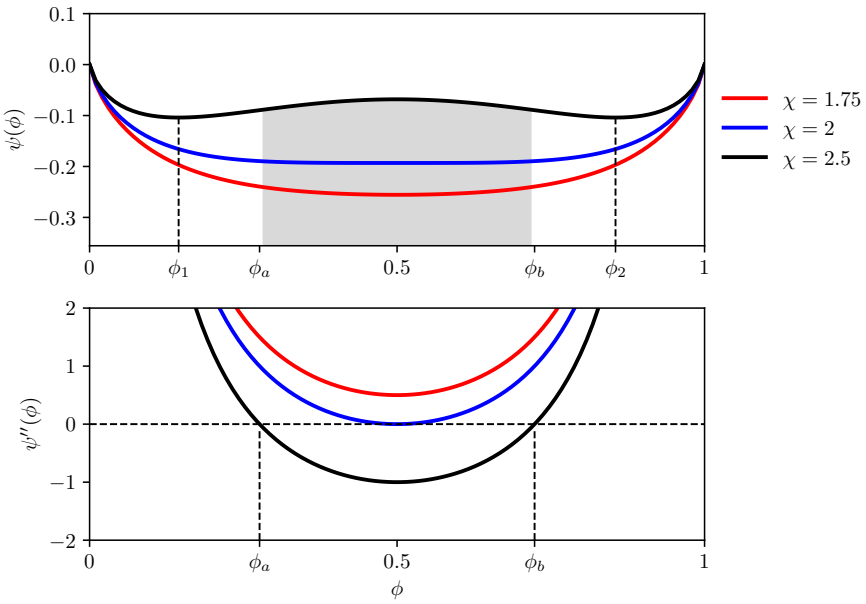

Figure 2.9: Flory–Huggins free energy of mixing for equal-size molecules. Top: $\psi_{\text{mix}}(\phi)$ becomes non-convex for $\chi > 2$, and a homogeneous mixture with $\phi \in (\phi_a, \phi_b)$ is locally unstable. Bottom: curvature $\psi''(\phi)$; the spinodal points ϕ_a and ϕ_b are defined by $\psi'' = 0$. Coexistence compositions (binodal points) are determined by the common-tangent construction on $\psi_{\text{mix}}(\phi)$.

two compositions ϕ_1 and ϕ_2 coexist when

$$\mu(\phi_1, T) = \mu(\phi_2, T), \tag{2.119}$$

$$\psi_{\text{mix}}(\phi_2, T) - \psi_{\text{mix}}(\phi_1, T) = \mu(\phi_1, T)\,(\phi_2 - \phi_1). \tag{2.120}$$

For the equal-size model $\psi_{\text{mix}}(\phi) = \psi_{\text{mix}}(1-\phi)$, so coexistence is symmetric: $\phi_2 = 1 - \phi_1$. The set of coexistence compositions forms the binodal curve. Figure 2.9 illustrates the transition from a convex free energy ($\chi \leq 2$) to a double-well shape ($\chi > 2$), together with the associated spinodal region.

Phase diagram The binodal (coexistence) and spinodal (instability) curves divide the (ϕ, χ) plane into three regimes (Fig. 2.10): (i) a stable single-phase region outside the

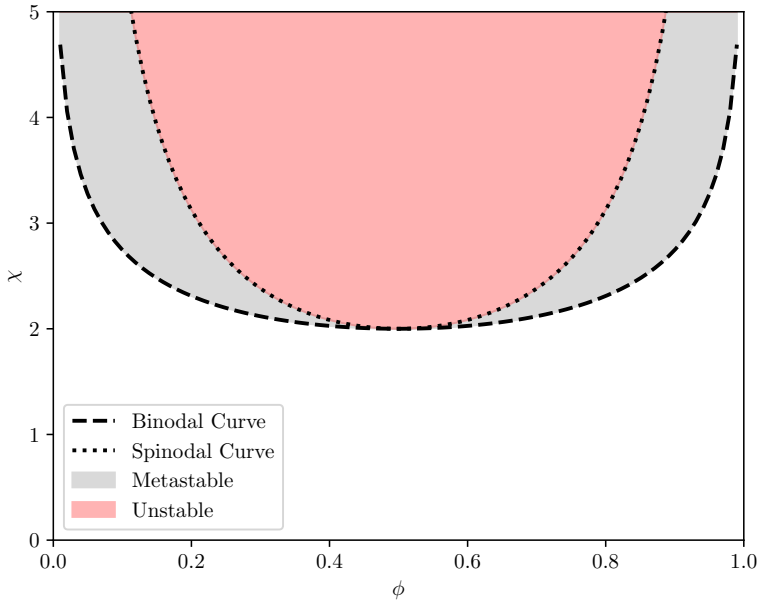

Figure 2.10: Phase diagram for the equal-size Flory–Huggins model in the (ϕ, χ) plane. The spinodal curve is defined by $\psi''(\phi) = 0$ and bounds the region of linear instability. The binodal curve is obtained from the common-tangent construction and gives the equilibrium coexistence compositions. Between binodal and spinodal the mixture is metastable (nucleation and growth); inside the spinodal it is unstable (spinodal decomposition).

binodal, where ψ_{mix} is globally convex; (ii) a metastable region between binodal and spinodal, where phase separation requires a finite perturbation and is driven by nucleation and growth; and (iii) an unstable region inside the spinodal, where infinitesimal fluctuations grow spontaneously and is termed spinodal decomposition. The binodal and spinodal meet at the critical point $(\phi_c, \chi_c) = (1/2, 2)$.

2.4.4 Mixing for polymer solution

In a polymer solution we identify species A as the solvent (s) and species B as the polymer (p), so that $v_A = v_s$ and $v_B = v_p$. We use the polymer volume fraction $\phi := \phi_p$ as the composition variable, with $\phi_s = 1 - \phi$.

Mixing energy for polymer solutions Starting from the general form (Eqn. (2.113)) and choosing the solvent molecular volume as the reference volume $v_0 = v_s$. The free energy density for a polymer solution becomes

$$\psi_{\mathrm{mix}}(\phi, T) = k_B T \left(\frac{\phi_s}{v_s} \ln \phi_s + \frac{\phi}{v_p} \ln \phi \right) + \frac{k_B T}{v_s} \chi \, \phi_s \phi, \qquad \phi_s = 1 - \phi. \tag{2.121}$$

If each polymer chain contains x_n repeat units of comparable size to the solvent molecule, we take $v_p = x_n v_s$. Substituting into Eqn. (2.121) yields the standard polymer-solution form

$$\psi_{\mathrm{mix}}(\phi, T) = \frac{k_B T}{v_s} \left[\phi_s \ln \phi_s + \frac{\phi}{x_n} \ln \phi + \chi(T) \, \phi_s \phi \right]. \tag{2.122}$$

which recovers the classical form defined in (Flory, 1942; Huggins, 1942). Compared with the equal-size case, the entropic contribution from the polymer is reduced by the factor $1/x_n$, reflecting the connectivity of monomers within a chain.

Local stability of a homogeneous composition ϕ is governed by the curvature $\psi'' = \partial^2 \psi_{\mathrm{mix}} / \partial \phi^2$. From Eqn. (2.122),

$$\psi''(\phi, T) = \frac{k_B T}{v_s} \left(\frac{1}{1 - \phi} + \frac{1}{x_n \, \phi} - 2\chi \right). \tag{2.123}$$

The critical value of χ corresponding to the spinodal condition is obtained by $\psi'' = 0$, giving

$$\chi_{\mathrm{sp}}(\phi; x_n) = \frac{1}{2} \left(\frac{1}{1 - \phi} + \frac{1}{x_n \, \phi} \right). \tag{2.124}$$

For fixed χ, increasing x_n decreases the stabilising entropic term $1/(x_n \phi)$ and therefore increases the range of compositions where $\psi'' < 0$.

Coexistence compositions ϕ_1 and ϕ_2 are determined by the common-tangent con-

struction on $\psi_{\mathrm{mix}}(\phi, T)$. Equivalently, introducing the chemical potential

$$\mu(\phi, T) = \frac{\partial \psi_{\mathrm{mix}}}{\partial \phi} = \frac{k_B T}{v_s}\left[\frac{1}{x_n}(\ln\phi + 1) - (\ln(1-\phi) + 1) + \chi(1-2\phi)\right], \quad (2.125)$$

coexistence satisfies

$$\mu(\phi_1, T) = \mu(\phi_2, T), \quad (2.126)$$

$$\psi_{\mathrm{mix}}(\phi_2, T) - \psi_{\mathrm{mix}}(\phi_1, T) = \mu(\phi_1, T)(\phi_2 - \phi_1). \quad (2.127)$$

Unlike the equal-size case, the polymer-solution free energy is generally asymmetric, and the two coexisting compositions are therefore not related by symmetry. For a fixed temperature T, the binodal compositions ϕ_1 and ϕ_2 are determined using the common-tangent construction on the free-energy density $\psi_T(\phi)$. This requires the chemical potentials of the two phases to be equal and the line connecting the two points on the free-energy curve to be tangent at both compositions:

$$\psi_T'(\phi_1) = \psi_T'(\phi_2) = \frac{\psi_T(\phi_2) - \psi_T(\phi_1)}{\phi_2 - \phi_1}. \quad (2.128)$$

In practice, these conditions are solved numerically as two nonlinear algebraic equations for ϕ_1 and ϕ_2, using initial guesses on the dilute and concentrated sides of the phase-separating composition range. For example, one may solve the residual equations

$$R_1(\phi_1, \phi_2) = \psi_T'(\phi_1) - \psi_T'(\phi_2) = 0, \quad (2.129)$$

and

$$R_2(\phi_1, \phi_2) = \psi_T'(\phi_1) - \frac{\psi_T(\phi_2) - \psi_T(\phi_1)}{\phi_2 - \phi_1} = 0 \quad (2.130)$$

with a Newton-type or other standard nonlinear root-finding method.

Figure 2.11 illustrates how increasing x_n turns a convex ψ_{mix} into a double-well

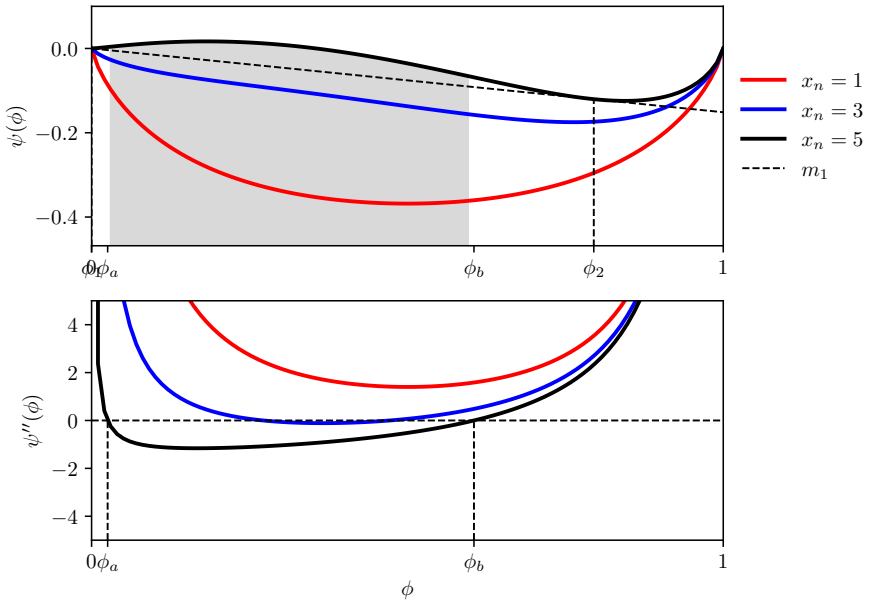

Figure 2.11: Flory–Huggins free energy of mixing for polymer solutions (top) and curvature $\psi''(\phi)$ (bottom) for increasing degree of polymerisation x_n at fixed interaction parameter $\chi = 1.3$.

shape at fixed $\chi = 1.3$. As x_n increases, the polymer entropy term decreases and the free energy can become non-convex, giving rise to a spinodal interval where $\psi'' < 0$. Coexistence compositions are obtained from the common-tangent construction on $\psi_{\mathrm{mix}}(\phi)$.

Phase diagram It is useful to visualise the phase behaviour in the three-dimensional space $\{\phi, \chi, x_n\}$. The spinodal surface is given explicitly by Eqn. (2.124); the binodal surface is obtained from the common-tangent (coexistence) conditions. Figure 2.12 summarises how polymer chain length controls miscibility in the mixing theory. For each fixed x_n, the (ϕ, χ) cross-section recovers the familiar binodal/spinodal structure: outside the binodal the mixture is stable, between binodal and spinodal it is metastable, and inside the spinodal it is unstable. As x_n increases, the polymer contributes less entropy to mixing, reflected by the factor $1/x_n$ in the term $(\phi/x_n)\ln\phi$. This loss of

entropy causes both the binodal and spinodal to move to smaller values of χ and expands the unstable region, meaning that even interactions that cannot lead to demixing for equal-size molecules, they can drive demixing once chains become sufficiently long. In the context of polymerisation-induced phase separation, polymerisation increases x_n in time, so a system may cross the spinodal curve and presents spontaneous demixing even if χ and the overall composition remain fixed. This phenomenon will be further discussed in Chap. 5.

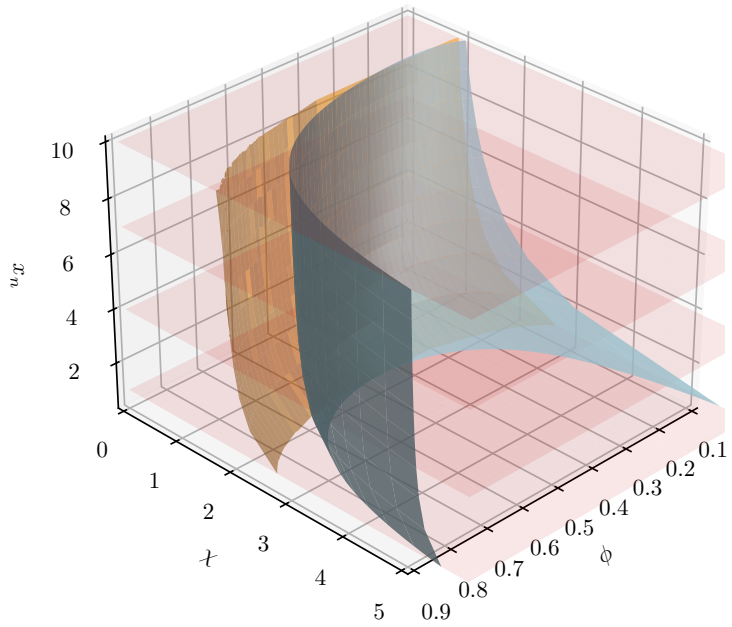

(a)

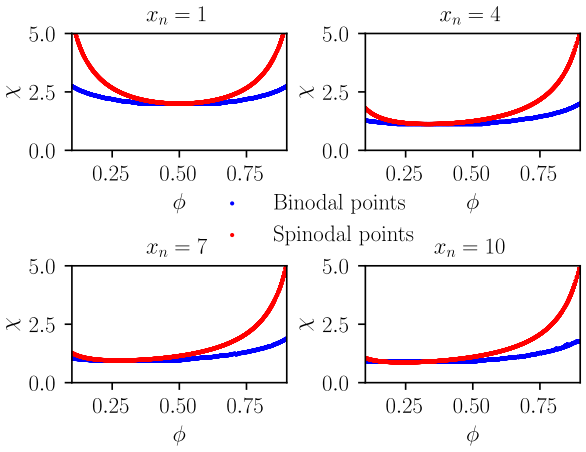

(b)

Figure 2.12: (a) Spinodal (blue) and binodal (orange) surfaces for a polymer solution in $\{\phi, \chi, x_n\}$ space. (b) Representative binodal and spinodal curves at selected x_n (corresponding to slices of the surfaces in (a)). Between binodal and spinodal the mixture is metastable (nucleation and growth); inside the spinodal it is unstable (spinodal decomposition).

3 | Mechanics of liquid crystal inclusions in soft matrices

This chapter presents work that has been published as Bai and Brassart (2025). This study investigates the mechanical response of liquid crystal inclusions embedded in soft matrices. We develop a variational continuum theory for an incompressible neo-Hookean matrix containing nematic liquid crystal inclusions, with the inclusion distortional elasticity described by a Landau-de Gennes formulation and anchoring effect represented through anisotropic surface tension. The theory is implemented numerically using the `FEniCSx` finite element code, enabling systematic parametric studies that clarify how competing physics govern both composite-level stiffening or softening, and inclusion-level director reorientation under applied mechanical loads. In particular, we show that the effective stiffness of the composite depends strongly on the elastocapillary number and anchoring strength. The associated `FEniCSx` code has been made available at `https://doi.org/10.5281/zenodo.14770753`.

3.1 Introduction

Liquid crystal is a state of matter that can flow like a liquid, but possesses certain orientational ordering in space due to the geometric anisotropy of the molecules (de Gennes and Prost, 1993). Due to its mobility, it can respond sensitively to external stimulus like temperature and electric or magnetic fields, and presents orientational-specific behaviour. In applications, liquid crystal materials are usually combined with stiffer materials to achieve suitable mechanical properties while preserving the mobility of the liquid crystal phase. For example, Polymer-Dispersed Liquid Crystal (PDLC) consisting of liquid crystal inclusions dispersed in a polymer matrix are commonly used in applications such as smart windows (Lu et al., 2024b; Ghosh, 2023; Kamal et al., 2022), photovoltaic de-

vices (Khalid et al., 2021) and smart lenses (Ren et al., 2005; Zhang et al., 2020). Fig. 3.1 illustrates the microstructure of a PDLC composite. In the liquid crystal phase, the average orientation of the molecules at a material point is described by the director vector $\boldsymbol{d}$. In the applications mentioned above, the in-service deformation is usually very small, so that the inclusion shape barely changes. Also, the matrix is much stiffer than the interface or the liquid crystal phase, so that the coupling between elastic deformation of the matrix and liquid crystal ordering can be neglected.

In recent years, liquid crystal inclusions embedded in soft matrices have been developed for applications such as sensors, wearable devices and all-solid electrolytes (Song et al., 2017; Zhang et al., 2023; Froyen and Schenning, 2023; Hadjichristov, 2023), combining the stimuli-responsiveness and optical properties of the liquid crystal and the extensibility of the soft polymeric matrix. Liquid crystal inclusions in soft matrices are also observed in nature. For example, filamentous phages produced by bacteria can self-assemble into liquid crystalline droplets encapsulating the bacteria to protect them from antibiotics (Tarafder et al., 2020). In these systems, a coupling between the elastic deformation of the matrix and liquid crystal ordering is expected. For example, Balenko et al. (2021) studied the mechano-optical properties of cholesteric liquid crystal inclusions embedded in polyurethane (PU). These authors found that liquid crystal molecules reorient under an applied deformation, resulting in colour change. In their more recent study, Balenko et al. (2023) also found that the sensitivity of deformation-induced colour change depends not only on the magnitude of the deformation, but also on the stiffness of the matrix. We interpret this phenomenon in the following way. When the elastic matrix is deformed, the displacement field at the matrix/inclusion interface changes the shape of the inclusion. This shape change of the interface in turn reorients the liquid crystal molecules in the inclusions through the anchoring of liquid crystal molecules at the interface. However, a theoretical model describing these coupled phenomena is lacking.

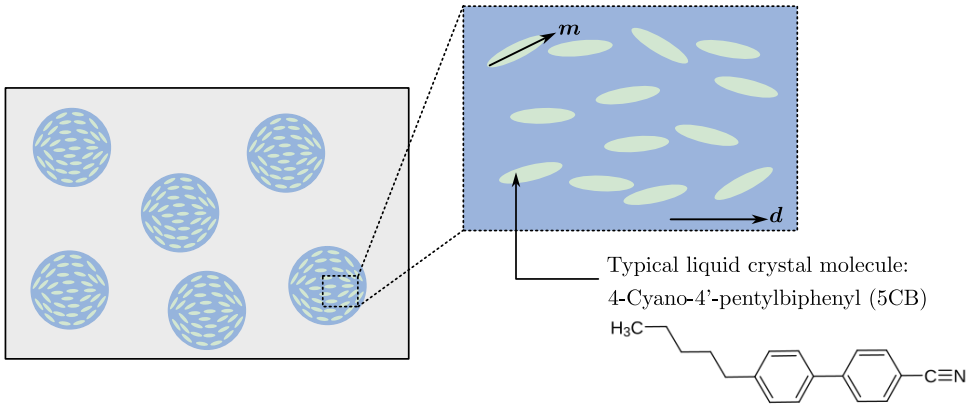

Figure 3.1: Schematic of a polymer dispersed liquid crystal composite. The liquid crystal phase consists of elongated molecules, such as 5CB.

Our problem is closely related to the problem of a soft matrix containing liquid inclusions. Style et al. (2015a) have shown that a soft silicone matrix (shear modulus $G = 1.7$ kPa) containing ionic liquid inclusions is stiffened by liquid inclusions when the inclusions are small ($\leq 6\mu$m). This effect is attributed to the coupling between matrix elasticity and surface energy of the interface (elasto-capillarity), so that small inclusions are resistant to deformations that increase their surface area. Elasto-capillary problems of isotropic liquids have been extensively studied since the foundational work by Gurtin and Murdoch (1975), followed by theoretical and numerical studies (Duan et al., 2005a; Style et al., 2015a; Henann and Bertoldi, 2014; Wang and Henann, 2016; Krichen et al., 2019; Ghosh and Lopez-Pamies, 2022; Zhu and Liu, 2023). Generalised theoretical and computational frameworks have also been proposed to deal with anisotropic surface energy (Steinmann, 2008; Javili and Steinmann, 2010). A typical model of anisotropic interfacial energy is the Rapini-Papoular energy model (Rapini and Papoular, 1969), where the interface not only favours a minimal surface area, but also penalises the deviation of the surface tangential direction from a preferred direction (sometimes referred to as "easy axis").

The coupling between liquid crystal ordering and interface deformation has also

received considerable attention. The orientational ordering of liquid crystals can be described by phenomenological continuum models like Ericksen-Leslie (Ericksen, 1962; Leslie, 1979) and Oseen-Frank (Oseen, 1933; Frank, 1958) director theories, and Landau-de Gennes (de Gennes and Prost, 1993) order parameter tensor theories, where the order parameter tensor describes not only the average orientation (director), but also the ordering of the molecules. For uniaxial nematic liquid crystals, the director field far from interfaces tends to be uniform. At the interface, the liquid crystal molecules tend to align parallel to the surface, i.e. the "easy axis" coincides with the director. This so-called "anchoring effect" introduces a gradient in the director field between the interface and the far field, which is accompanied by an increase in elastic free energy. The competition between the distortional elastic energy of the liquid crystal and the interfacial energy ultimately determines the shape of the liquid crystal inclusion. Problems of (nematic) liquid crystal inclusions with free surfaces have long been studied (Casagrande et al., 1987; Virga, 2019). Kaznacheev et al. (2002) and Prinsen and van der Schoot (2003, 2004) proposed semi-analytical, approximate approaches by treating the surface and director fields as revolving circular arcs with different radii. Numerical simulations including Monte Carlo simulations (Bates, 2003) and finite element simulations (DeBenedictis and Atherton, 2016; Adler et al., 2023) have also been conducted to solve these problems.

Although the interaction between liquid crystal orientational ordering and interface, and between the interface and matrix elasticity have been studied separately in different contexts, the coupling of these two problems has not been investigated. In this chapter, we propose a continuum mechanics model taking into account all the physics described above. We look at a model system consisting of an incompressible hyperelastic matrix containing nematic liquid crystal inclusions modelled by Landau-de Gennes theory. We follow Steinmann (2008); Javili and Steinmann (2010) on the modelling of a Rapini-Papoular type interfacial energy (Rapini and Papoular, 1969; Fournier and Galatola,

2005) to model anchoring. Through a variational formulation of the problem based on the principle of minimum potential energy, we obtain the weak and strong forms of the governing equations. The proposed model is then implemented in the FEniCSx finite element code using a mixed formulation. We first validate our computational model by comparing its predictions to experimental data, as well as to previous theoretical estimates for the free liquid crystal droplet problem (Virga, 2019). We then investigate the effective and microscopic properties of composites made of liquid crystal inclusions embedded in a soft matrix.

The chapter is organised as follows. In Section 3.2, we present the continuum framework, including kinematics (Section 3.2.1), free energy functions (Section 3.2.2), and variational formulation (Section 3.2.3). In Section 3.3, we detail how the theory is implemented into a finite element code, where in Section 3.3.1 we define the geometry and meshes and in Section 3.3.2 we present the mixed finite element formulation of the problem. We also identify in Sections 3.3.3 and 3.3.4 dimensionless parameters that are of interest in this study. In Section 3.4, we present numerical results from finite element simulations, including the determination of the equilibrium shape of a free liquid crystal droplet in a fluidic environment (Section 3.4.1), and the parametric study on the effect of dimensionless parameters on the effective mechanical properties of the composite as well as the coupling effects between external loading and the liquid crystal orientational ordering (Section 3.4.2). Concluding remarks are given in Section 3.5.

3.2 Theory

3.2.1 Kinematics

We consider a body made of an elastic matrix and a liquid crystal inclusion which takes the initial, reference configuration $\mathcal{B}_0$ at time $t = 0$, see Fig. 3.2. The subdomains occupied by the matrix and inclusion are denoted by $\mathcal{B}_0^m$ and $\mathcal{B}_0^i$, respectively, and are

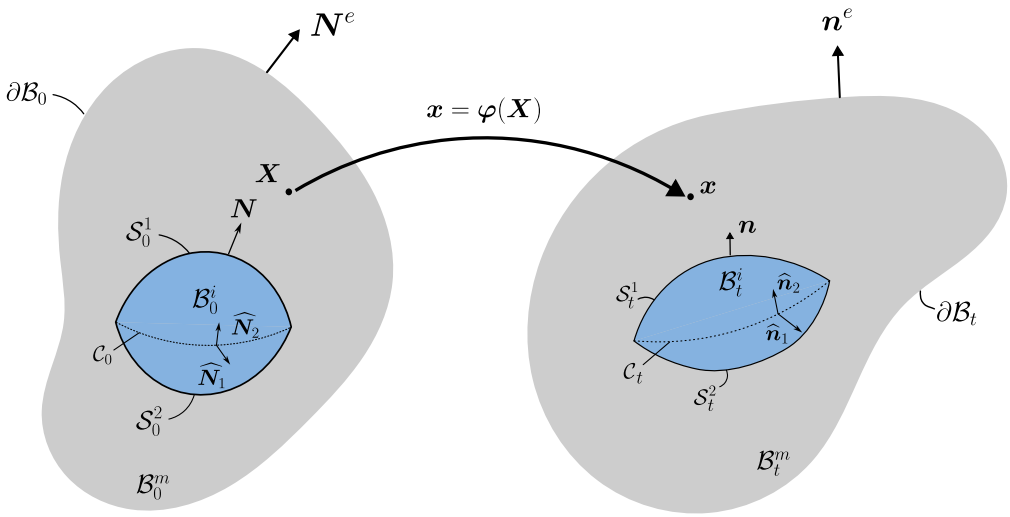

Figure 3.2: Schematic of the initial and current configurations for a liquid crystal inclusion embedded in a matrix.

such that $\mathcal{B}_0 = \mathcal{B}_0^m \cup \mathcal{B}_0^i$. The external boundary of the body is denoted by $\partial\mathcal{B}_0$, and its outward unit normal is $\boldsymbol{N}^e$. The interface between the matrix and the inclusion is denoted by $\mathcal{S}_0$, and we write $\boldsymbol{N}$ its unit normal pointing towards the matrix. For the sake of illustration, the interface is further decomposed into two subsurfaces: $\mathcal{S} = \mathcal{S}_0^1 \cup \mathcal{S}_0^2$, bounded by the closed curve $\mathcal{C}_0 = \partial\mathcal{S}_0^1 = \partial\mathcal{S}_0^2$ (Henann and Bertoldi, 2014). The current configuration of the body at time $t > 0$ is denoted by $\mathcal{B}_t = \mathcal{B}_t^m \cup \mathcal{B}_t^i$, with $\mathcal{B}_t^m$ and $\mathcal{B}_t^i$ the matrix and inclusion subdomains in the current configuration. The external boundary in the current configuration is written as $\partial\mathcal{B}_t$ and its outward unit normal is denoted by $\boldsymbol{n}^e$. The matrix-inclusion interface in the current configuration is written as $\mathcal{S}_t = \mathcal{S}_t^1 \cup \mathcal{S}_t^2$, with $\mathcal{C}_t = \partial\mathcal{S}_t^1 = \partial S_t^2$. The unit normal to the interface pointing towards the matrix in the current configuration is written $\boldsymbol{n}$.

Let $\boldsymbol{X} \in \mathcal{B}_0$ and $\boldsymbol{x} \in \mathcal{B}_t$ be the position vectors of material points in the initial and current configurations, respectively. These are related by the one-to-one map (we do not list time as a variable for conciseness):

$$\boldsymbol{x} = \boldsymbol{\varphi}(\boldsymbol{X}) \tag{3.1}$$

The associated deformation gradient mapping line elements from the initial to the current configuration is defined as[1]:

$$\boldsymbol{F} = \text{Grad}\, \boldsymbol{\varphi}(\boldsymbol{X}) \tag{3.2}$$

The bulk jacobian of the transformation maps volume elements from the initial to the current configuration: $dv = JdV$, with $J = \det \boldsymbol{F} > 0$. We also define $\boldsymbol{f} = \boldsymbol{F}^{-1}$.

We define the (non-invertible) interface deformation gradient mapping line elements on the interface from the initial to the current configuration as:

$$\widehat{\boldsymbol{F}} = \widehat{\text{Grad}}\, \boldsymbol{\varphi}(\boldsymbol{X}) = \text{Grad}\, \boldsymbol{\varphi}(\boldsymbol{X}) \cdot \widehat{\boldsymbol{I}} \tag{3.3}$$

where $\widehat{\boldsymbol{I}}$ is the surface projection tensor:

$$\widehat{\boldsymbol{I}} = \boldsymbol{I} - \boldsymbol{N} \otimes \boldsymbol{N} \tag{3.4}$$

where $\boldsymbol{I}$ is the unit tensor in the reference configuration. The surface jacobian of the transformation maps surface elements from the initial to the current configuration: $da = \widehat{J}dA$, with $\widehat{J} = \widehat{\det}\widehat{\boldsymbol{F}} = J|\boldsymbol{F}^{-T} \cdot \boldsymbol{N}|$. The latter relation is the scalar version of the Nanson formula:

$$\boldsymbol{n}da = J\boldsymbol{F}^{-T} \cdot \boldsymbol{N}dA \tag{3.5}$$

where the surface normal in the current configuration can be related to the surface normal in the reference configuration as:

$$\boldsymbol{n} = \frac{\boldsymbol{N} \cdot \boldsymbol{f}}{|\boldsymbol{N} \cdot \boldsymbol{f}|} \tag{3.6}$$

[1]We follow the notation convention used in (Steinmann, 2008), where Grad(•) and grad(•) denote the gradient with respect to the initial and current configurations, respectively. Similarly, Div(•) and div(•) respectively denote the divergence with respect to the initial and current configurations.

We also introduce the surface projection operator in the current configuration:

$$\widehat{\boldsymbol{i}} = \boldsymbol{i} - \boldsymbol{n} \otimes \boldsymbol{n} \tag{3.7}$$

where $\boldsymbol{i}$ is the unit tensor in the current configuration.

We describe the orientation of each liquid crystal molecule by a unit vector $\boldsymbol{m}$ (see Fig. 3.1), which is aligned with the major axis of the molecule. For nematic liquid crystals, the average orientation of the molecules and their degree of alignment in the liquid crystal phase can be simultaneously described using a second order, traceless, symmetric tensor $\boldsymbol{Q}$, defined as (de Gennes and Prost, 1993):

$$\boldsymbol{Q} = \frac{1}{N} \sum_i \left(\boldsymbol{m}^{(i)} \otimes \boldsymbol{m}^{(i)} - \frac{\boldsymbol{I}}{3} \right) \tag{3.8}$$

where the summation is performed over N molecules in a representative volume element of the liquid crystal phase. Note that this expression can be applied to other types of liquid crystals to describe their orientational ordering, although additional order parameters may be required (e.g. translational order parameter for smectic liquid crystals (de Gennes and Prost, 1993)). Let α_i $(i = 1, 2, 3)$ be the principal values of the $\boldsymbol{Q}$-tensor, with $\alpha_1 + \alpha_2 + \alpha_3 = 0$, and $\boldsymbol{d}_i$ the corresponding principal directions. Due to its traceless property, the $\boldsymbol{Q}$-tensor can be expressed as:

$$\boldsymbol{Q} = S_1(\boldsymbol{d}_1 \otimes \boldsymbol{d}_1) + S_2(\boldsymbol{d}_2 \otimes \boldsymbol{d}_2) - \frac{S_1 + S_2}{3}\boldsymbol{I} \tag{3.9}$$

where the parameters S_1 and S_2 are related to the principal values by

$$S_1 = 2\alpha_1 + \alpha_2, \quad S_2 = 2\alpha_2 + \alpha_1 \tag{3.10}$$

For uniaxial nematic liquid crystals, the $\boldsymbol{Q}$-tensor is transversely isotropic, which im-

plies that two of its eigenvalues coincide. Without loss of generality, let $\boldsymbol{d}_1$ be the direction of transverse isotropy, so that $\alpha_2 = \alpha_3$ and $S_2 = 0$. The $\boldsymbol{Q}$-tensor (3.9) simplifies as:

$$\boldsymbol{Q} = S\left(\boldsymbol{d} \otimes \boldsymbol{d} - \frac{\boldsymbol{I}}{3}\right) \tag{3.11}$$

where $\boldsymbol{d} \equiv \boldsymbol{d}_1$ and $S \equiv S_1$. When all the molecules are perfectly aligned, it is easily seen from Eq. (3.8) that $S = 1$. The case where all molecules are randomly oriented corresponds to $S = 0$. Finally, the case where all molecules are isotropically distributed in a plane perpendicular to $\boldsymbol{d}$ corresponds to $S = -\frac{1}{2}$. Thus, the parameter S describes the degree of alignment of the molecules relative to the director. In general, $-\frac{1}{2} \leq S \leq 1$ (Andrienko, 2018). The director $\boldsymbol{d}$ and scalar order parameter S together describe the average orientation and degree of disorder of the molecules at a point in the nematic liquid crystal phase.

3.2.2 Free energy function

Bulk energy The free energy in the bulk (matrix or liquid crystal phase) is additively decomposed into elastic, distortion and residual contributions:

$$U(\boldsymbol{F}, \text{grad}\, \boldsymbol{Q}; \boldsymbol{X}) = U_e(\boldsymbol{F}; \boldsymbol{X}) + U_Q(\boldsymbol{F}, \text{grad}\, \boldsymbol{Q}; \boldsymbol{X}) + U_r(\boldsymbol{F}; \boldsymbol{X}) \tag{3.12}$$

where U_e is the free energy density of elastic deformation, U_Q is the free energy density associated with distorting the director field, and U_r is the energy density associated with the residual stress field. The capital letter U represents the free energy per unit volume in the reference configuration. The parametric dependence in $\boldsymbol{X}$ is used to indicate that material parameters depend on the phase. The free energy functions used in this theory are required to be satisfying the principle of objectivity and specifically, the elastic energy should satisfy the principle of poly-convexity.

The elastic free energy density is taken of the (incompressible) neo-Hookean form:

$$U_e(\boldsymbol{F};\boldsymbol{X}) = \frac{G(\boldsymbol{X})}{2}\left[\text{tr}(\boldsymbol{F}^T\cdot\boldsymbol{F}) - 3\right] \tag{3.13}$$

where G is the shear modulus, taken uniform in each phase: $G(\boldsymbol{X}) = G^r$ when $\boldsymbol{X} \in \mathcal{B}_0^r$ with $r = m, i$. Following Ghosh and Lopez-Pamies (2022), the liquid crystal inclusion is treated as a hyperelastic fluid and therefore $G^i \to 0$.

Strictly speaking, the expression in Eqn. 3.13 represents an incompressible Neo-Hookean energy only when the deformation gradient satisfies the incompressibility constraint

$$J = \det \boldsymbol{F} = 1. \tag{3.14}$$

For a general deformation with $J \neq 1$, the isochoric part of the deformation should be used instead. We define

$$\tilde{\boldsymbol{F}} = J^{-1/3}\boldsymbol{F}, \qquad \det \tilde{\boldsymbol{F}} = 1, \tag{3.15}$$

and the corresponding modified invariant

$$\tilde{I}_1 = \text{tr}\left(\tilde{\boldsymbol{F}}^T\tilde{\boldsymbol{F}}\right) = J^{-2/3}I_1. \tag{3.16}$$

The Neo-Hookean energy should therefore be interpreted as

$$U_e = \frac{G(\boldsymbol{X})}{2}\left(\tilde{I}_1 - 3\right). \tag{3.17}$$

In the incompressible case considered here, the constraint $J = 1$ is enforced by the Lagrange multiplier p, so that $\tilde{\boldsymbol{F}} = \boldsymbol{F}$ and $\tilde{I}_1 = I_1$. Therefore, the simpler expression $U_e = G(\boldsymbol{X})(I_1 - 3)/2$ is recovered. For convenience, we use $\boldsymbol{F}$ over $\tilde{\boldsymbol{F}}$ in the rest of the derivation.

The free energy arising from the spatial variation of the order parameter is given by:

$$U_Q(\boldsymbol{F}, \text{grad}\, \boldsymbol{Q}; \boldsymbol{X}) = J u_Q(\text{grad}\, \boldsymbol{Q}; \boldsymbol{X}) \tag{3.18}$$

where u_Q is Landau-de Gennes elastic energy density (energy per unit volume in the current configuration). For a uniaxial nematic liquid crystal, a free energy form with three invariant combinations of the gradient of $\boldsymbol{Q}$ is adopted (Mottram and Newton, 2014):

$$u_Q(\text{grad}\, \boldsymbol{Q}; \boldsymbol{X}) = \frac{L_1(\boldsymbol{X})}{2}\left(Q_{ij,k}Q_{ij,k}\right) + \frac{L_2(\boldsymbol{X})}{2}\left(Q_{ij,j}Q_{ik,k}\right) + \frac{L_3(\boldsymbol{X})}{2}\left(Q_{ik,j}Q_{ij,k}\right) \tag{3.19}$$

where the index notation $Q_{ij,k}$ refer to the gradient with respect to coordinates in the current configuration. This free energy form has been constructed based on mathematical considerations of objectivity, neglecting higher-order terms. There have been studies and proofs of the general objectivity constraint of the free energy density function, which will not be presented in this chapter. Interested readers can refer to Chapter 4 in Sonnet and Virga (2012) and appendices in Zhang et al. (2019b). For simplicity, we assume that all three terms equally contribute to the excess free energy due to distortion, so that $L_1(\boldsymbol{X}) = L_2(\boldsymbol{X}) = L_3(\boldsymbol{X}) \equiv L(\boldsymbol{X})$ (one-constant approximation). We take $L(\boldsymbol{X}) = L$ when $\boldsymbol{X} \in \mathcal{B}_0^i$, and $L(\boldsymbol{X}) = 0$ when $\boldsymbol{X} \in \mathcal{B}_0^m$.

Due to the presence of surface tension and spatial variation of the order parameter tensor $\boldsymbol{Q}$, a residual (first Piola-Kirchhoff) stress field $\boldsymbol{P}_r(\boldsymbol{X})$ is in general needed to achieve mechanical equilibrium in the reference configuration. The corresponding residual energy takes the form:

$$U_r(\boldsymbol{F}; \boldsymbol{X}) = \boldsymbol{P}_r(\boldsymbol{X}) : \boldsymbol{F} \tag{3.20}$$

In the case of spherical liquid inclusions with isotropic surface tension, the residual

stress field in the inclusion is of the form $\boldsymbol{P}_r = pJ\boldsymbol{F}^{-T}$ and balances the isotropic surface tension, where p is the Lagrange multiplier. The corresponding residual energy per unit volume in the inclusion is simply given by pJ (Ghosh and Lopez-Pamies, 2022). This result is nothing else than the standard Young-Laplace equation, which describes balance between the pressure on the inner side of an interface and a uniformly distributed surface tension. For a liquid inclusion with radius R_0, the pressure is $p = \frac{2\gamma}{R_0}$ and the residual stress in the matrix vanishes. When the (liquid) inclusion is not spherical, the non-uniform curvature of the interface leads to a non-uniform surface tension, which drives the inclusion shape towards the spherical shape. Non-spherical inclusion shape cannot be balanced solely by the pressure in the inclusion and a residual stress field in the matrix is also required to equilibrate the reference configuration. Similarly, liquid crystal inclusions of arbitrary shape and anisotropic surface tension generally require residual stress fields in both the inclusion and the matrix to equilibrate the reference configuration. The main difference with the liquid inclusion case is that the residual stress field in the liquid crystal inclusion is no longer a uniformly distributed pressure, but a stress field taking into account the contribution of the $\boldsymbol{Q}$-field. In this work, for simplicity, we will consider that liquid crystal inclusions adopt the free-droplet shape in the reference state (i.e., the shape that the liquid crystal inclusion would adopt at equilibrium in a fluidic medium), so that the inclusion residual stress balances the anisotropic surface tension, and the residual stress in the matrix vanishes. Details about the determination of the residual stress field will be presented in Section 3.4.2.

Interface energy The interface free energy is taken of the following form:

$$\widehat{U}(\widehat{\boldsymbol{F}}, \boldsymbol{Q}, \boldsymbol{N}) = \widehat{J}\widehat{u}(\boldsymbol{Q}, \boldsymbol{n}) \tag{3.21}$$

where $\widehat{u}$ is the interface energy per unit area in the current configuration, which is taken of the form:

$$\widehat{u}(\boldsymbol{Q},\boldsymbol{n}) = \gamma\left[1+\omega_1\left(\boldsymbol{d}\cdot\boldsymbol{n}\right)^2+\omega_2\left(S^2-S_0^2\right)^2\right] \tag{3.22}$$

where γ is the surface tension, ω_1 is the anchoring strength of the director, ω_2 is the anchoring strength of the scalar order parameter and S_0 is the preferred scalar order parameter of the liquid crystal on the surface (Fournier and Galatola, 2005). For a tangentially anchoring interfacial behaviour, the anchoring strength ω_1 has to be positive. In Eq. (3.22), the first term penalises the increase in surface area, the second term promotes the alignment of the director field with the interface plane. The first two terms together constitute the classical Rapini-Papoular form of anisotropic surface energy. The third term is added to specify the preferred scalar order parameter at the interface (Fournier and Galatola, 2005). Expression (3.22) is commonly adopted to describe interfaces of droplets bounded by isotropic fluids (Warenghem et al., 1984) or soft polymer interfaces (Ramdane et al., 2000). The isotropic surface energy model is recovered simply by setting $\omega_1 = \omega_2 = 0$.

3.2.3 Variational formulation

We obtain the governing equations for liquid crystal inclusion reinforced composites starting from a variational formulation of the boundary value problem. We consider a body subjected to a field of body force $\boldsymbol{B}$ in $\mathcal{B}_0$ and to a field of external tractions $\boldsymbol{T}$ applied on its external boundary $\partial\mathcal{B}_0$. The total potential energy of the body is given by:

$$\begin{aligned} I(\boldsymbol{\varphi},\boldsymbol{Q},\operatorname{grad}\boldsymbol{Q},p) = &\int_{\mathcal{B}_0} U(\boldsymbol{F},\operatorname{grad}\boldsymbol{Q};\boldsymbol{X})\,dV + \int_{\mathcal{S}_0}\widehat{U}(\boldsymbol{F},\boldsymbol{Q};\boldsymbol{X},\boldsymbol{N})dS \\ &+\int_{\mathcal{B}_0} p(J-1)\,dV - \int_{\mathcal{B}_0}\boldsymbol{B}\cdot\boldsymbol{\varphi}\,dV - \int_{\partial\mathcal{B}_0}\boldsymbol{T}\cdot\boldsymbol{\varphi}\,dS \end{aligned} \tag{3.23}$$

where p is a scalar Lagrange multiplier field enforcing the incompressibility constraint $J = 1$. On the right-hand side of the above equation, the first term represents the total energy of the matrix and the inclusion, the second term is the total surface energy of the interface, the third term is the penalty term associated with incompressibility, and the last two terms represent the potential energy of the body force and external tractions, respectively. We seek to find the stationary point of the total potential energy with respect to all admissible fields $\boldsymbol{\varphi}$, $\boldsymbol{Q}$ and p. The tensorial variable $\boldsymbol{Q}$ is required to be traceless and symmetric, which we do not introduce further weak imposition through Lagrange multiplier for convenience. The treatment on this restriction is explained in more details later in Section 3.3.2.

3.2.3.1 Variation $\delta\boldsymbol{\varphi}$

The following derivations are based on similar derivations obtained by Steinmann (2008) and Javili and Steinmann (2010) for bulk elastic and surface energies, now including the orientation energy of liquid crystal following Virga (2019). We consider the first variation from $\boldsymbol{\varphi} \to \boldsymbol{\varphi} + \varepsilon\delta\boldsymbol{\varphi}$ around the true solution $(\boldsymbol{\varphi}, \boldsymbol{Q}, p)$. The corresponding variation of the potential energy is identified as:

$$\delta_{\varphi} I = \frac{d}{d\varepsilon} \left[I(\boldsymbol{\varphi} + \varepsilon\delta\boldsymbol{\varphi}, \boldsymbol{Q}, p) \right] |_{\varepsilon=0} \tag{3.24}$$

The true solution corresponds to a stationary point of the functional: $\delta_{\varphi} I = 0$, solving which gives us the following weak form:

$$\int_{\mathcal{B}_0} \boldsymbol{P} : \text{Grad}\, \delta\boldsymbol{\varphi}\, dV + \int_{\mathcal{S}_0} \widehat{\boldsymbol{P}} : \widehat{\text{Grad}}\, \delta\boldsymbol{\varphi}\, dS = \int_{\mathcal{B}_0} \boldsymbol{B} \cdot \delta\boldsymbol{\varphi}\, dV + \int_{\partial\mathcal{B}_0} \boldsymbol{T} \cdot \delta\boldsymbol{\varphi}\, dS \tag{3.25}$$

where $\boldsymbol{P}$ represents the bulk first Piola-Kirchhoff stress, here given by:

$$\boldsymbol{P} = \boldsymbol{P}_e + pJ\boldsymbol{f}^T + Ju_Q\boldsymbol{f}^T + J\boldsymbol{\sigma}^Q \cdot \boldsymbol{f}^T + \boldsymbol{P}_r \tag{3.26}$$

where $\boldsymbol{P}_e$ is the stress derived from the elastic strain energy (3.13) and given by:

$$\boldsymbol{P}_e = \frac{\partial U_e}{\partial \boldsymbol{F}} = G(\boldsymbol{X})\boldsymbol{F} \tag{3.27}$$

In Eq. (3.26), p is the Lagrange multiplier arising from the incompressibility constraint. The term $Ju_Q\boldsymbol{f}^T$ represents the Landau-de Gennes energy in the reference configuration under given deformation gradient. $\boldsymbol{\sigma}^Q$ arises from the distortion of the $\boldsymbol{Q}$-field, which is analogous to the Ericksen stress (Ericksen, 1962) and is given by:

$$\boldsymbol{\sigma}^Q = -\text{grad}\,\boldsymbol{Q} \odot \frac{u_Q}{\partial \text{grad}\,\boldsymbol{Q}} \tag{3.28}$$

or, in index notation:

$$\sigma^Q_{ij} = -Q_{kl,i}\frac{\partial u_Q}{\partial Q_{kl,j}} \tag{3.29}$$

With u_Q of the form (3.19) under the one-constant approximation, the latter expression becomes:

$$\sigma^Q_{ij} = -L(\boldsymbol{X})Q_{kl,i}(Q_{kl,j} + \delta_{lj}Q_{km,m} + Q_{kj,l}) \tag{3.30}$$

In Eq. (3.25), $\widehat{\boldsymbol{P}}$ represents the surface first Piola-Kirchhoff stress and can be decomposed as:

$$\widehat{\boldsymbol{P}} = \widehat{J}\widehat{u}\widehat{\boldsymbol{f}}^T + \boldsymbol{n} \otimes \widehat{\boldsymbol{S}}_0 \tag{3.31}$$

where $\widehat{\boldsymbol{S}}_0$ is the so-called deformational surface shear (Steinmann, 2008):

$$\widehat{\boldsymbol{S}}_0 = \widehat{\boldsymbol{\pi}}_t \cdot \widehat{J}\widehat{\boldsymbol{f}}^T \quad \text{with} \quad \widehat{\boldsymbol{\pi}}_t = -\frac{\partial \widehat{u}}{\partial \boldsymbol{n}} \cdot \widehat{\boldsymbol{i}} \tag{3.32}$$

Inserting Eq. (3.21) into Eq. (3.32), we obtain:

$$\begin{aligned} \widehat{\boldsymbol{\pi}}_t &= -2\gamma\omega_1 \cos\langle \boldsymbol{d}, \boldsymbol{n}\rangle(\boldsymbol{d} - \cos\langle \boldsymbol{d}, \boldsymbol{n}\rangle \boldsymbol{n}) \\ \widehat{\boldsymbol{S}}_0 &= -2\widehat{J}\gamma\omega_1 \cos\langle \boldsymbol{d}, \boldsymbol{n}\rangle(\boldsymbol{d} - \cos\langle \boldsymbol{d}, \boldsymbol{n}\rangle \boldsymbol{n})\widehat{\boldsymbol{f}}^T \end{aligned} \tag{3.33}$$

where $\langle \boldsymbol{d}, \boldsymbol{n} \rangle$ represents the angle between the director and the surface normal in the current configuration. The first term in Eq. (3.31) describes the contribution to the surface stress due to increasing the surface area, and the second term represents the contribution to the surface stress due to anchoring effects. In the particular case where $\omega_1 = \omega_2 = 0$, $\widehat{u} = \gamma$, and the surface stress reduces to $\widehat{\boldsymbol{P}} = \widehat{J}\gamma\widehat{\boldsymbol{f}}^T$.

We illustrate the physical interpretation of surface shear in a simple 2D example in 2D. In a 2D Cartesian coordinate system with basis vectors $\{\boldsymbol{e}_x, \boldsymbol{e}_y\}$, the director field can be written as: $\boldsymbol{d} = \cos\theta\boldsymbol{e}_x + \sin\theta\boldsymbol{e}_y$, where θ represents the angle between the director and $\boldsymbol{e}_x$. The liquid crystal is in contact with with a flat surface with normal vector $\boldsymbol{n} = \boldsymbol{e}_y$. In this case, the deformational surface shear in the current configuration is obtained as:

$$\widehat{\boldsymbol{\pi}}_t = -\gamma\omega_1 \sin 2\theta \boldsymbol{e}_x \tag{3.34}$$

From this expression we can easily see that when $\theta = k\pi/2$, $k = 0, \pm1, \pm2, \ldots$, $\widehat{\boldsymbol{\pi}}_t = 0$, which corresponds to cases where the director is either parallel or perpendicular to the surface. When $\theta = \pi/4 + k\pi/2$, the surface shear reaches its maximum absolute value. Thus, there exists a tendency for the director field to be reoriented towards the surface tangential plane, or equivalently, for the surface to be tilted along the director. The resultant droplet shape and director field are dependent on the relative strength between the surface and distortional energy.

Using integration by part and the divergence theorem in the bulk and on the interface, the following strong form can be obtained from Eq. (3.25):

$$\text{Div}\, \boldsymbol{P} + \boldsymbol{B} = \boldsymbol{0} \quad \text{in } \mathcal{B}_0 \tag{3.35}$$

$$\boldsymbol{P} \cdot \boldsymbol{N} = \boldsymbol{T} \quad \text{on } \partial\mathcal{B}_0 \tag{3.36}$$

$$\widehat{\text{Div}}\, \widehat{\boldsymbol{P}} = (\boldsymbol{P}^i - \boldsymbol{P}^m) \cdot \boldsymbol{N} \quad \text{on } \mathcal{S}_0 \tag{3.37}$$

$$\widehat{\boldsymbol{P}} \cdot \widehat{\boldsymbol{N}}_1 + \widehat{\boldsymbol{P}} \cdot \widehat{\boldsymbol{N}}_2 = \boldsymbol{0} \quad \text{on } \mathcal{C}_0 \tag{3.38}$$

Eqs (3.35)-(3.38) recover the classical mechanics equations in the presence of surface stresses (Steinmann, 2008). The only difference is the Landau-de Gennes elasticity contribution included in the expression (3.26) of the total stress. Eq. 3.38 is a result from surface divergence theorem, and is not used in this chapter. See 3.A.1 for derivations details of the weak and strong form.

3.2.3.2 Variation $\delta \boldsymbol{Q}$

Now we look at the first variation from $\boldsymbol{Q} \to \boldsymbol{Q} + \eta\delta\boldsymbol{Q}$ around the true solution:

$$\delta_{\boldsymbol{Q}} I = \frac{d}{d\eta} \left[I(\boldsymbol{\varphi}, \boldsymbol{Q} + \eta\delta\boldsymbol{Q}, p) \right] |_{\eta=0} \tag{3.39}$$

Solving $\delta_{\boldsymbol{Q}} I = 0$, we arrive at the weak form:

$$\int_{\mathcal{B}_t} \left[\boldsymbol{s}^{Q} \vdots \text{grad}\, \delta\boldsymbol{Q} \right] dV + \int_{S_t} \frac{\partial \widehat{u}}{\partial \boldsymbol{Q}} : \delta\boldsymbol{Q} dS = 0 \tag{3.40}$$

where $\boldsymbol{s}^{Q}$ is the torque stress, given by:

$$\boldsymbol{s}^{Q} = \frac{\partial u_Q}{\partial \text{grad}\, \boldsymbol{Q}} \tag{3.41}$$

The torque stress can be interpreted as an analogue to the elastic stress, except that it conjugates with the gradient of the order parameter $\boldsymbol{Q}$. Using Eq. (3.19), the torque stress specialises as:

$$s^{Q}_{ij,k} = Q_{ij,k} + \delta_{jk} Q_{im,m} + Q_{ik,j} \tag{3.42}$$

In Eq. (3.40), the operator $\vdots$ is defined as:

$$A_{ijk} \boldsymbol{e}_i \otimes \boldsymbol{e}_j \otimes \boldsymbol{e}_k \vdots B_{lmn} \boldsymbol{e}_l \otimes \boldsymbol{e}_m \otimes \boldsymbol{e}_n = A_{ijk} B_{ijk} \tag{3.43}$$

Using again integration by parts and the divergence theorem, the corresponding

strong form of the governing equations for the order parameter are obtained:

$$\text{div}\boldsymbol{s}^Q = 0 \quad \text{in } \mathcal{B}_t \tag{3.44}$$

$$\boldsymbol{s}^Q \cdot \boldsymbol{n} + \frac{\partial \widehat{u}}{\partial \boldsymbol{Q}} = 0 \quad \text{on } \mathcal{S}_t \tag{3.45}$$

$$\boldsymbol{s}^Q \cdot \boldsymbol{n} = 0 \quad \text{on } \partial\mathcal{B}_t \tag{3.46}$$

Eqs (3.44)-(3.46) recover the governing equations for liquid crystal problems presented in Sonnet and Virga (2012).

3.2.3.3 Variation δp

Finally, we take the first variation from $p \to p + \xi\delta p$, which gives the following condition:

$$\int_{\mathcal{B}_0} (J-1)\delta p \, dV = 0 \tag{3.47}$$

The corresponding strong form is equivalent to the incompressibility constraint $J = 1$.

3.2.4 Summary of the governing equations

In summary, the solution of the boundary-value problem for a liquid crystal inclusion in an elastic matrix subjected to a field of mechanical body forces and surface traction can be stated as follows.

Weak form Find $(\boldsymbol{\varphi}, \boldsymbol{Q}, p)$ that satisfy:

$$\int_{\mathcal{B}_0} \boldsymbol{P} : \text{Grad}\, \delta\boldsymbol{\varphi}\, dV + \int_{\mathcal{S}_0} \widehat{\boldsymbol{P}} : \widehat{\text{Grad}}\, \delta\boldsymbol{\varphi}\, dS - \int_{\mathcal{B}_0} \boldsymbol{B} \cdot \delta\boldsymbol{\varphi}\, dV - \int_{\partial\mathcal{B}_0} \boldsymbol{T} \cdot \delta\boldsymbol{\varphi}\, dS = 0 \tag{3.48}$$

$$\int_{\mathcal{B}_0} J\boldsymbol{s}^Q \vdots \text{grad}\, \delta\boldsymbol{Q}\, dV + \int_{\mathcal{S}_0} \widehat{J}\frac{\partial\widehat{u}}{\partial\boldsymbol{Q}} : \delta\boldsymbol{Q}\, dS = 0 \tag{3.49}$$

$$\int_{\mathcal{B}_0} (J-1)\delta p\, dV = 0 \tag{3.50}$$

together with the constitutive relations for $\boldsymbol{P}$, $\widehat{\boldsymbol{P}}$, $\boldsymbol{s}^Q$ and $\hat{u}$.

Strong form Find $(\boldsymbol{\varphi}, \boldsymbol{Q}, p)$ that satisfy:

$$\text{Div}\, \boldsymbol{P} + \boldsymbol{B} = \boldsymbol{0} \quad \text{in } \mathcal{B}_0 \tag{3.51}$$

$$\text{div}\, \boldsymbol{s}^Q = 0 \quad \text{in } \mathcal{B}_t \tag{3.52}$$

$$J = 1 \quad \text{in } \mathcal{B}_0 \tag{3.53}$$

together with the following boundary and interface conditions:

$$\boldsymbol{P} \cdot \boldsymbol{N} = \boldsymbol{T} \quad \text{on } \partial\mathcal{B}_0 \tag{3.54}$$

$$\widehat{\text{Div}}\, \widehat{\boldsymbol{P}} = (\boldsymbol{P}^i - \boldsymbol{P}^m) \cdot \boldsymbol{N} \quad \text{on } \mathcal{S}_0 \tag{3.55}$$

$$\boldsymbol{s}^Q \cdot \boldsymbol{n} + \frac{\partial\widehat{u}}{\partial\boldsymbol{Q}} = 0 \quad \text{on } \mathcal{S}_t \tag{3.56}$$

$$\widehat{\boldsymbol{P}} \cdot \widehat{\boldsymbol{N}}_1 + \widehat{\boldsymbol{P}} \cdot \widehat{\boldsymbol{N}}_2 = \boldsymbol{0} \quad \text{on } \mathcal{C}_0 \tag{3.57}$$

and the constitutive relations.

3.3 Numerical implementation

We have implemented the theory into a finite element code using the open source finite element library FEniCSx (Alnæs et al., 2015).

3.3.1 Geometry and mesh

We consider a periodic composite consisting of aligned axisymmetric prolate liquid crystal inclusions arranged on a rectangular lattice (Fig. 3.3). The assumption of axisymmetric inclusions is motivated by experimental observations reported by Kaznacheev et al. (2002), which show that the shape of the liquid crystal droplet and the director field are axisymmetric in the natural state. We also assume that the interface consists of a single smooth surface, i.e. we do not account for line interfaces. Virga (2019) (Chapter 5) has shown that when the interfacial energy is represented by the Rapini-Papoular model, there is no line singularity on the interface when the anchoring effect is tangential to the interface (i.e. $\omega_1 > 0$). We write ϕ the volume fraction of the inclusions. The inclusions have semi-major axis a in the z-direction, and semi-minor axis b in the x- and y-directions. The aspect ratio of the inclusions is defined as $\epsilon = \frac{a}{b} \geq 1$. For simplicity, and to reduce the computational cost, we represent the composite using an axisymmetric Unit Cell (UC) with radius R_0 and height $2H_0$ and containing a single inclusion at its centre (Fig. 3.3b). We consider the aspect ratio of the UC to be identical to the inclusion aspect ratio: $\frac{H_0}{R_0} = \epsilon$. The volume fraction of the inclusion is given by $\phi = \frac{V^i}{V}$ where V^i is the inclusion volume and $V = 2\pi H_0 R_0^2$ is the UC volume. The geometry is defined in a cylindrical coordinate system with origin at the centre of the inclusion and fixed polar angle $\theta = 0$, and with basis vector $\{\boldsymbol{e}_r, \boldsymbol{e}_z\}$. The geometry is discretised in a 2D triangular mesh using the software GMSH (Geuzaine and Remacle, 2009), accounting for axisymmetry and periodicity, as shown in Fig. 3.3c. The simulations in this paper use about 400 elements and we have verified

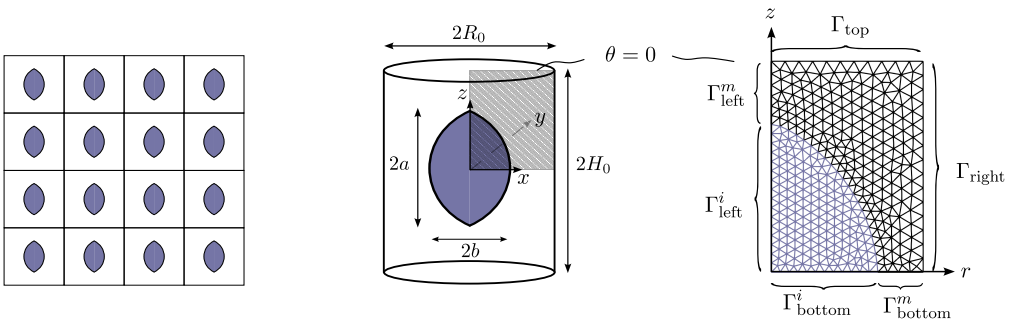

Figure 3.3: (a) Schematic of the periodic composite; (b) Approximation using axisymmetric unit cell; (c) 2D finite element mesh.

that the number of elements was sufficient to achieve convergence.

The numerical solution obtained using this 2D axisymmetric UC is an approximation of the true solution for the composite shown in Fig. 3.3a, and is limited to the case where the loading conditions are symmetric with respect to the major axis. We adopted the axisymmetric approximation because it is sufficient to investigate the main coupling effects in these composites, while keeping the computational cost low. For comparison, we have also implemented our theory in 3D. We have verified that the 2D axisymmetric approximation is in good agreement with reference calculations obtained on 3D cells, see 3.C.

3.3.2 Mixed finite element formulation

As stated in Section 3.2, the variables of the boundary value problem consist of $\boldsymbol{\varphi}$, $\boldsymbol{Q}$ and p, which are vector, tensor and scalar, respectively. We adopt a standard mixed formulation for the displacement field and pressure field, see Chapter 8 in Boffi et al. (2013), that is, second order continuous Galerkin elements (CG-2) for the displacement field and zeroth order (scalar) discrete Galerkin element (DG-0) for the pressure field, which is proved to be stable for triangular elements. As for the $\boldsymbol{Q}$-field, using the traceless and symmetric nature of $\boldsymbol{Q}$, we first note that in the 2D axisymmetric case, the

$\boldsymbol{Q}$-tensor only has two independent components: the scalar order parameter S and one independent component of the director $\boldsymbol{d}$ (the other two components are constrained by the condition $|\boldsymbol{d}| = 1$ and axisymmetry). We parametrise $\boldsymbol{d}$ using the angle ψ between the director and the r-axis so that $\boldsymbol{d} = \cos\psi \boldsymbol{e}_r + \sin\psi \boldsymbol{e}_z$. The $\boldsymbol{Q}$-tensor is then parametrised in terms of ψ and the scalar order parameter S:

$$[\boldsymbol{Q}] = S \begin{bmatrix} \cos^2\psi - \frac{1}{3} & 0 & \cos\psi\sin\psi \\ 0 & -\frac{1}{3} & 0 \\ \cos\psi\sin\psi & 0 & \sin^2\psi - \frac{1}{3} \end{bmatrix} \tag{3.58}$$

We interpolate the scalar functions ψ and S with first-order continuous Galerkin elements (CG-1). When treating the problem with axisymmetric elements, we also need expressions of the gradient of vector and tensor fields in cylindrical coordinates. Expressions for these operators can be found in 3.B. In addition, since state variables ψ and S are only defined in the inclusion domain, $\mathcal{B}_0^i$, we used the package multiphenicsx (Ballarin, 2024) to restrict the variables within the inclusion subdomain.

3.3.3 Dimensionless parameters

In our parametric study, we focus mainly on the effect of three dimensionless material parameters: the relative anchoring strength ω_1, the dimensionless inclusion volume v and the elasto-capillary number ξ. The physical meaning of these parameters is described below.

The relative anchoring strength ω_1 quantifies the relative contributions of surface anchoring and surface tension, as evident from Eq. (3.22).

The dimensionless volume v characterises the tendency of the director field in an inclusion of a given size to be distorted as a result of interface anchoring. The ratio of distortional elastic constant L (energy per length) to the anchoring energy $\gamma\omega_1$ (energy

per area) defines a material length, known as the surface extrapolation length (de Gennes and Prost, 1993):

$$\ell = \frac{L}{\gamma \omega_1} \tag{3.59}$$

The surface extrapolation length represents the distance from the actual interface to an imaginary surface where the director is completely aligned with the surface. In other words, ℓ sets the length scale for the distortion of the director field due to an anchoring surface. When ℓ is "large", distortional elasticity prevails over surface anchoring. The extrapolation length should be compared to the characteristic size of the inclusion. To this end, the dimensionless inclusion volume (Prinsen and van der Schoot, 2003) is introduced:

$$v = \frac{V^i}{\ell^3} \tag{3.60}$$

When the inclusion size is small relative to the extrapolation length ($v \ll 1$), the director field is unable to reorient over the inclusion length scale and remains relatively unaffected by surface anchoring. When the inclusion size is large relative to the extrapolation length ($v \gg 1$), the director is able to reorient and to align with the interface. The ability of the director field to anchor at the interface thus depends on the inclusion size.

The elasto-capillary number ξ is defined as:

$$\xi = \frac{\gamma}{G^m \tilde{R}} \tag{3.61}$$

where $\tilde{R}$ is a characteristic size of the inclusion related to the inclusion volume as:

$$V^i = \frac{4}{3}\pi \tilde{R}^3 \tag{3.62}$$

The elasto-capillary number describes the relative strength of surface tension relative to the elasticity of the matrix. When the elasto-capillary number is small ($\xi \to 0$), the

matrix deformation is unaffected by the surface tension at the interface. Elasto-capillary effects become significant ($\xi > 1$) when the inclusion is small and/or the matrix is soft.

Additional dimensionless parameters are ω_2 and S_0, which dictate the evolution of the order parameter S. However, the order parameter does not affect the orientation of the director field, which is our primary interest in this study. Therefore, in this chapter, we adopt the value of $S_0 = 1$ and set $\omega_2 = 20$ in all our simulations.

3.3.4 Bipolarness

We adopt the concept of "bipolarness" introduced by Prinsen and van der Schoot (2004) to describe the director field within a liquid crystal droplet. In this representation, the directors are assumed to be oriented tangentially to revolving circular arcs with equation:

$$(r + r_0)^2 + z^2 = m^2 \tag{3.63}$$

where m is the radius of the circle and $r_0 > 0$ is the distance between the origin and the centre of the circle, see Fig. 3.4. The intersection of the circular arcs with the z-axis is denoted $\tilde{a}$. The ratio between $\tilde{a}$ and a can then be used as a measure of the degree of distortion of the director field inside a droplet. When $\frac{a}{\tilde{a}} \to 1$, the circular arcs representing the director orientations meet the tips of the droplet, and the director field inside the droplet is perfectly bipolar. When $\frac{a}{\tilde{a}} \to 0$, the circular arcs are parallel straight lines, corresponding to complete alignment of the directors inside the droplet.

In practice, we obtain the equation of the circular arcs from finite element simulation results in the following way. For a given node P_i with coordinates (r_i, z_i) and director orientation ψ_i, Eq. (3.63) particularises as:

$$(r_i + r_{0i})^2 + z_i^2 = m_i^2 \tag{3.64}$$

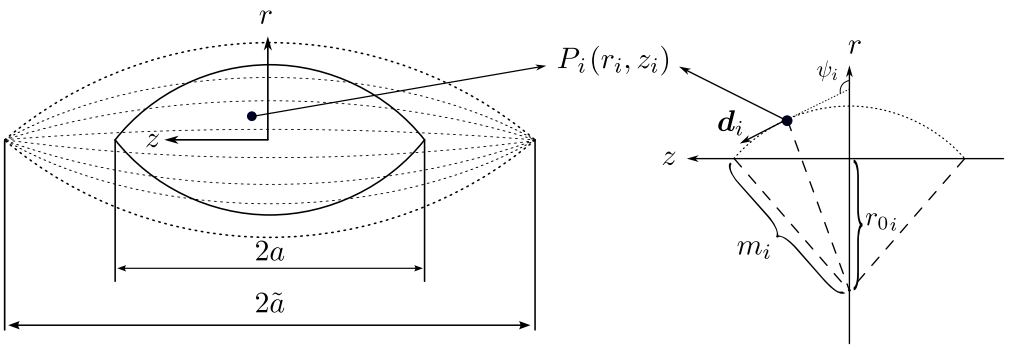

Figure 3.4: Approximation of the director field inside the inclusion using circular arcs. The ratio $\frac{a}{\tilde{a}}$ defines the the bipolarness of the director field.

By definition, the director is tangential to the arc at this point, giving:

$$\sin\left(\psi_i - \frac{\pi}{2}\right) = \frac{z_i}{m_i} \tag{3.65}$$

As shown in the next section, for $x > 0$ and $z > 0$, ψ is always larger than $\frac{\pi}{2}$. Eq. (3.65) gives the radius of the circle m_i at node P_i. Substituting into Eq. (3.64) gives the distance r_{0i} as:

$$r_{0i} = -r_i + \frac{z_i}{\tan(\psi_i - \frac{\pi}{2})} \tag{3.66}$$

The distance between the tip of the circular arc and the origin is obtained as:

$$\tilde{a}_i = \sqrt{m_i^2 - r_{0i}^2} \tag{3.67}$$

Since the representation of the director field orientation using circular arcs is not exact, the distance $\tilde{a}_i$ varies from node to node. Therefore, we consider the average bipolarness of the director field:

$$\frac{a}{\bar{\tilde{a}}} = \frac{a}{N}\sum_{i}^{N}\frac{1}{\tilde{a}_i} \tag{3.68}$$

where N is the number of nodes in the inclusion domain.

3.4 Results

In this section, we consider two classes of problems to illustrate the underlying physics of the composite system through parametric analyses. The first one (Section 3.4.1) is the free droplet problem, where we investigate the equilibrium shape and director field of a liquid crystal droplet in an isotropic fluid environment. The second one consists of the problem of an inclusion embedded in a soft matrix and subjected to external mechanical loads.

3.4.1 Free droplet

Simulation method When the inclusion is surrounded by a fluidic environment, the problem reduces to the classical problem of finding the equilibrium shape of a liquid crystal droplet with deformable boundaries (Kaznacheev et al., 2002; Prinsen and van der Schoot, 2003, 2004). The equilibrium shape of the droplet is then dictated by the competition between the interfacial energy and the distortional energy of the liquid crystal. Previously, the numerical modelling on the free droplet problem has been investigated through Monte Carlo simulations (Bates, 2003), molecular dynamics (Vanzo et al., 2012), phase field simulations (Diegel and Walker, 2017) as well as staggered algorithms (DeBenedictis and Atherton, 2016; Adler et al., 2023), i.e. iteratively solving for the order parameter field with a fixed interface, and for the inclusion shape with fixed order parameter. In contrast, in our approach we obtain the $\boldsymbol{Q}$-tensor field and the shape of the inclusion simultaneously for a finite value of the shear modulus $G^m = G^i$, and iteratively reduce the moduli until reaching the equilibrium shape, as explained below.

For the reference configuration, we consider a spherical droplet with radius $\tilde{R}$ embedded in a matrix. In the reference configuration, both the matrix and the inclusion are endowed with bulk elastic energy of the form (3.13), with $G^m = G^i = G^{\text{initial}}$, and we do not consider surface tension. In this case, the reference configuration is at equilib-

rium without any residual stress inside the droplet, and the order parameter is uniform in the inclusion. The boundary conditions are:

$$\begin{aligned} \varphi_r &= 0 && && \text{on} && \Gamma_{\text{left}}, \\ \varphi_z &= 0 && && \text{on} && \Gamma_{\text{bottom}}, \\ \boldsymbol{\sigma}\cdot\boldsymbol{n} &= \mathbf{0} && && \text{on} && \Gamma_{\text{right}}\cup\Gamma_{\text{top}}, \\ \psi &= \frac{\pi}{2}, && \frac{\partial S}{\partial \boldsymbol{n}} = 0 && \text{on} && \Gamma^i_{\text{left}}\cup\Gamma^i_{\text{bottom}}. \end{aligned} \tag{3.69}$$

Here, we used Dirichlet boundary conditions for the angle ψ on $\Gamma^i_{\text{left}}\cup\Gamma^i_{\text{bottom}}$, instead of the natural boundary condition $\frac{\partial\psi}{\partial\boldsymbol{n}}=\mathbf{0}$. We have verified that the numerical solution obtained using natural boundary conditions indeed gives $\psi=\pi/2+k\pi$, $k=0,\pm1,\pm2,\ldots$ (the other admissible solution in terms of symmetry would be $\psi=0+k\pi$). We adopted the Dirichlet boundary condition in the parametric study because it facilitated convergence and avoids the multiple solutions of ψ due to periodicity. We then apply the (anisotropic) surface tension, similar to an external load (Henann and Bertoldi, 2014). The applied surface tension is ramped gradually to facilitate convergence. Activating the anisotropic surface tension tends to deform the droplet shape and in turn distorts the order parameter field, while the droplet deformation is resisted by the elastic matrix. After having equilibrated the system, we then decrease the shear moduli of both the matrix and the inclusion, and recalculate the new equilibrium shape and director field. The procedure is repeated for gradually decreasing shear moduli, $G^m=G^i\to 0$, until the droplet reaches its fully relaxed configuration. In practice, we consider that the droplet is fully relaxed when the change in its aspect ratio $\triangle\epsilon$ between two increments in shear moduli is smaller than 10^{-4}. Note that during relaxation, the mesh can be distorted significantly, causing convergence issues before the tolerance is reached. In such cases, we re-mesh the domain whenever the solver fails to converge and continue the relaxation process with the new mesh. We verified that the equilibrium shape of the droplet is

independent on the volume fraction of the inclusion, as expected.

Comparison to experimental data To validate our model, we compare numerical predictions to experimental data reported by Kaznacheev et al. (2002) for a dispersion of 0.33 wt% of vanadium pentoxide in water. In that study, snapshots of equilibrated droplets in solution were taken, and the aspect ratio and semi-major axis of each droplet were measured. Material parameters were set as follows: $\omega_1 = 5$, $\gamma = 0.003$ J/m^2 and $L = 10^{-8}$ J/m, which were fitted to experimental data. Liquid crystal droplets with varying volume V^i (i.e. different characteristic sizes $\tilde{R}$) were simulated. For each $\tilde{R}$, we calculated the equilibrium semi-major axis a and aspect ratio $\epsilon = \frac{a}{b}$. We also calculated the average bipolarness, as described in Section 3.3.4. The comparison between simulation results and experimental data is shown in Fig. 3.5, showing good agreement. Results show that, when the volume of the inclusion increases (i.e. the dimensionless volume v increases), the aspect ratio decreases and bipolarness increases. Indeed, increasing the dimensionless volume facilitates the disorientation of the director field, allowing the droplet to adopt a more circular shape to minimise its surface energy. In contrast, at small dimensionless volume, the director field remains strongly aligned, forcing the droplet to adopt a more elongated shape to reduce the cost of interfacial misalignment.

Parametric study We conducted a parametric study to assess the effect of the relative anchoring strength ω_1 for different values of v, adjusted via the inclusion size $\tilde{R}$ at constant $L = 10^{-8}$ J/m and $\gamma = 0.003$ J/m^2. The evolution of the droplet aspect ratio is shown as a function of the relative anchoring strength ω_1 in Fig. 3.6a for three values of v, and the corresponding evolution of the bipolarness is shown in Fig. 3.6b. The figure also shows the estimate obtained using the Wulff's construction method (Virga, 2019), according to which the equilibrium shape of an incompressible body is obtained by minimising a known functional. Wulff's method applies only in the limit $v \to 0$,

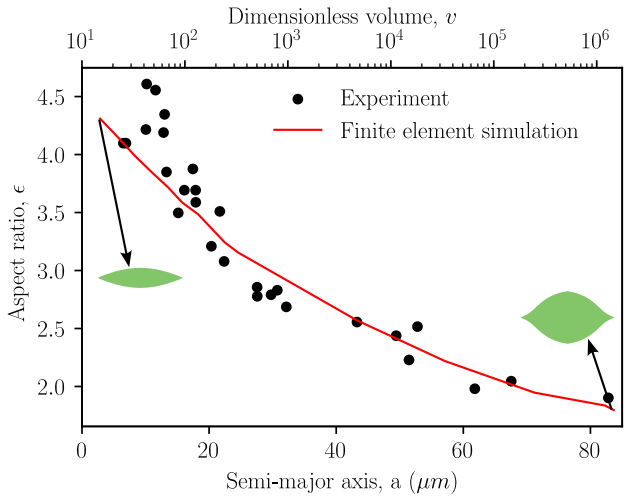

Figure 3.5: Comparison between experimental and finite element simulation results for the evolution of the droplet shape (aspect ratio, ϵ) with the inclusion size (semi-major axis a, or dimensionless volume v). Parameters were identified as: $\omega_1 = 5$, $\gamma = 0.003\text{J/m}^2$, and $L = 10^{-8}\text{J/m}$.

corresponding to a perfectly ordered liquid crystal. In the case where $\omega_1 = 0$, there is no cost associated with misaligning the director with the surface and the droplet adopts a spherical shape ($\epsilon = 1$). Inside the droplet, the director is perfectly aligned to minimise the distortional energy and the bipolarness tends to zero. As ω_1 increases, due to anisotropic surface tension, the aspect ratio of the droplet increases and the bipolarness also increases.

The change of aspect ratio with an increasing dimensionless volume is shown in Fig. 3.6c. For a given anchoring strength, the aspect ratio decreases as the dimensionless volume increases, and tends to one for $v \to \infty$. We also show the evolution of the bipolarness of the director field in Fig. 3.6d. The bipolarness tends to zero as $v \to 0$, because the cost of misaligning the director field becomes much larger than the cost of misalignment at the interface, and the director field becomes nearly uniform. As v increases, the director field becomes able to reorient to align with the surface, and the bipolarness increases.

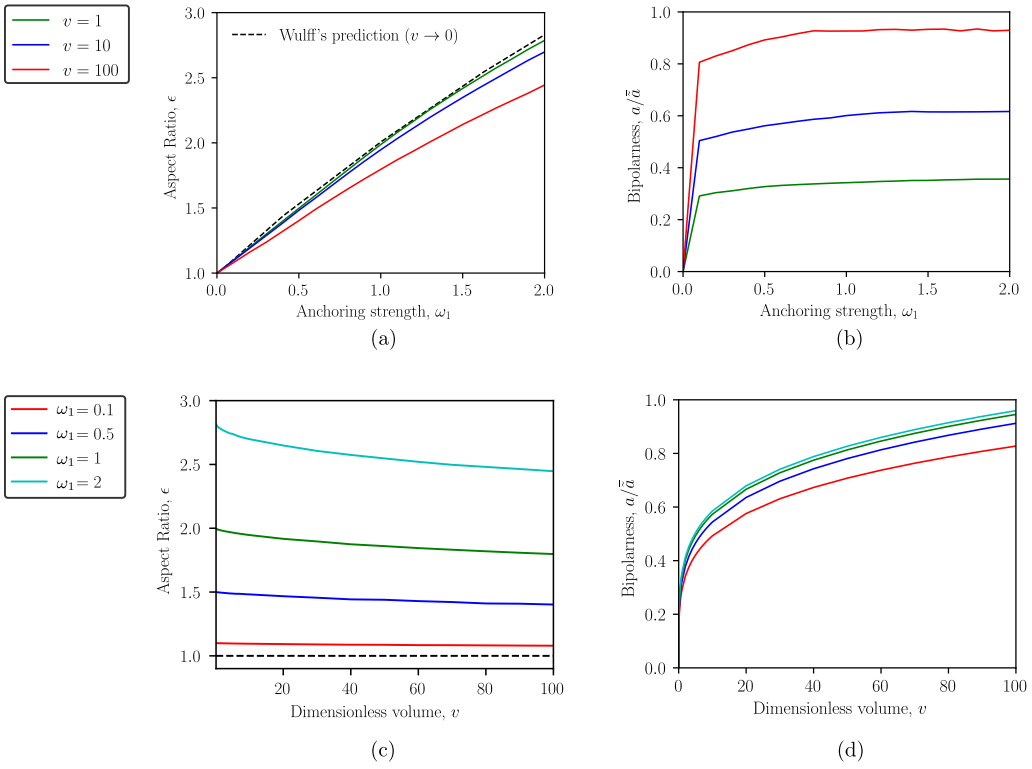

Figure 3.6: Predicted evolutions of the aspect ratio ϵ and bipolarness $\frac{a}{\bar{a}}$ as a function of (a)-(b) the anchoring strength ω_1 and (c)-(d) the dimensionless volume v. Other parameters were set as $L = 10^{-8}$ J/m and $\gamma = 0.003$ J/m^2.

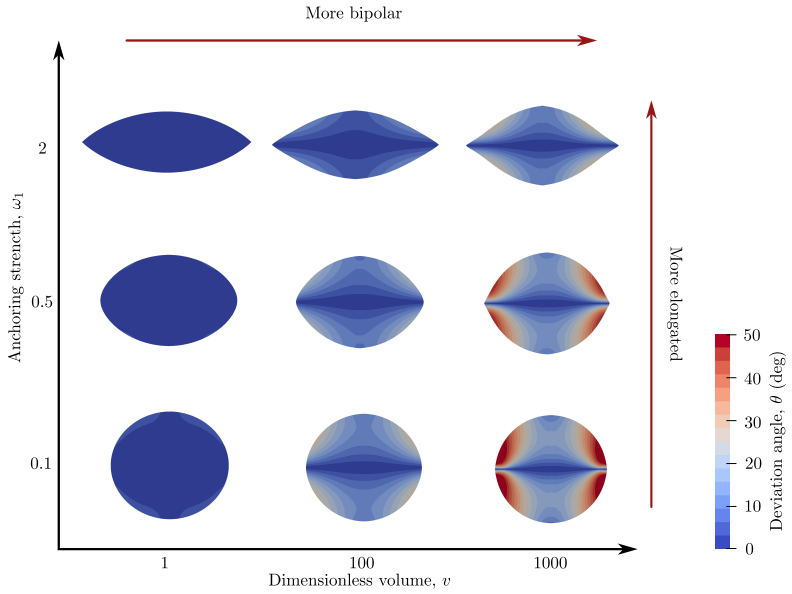

Figure 3.7: Illustration of inclusion shape and director field orientation in liquid crystal droplets with different anchoring strength and dimensionless volume.

Fig. 3.7 illustrates the shape of the droplet and orientation of the director field for different combinations of ω_1 and v. The contour plots represent the deviation angle $\theta = (\psi - \frac{\pi}{2})$ between the director and the z-axis. Note that the deviation angle was only calculated in the meshed region $x \geq 0$, $z \geq 0$, where ψ is larger than $\frac{\psi}{2}$, and mirrored in the three other quadrants for visualisation. When the dimensionless volume is small $(v = 1)$, the director field is almost uniaxial and aligned with the symmetry axis, and the deviation angle is close to zero. Increasing the anchoring strength elongates the droplet, with the appearance of point defects (called "boojums") visible for $\omega_1 = 2$. The droplet is then referred to as "tactoid". As the dimensionless volume increases, the local deviation angle becomes heterogeneous to reduce misalignment with the interface. At large v and small ω_1, the droplet is able to preserve a roughly spherical shape by allowing large distortions of the director field near the surface. At large v and large ω_1, the tactoid shape becomes more complex as a result of the competition between distortional energy and anisotropic surface energy.

3.4.2 Liquid crystal inclusion in a soft matrix

Reference configuration We hypothesise that inclusions in the composite initially have the same shape and director field orientation as the corresponding inclusions in a liquid. By adopting the shape and director field of the fully-relaxed free droplet in the reference configuration of the composite problem, we ensure that the matrix in the reference configuration is stress-free. Let $\boldsymbol{Q}^{\text{FD}}$ be the order parameter and p^{FD} the hydrostatic pressure in the relaxed free droplet. According to Eq. (3.26), the residual stress $\boldsymbol{P}_r$ that balances the surface tension and the distortion of the order parameter is given by:

$$\boldsymbol{P}_r^i = u^Q(\text{grad}\,\boldsymbol{Q}^{FD})J\boldsymbol{F}^{-T} + J\boldsymbol{\sigma}^Q(\text{grad}\,\boldsymbol{Q}^{FD})\boldsymbol{F}^{-T} + p^{FD}J\boldsymbol{F}^{-T}, \quad \boldsymbol{P}_r^m = 0 \tag{3.70}$$

In practice, we first solve the free droplet problem using the methodology described in the previous section, and obtain the inclusion shape and the $\boldsymbol{Q}$-field. We then calculate the residual stress field from Eq. (3.70). Next, we create a new mesh on the free droplet geometry and interpolate the numerical values of $\boldsymbol{P}_r^i$ onto the new mesh. The inclusion is then embedded in the soft matrix, and the matrix domain is also meshed. The self-equilibrated free-droplet embedded in the matrix is used as the reference configuration (with $\boldsymbol{F} = \boldsymbol{I}$) for subsequent composite simulations. Note that as the interpolation is performed on two different meshes, it leads to a numerical error. However, we have verified that the numerical error on the stress field is small so that it does not impact subsequent results.

Boundary conditions We subject the composite UC to uniaxial tension and compression tests in the z-direction, which satisfy the condition of axisymmetry. Similar to the free droplet problem, the composite is subjected to symmetric boundary conditions on

$\Gamma_{\text{left}} = \Gamma^i_{\text{left}} \cup \Gamma^m_{\text{left}}$ and $\Gamma_{\text{bottom}} = \Gamma^i_{\text{bottom}} \cup \Gamma^m_{\text{bottom}}$:

$$\begin{aligned} &\varphi_x = 0 \qquad \text{on } \Gamma_{\text{left}} \\ &\varphi_z = 0 \qquad \text{on } \Gamma_{\text{bottom}} \\ &\psi = \frac{\pi}{2}, \ \frac{\partial S}{\partial \boldsymbol{n}} = 0 \qquad \text{on } \Gamma^i_{\text{left}} \cup \Gamma^i_{\text{bottom}} \end{aligned} \tag{3.71}$$

We apply prescribed displacement boundary conditions on the top edge:

$$\varphi_z = (\lambda_z - 1) H_0 \quad \text{on } \Gamma_{\text{top}} \tag{3.72}$$

where λ_z is the stretch in z-direction. The right edge is kept straight to account for periodicity, and hence interactions between neighbouring inclusions (subject to the approximation of axisymmetric UC). This constraint is weakly imposed to the edge by adding the following term to the total potential:

$$\int_{\Gamma_{\text{right}}} \beta \left(\frac{\partial \varphi_r}{\partial z} \right) \, dS \tag{3.73}$$

where β is a Lagrange multiplier defined only on the right edge using the multiphenicsx package (Ballarin, 2024).

In the following, we conduct a parametric study to explore the role of various parameters on the macroscopic response of the composite. We also investigate the effect of mechanical loads on the orientation of the director field. In the simulations below, the Landau-de Gennes elastic constant is $L = 10^{-8}\text{J/m}$, and the surface tension is $\gamma = 0.003\text{J/m}^2$. We vary the value of v by changing the value of $\tilde{R}$. We change the value of ξ by changing the value of G^m. The volume fraction of the liquid crystal inclusion is kept constant: $\phi = 0.2$.

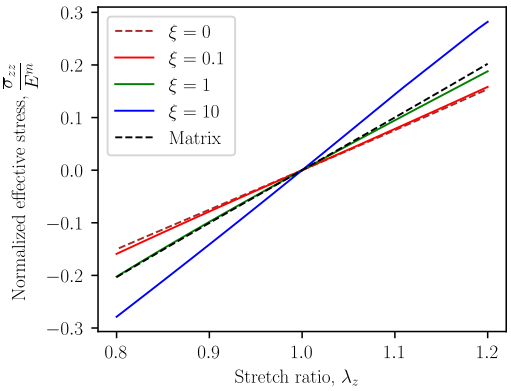

Figure 3.8: Normalised stress-stretch curves for composites made of liquid crystal inclusions embedded in an elastic matrix under uniaxial tension and compression loading. Material parameters are: $v = 100, \omega_1 = 0.5$

Parametric study We first consider the stress-strain response of the composite subjected to uniaxial tension and compression tests. Fig. 3.8 shows the effective Cauchy stress $\bar{\sigma}_{zz}$ (calculated by dividing the resultant force on the top surface by the current area) normalised by the Young modulus of the matrix ($E^m = 3G^m$), for different values of ξ. The anchoring strength and the dimensionless volume are $\omega_1 = 0.5$ and $v = 100$. For comparison, we have also plotted the response of the composite when the inclusion is replaced with an incompressible isotropic liquid and negligible surface tension ($\xi = 0$). When $\xi = 0.1$, the elasto-capillary effect is weak and the response of the composite is softer than that of the matrix and only slightly stiffer than that of a composite with liquid inclusion and no surface tension effects. As ξ increases by decreasing the matrix modulus, the composite modulus also decreases, but not as fast as the matrix modulus, so that for $\xi = 10$, the composite is stiffer than the matrix. These results parallel previously-reported results for liquid inclusions in soft matrices, see Style et al. (2015a,b); Wang and Henann (2016); Ghosh and Lopez-Pamies (2022).

Fig. 3.9 shows the effective Young modulus of the composite in the z-direction, $\bar{E}_z$, normalised by the matrix modulus as a function of the elasto-capillary number ξ,

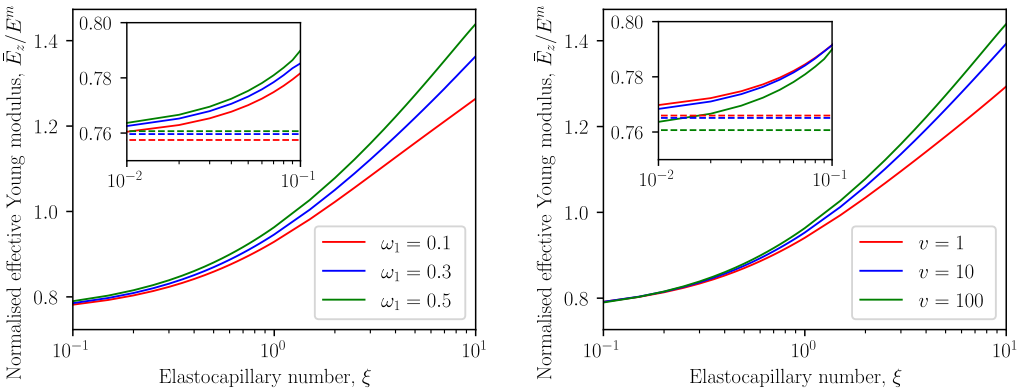

Figure 3.9: Evolution of the normalised effective Young modulus of the composite with the elasto-capillary number ξ for (a) different values of anchoring strength ω_1 at fixed dimensionless volume $v = 100$, and (b) different values of dimensionless volume v at fixed anchoring strength ω_1. The insets also compare the response of the composite with liquid crystal inclusions (continuous lines) to the response of a composite containing incompressible liquid inclusions with the same shape as in the original composite and with no surface tension effects (dashed lines).

for different values of the anchoring strength and dimensionless volume. Each combination (v, ω_1) corresponds to a given self-equilibrated configuration of the droplet, as described in Section 3.4.1, while the elasto-capillary number ξ is varied by changing the matrix stiffness. As noted previously, the normalised composite modulus increases with ξ at constant values of v and ω_1. For a fixed dimensionless volume ($v = 100$, Fig. 3.9a), the effective modulus increases when the anchoring strength increases. This can be explained based on the difference in aspect ratio of the underlying free droplet: indeed, the aspect ratio increases from $\epsilon = 1.08$ for $\omega_1 = 0.1$ to $\epsilon = 1.4$ for $\omega = 0.5$ (see also Fig. 3.6). It is well established that the longitudinal modulus of composites reinforced by elongated inclusions increases with the inclusion aspect ratio (Lee and Paul, 2005). When ξ tends to zero, the effective modulus of the composite with liquid crystal inclusion approaches the response of a composite with the same initial inclusion shape but filled with an isotropic incompressible liquid and no surface tension, as illustrated in dashed lines in the inset of Fig. 3.9a. This indicates that in the small-ξ limit (reached

by increasing the matrix modulus), the contributions due to anisotropic surface tension and distortional energy of the liquid crystal phase are negligible compared to the elastic energy of the matrix. We have verified that these trends remain the same at smaller values of v.

For a fixed anchoring strength ($\omega_1 = 0.5$, Fig. 3.9b), the effective modulus decreases when the dimensionless volume decreases at given $\xi \gtrsim 0.15$. In this case, the aspect ratios of the inclusion in the reference configuration are very close: $\epsilon = 1.49$ for $v = 1$ and $\epsilon = 1.4$ for $v = 100$. However, the two inclusions differ dramatically in their initial director orientation: for $v = 1$, the director field is aligned, whereas for $v = 100$, the director field is highly distorted and closely follows the shape of the inclusion, see Section 3.4.1, Fig. 3.7. Due to a larger orientational mismatch between the director field and the surface in the case $v = 1$, stretch-induced elongation of the inclusion brings about a larger decrease in anisotropic surface energy, and therefore the effective modulus of the composite is smaller for smaller v. In contrast, at small $\xi \lesssim 0.15$, the overall response is close to the response of a composite with isotropic incompressible liquid inclusions and negligible surface tension, as shown in the inset of Fig. 3.9b. We have verified that these trends remain the same at smaller values of ω_1.

We next investigate the effect of mechanical loading on the inclusion shape and orientation of the director field. Fig. 3.10 shows the inclusion response in the case where $v = 100$ and $\omega_1 = 0.5$, and for two values of ξ. The reference configuration of the droplet, corresponding to $\lambda_z = 1$, was previously shown in Fig. 3.7. When $\xi = 0.01$, the inclusion shape changes significantly with the external loading in both tension and compression, while it remains almost unchanged when $\xi = 10$. The director in the inclusion is also more prone to reorientation when $\xi = 0.01$, compared to the case where $\xi = 10$ (Fig. 3.10, left). This suggests that the distortion of the director field is driven by the shape change of the interface. The scalar order parameter becomes smaller in compression and larger in tension (Fig. 3.10, right), indicating that not only do the

directors become more aligned when the inclusion is elongated, but at a smaller scale, the molecules at each material point also become less dispersed. The case of a smaller anchoring strength ($\omega_1 = 0.1$) but same dimensionless volume ($v = 100$) is illustrated in Fig. 3.11. The response of the director field under external loading is similar to the case where $\omega_1 = 0.5$, noting that the director and order parameter fields present a larger spatial gradient in the initial state.

Fig. 3.12 shows the contour plots of deviation angle and scalar order parameter of inclusions with dimensionless volume $v = 1$ and anchoring strength $\omega_1 = 0.5$. Note the range of the colour bar (0-2.9 deg for deviation angle and 0.98-1 for scalar order parameter), indicating that the molecules are almost aligned in the reference configuration, see also Fig. 3.7. In contrast to the previous examples, when the dimensionless volume is small, the director field becomes more aligned when the composite is being compressed, while the director field remains almost unchanged in tension. In particular, when $\xi = 10$, although the surface is barely deformed, the deviation angle becomes smaller when the composite is being compressed. We are currently not able to explain this phenomenon. We note, however, that changes in the order parameter field are very small (of the order of 1 deg for the deviation angle and 0.01 for the scalar order parameter). Finally, Fig. 3.13 shows the response of the inclusion for $v = 1$ and $\omega_1 = 0.1$. The effect of elasto-capillary number is the same as in previous results, while the alignment of the director field due to compression is more significant. Similar to Fig. 3.12, the changes in the absolute values of deviation angle and scalar order parameter are very small compared to the cases shown in Figs 3.10 and 3.11.

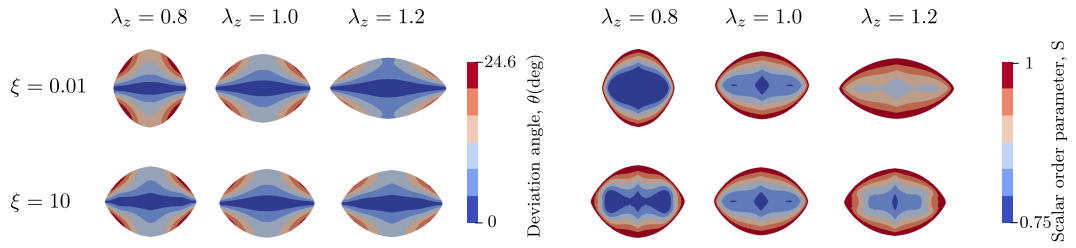

Figure 3.10: The response of liquid crystal inclusions in a soft matrix under external loading. Contour plots of the director deviation angle θ (left) and scalar order parameter S (right). Material parameters are $v = 100$ and $\omega_1 = 0.5$.

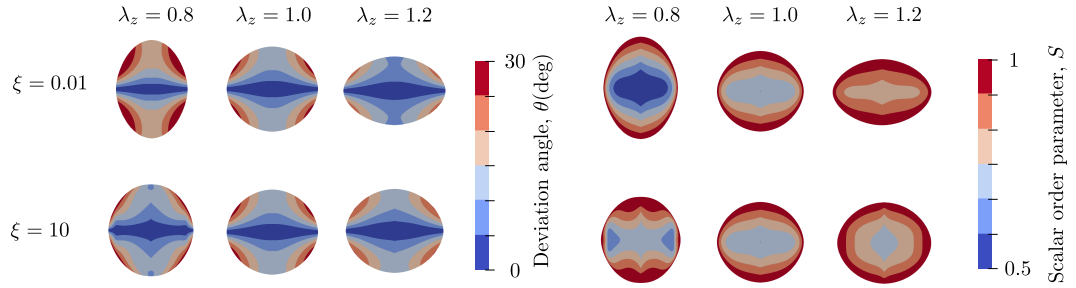

Figure 3.11: The response of liquid crystal inclusions in a soft matrix under external loading. Contour plots of the director deviation angle θ (left) and scalar order parameter S (right). Material parameters are $v = 100$ and $\omega_1 = 0.1$.

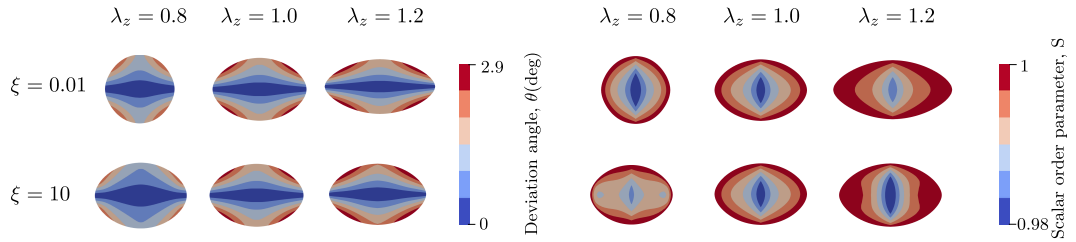

Figure 3.12: The response of liquid crystal inclusions in a soft matrix under external loading. Contour plots of the director deviation angle θ (left) and scalar order parameter S (right). Material parameters are $v = 1$ and $\omega_1 = 0.5$.

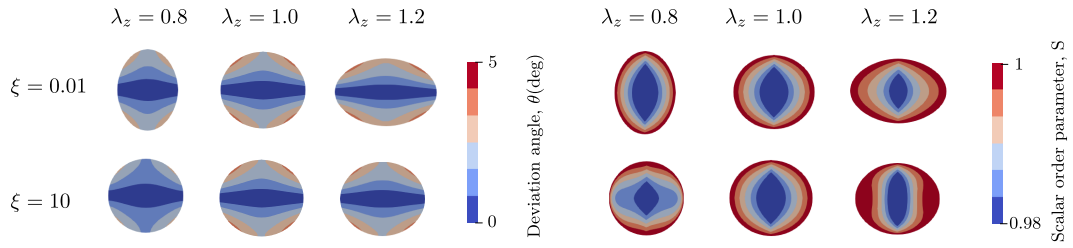

Figure 3.13: The response of liquid crystal inclusions in a soft matrix under external loading. Contour plots of the director deviation angle θ (left) and scalar order parameter S (right). Material parameters are $v = 1$ and $\omega_1 = 0.1$.

3.5 Conclusions

In this work, we have developed a continuum theory for analysing the coupling between elasticity, anisotropic surface tension, and orientational order in composites consisting of nematic liquid crystal inclusions embedded in soft matrices. The theory can also describe liquid crystal inclusions in liquids as a special case. We have implemented our theory in the open-source finite element software FEniCSx, in both axisymmetric and 3D, and conducted parametric studies. Key findings regarding the behaviour of liquid crystal inclusions in soft matrices can be summarised as follows:

- Similar to the case of composites consisting of liquid inclusions in soft matrices, the inclusions reinforce the matrix when the elastocapillary number is large ($\xi > 1$), and weaken the composite when the elastocapillary number is small ($\xi < 1$).
- The reinforcement effect of the liquid crystal inclusion is enhanced by larger anchoring strength, which primarily follows from a composite effect associated with different inclusion aspect ratios in the reference configuration. For a given anchoring strength, the reinforcement effect is reduced when the dimensionless volume is small, due to the alignment of the interface with the director.
- The response of the order parameter field in the inclusion is primarily mediated by the deformation of the interface. Therefore, it is more sensitive to the external loading when the elasto-capillary number is small. Reorientation of the director field is more significant when the dimensionless inclusion volume is large and the anchoring strength is small.

These results are based on the assumption that the shape and order parameter field of the liquid crystal inclusion in the reference configuration of the composite are the same as that of a liquid crystal inclusion with the same properties in a liquid. This may not be exactly the case in experiments, depending on the fabrication method. In addition, results

for the composite have been obtained assuming a periodic array of aligned inclusions, loaded along their symmetry axis. Additional numerical studies are need to investigate more general microstructures and loading conditions. However, the continuum theory proposed in this work is general and can be used to simulate other scenarios.

The proposed theory and numerical results are relevant for the design of smart composite materials, for example to optimise the director reorientation under applied mechanical loads. Conversely, the proposed theoretical and numerical methods could be used in conjunction with experimental measurements to estimate material parameters which are difficult to measure directly, for example in natural biological systems. In future work, the theory will be extended to include the couplings with applied electric field. The application of electric field may generate considerable deformation, which could be useful for the design of smart stimuli-responsive materials.

Appendix 3.A Derivation of the weak and strong form

3.A.1 Variation $\delta\boldsymbol{\varphi}$

Using Eqs. (3.12) and (3.18), the variation of the bulk free energy gives:

$$\delta_{\boldsymbol{\varphi}} U = \frac{\partial U_e}{\partial \boldsymbol{F}} : \delta_{\boldsymbol{\varphi}} \boldsymbol{F} + u_{LdG} \delta_{\varphi} J + J \frac{\partial u_{LdG}}{\partial \text{grad} \boldsymbol{Q}} \vdots \delta_{\boldsymbol{\varphi}} \text{grad} \boldsymbol{Q} \tag{3.74}$$

Note the following results:

$$\delta_{\boldsymbol{\varphi}} \boldsymbol{F} = \text{Grad}\, \delta\boldsymbol{\varphi} \tag{3.75}$$

$$\delta_{\boldsymbol{\varphi}} \boldsymbol{f} = -\boldsymbol{f} \cdot \delta_{\boldsymbol{\varphi}} \boldsymbol{F} \cdot \boldsymbol{f} \tag{3.76}$$

$$\delta_{\boldsymbol{\varphi}} J = J \boldsymbol{f}^T : \delta_{\boldsymbol{\varphi}} \boldsymbol{F} \tag{3.77}$$

$$\delta_{\boldsymbol{\varphi}} \text{grad}\, \boldsymbol{d} = \text{Grad}\, \boldsymbol{d} \cdot \delta_{\boldsymbol{\varphi}} \boldsymbol{f} \tag{3.78}$$

Inserting results (3.75)-(3.78) into (3.74) renders the first term on the left hand side of Eq. (3.25). Using Eqn. (3.21), the variation of the surface free energy gives:

$$\delta_{\boldsymbol{\varphi}} \widehat{U} = \widehat{u} \delta_{\boldsymbol{\varphi}} \widehat{J} + \widehat{J} \frac{\partial \widehat{u}}{\partial \boldsymbol{n}} \cdot \delta_{\boldsymbol{\varphi}} \boldsymbol{n} \tag{3.79}$$

Note the following results (Steinmann, 2008):

$$\delta_{\boldsymbol{\varphi}} \widehat{\boldsymbol{F}} = \widehat{\text{Grad}}\, \delta\boldsymbol{\varphi} \tag{3.80}$$

$$\delta_{\boldsymbol{\varphi}} \widehat{J} = \widehat{J} \widehat{\boldsymbol{f}}^T : \delta_{\boldsymbol{\varphi}} \widehat{\boldsymbol{F}} \tag{3.81}$$

$$\delta_{\boldsymbol{\varphi}} \boldsymbol{n} = -\boldsymbol{n} \cdot \widehat{\text{grad}}\, \delta\boldsymbol{\varphi} \tag{3.82}$$

Using the latter result, we can calculate:

$$\frac{\partial \widehat{u}}{\partial \boldsymbol{n}} \cdot \delta_{\boldsymbol{\varphi}} \boldsymbol{n} = -[\boldsymbol{n} \otimes \frac{\partial \widehat{u}}{\partial \boldsymbol{n}} \cdot \widehat{\boldsymbol{i}} \cdot \widehat{\boldsymbol{f}}^{T}] : \widehat{\text{Grad}}\, \delta\boldsymbol{\varphi} \tag{3.83}$$

Inserting results (3.80)-(3.83) into Eqn. (3.79) renders the second term on the left hand side of Eqn. (3.25).

The strong form corresponding to the weak form (3.25) is obtained as follows. First use integration by parts:

$$\begin{aligned} \int_{\mathcal{B}_0} [\text{Div}(\delta\boldsymbol{\varphi} \cdot \boldsymbol{P}) - (\text{Div}\, \boldsymbol{P}) \cdot \delta\boldsymbol{\varphi}]\; dV + \int_{\mathcal{S}_0} \left[\widehat{\text{Div}}\, (\delta\boldsymbol{\varphi} \cdot \widehat{\boldsymbol{P}}) - (\widehat{\text{Div}}\, \widehat{\boldsymbol{P}}) \cdot \delta\boldsymbol{\varphi}\right]\; dS \\ = \int_{\mathcal{B}_0} \boldsymbol{B} \cdot \delta\boldsymbol{\varphi}\; dV + \int_{\partial\mathcal{B}_0} \boldsymbol{T} \cdot \delta\boldsymbol{\varphi}\; dS \end{aligned} \tag{3.84}$$

Then use the divergence theorem in the bulk and on the interface:

$$\begin{aligned} \int_{\mathcal{B}_0} -[\text{Div}\, \boldsymbol{P} + \boldsymbol{B}] \cdot \delta\boldsymbol{\varphi}\; dV + \int_{\partial\mathcal{B}_0} (\boldsymbol{P} \cdot \boldsymbol{N} - \boldsymbol{T}) \cdot \delta\boldsymbol{\varphi}\; dS \\ + \int_{\mathcal{S}_0} \left[\widehat{\text{Div}}\, \widehat{\boldsymbol{P}} + \boldsymbol{P}^i \cdot \boldsymbol{N} - \boldsymbol{P}^m \cdot \boldsymbol{N}\right] \cdot \delta\boldsymbol{\varphi}\; dS = 0 \\ + \int_{\mathcal{C}_0} (\widehat{\boldsymbol{P}} \cdot \widehat{\boldsymbol{N}_1} + \widehat{\boldsymbol{P}} \cdot \widehat{\boldsymbol{N}_2}) \cdot \delta\boldsymbol{\varphi}\; dL = 0 \end{aligned} \tag{3.85}$$

where $\boldsymbol{P}^i$ and $\boldsymbol{P}^m$ represent the stress tensor in the inclusion and the matrix, respectively. When using the surface divergence theorem, we have used the fact that $\widehat{\boldsymbol{P}} \cdot \boldsymbol{N} = \boldsymbol{0}$.

3.A.2 Variation $\delta \boldsymbol{Q}$

The variation of the bulk energy gives:

$$\delta_{\boldsymbol{Q}} U = J \delta_{\boldsymbol{Q}} u_{LdG} = \frac{\partial u_{LdG}}{\partial \boldsymbol{Q}} : \delta \boldsymbol{Q} + \frac{\partial u_{LdG}}{\partial \text{grad } \boldsymbol{Q}} \vdots \text{grad } \delta \boldsymbol{Q} \tag{3.86}$$

The variation of the interfacial energy gives:

$$\delta_{\boldsymbol{Q}} \widehat{U} = \widehat{J} \frac{\partial \widehat{u}}{\partial \boldsymbol{Q}} : \delta \boldsymbol{Q} \tag{3.87}$$

Appendix 3.B Expression of operators in cylindrical coordinate system

In cylindrical coordinate system with a basis of $(\boldsymbol{e}_r, \boldsymbol{e}_\theta, \boldsymbol{e}_z)$, the gradient of an arbitrary vector u w.r.t. the coordinates in the reference configuration with an axisymmetric formulation is:

$$\text{Grad } \boldsymbol{u} = \begin{bmatrix} \dfrac{\partial u_r}{\partial R} & 0 & \dfrac{\partial u_r}{\partial Z} \\ 0 & \dfrac{u_r}{R} & 0 \\ \dfrac{\partial u_z}{\partial R} & 0 & \dfrac{\partial u_z}{\partial Z} \end{bmatrix} \tag{3.88}$$

The gradient of an arbitrary tensor $\boldsymbol{T}$ is w.r.t. the reference coordinates is:

$$\text{Grad } \boldsymbol{T} = \left[\begin{bmatrix} \dfrac{\partial T_{rr}}{\partial R} & 0 & \dfrac{\partial T_{rz}}{\partial R} \\ 0 & \dfrac{\partial T_{\theta\theta}}{\partial R} & 0 \\ \dfrac{\partial T_{zr}}{\partial R} & 0 & \dfrac{\partial T_{zz}}{\partial R} \end{bmatrix} \begin{bmatrix} 0 & \dfrac{T_{rr} - T_{\theta\theta}}{R} & 0 \\ \dfrac{T_{rr} - T_{\theta\theta}}{R} & 0 & \dfrac{T_{rz}}{R} \\ 0 & \dfrac{T_{rz}}{R} & 0 \end{bmatrix} \begin{bmatrix} \dfrac{\partial T_{rr}}{\partial Z} & 0 & \dfrac{\partial rz}{\partial Z} \\ 0 & \dfrac{\partial T_{\theta\theta}}{\partial Z} & 0 \\ \dfrac{\partial T_{zr}}{\partial Z} & 0 & \dfrac{\partial T_{zz}}{\partial Z} \end{bmatrix} \right] \tag{3.89}$$

Appendix 3.C Finite element simulation with 3D unit cell

We have also developed finite element code using a 3D prismatic UC, with dimensions $\{2L_0, 2L_0, 2H_0\}$ in a Cartesian coordinate system. The volume of the UC is $V = 8L_0^2H_0$. Accounting for symmetry, only one quarter of the UC is considered in the numerical simulations (Fig. 3.14(a)). In 3D, there are three degrees of freedom to define the tensor $\boldsymbol{Q}$: two independent components of the director $\boldsymbol{d}$ (the third one is constrained by the condition $|\boldsymbol{d}| = 1$) and the order parameter S. We adopt the following parametrisation of the director:

$$\boldsymbol{d} = \cos\theta\cos\psi\ \boldsymbol{e}_x + \sin\theta\ \boldsymbol{e}_y + \cos\theta\sin\psi\ \boldsymbol{e}_z \tag{3.90}$$

where θ is the angle between the director and the $x-z$ plane, and ψ is the angle between the projection of the director onto the $x-z$ plane and the x-axis. From its definition (3.11), the order parameter tensor can then be written as:

$$[\boldsymbol{Q}] = S\begin{bmatrix} \cos^2\theta\cos^2\psi - \dfrac{1}{3} & \sin\theta\cos\theta\cos\psi & \cos^2\theta\sin\psi\cos\psi \\ \sin\theta\cos\theta\cos\psi & \sin^2\psi - \dfrac{1}{3} & \cos\theta\sin\theta\sin\psi \\ \cos^2\theta\sin\psi\cos\psi & \cos\theta\sin\theta\sin\psi & \sin^2\theta - \dfrac{1}{3} \end{bmatrix} \tag{3.91}$$

The boundary conditions for the 3D UC under uniaxial tension and compression

write as:

$$\begin{aligned}
&\varphi_x = 0 \qquad \text{on } \Gamma^i_{\text{left}} \cup \Gamma^m_{\text{left}} \\
&\varphi_y = 0 \qquad \text{on } \Gamma^i_{\text{bottom}} \cup \Gamma^m_{\text{bottom}} \\
&\varphi_z = 0 \qquad \text{on } \Gamma_{\text{back}} \\
&\varphi_z = 2L_0(\lambda_z - 1) \qquad \text{on } \Gamma_{\text{front}} \\
&\theta = 0,\ \psi = \frac{\pi}{2},\ \frac{\partial S}{\partial \boldsymbol{n}} = 0 \qquad \text{on } \Gamma^i_{\text{left}} \cup \Gamma^i_{\text{bottom}}
\end{aligned} \tag{3.92}$$

The right and top faces of the UC are constrained to remain flat for periodical boundary condition. This constraint is weakly imposed to the faces by adding the following term to the total potential:

$$\int_{\Gamma_{\text{right}}} \left[\beta_1 \left(\frac{\partial \varphi_x}{\partial z} \right) + \beta_2 \left(\frac{\partial \varphi_x}{\partial y} \right) \right] dS + \int_{\Gamma_{\text{top}}} \left[\beta_3 \left(\frac{\partial \varphi_y}{\partial x} \right) + \beta_4 \left(\frac{\partial \varphi_y}{\partial z} \right) \right] dS \tag{3.93}$$

where $\beta_1, \beta_2, \beta_3, \beta_4$ are Lagrange multipliers defined on the faces.

Fig. 3.14(b) shows the normalised effective stress-stretch curves for simulations with 3D UC (scatter) and 2D axisymmetric UC (solid). Material parameters were the following: Case 1: $\omega_1 = 0.1, v = 1$ and $\xi = 1$ (black curves); Case 2: $\omega_1 = 0.2$, $v = 1$ and $\xi = 0.01$ (red curves). $\phi = 0.2$, $\gamma = 0.003$ J/m^2, and $L = 10^{-8}$ for all cases. Predictions of from both types of UCs are almost identical.

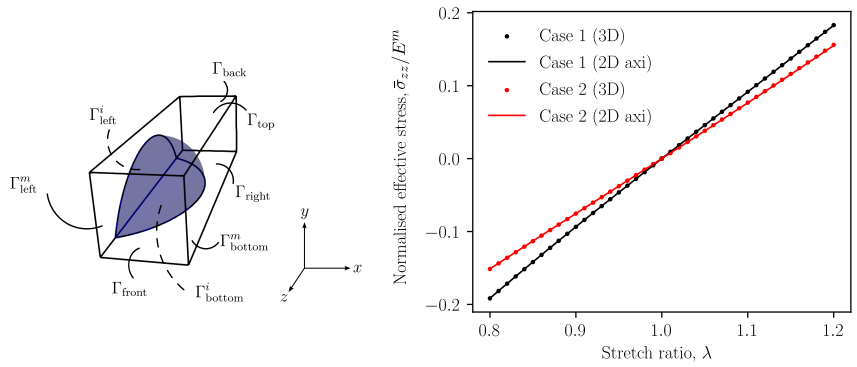

(a) (b)

Figure 3.14: (a) Schematic of 3D unit cell. (b) Comparison between normalised effective stress-stretch relationships obtained using 2D axisymmetric (solid line) and 3D (scatter) UCs

4 | Liquid crystal inclusions in soft matrices under an electric field

This chapter examines the electromechanical response of liquid crystal inclusions embedded in soft matrices subjected to external electric fields. Electric fields promote director alignment within the inclusion, while interfacial anchoring and matrix elasticity constrain this reorientation and convert it into a mechanical driving force for inclusion shape change and matrix deformation. The resulting behaviour is governed by the competition between electrostatic, interfacial, and elastic energy, and can be characterised using a small set of dimensionless parameters. In particular, the dimensionless inclusion volume and the elastocapillary number control both the sensitivity of the inclusions to the applied field and the magnitude of the induced deformation. These coupled mechanisms provide a physical basis for designing responsive soft composites in which electrically driven inclusion deformation can be utilised for functional actuation and tunable surface morphologies. In particular, comparing to the last chapter, we introduce novel free energy functions to describe the interfacial behaviours, which significantly improves the numerical convergence of the system.

4.1 Introduction

Composites consisting of liquid crystal inclusions dispersed within solid matrices have long been used in engineering applications (Manaila-Maximean, 2021; Hakemi, 2019; Baratta et al., 2022; Kamal et al., 2022; Aphonin et al., 1993; Ghorapade and Wang, 2024). The design strategy of these devices is to utilise the sensitivity of liquid crystal molecules to electric fields. Two ingredients are essential: the fluidic nature of the liquid crystal, which permits reorientation of the director, and the anisotropic dielectric response, which couples this reorientation to the external field.

In traditional polymer-dispersed liquid crystal (PDLC) devices with stiff matrices, the equilibrium orientation of the liquid crystal is governed by a balance between distortion elasticity of the director field, anchoring at the liquid crystal-matrix interface, and dielectric coupling to the applied field (Wu et al., 1989; Lin et al., 1995; Drzaic, 1995). The anchoring strength at the interface controls how easily the director can rotate away from its preferred surface orientation and therefore sets the threshold for field-induced reorientation. In the strong-anchoring limit, where the extrapolation length is much smaller than the droplet size, the director is effectively pinned at the interface (Drzaic, 1995; Stewart, 2021). If the applied field favours a different orientation, the director must vary spatially to interpolate between the anchoring boundary condition and the field-preferred orientation. This mismatch generates additional distortional elastic energy, and therefore a larger electric field is required to induce switching of the director field. The dielectric term provides the driving torque for reorientation which increases with the strength of the applied field and the anisotropy of the dielectric property. Consequently, the threshold field depends not only on anchoring and elastic distortion penalties but also on the dielectric anisotropy. Overall, electro-optic switching in PDLCs results from the balance between surface anchoring constraints, bulk elastic resistance to director gradients, and dielectric alignment under the applied field. The competition between these surface, bulk, and dielectric contributions determines both the equilibrium director configuration and the threshold field strength for electro-optic switching. In general, PDLC-based devices are used either in sensing-type applications or in actuation-type modulation, such as smart windows. In sensing applications, changes in the external electric, thermal, or chemical environment induce a reorientation of the liquid crystal, which in turn modifies the optical properties of the composite, for example its light transmittance and scattering (Lai et al., 2014; Kim et al., 2012; Pagidi et al., 2022; Pesch and Vetter, 2025). These changes in transmitted or scattered intensity can be detected by optical instruments or directly by the naked eye and thus

serve as the sensing signal. For PDLC devices with stiff matrices, actuation-type modulation devices mainly refers to optical actuations. The field-induced reorientation is used directly to switch the composite between a highly scattering, opaque state (field off) and a more transparent state (field on), enabling applications such as privacy glass and energy-saving smart windows (Zhang et al., 2019a; Oh et al., 2022; Alghamdi and Almawgani, 2019; Hemaida et al., 2020; Zhang et al., 2024; Meng et al., 2022; Khalid et al., 2021).

Recently, related composite systems have been adopted in engineering designs such as liquid crystal biosensors and liquid crystal-polymer composite electrolytes, in which the surrounding matrix is soft rather than stiff (Deng et al., 2019; Zhang et al., 2022; Lu et al., 2024a; Zhang et al., 2023; Sharma et al., 2025; Wu et al., 2022). In this regime, the elastic strain energy associated with deformation of the matrix can no longer be neglected. When an external electric field is applied, the liquid crystal molecules reorient as in conventional PDLCs, but unlike in the stiff-matrix case, the interface and the surrounding soft matrix can deform to reduce the excess free energy associated with interfacial anchoring. This electromechanical coupling between director reorientation, interfacial shape, and matrix elasticity introduces an additional mode of sensing and actuation: field-driven reorientation of the liquid crystal can induce appreciable mechanical deformation of the composite, which can be exploited either as a mechanical signal in mechano-sensing concepts or as a basis for soft, mechano-elastic actuation (Yu et al., 2011, 2014; Cheng et al., 2015) .

A wide range of modelling approaches have been developed to describe the electric switching in PDLCs. At the device level, phenomenological models relate the field-dependent optical response to an ensemble of droplets (Drzaic, 1995; Doane et al., 1986; Bloisi et al., 1997; Cox et al., 1998; Kelly and Palffy-Muhoray, 1994). In these models, the director field within each droplet is typically represented by an averaged quantity. At the single-droplet level, continuum theories based on director elasticity, together with

interfacial anchoring and dielectric coupling, have been used to predict equilibrium director fields inside droplets (Kaznacheev et al., 2002; Safdari et al., 2021; Shadkami and Chan, 2023; Rudyak et al., 2013). Some studies have also used Landau–de Gennes (or Q-tensor) formulations coupled to electrostatics to resolve spatially inhomogeneous switching and defect dynamics (Mottram and Newton, 2014; Luo et al., 2012). However, these models either assume a mechanically rigid matrix and a prescribed inclusion shape, or describe liquid-crystal droplets in fluidic environments; consequently, the coupling between director reorientation, interfacial tractions, and matrix deformation is neglected. This coupling is essential for describing soft composites containing liquid-crystal inclusions. The goal of the present work is to address this gap by developing a unified variational framework for liquid crystal inclusions embedded in a deformable solid, combining bulk director elasticity, surface anchoring, dielectric coupling, and matrix elasticity within a finite-element implementation. With the proposed theoretical and numerical model, we aim to predict both field-induced director realignment and the accompanying inclusion and matrix deformation.

In this chapter, we first review the basics of dielectric modelling of liquid crystal in Section 4.2. Then we propose the theoretical model in Section 4.3 to describe the problem, including kinematics, free energy and governing equations obtained from variational analysis. We illustrate free droplet problems in Section 4.4, and present the behaviour of liquid crystal inclusions in Section 4.5.

4.2 Polarisation in liquid crystals

Before introducing the full electro-elastic model, we briefly recall the basic notions of dielectric response in a form that will be used later. In electromagnetism, a dielectric material or dielectric medium is an electrical insulator in which electric charges cannot flow freely through the medium as they do in a conductor. Instead of drifting through

the material, bound charges shift slightly from their average equilibrium positions when an electric field is applied. This shifting is termed dielectric polarisation. After polarisation, positive charges are displaced in the direction of the field, and negative charges shift in the opposite direction. This creates an internal electric field that reduces the overall field within the dielectric material and allows energy to be stored in electrostatic form. This energy storage capacity is governed by the polarisability of the material. For example, for a dielectric material between the metallic plates of a capacitor, the larger the polarisability of the dielectric, the more surface charge is present on the plates for a given electric field strength. Dielectric materials are everywhere in our daily lives, such as air, pure water, paper, and many polymers. These materials are in general isotropic dielectrics, i.e. the polarisation behaviour of the material is independent of the orientation of the applied electric field. However, for liquid crystals and some solid crystals, the dielectric behaviour is anisotropic, since the shifting of electric charges is usually easier along the major axis of the liquid crystal molecule than in the perpendicular orientation. One important consequence of dielectric anisotropy is an optically birefringent response, i.e. different refractive indices for different directions of propagation or polarisation of light (de Gennes and Prost, 1993).

The polarisation behaviour mentioned above is termed induced polarisation, as it only appears in the presence of an external electric field. In addition, certain types of liquid crystals exhibit polarisation even in the absence of an applied field, which is termed spontaneous polarisation. Typical spontaneous polarisation mechanisms in liquid crystals include ferroelectric (Chen et al., 2020), flexoelectric (Meyer, 1969), and order-electric (Barbero et al., 1986) contributions. The existence of ferroelectric liquid crystals was predicted theoretically by Born (Born, 1916), but such phases were not identified experimentally for almost a century (Lavrentovich, 2020), and were only recently observed by Chen et al. (Chen et al., 2020). However, ferroelectric polarisation requires a polar molecular or supramolecular arrangement and therefore breaks the

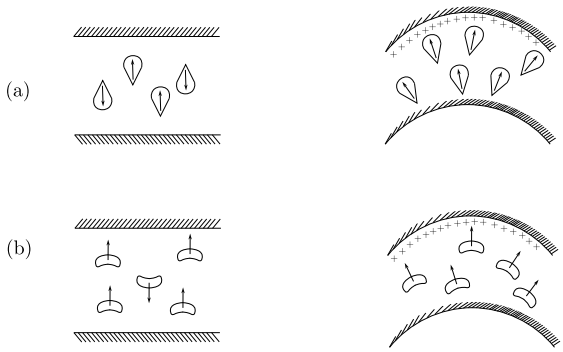

Figure 4.1: Schematic of the polarisation mechanisms of (a) wedge-shaped and (b) bent-core liquid crystal molecules. Adapted from (Meyer, 1969).

classical nematic symmetry assumption that $\boldsymbol{d}$ and $-\boldsymbol{d}$ are equivalent. In this study, we focus on nematic liquid crystals with apolar molecular order and consequently we do not consider ferroelectricity in the following.

Flexoelectric polarisation arises when a nematic director field is distorted in space. In a uniform nematic, microscopic dipoles or polar groups are arranged symmetrically and their contributions cancel, so the macroscopic polarisation vanishes. When the director is curved, for example by splay or bend deformations, this symmetry is broken. Although this phenomenon theoretically exists for all nematic liquid crystals, the degree of polarisation is usually negligible for rod-shaped molecules. On the other hand, wedge-shaped or bent-core molecules (Figure 4.1) exhibit more significant polarisation due to spatial variations of the director field. In addition, when the scalar order parameter varies in space, e.g. near a nematic-isotropic interface, a defect core or close to interfaces where the liquid crystal becomes partially disordered, order-electric effects also contribute to the total polarisation (Barbero et al., 1986; Durand, 1990; Porenta et al., 2011). In this subsection, we will show classical theories of electrostatics in liquid crystal, especially the polarisation behaviours in a $\boldsymbol{Q}$ tensor based framework.

In classical electrostatics, the electric field $\boldsymbol{E}$ can be expressed as the gradient of a scalar electric potential ϕ,

$$\boldsymbol{E} = -\nabla\phi. \tag{4.1}$$

The electric displacement field is related to the electric field and the polarisation by

$$\boldsymbol{D} = \varepsilon_0 \boldsymbol{E} + \boldsymbol{P}, \tag{4.2}$$

where ε_0 is the permittivity of free space and $\boldsymbol{P}$ is the total polarisation density, including both induced and spontaneous contributions. The total polarisation $\boldsymbol{P}$ in the material is written as the sum of an induced contribution and a spontaneous contribution,

$$\boldsymbol{P} = \boldsymbol{P}_i + \boldsymbol{P}_s, \tag{4.3}$$

where $\boldsymbol{P}_i$ denotes the polarisation that is induced by the electric field, and $\boldsymbol{P}_s$ collects spontaneous contributions that may exist without an applied electric field. For a linear dielectric, the induced polarisation is taken to be proportional to the electric field,

$$\boldsymbol{P}_i = \varepsilon_0 \boldsymbol{\varepsilon}_r \boldsymbol{E}, \tag{4.4}$$

where $\boldsymbol{\varepsilon}_r$ is the relative permittivity tensor. For isotropic dielectrics, $\boldsymbol{\varepsilon}_r = \varepsilon_r \boldsymbol{I}$ is a scalar multiple of the identity, and the induced polarisation is independent of orientation. For nematic liquid crystals, $\boldsymbol{\varepsilon}_r$ is anisotropic and depends on the local orientational order (de Gennes and Prost, 1993) and is given by

$$\boldsymbol{\varepsilon}_r = \bar{\varepsilon} \boldsymbol{I} + \Delta\varepsilon^* \boldsymbol{Q}, \tag{4.5}$$

where $\boldsymbol{Q}$ is the nematic order parameter tensor and $\bar{\varepsilon}$ and $\Delta\varepsilon^*$ are material parameters that characterise the isotropic and anisotropic parts of the permittivity (Mottram and Newton, 2014). The induced polarisation depends on the liquid crystal configuration through the anisotropic permittivity, providing the basic coupling between the electrostatics and the orientational order.

Within a $\boldsymbol{Q}$-tensor framework, the contribution from flexoelectricity and order elec-

tricity can be expressed together with an effective spontaneous polarisation that is linear in the divergence of the order parameter tensor. Following Mottram and Newton (Mottram and Newton, 2014), we adopt the form given by

$$\boldsymbol{P}_s = \bar{e}\,\nabla \cdot \boldsymbol{Q}, \tag{4.6}$$

where $\bar{e}$ is an effective flexo-order-electric coefficient. This compact expression captures the spontaneous polarisation arising from spatial variations of the director field and scalar order parameter, and is convenient for the variational formulation and numerical implementation developed in the subsequent sections.

4.3 Continuum theory

This section presents the continuum framework used to model a liquid-crystal inclusion embedded in a deformable solid matrix under an applied electric field. The aim is to formulate the coupled electro–chemo–mechanical problem in a variational setting. The presentation is organised as follows. We specify the free-energy contributions (bulk elasticity, director distortional elasticity, surface anchoring, and dielectric coupling) and the associated constitutive relations in Section 4.3.2. Finally in Section 4.3.3, we derive the governing equations and natural boundary/interface conditions by taking variations of the total potential.

4.3.1 Kinematics

The kinematic framework used in this chapter follows that introduced in Section 3.2.1. To avoid repetition, only the additional constitutive and coupling assumptions specific to the present problem are discussed below.

4.3.2 Free energy

Bulk energy The free energy in the bulk (matrix or liquid crystal phase) is additively decomposed into elastic, distortion and residual contributions:

$$\begin{aligned} U(\boldsymbol{F}, \boldsymbol{Q}, \operatorname{grad} \boldsymbol{Q}, \operatorname{grad} \phi; \boldsymbol{X}) = U_e(\boldsymbol{F}; \boldsymbol{X}) + U_Q(\boldsymbol{F}, \boldsymbol{Q}, \operatorname{grad} \boldsymbol{Q}; \boldsymbol{X}) \\ + U_{es}(\boldsymbol{F}, \boldsymbol{Q}, \operatorname{grad} \boldsymbol{Q}, \operatorname{grad} \phi; \boldsymbol{X}) + U_r(\boldsymbol{F}; \boldsymbol{X}), \end{aligned} \tag{4.7}$$

where U_e is the free energy density of elastic deformation, U_Q is the free energy density associated with distorting the liquid crystal order, U_{es} is the energy density due to the electrostatic field, and U_r is the energy density associated with the residual stress field. The capital letter U denotes the free energy per unit volume in the reference configuration. The explicit dependence on $\boldsymbol{X}$ indicates that material parameters depend on the phase.

The elastic free energy density is taken to be of (incompressible) neo-Hookean form:

$$U_e(\boldsymbol{F}; \boldsymbol{X}) = \frac{G(\boldsymbol{X})}{2} \left[\operatorname{tr}(\boldsymbol{F}^T \boldsymbol{F}) - 3 \right], \tag{4.8}$$

where G is the shear modulus, taken to be uniform in each phase: $G(\boldsymbol{X}) = G^r$ when $\boldsymbol{X} \in \mathcal{B}_0^r$ with $r = m, i$. Following Ghosh and Lopez-Pamies (2022), the liquid crystal inclusion is treated as a hyperelastic fluid and therefore $G^i \to 0$.

The free energy associated with the liquid crystal is given by

$$U_Q(\boldsymbol{F}, \boldsymbol{Q}, \operatorname{grad} \boldsymbol{Q}; \boldsymbol{X}) = J\, u_Q(\boldsymbol{Q}, \operatorname{grad} \boldsymbol{Q}; \boldsymbol{X}), \tag{4.9}$$

where u_Q is the Landau-de Gennes energy density (energy per unit volume in the current configuration). This energy consists of two contributions: a thermotropic energy dictating the preferred scalar order parameter, and an elastic energy penalising spatial

variations of the order parameter, i.e.

$$u_Q = u_Q^t + u_Q^e \tag{4.10}$$

For uniaxial nematic liquid crystals, the thermotropic energy is written as (Mottram and Newton, 2014)

$$u_Q^t(\boldsymbol{Q}; \boldsymbol{X}) = a\,\mathrm{tr}(\boldsymbol{Q}^2) + \frac{2b}{3}\,\mathrm{tr}(\boldsymbol{Q}^3) + c\,\mathrm{tr}(\boldsymbol{Q}^4), \tag{4.11}$$

and the elastic energy as

$$u_Q^e(\mathrm{grad}\,\boldsymbol{Q}; \boldsymbol{X}) = \frac{L_1(\boldsymbol{X})}{2} Q_{ij,k} Q_{ij,k} + \frac{L_2(\boldsymbol{X})}{2} Q_{ij,j} Q_{ik,k} + \frac{L_3(\boldsymbol{X})}{2} Q_{ik,j} Q_{ij,k}, \tag{4.12}$$

where the index notation $Q_{ij,k}$ refers to the gradient with respect to coordinates in the current configuration. This free energy form has been constructed based on mathematical considerations of objectivity, neglecting higher-order terms. General objectivity constraints on the free energy density have been studied in detail elsewhere; see, for example, Chapter 4 of Sonnet and Virga (2012) and the appendices of Zhang et al. (2019b). For simplicity, we assume that all three terms contribute equally to the excess free energy due to distortion, so that $L_1(\boldsymbol{X}) = L_2(\boldsymbol{X}) = L_3(\boldsymbol{X}) \equiv L_{LdG}(\boldsymbol{X})$ (one-constant approximation). We take $L_{LdG}(\boldsymbol{X}) = L_{LdG}$ when $\boldsymbol{X} \in \mathcal{B}_0^i$, and $L_{LdG}(\boldsymbol{X}) = 0$ when $\boldsymbol{X} \in \mathcal{B}_0^m$.

Remark 1. *Unlike Chapter 3, this chapter includes the thermotropic free energy of the liquid crystal. In Chapter 3, the interface was modelled as having a prescribed preferred scalar order parameter, which corresponds to a special case of the interfacial description. Here, this restriction is removed and a more general interfacial energy is introduced. As a result, the scalar order parameter is no longer directly constrained by the interfacial term. The thermotropic free energy therefore provides a natural bulk contribution that regulates the magnitude of the scalar order parameter and determines*

its energetically preferred value.

Due to the presence of surface tension and spatial variations of the order parameter tensor $\boldsymbol{Q}$, a residual (first Piola-Kirchhoff) stress field $\boldsymbol{P}_r(\boldsymbol{X})$ is in general required to achieve mechanical equilibrium in the reference configuration. The corresponding residual energy takes the form

$$U_r(\boldsymbol{F};\boldsymbol{X}) = \boldsymbol{P}_r(\boldsymbol{X}) : \boldsymbol{F}. \tag{4.13}$$

In the case of spherical liquid inclusions with isotropic surface tension, the residual stress field in the inclusion is of the form $\boldsymbol{P}_r = p\,J\,\boldsymbol{F}^{-T}$ and balances the isotropic surface tension, where p is a hydrostatic pressure. The corresponding residual energy per unit volume in the inclusion is then simply pJ (Ghosh and Lopez-Pamies, 2022). The electrostatic free energy density due to an external electric field is expressed as

$$U_{es}(\boldsymbol{F},\boldsymbol{Q},\operatorname{grad}\boldsymbol{Q},\operatorname{grad}\phi;\boldsymbol{X}) = J\,u_{es}(\boldsymbol{Q},\operatorname{grad}\boldsymbol{Q},\operatorname{grad}\phi;\boldsymbol{X}), \tag{4.14}$$

where u_{es} is the electrostatic energy density per unit volume in the current configuration. In this work, we assume a linear dielectric response, so that the electric displacement is linearly related to the electric field (Eqn. 4.2). Under this linear dielectric assumption, the electrostatic contribution to the free-energy density writes

$$u_{es} = -\frac{1}{2}\,\boldsymbol{D}\cdot\boldsymbol{E}. \tag{4.15}$$

For a nonlinear dielectric, this quadratic expression is no longer generally valid. In that case, the electrostatic energy density should instead be written in integral form as

$$u_{es}(\boldsymbol{E}) = -\int_{\boldsymbol{0}}^{\boldsymbol{E}} \boldsymbol{D}(\widetilde{\boldsymbol{E}})\cdot d\widetilde{\boldsymbol{E}}, \tag{4.16}$$

which reduces to Eqn. 4.15 only when $\boldsymbol{D}$ depends linearly on $\boldsymbol{E}$. Substituting the expressions in Section 4.2 (Eqn. 4.1 - Eqn. 4.6) into Eqn. (4.15) we obtain the explicit form of the electrostatic energy given by

$$u_{es} = -\frac{\varepsilon_0}{2}\left(\Delta\varepsilon^*\boldsymbol{Q} + \bar{\varepsilon}\,\boldsymbol{I}\right) : \left(\operatorname{grad}\phi \otimes \operatorname{grad}\phi\right) + \bar{e}\operatorname{div}\boldsymbol{Q}\cdot\operatorname{grad}\phi. \tag{4.17}$$

Interface energy The interfacial free energy is taken to be of the form

$$\widehat{U}(\widehat{\boldsymbol{F}}, \boldsymbol{Q}, \boldsymbol{N}) = \widehat{J}\,\widehat{u}(\boldsymbol{Q}, \boldsymbol{n}), \tag{4.18}$$

where $\widehat{u}$ is the interface energy per unit area in the current configuration, taken as

$$\widehat{u}(\boldsymbol{Q}, \boldsymbol{n}) = \gamma\left[1 + \omega\left(\boldsymbol{d}\cdot\boldsymbol{n}\right)^2 + \alpha\left(\ln\widehat{J}\right)^2\right], \tag{4.19}$$

with γ the surface tension, ω the anchoring strength of the director, and α a penalising parameter. In Eqn. (4.19), the first term penalises increases in surface area, and the second term promotes alignment of the director field with the interface plane. The first two terms together constitute the classical Rapini-Papoular form of anisotropic surface energy. For better numerical performance, the third term is added to restrict the surface area from shrinking to zero. This avoids large distortions of elements in finite element models. Expression (4.19) is commonly adopted to describe interfaces of droplets bounded by isotropic fluids (Warenghem et al., 1984) or soft polymer interfaces (Ramdane et al., 2000). It is worth noting that the present formulation differs from that used in our previous study (Chap. 3), where the term specifying the preferred scalar order parameter at the interface was removed and this preference was instead enforced through Eqn. 4.11.

4.3.3 Variational theory

In this subsection, we derive the governing equations and state laws through a variational analysis. Similar to Chapter 3, we present the variational formulation of the electrostatic-mechanical coupling of liquid crystal inclusions in order to obtain the governing equations. We consider a body subjected to a body force field $\boldsymbol{B}$ in $\mathcal{B}_0$ and a traction field $\boldsymbol{T}$ applied on its external boundary $\partial\mathcal{B}_0$. The total potential energy of the body is given by

$$\begin{aligned} I(\boldsymbol{\varphi}, \boldsymbol{Q}, \operatorname{grad}\boldsymbol{Q}, \phi, \operatorname{grad}\phi.p) = &\int_{\mathcal{B}_0} U(\boldsymbol{F}, \boldsymbol{Q}, \operatorname{grad}\boldsymbol{Q}, \operatorname{grad}\phi; \boldsymbol{X})\, dV \\ &+ \int_{\mathcal{S}_0} \widehat{U}(\boldsymbol{F}, \boldsymbol{Q}; \boldsymbol{X}, \boldsymbol{N})\, dS \\ &+ \int_{\mathcal{B}_0} p\,(J-1)\, dV - \int_{\mathcal{B}_0} \boldsymbol{B}\cdot\boldsymbol{\varphi}\, dV - \int_{\partial\mathcal{B}_0} \boldsymbol{T}\cdot\boldsymbol{\varphi}\, dS, \end{aligned} \tag{4.20}$$

where p is a scalar Lagrange multiplier that weakly enforces the incompressibility constraint on the domain. For the electric problem, the boundary is decomposed into a Dirichlet part Γ_ϕ^D and a Neumann part Γ_ϕ^N, such that

$$\Gamma_\phi^D \cup \Gamma_\phi^N = \partial\mathcal{B}_t, \qquad \Gamma_\phi^D \cap \Gamma_\phi^N = \emptyset. \tag{4.21}$$

The electric potential is prescribed on Γ_ϕ^D,

$$\phi = \bar{\phi} \qquad \text{on } \Gamma_\phi^D, \tag{4.22}$$

and the admissible variations therefore satisfy

$$\delta\phi = 0 \qquad \text{on } \Gamma_\phi^D. \tag{4.23}$$

On the remaining part of the boundary, Γ_ϕ^N, the natural boundary condition corresponds to a prescribed normal electric displacement. In the absence of free surface charge, this reduces to an electrically insulated condition. The terms on the right-hand side correspond to the bulk free energy, interfacial energy, constraint potential, and the work done by external forces. We seek stationary points of the total potential energy I with respect to admissible variations in the deformation map $\boldsymbol{\varphi}$, the order parameter tensor $\boldsymbol{Q}$, the electric potential ϕ, and the Lagrange multiplier p.

4.3.3.1 Variation $\delta\boldsymbol{\varphi}$

Consider the first variation $\boldsymbol{\varphi} \to \boldsymbol{\varphi} + \varepsilon\,\delta\boldsymbol{\varphi}$ around the true solution $(\boldsymbol{\varphi}, \boldsymbol{Q}, \phi, p)$. The corresponding variation of the potential energy is

$$\delta_{\boldsymbol{\varphi}} I = \left.\frac{d}{d\varepsilon} I(\boldsymbol{\varphi} + \varepsilon\,\delta\boldsymbol{\varphi}, \boldsymbol{Q}, \phi, p)\right|_{\varepsilon=0}. \tag{4.24}$$

The variation of the bulk energy gives

$$\delta_{\boldsymbol{\varphi}} U = \frac{\partial U_e}{\partial \boldsymbol{F}} : \delta_{\boldsymbol{\varphi}}\boldsymbol{F} + u_Q\,\delta_{\boldsymbol{\varphi}} J + J\,\frac{\partial u_Q}{\partial \operatorname{grad}\boldsymbol{Q}} \vdots \delta_{\boldsymbol{\varphi}}\operatorname{grad}\boldsymbol{Q} + u_{es}\,\delta_{\boldsymbol{\varphi}} J + J\,\frac{\partial u_{es}}{\partial \operatorname{grad}\phi}\,\delta_{\boldsymbol{\varphi}}\operatorname{grad}\phi. \tag{4.25}$$

Similarly, we obtain

$$\delta_{\boldsymbol{\varphi}}\boldsymbol{F} = \operatorname{Grad}\delta\boldsymbol{\varphi}, \tag{4.26}$$

$$\delta_{\boldsymbol{\varphi}}\boldsymbol{f} = -\,\boldsymbol{f}\cdot\delta_{\boldsymbol{\varphi}}\boldsymbol{F}\cdot\boldsymbol{f}, \tag{4.27}$$

$$\delta_{\boldsymbol{\varphi}} J = J\,\boldsymbol{f}^T : \delta_{\boldsymbol{\varphi}}\boldsymbol{F}, \tag{4.28}$$

$$\delta_{\boldsymbol{\varphi}}\operatorname{grad}\boldsymbol{Q} = \operatorname{Grad}\boldsymbol{Q}\cdot\delta_{\boldsymbol{\varphi}}\boldsymbol{f}, \tag{4.29}$$

$$\delta_{\boldsymbol{\varphi}}\operatorname{grad}\phi = \operatorname{Grad}\phi\cdot\delta_{\boldsymbol{\varphi}}\boldsymbol{f}. \tag{4.30}$$

The true solution corresponds to a stationary point of the functional, $\delta_{\boldsymbol{\varphi}} I = 0$. In-

serting Eqs. (4.26)-(4.30) into the variation and collecting terms yields the following weak form:

$$\int_{\mathcal{B}_0} \boldsymbol{P} : \operatorname{Grad} \delta\boldsymbol{\varphi}\, dV + \int_{\mathcal{S}_0} \widehat{\boldsymbol{P}} : \widehat{\operatorname{Grad}}\, \delta\boldsymbol{\varphi}\, dS = \int_{\mathcal{B}_0} \boldsymbol{B} \cdot \delta\boldsymbol{\varphi}\, dV + \int_{\partial\mathcal{B}_0} \boldsymbol{T} \cdot \delta\boldsymbol{\varphi}\, dS, \quad (4.31)$$

where $\boldsymbol{P}$ denotes the bulk first Piola-Kirchhoff stress, given by

$$\boldsymbol{P} = \boldsymbol{P}_e + pJ\, \boldsymbol{f}^T + Ju_Q\, \boldsymbol{f}^T + J\, \boldsymbol{\sigma}^Q \cdot \boldsymbol{f}^T + Ju_{es}\, \boldsymbol{f}^T + J\, \boldsymbol{\sigma}^{es} \cdot \boldsymbol{f}^T + \boldsymbol{P}_r, \quad (4.32)$$

where $\boldsymbol{P}_e$ is the stress derived from the elastic strain energy (4.8) and is given by

$$\boldsymbol{P}_e = \frac{\partial U_e}{\partial \boldsymbol{F}} = G(\boldsymbol{X})\, \boldsymbol{F}. \quad (4.33)$$

In Eqn. (4.32), p physically represents the hydrostatic pressure arising from the incompressibility constraint. The term $Ju_Q \boldsymbol{f}^T$ represents the Landau-de Gennes contribution in the reference configuration under a given deformation gradient. The tensor $\boldsymbol{\sigma}^Q$ arises from distortions of the $\boldsymbol{Q}$-field, is analogous to the Ericksen stress (Ericksen, 1962), and is given by

$$\boldsymbol{\sigma}^Q = -\operatorname{grad} \boldsymbol{Q} \odot \frac{\partial u_Q}{\partial \operatorname{grad} \boldsymbol{Q}}, \quad (4.34)$$

or, in index notation,

$$\sigma^Q_{ij} = -Q_{kl,i} \frac{\partial u_Q}{\partial Q_{kl,j}}. \quad (4.35)$$

The tensor $\boldsymbol{\sigma}^{es}$ is a stress term due to the spatial variation of the electric potential,

$$\boldsymbol{\sigma}^{es} = -\operatorname{grad} \phi \cdot \frac{\partial u_{es}}{\partial \operatorname{grad} \phi}. \quad (4.36)$$

In Eqn. (4.31), $\widehat{\boldsymbol{P}}$ denotes the surface first Piola-Kirchhoff stress and can be decomposed as

$$\widehat{\boldsymbol{P}} = \widehat{J}\, \widehat{u}\, \widehat{\boldsymbol{f}}^T + \boldsymbol{n} \otimes \widehat{\boldsymbol{S}}_0, \quad (4.37)$$

where $\widehat{\boldsymbol{S}}_0$ is the so-called deformational surface shear (Steinmann, 2008):

$$\widehat{\boldsymbol{S}}_0 = \widehat{\boldsymbol{\pi}}_t \cdot \widehat{J}\,\widehat{\boldsymbol{f}}^T, \qquad \widehat{\boldsymbol{\pi}}_t = -\frac{\partial \widehat{u}}{\partial \boldsymbol{n}} \cdot \widehat{\boldsymbol{i}}. \tag{4.38}$$

Using integration by parts and the divergence theorem in the bulk and on the interface, we obtain the following strong form:

$$\operatorname{Div} \boldsymbol{P} + \boldsymbol{B} = \boldsymbol{0} \qquad \text{in } \mathcal{B}_0, \tag{4.39}$$

$$\boldsymbol{P}\boldsymbol{N} = \boldsymbol{T} \qquad \text{on } \partial\mathcal{B}_0, \tag{4.40}$$

$$\widehat{\operatorname{Div}}\, \widehat{\boldsymbol{P}} = (\boldsymbol{P}^i - \boldsymbol{P}^m)\boldsymbol{N} \qquad \text{on } \mathcal{S}_0, \tag{4.41}$$

$$\widehat{\boldsymbol{P}}\,\widehat{\boldsymbol{N}}_1 + \widehat{\boldsymbol{P}}\,\widehat{\boldsymbol{N}}_2 = \boldsymbol{0} \qquad \text{on } \mathcal{C}_0. \tag{4.42}$$

4.3.3.2 Variation $\delta\boldsymbol{Q}$

We now consider the first variation $\boldsymbol{Q} \to \boldsymbol{Q} + \eta\,\delta\boldsymbol{Q}$ around the true solution:

$$\delta_{\boldsymbol{Q}} I = \frac{d}{d\eta} I(\boldsymbol{\varphi}, \boldsymbol{Q} + \eta\,\delta\boldsymbol{Q}, \phi, p)\Big|_{\eta=0}. \tag{4.43}$$

Enforcing $\delta_{\boldsymbol{Q}} I = 0$ yields the weak form

$$\int_{\mathcal{B}_t} \left(\boldsymbol{r}^Q : \delta\boldsymbol{Q} + \boldsymbol{s}^Q \vdots \operatorname{grad} \delta\boldsymbol{Q} \right) dV + \int_{\mathcal{S}_t} \frac{\partial \widehat{u}}{\partial \boldsymbol{Q}} : \delta\boldsymbol{Q}\, dS = 0, \tag{4.44}$$

where

$$\boldsymbol{r}^Q = \frac{\partial u_{es}}{\partial \boldsymbol{Q}} \tag{4.45}$$

is the quantity energetically conjugate to the order parameter tensor. If the electrostatic energy is taken in the form of Eqn. 4.15, $\boldsymbol{r}^Q$ can be written as

$$\boldsymbol{r}^Q = -\frac{1}{2}\,\varepsilon_0 \Delta\varepsilon^* \operatorname{grad}\phi \otimes \operatorname{grad}\phi = -\frac{1}{2}\,\varepsilon_0 \Delta\varepsilon^*\, \boldsymbol{E} \otimes \boldsymbol{E}. \tag{4.46}$$

Physically, $\boldsymbol{r}^Q$ is the dielectric contribution to the molecular field as it represents the local driving force that tends to align the principal axis of the nematic order parameter with the electric field when $\Delta\varepsilon^* > 0$, or perpendicular to it when $\Delta\varepsilon^* < 0$. In this variational equation, $\boldsymbol{r}^Q$ therefore plays the role that forces the equilibrium $\boldsymbol{Q}$ towards the electric field direction.

$$\boldsymbol{s}^Q = \frac{\partial u_Q}{\partial \text{grad}\, \boldsymbol{Q}} + \frac{\partial u_{es}}{\partial \text{grad}\, \boldsymbol{Q}} \tag{4.47}$$

is the torque stress that provides the elastic restoring torque that tends to smooth out gradients in $\boldsymbol{Q}$.

The strong form is slightly different from that obtained in the previous chapter due to the presence of the term $\boldsymbol{r}^Q$, and reads

$$\text{div}\, \boldsymbol{s}^Q - \boldsymbol{r}^Q = \boldsymbol{0} \qquad \text{in } \mathcal{B}_t, \tag{4.48}$$

$$\boldsymbol{s}^Q \cdot \boldsymbol{n} + \frac{\partial \widehat{u}}{\partial \boldsymbol{Q}} = \boldsymbol{0} \qquad \text{on } \mathcal{S}_t, \tag{4.49}$$

$$\boldsymbol{s}^Q \cdot \boldsymbol{n} = \boldsymbol{0} \qquad \text{on } \partial\mathcal{B}_t. \tag{4.50}$$

4.3.3.3 Variation $\delta\phi$

Consider now the first variation $\phi \to \phi + \xi\, \delta\phi$ around the true solution:

$$\delta_\phi I = \frac{d}{d\xi} I(\boldsymbol{\varphi}, \boldsymbol{Q}, \phi + \xi\, \delta\phi, p)\Big|_{\xi=0}. \tag{4.51}$$

Enforcing $\delta_\phi I = 0$ yields the weak form

$$\int_{\mathcal{B}_t} \boldsymbol{D} \cdot \text{grad}\, \delta\phi\, dV = 0, \tag{4.52}$$

where

$$\boldsymbol{D} = \frac{\partial u_{es}}{\partial \text{grad}\, \phi} \tag{4.53}$$

is the electric displacement. The associated strong form is then

$$\text{div}\, \boldsymbol{D} = 0 \qquad \text{in } \mathcal{B}_t, \tag{4.54}$$

$$\phi = \bar{\phi} \qquad \text{on } \Gamma_\phi^D, \tag{4.55}$$

$$\boldsymbol{D} \cdot \boldsymbol{n} = \bar{q} \qquad \text{on } \Gamma_\phi^N. \tag{4.56}$$

Here $\bar{q}$ is the prescribed free surface charge density. In the present simulations, the non-electrode boundaries are taken to be electrically insulated, so that $\bar{q} = 0$ and hence $\boldsymbol{D} \cdot \boldsymbol{n} = 0$ on those boundaries.

For example, when an electric field is applied through the thickness, one may take

$$\phi = 0 \quad \text{on } \Gamma_{\text{bottom}}, \qquad \phi = \Phi_0 \quad \text{on } \Gamma_{\text{top}}, \tag{4.57}$$

with $\boldsymbol{D} \cdot \boldsymbol{n} = 0$ on the remaining boundaries.

4.3.3.4 Variation δp

Finally, we take the first variation $p \to p + \zeta\, \delta p$, which gives

$$\int_{\mathcal{B}_0} (J - 1)\, \delta p\, dV = 0. \tag{4.58}$$

The corresponding strong form is equivalent to the incompressibility constraint $J = 1$.

4.3.4 Mixed finite element formulation

In order to implement this variational theory in a finite element code, we discretise the electric potential ϕ, the director orientation α, and the scalar order parameter S with

first-order continuous Galerkin elements (CG-1), the displacement field $\boldsymbol{\varphi}$ with second-order continuous Galerkin elements (CG-2), and the hydrostatic pressure p with zeroth-order discontinuous Galerkin elements (DG-0). The resulting finite element problem is a coupled mixed variational problem, since all fields are solved simultaneously and the pressure acts as a Lagrange multiplier enforcing the incompressibility constraint. Therefore, the displacement-pressure discretisation requires particular care, as an unsuitable choice may lead to volumetric locking or spurious pressure modes. The CG-2/DG-0 choice is used here to give a richer approximation of the deformation field while representing the pressure as an element-wise multiplier. The scalar fields ϕ, α and S are discretised using CG-1 elements because their weak forms involve the fields and their first gradients, and this choice provides a simple continuous approximation that is sufficient for the numerical studies considered here. This mixed formulation is implemented through `FEniCSx` (Alnæs et al., 2015), and the liquid crystal specific variables are restricted in the inclusion subdomain with `multiphenicsx` (Ballarin, 2024).

4.4 Free droplet problem

In this section, we present numerical simulations of a liquid-crystal droplet surrounded by a fluidic environment taking into account the anisotropic surface tension, the distortional elasticity and the effect of an external electric field. Section 4.4.1 summarises the experimental setup of Metselaar et al. (2017) and describes the corresponding numerical implementation, including the geometry, mesh, and boundary conditions used to mimic the experiments. Section 4.4.2 presents the finite-element results and compares them with the experimental measurements. Finally, Section 4.4.3 investigates the influence of spontaneous polarisation by computing the equilibrium droplet shape in the absence of an applied electric field for a liquid crystal with flexoelectric and order-electric properties.

4.4.1 Physical setting and numerical implementation

Experimental motivation In the experiments of Metselaar et al. (2017), a suspension containing many nematic droplets was placed between two *external* electrodes (aluminium foil attached to the outside of the container), and uniform electric fields of strength $E = 0$ V/mm, 154 V/mm, and 309 V/mm were applied. Droplets were imaged under the applied field and the major-axis length L and minor-axis width W of each droplet were extracted from micrographs, yielding a statistical dataset over a range of droplet volumes. To compare droplets of different sizes, they used LW^2 as a scalar measure of droplet size. Approximating the droplet as a prolate spheroid gives $V = (\pi/6)LW^2$, so LW^2 is directly proportional to volume and can be inferred directly from the reported geometrical measurements. Our numerical setup is designed to reproduce this configuration at the single-droplet level by imposing a far-field axial electric field and avoiding any mechanical confinement, enabling a direct comparison of the predicted and measured droplet dimensions.

Geometry and mesh We model the droplet in an axisymmetric computational domain in the (r, z) plane, interpreted as a three-dimensional body of revolution about the symmetry axis $r = 0$ (Fig. 4.2). The axisymmetric implementation in `FEniCSx` is to simply write the weak from with a cylindrical integral, i.e. $\int F(r)rdr$ (cf. Section 3.3). The droplet is placed on the symmetry axis and the applied electric field is taken to be aligned with the axial direction (z-direction). This is a simplification of the experimental configuration considered in Metselaar et al. (2017), where the free droplet long axes reorient along the field direction. The surrounding medium is truncated using an outer boundary whose height and radius are set to 20 and 10 times the initial droplet radius, respectively, which is sufficient to approximate an unbounded fluidic environment. The mesh is generated using Gmsh and consists of approximately 1×10^3 triangular elements. Local refinement is applied near the droplet interface, and a coarser

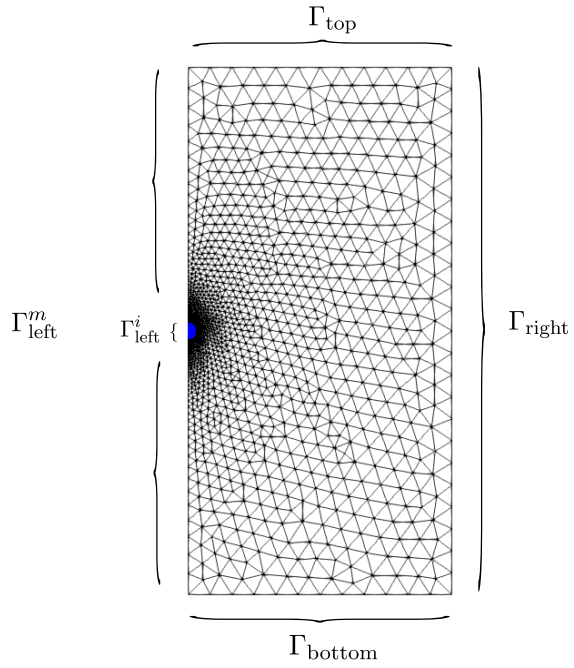

Figure 4.2: Triangular mesh generated for axisymmetric simulations on the free droplet problem coupled with external electric field.

discretisation is used away from the droplet to reduce computational cost.

Electric-field loading. The boundary $\Gamma_{\text{left}} = \Gamma^i_{\text{left}} \cup \Gamma^m_{\text{left}}$ is the axis of symmetry ($r = 0$). The boundaries Γ_{top} and Γ_{bottom} represent electrodes used to generate an approximately uniform axial electric field in the far field. Prescribing an electric potential difference ϕ_{applied} across the height H of the domain corresponds to a nominal field strength $E \approx \phi_{\text{applied}}/H$ oriented along the z-direction.

Dirichlet boundary conditions. The imposed Dirichlet boundary conditions are

$$\begin{aligned} \varphi_r &= 0 \quad \text{on } \Gamma_{\text{left}}, \\ \phi &= \phi_{\text{applied}} \quad \text{on } \Gamma_{\text{top}}, \\ \varphi_z &= 0,\ \phi = 0 \quad \text{on } \Gamma_{\text{bottom}}, \end{aligned} \tag{4.59}$$

where φ_r and φ_z are the radial and axial displacement components and ϕ is the electric potential. The condition $\varphi_r = 0$ enforces axisymmetry. The constraint $\varphi_z = 0$ on Γ_{bottom} removes rigid-body translation. The electrical boundary conditions $\phi = \phi_{\text{applied}}$ (top) and $\phi = 0$ (bottom) impose a prescribed voltage drop, mimicking the externally applied field used in the experiments.

Natural boundary conditions. The natural boundary conditions are

$$\begin{aligned} \boldsymbol{\sigma} \cdot \boldsymbol{n} &= 0 \quad \text{on } \Gamma_{\text{right}} \cup \Gamma_{\text{top}}, \\ \boldsymbol{t}_t &= 0 \quad \text{on } \Gamma_{\text{left}} \cup \Gamma_{\text{bottom}} \\ \frac{\partial \phi}{\partial \boldsymbol{n}} = 0,\ \frac{\partial \psi}{\partial \boldsymbol{n}} &= 0,\ \frac{\partial S}{\partial \boldsymbol{n}} = 0 \quad \text{on } \Gamma^i_{\text{left}} \cup \Gamma_{\text{right}}, \end{aligned} \tag{4.60}$$

where $\boldsymbol{\sigma}$ is the Cauchy stress and $\boldsymbol{n}$ the outward unit normal. $\boldsymbol{t}_t = (\boldsymbol{I} - \boldsymbol{n} \otimes \boldsymbol{n})\boldsymbol{\sigma}\boldsymbol{n}$ is the shear traction. The traction-free condition on right and top boundary along with the shear-traction free condition represents a droplet in a mechanically unconfined fluidic environment (no externally applied tractions on the truncated boundary).

Numerical method to obtain equilibrium free droplet shape We adopt the same approach described in Section 3.3 to obtain the equilibrium shape of the liquid crystal droplet by gradually reducing the shear modulus of the inclusion and the matrix until the droplet shape becomes insensitive to the changing elastic modulus.

4.4.2 Theory validation

Our validation and parameter calibration follow the same sequence as Metselaar et al. (2017). First, we fit the *non-dielectric* parameters using the zero-field deformation trend. Specifically, Fig. 4.3(a) compares the experimental L-W relation (scattered points) to finite-element predictions (solid curves) at $E = 0\,\mathrm{V/mm}$ and is used to identify parameters other than the dielectric response. In this validation simulation, we do not

consider the effect of spontaneous polarisation as the liquid crystal material used in the experiment (chitin) is considered rod shape and show weak flexoelectricity, therefore $\bar{e} = 0$. The fitted values are $L_{\mathrm{LdG}} = 10^{-10}$ J/m, $\gamma = 10^{-10}$ J/mm^2 $= 10^{-4}$ N/m, and $\omega = 1$, which lie within commonly reported ranges for distortional elasticity and LC-polymer interfacial energies (Mottram and Newton, 2014; Wu et al., 2006). Second, Fig. 4.3(b) calibrates the dielectric response at $E = 154$ V/mm, yielding $\Delta\varepsilon^* = 11$. Finally, Fig. 4.3(c) shows the predictions by comparing model results to the experimental dataset at the higher field strength $E = 309$ V/mm without further parameter adjustment. The close agreement across droplet sizes and field strengths indicates that the model captures the essential physics governing equilibrium droplet deformation, and it supports using the calibrated parameters in the subsequent inclusion-in-matrix simulations.

Figures 4.3 and 4.4 together illustrate how the balance between interfacial, elastic and electric-field effects changes with droplet size and field strength. At zero field, Fig. 4.3(a) shows that both the length and width increase smoothly with the volumetric measure LW^2, and the droplets remain moderately elongated. This can be seen more clearly in Fig. 4.4, where the aspect ratio L/W is essentially constant at a value of about 2 over the full range of LW^2. In this regime the droplet shape is set by the competition between anisotropic surface tension, which favours a elongated droplet aligned with the nematic director, and bulk elastic distortions of the director field, which penalise strong curvature of the director near the interface. Changing the volume only weakly perturbs this balance, so the aspect ratio is nearly volume-independent.

When an electric field of $E = 154\ \mathrm{V/mm}$ is applied, Fig. 4.3(b) shows that the behaviour becomes strongly size dependent. For small droplets (low LW^2), the simulated length and width lie close to the zero-field curves, and Fig. 4.4 confirms that the aspect ratio remains close to 2. In this range, the contribution of the electric field to the free energy is still small compared with the surface and elastic terms, so the droplet shape

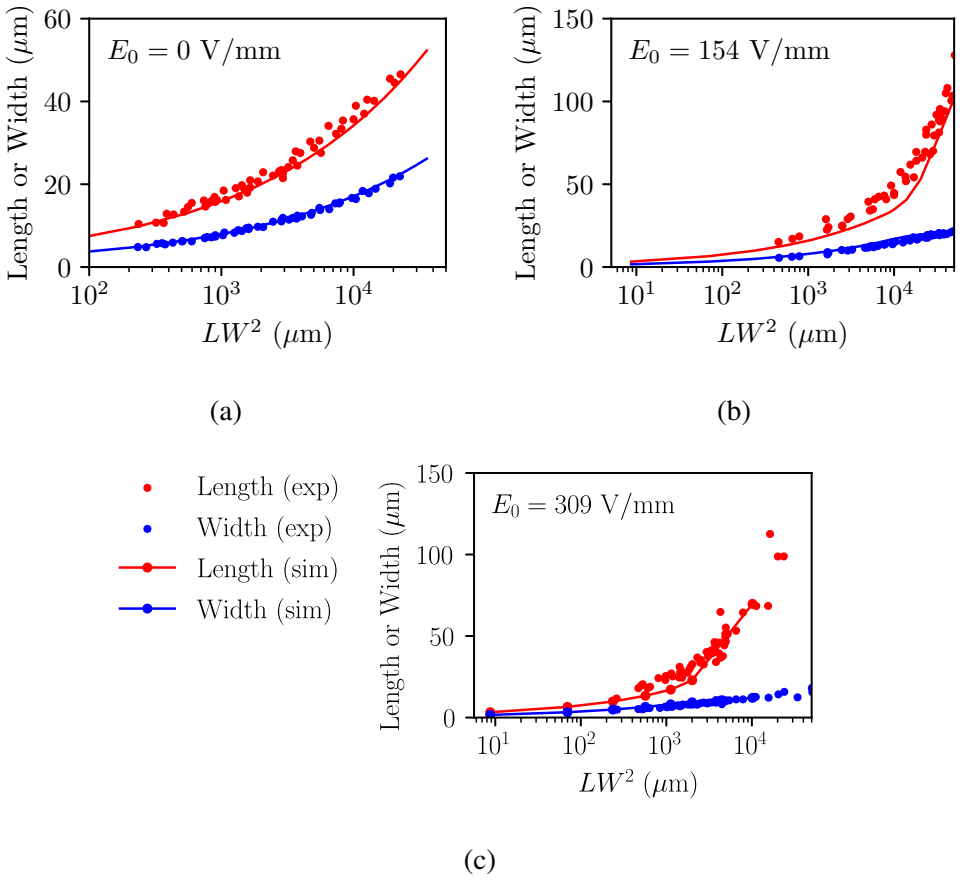

Figure 4.3: Relation between length and width of the droplet and the volume under applied electric field with strength (a) $E = 0\,\mathrm{V/mm}$, (b) $E = 154\,\mathrm{V/mm}$, (c) $E = 309\,\mathrm{V/mm}$

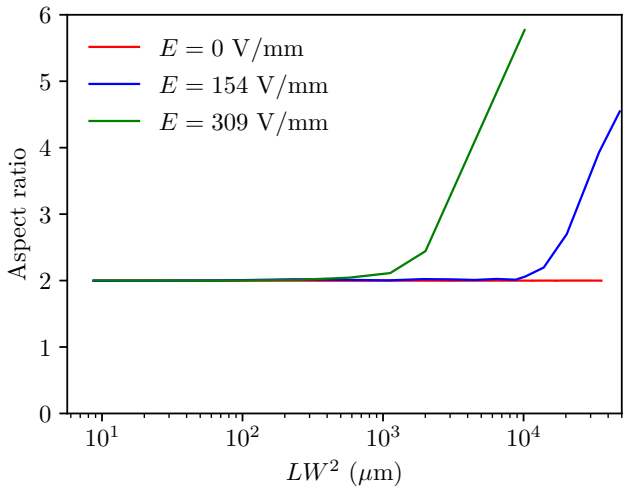

Figure 4.4: Relationship between aspect ratio and the volume of the droplets.

remains essentially unchanged. Beyond a critical effective volume, the curve for the length starts to deviate markedly from the zero-field trend, while the width increases only weakly. Correspondingly, the aspect ratio in Fig. 4.4 starts to rise above 2. This reflects the fact that the electric-field contribution, which scales with droplet volume, becomes comparable to the interfacial and elastic contributions. The director field then reorients towards the field direction, and the droplet elongates along the field to reduce both the anisotropic surface energy and the elastic distortion.

At the higher field $E = 309$ V/mm, Fig. 4.3(c) demonstrates that this behaviour is amplified. The deviation of the length from the zero-field trend now occurs at smaller values of LW^2, and for larger droplets the length grows very rapidly whereas the width remains almost unchanged. In Fig. 4.4 this appears as a sharp increase of the aspect ratio with LW^2, reaching values above 5 for the largest droplets considered. The droplets therefore become highly elongated, indicating that the electric-field term now dominates the energetic balance over most of the volume range. In other words, as the control parameters (effective droplet size and field strength) are increased, the system passes from a regime where the equilibrium shape is governed mainly by surface tension and

bulk elasticity to a regime where minimisation of the electrostatic energy results in a more elongated equilibrium configuration.

4.4.3 Effect of spontaneous polarisation

Physical setting and boundary conditions. In this subsection we investigate the effect of spontaneous polarisation generated by liquid-crystal inhomogeneities (flexoelectric and order-electric contributions) on the equilibrium shape and order parameter field of a free droplet. In contrast to the validation study in Section 4.4.2, no external electric field is applied. The equilibrium shape of the droplet is therefore driven purely by the competition between interfacial energy, bulk liquid-crystal elasticity, and the additional electrostatic energy associated with the spontaneous polarisation induced by order-parameter gradients. Numerically, we use the same axisymmetric geometry as before. To remove rigid-body motion while keeping the environment mechanically unconfined, we fix the axial displacement at the bottom boundary and enforce symmetry on the axis, i.e. $\varphi_z = 0$ on Γ_{bottom} and $\varphi_r = 0$ on Γ_{left}, while all other mechanical boundaries are traction-free. Electrically, we set the applied potential difference to zero so that $\phi = 0$ on the electrode boundaries, and we impose natural (zero-flux) boundary conditions for the electrostatic on the remaining outer boundaries. This setup ensures that any non-trivial electric potential and field arise solely from spontaneous polarisation within the droplet rather than from external loading. The equilibrium shape is obtained by reducing the modulus of the droplet and its surrounding like we did in previous subsection and Section 3.3.

Figure 4.5 shows the relation between the aspect ratio and the anchoring strength ω for droplets with $\bar{e} = 0\,\mathrm{C/m}$ and $\bar{e} = 10^{-10}\,\mathrm{C/m} = 100\,\mathrm{pC/m}$, respectively (typical values of $\bar{e}$ for flexoelectric liquid crystals are within $50\,\mathrm{pC/m} \sim 250\,\mathrm{pC/m}$ (Skarabot et al., 2022)). As the anchoring strength increases, the aspect ratio increases in both cases, indicating more elongated droplets. However, the elongation is much stronger

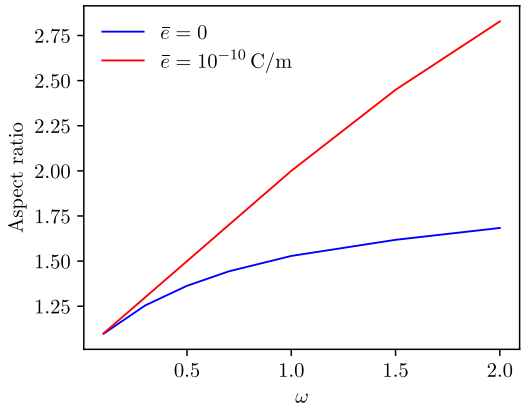

Figure 4.5: Relation between aspect ratio and anchoring strength for a relaxed 2D liquid crystal droplet.

when $\bar{e} \neq 0$.

This behaviour can be understood as follows. Increasing ω enforces the preferred director orientation at the interface more strongly, which enhances distortion of the director field inside the droplet and therefore raises the distortional elastic energy. When spontaneous polarisation is present, these distortions also generate additional electrostatic energy through the coupling between director gradients and polarisation. As a result, configurations with strong director distortions become even more energetically costly when $\bar{e}$ is large. The system then reduces its total free energy by adopting a more uniformly aligned director field in the bulk and deforming the interface further, leading to a smaller mismatch between the director and the local surface tangent and hence a more elongated droplet shape.

4.5 Liquid crystal inclusion problem

We now consider liquid-crystal inclusions embedded in a deformable elastic matrix and study how an applied electric field can be used to (i) reorient the director field inside the inclusions (sensing) and (ii) generate measurable macroscopic deformation of the

composite (actuation). The sensing capability is characterised by the sensitivity of the inclusion director field to the external field, while the actuation capability is quantified by the field-induced deformation of the inclusion and the resulting deformation of the surrounding matrix. Two geometries are investigated: a bulk-like composite represented by a two-dimensional array of repeated unit cells, and a thin composite membrane represented by a single row of unit cells.

4.5.1 Physical setting and numerical implementation

The composite is modelled in two dimensions under a plane-strain assumption using a representative volume element (RVE) consisting of an $N \times M$ array of identical unit cells (Fig. 4.6). Physically, this represents infinitely long liquid crystal fibres embedded in a matrix, and all fields are uniform in the out-of-plane direction. Each unit cell contains a single liquid-crystal inclusion located at its centre. The inclusion size is prescribed by an initial radius R_0, defined as the radius of a circular inclusion with the same cross sectional area $A_0 = \pi R_0^2$. This circular geometry is the same initial shape used in the free-droplet relaxation simulations. The unit-cell width is taken as $L_0 = 3R_0$. In the simulations below we set $R_0 = 0.1$ mm.The height of the unit cell is chosen as $H_0/L_0 = \epsilon_0$, where ϵ_0 denotes the inclusion aspect ratio in the reference configuration. Unless otherwise stated, the remaining parameters are $\omega = 1$, $L_{\mathrm{LdG}} = 10^{-10}$ J/m, and $\gamma = 10^{-7}$ N/mm $= 10^{-4}$ N/m. The reference configuration for the inclusion-in-matrix problem is constructed by first computing the equilibrium shape of a free droplet through gradually reducing the modulus of the inclusion and the matrix (cf. Sections 4.4 and 3.4.1). The boundary nodes of this equilibrium droplet are then used to generate an inclusion of the same shape embedded within the matrix, after which the coupled electro-elastic equilibrium problem is solved. The array size is selected based on a convergence study, which confirms that the central-cell response is insensitive to further increases in N and M, indicating that edge effects are negligible.

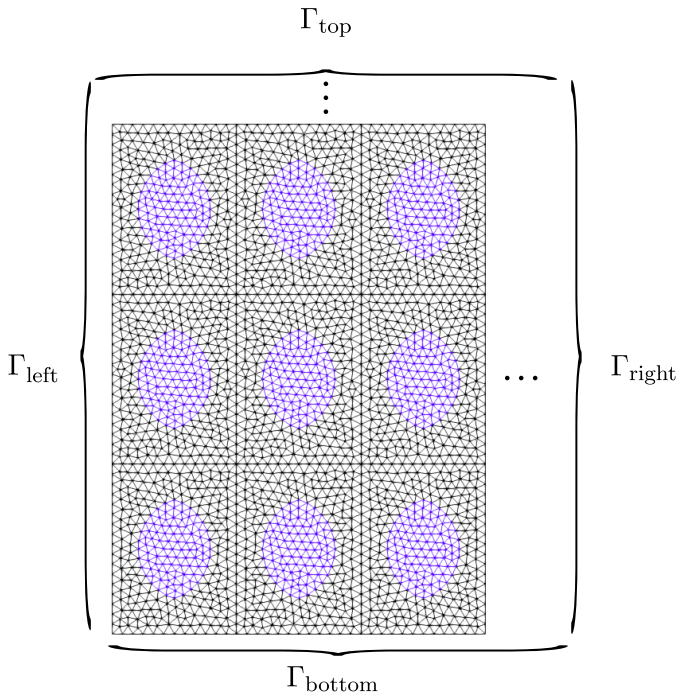

Figure 4.6: Triangular mesh generated for the 2D liquid crystal inclusion simulations under an applied electric field.

A more compact formulation would enforce exact periodicity directly on a single unit cell by means of multi-point constraints (MPC). At the time of writing, MPC functionality for FEniCSx is available via the `dolfinx_mpc` package, but this is not compatible with `multiphenicsx`, which we use to restrict the state variables to the appropriate subdomains. For this reason, we adopt the larger RVE strategy described above rather than imposing periodic MPC constraints on a single unit cell.

4.5.2 Response of bulk composite

We first consider a soft composite consisting of nematic liquid-crystal inclusions embedded in an elastic matrix, motivated by electro-responsive materials in which electrically driven director reorientation within the inclusions can lead to a macroscopic mechanical response. In such systems, the inclusions act as field-responsive micro-actuators: an applied electric field tends to align the director, thereby altering the balance between bulk liquid-crystal elasticity and anisotropic interfacial effects, and can drive inclusion shape changes. These local shape changes transmit tractions to the surrounding matrix and are, in turn, constrained by the matrix elasticity, which we characterise using the elastocapillary number $\chi = GR_0/\gamma$. The objectives of the present simulations are to quantify the sensing response by examining the field sensitivity of the inclusion director field, and to quantify the actuation response by measuring the inclusion aspect ratio as a function of the applied field strength.

We investigate this problem using a 7×7 array of unit cells. To remove rigid-body motion while keeping the outer boundary otherwise mechanically free, we impose the following mechanical Dirichlet boundary conditions:

$$\begin{aligned} \varphi_x &= 0 \quad \text{on } \Gamma_{\text{left}}, \\ \varphi_y &= 0 \quad \text{on } \Gamma_{\text{bottom}}. \end{aligned} \tag{4.61}$$

Here, φ_x and φ_y denote the displacement components in the x- and y-directions. The right and top boundaries is traction-free and no displacement is prescribed. Shear tractions vanish on the left and bottom boundaries where only one displacement component is constrained, i.e.,

$$\begin{aligned} \boldsymbol{\sigma}\,\boldsymbol{n} &= \mathbf{0} \quad \text{on } \Gamma_{\text{right}} \cup \Gamma_{\text{top}}, \\ \big(\boldsymbol{I} - \boldsymbol{n}\otimes\boldsymbol{n}\big)\,\boldsymbol{\sigma}\,\boldsymbol{n} &= \mathbf{0} \quad \text{on } \Gamma_{\text{left}} \cup \Gamma_{\text{bottom}}, \end{aligned} \tag{4.62}$$

where $\boldsymbol{\sigma}$ is the Cauchy stress, $\boldsymbol{n}$ is the outward unit normal, and $\boldsymbol{I}$ is the identity tensor.

In the reference configuration, the director field inside the inclusion is predominantly aligned with the y-direction. To probe the anisotropic electro-mechanical response, we apply electric fields along both the y- and x-directions by prescribing the electric potential on opposite outer boundaries:

$$\begin{aligned} \phi &= \phi_{\text{applied}} \quad \text{on } \Gamma_{\text{top}} \text{ or } \Gamma_{\text{right}}, \\ \phi &= 0 \quad \text{on } \Gamma_{\text{bottom}} \text{ or } \Gamma_{\text{left}}. \end{aligned} \tag{4.63}$$

On all remaining outer boundaries (i.e. those not used as electrodes), the electric boundary condition is natural and corresponds to electrical insulation (no free surface charge), which in potential form reads

$$\frac{\partial \phi}{\partial \boldsymbol{n}} = 0 \quad \text{on the non-electrode boundaries,} \tag{4.64}$$

Imposing a potential difference ϕ_{applied} across a pair of opposite boundaries generates an approximately uniform far-field electric field within the domain: choosing $\Gamma_{\text{top}}/\Gamma_{\text{bottom}}$ produces a vertical field (along y), whereas choosing $\Gamma_{\text{right}}/\Gamma_{\text{left}}$ produces a horizontal field (along x). In all cases, we report the response of the central unit cell of the 7×7 array, where edge effects are minimal and the environment is approximately periodic. Therefore, the applied electric field can be obtained from a given far field

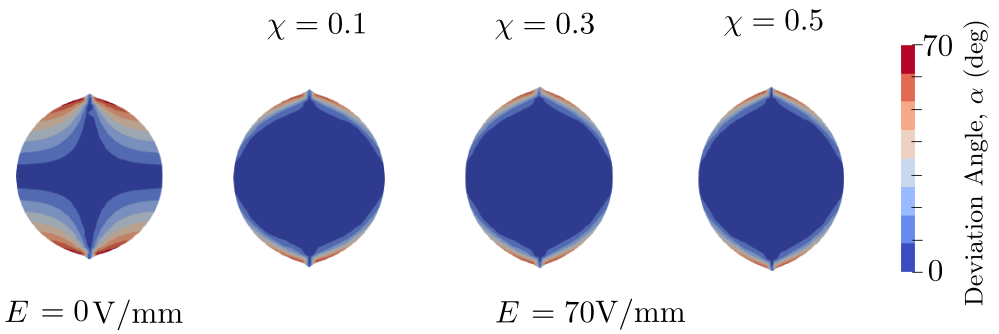

Figure 4.7: Director-field response under a vertically applied electric field. The colour scale shows the deviation angle between the director and the vertical (y) axis.

electric field strength E by

$$\phi_{\text{applied}} = \begin{cases} E\,(7H_0), & \text{for a vertical field}), \\ E\,(7L_0), & \text{for a horizontal field}). \end{cases} \tag{4.65}$$

In practice, ϕ_{applied} is applied to the electrode boundaries incrementally from $0\,\mathrm{V}$ using 50 steps.

Vertically applied electric field. Figure 4.7 shows the director field inside the inclusion under a vertical electric field, visualised by the deviation angle between the director and the y-axis. At zero field (left inclusion), the director configuration is determined by the competition between anisotropic interfacial effects (surface tension and anchoring) and distortional elasticity. The director is approximately vertical in the interior but bends near the interface to satisfy the anchoring condition, producing non-zero deviation angles over an interfacial region. When a vertical field is applied (right inclusions), dielectric coupling favours alignment with the field. As the field increases, the deviation angle decreases throughout the inclusion and the remaining distortions become confined to a thin boundary layer close to the interface, where anchoring constraints must still be satisfied.

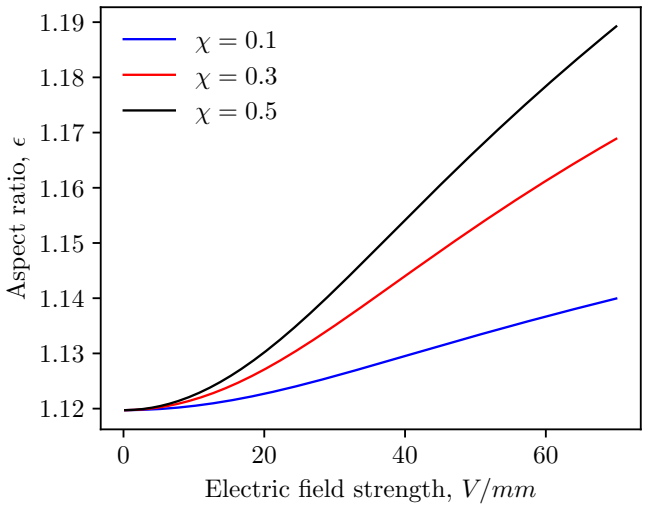

Figure 4.8: Inclusion deformation under a vertically applied electric field. The aspect ratio is shown as a function of field strength for different elastocapillary numbers χ.

The associated shape response is quantified in Fig. 4.8, which plots the inclusion aspect ratio as a function of the applied field strength for different elastocapillary numbers χ. The aspect ratio increases monotonically, indicating that the inclusion elongates along the field direction. This elongation reduces the total free energy when the director is nearly field-aligned in the bulk by adjusting the local surface normals so that the director is closer to its anchoring-preferred orientation along most of the interface. Deforming the surrounding elastic matrix provides the primary resistance to this shape change. The dependence on χ reflects the balance between interfacial energy and matrix stiffness: larger χ corresponds to stronger capillary effects relative to elastic resistance, resulting in a larger shape change for the same applied field.

Horizontally applied electric field. When the field is applied along the x-direction, the director and mechanical responses are qualitatively different. Figure 4.9 shows that applying a horizontal field drives the director to tilt towards the x-direction, particularly in the central region of the inclusion. The resulting director pattern becomes shear-like and loses the left–right symmetry of the zero-field configuration, reflecting a stronger

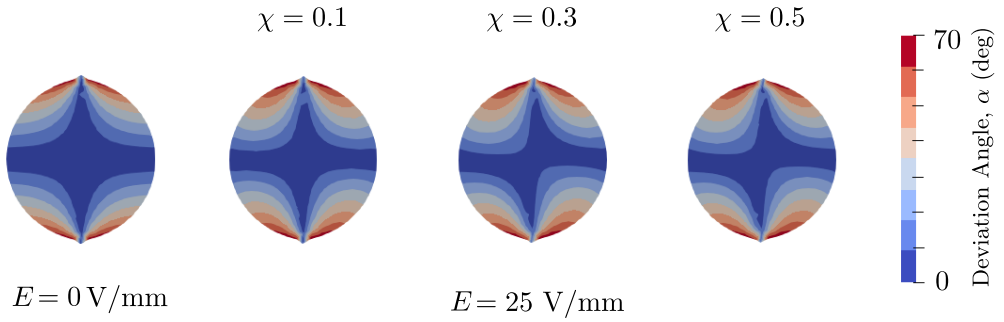

Figure 4.9: Director-field response under a horizontally applied electric field. The colour scale shows the deviation angle between the director and the vertical (y) axis for the zero-field case (left) and for $E = 25\,\mathrm{V/mm}$ at different elastocapillary numbers χ.

competition between field alignment in the bulk and anchoring constraints at the interface. This competition is amplified as χ increases because stronger interfacial effects promote larger distortions.

Figure 4.10 quantifies the corresponding shape change. In contrast to the vertical-field case, the inclusion aspect ratio decreases with increasing horizontal field strength, indicating a net shortening along the y-direction (and widening in the field direction). Physically, as the director is driven towards a more uniform horizontal state, the elongated reference shape becomes unfavourable because large sidewall regions then experience strong misalignment between the director and the anchoring-preferred tangential orientation. By flattening, the inclusion reduces the area of these poorly aligned regions and increases the interfacial area where the director can remain closer to tangential, thereby lowering the combined anchoring and elastic contributions at the expense of deforming the surrounding matrix. For sufficiently large fields the simulations fail to converge, suggesting that more robust numerical strategies would be required to explore the regime of large director rotations and large deformations under strong horizontal fields.

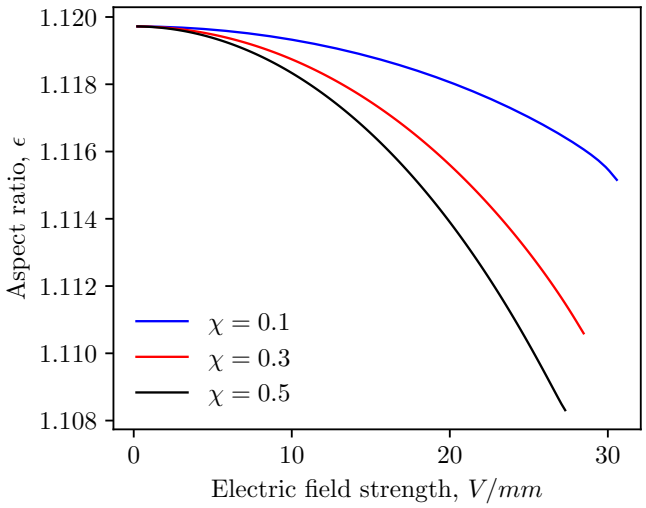

Figure 4.10: Inclusion deformation under a horizontally applied electric field. The aspect ratio is shown as a function of field strength for different elastocapillary numbers χ.

4.5.3 Response of composite membrane

We next consider a thin composite membrane consisting of a single row of inclusions ($M = 1$) to test whether electrically driven inclusion deformations can be converted into a controllable surface topography. Surface wrinkling is a widely used mechanism for creating functional textures, because periodic height modulations can tune optical scattering/reflectance, wettability, adhesion, and transport properties (Chan et al., 2008; Hou et al., 2019; Liu et al., 2023). For example, surface wrinkles can introduce roughness at the surface, which amplifies the wettability. Also, a large amplitude and wavelength ratio of the surface leads to lower adhesion (Davis and Crosby, 2011). Conventional wrinkling strategies rely on mechanical pre-strain or multilayer/bilayer mismatches; here, the aim is to assess an alternative actuation route in which the inclusions act as embedded micro-actuators. When an electric field elongates the inclusions, the resulting interfacial tractions load the surrounding matrix non-uniformly and can induce a periodic displacement of the free surface. The objective of this subsection is therefore

to quantify (i) whether the induced surface modulation is appreciable in magnitude, and (ii) how it scales with field strength and with the elastocapillary coupling.

The problem is defined on a 7×1 unit-cell mesh. To minimise boundary effects, all surface metrics are extracted from the central unit cells. Rigid-body motion is removed by fixing the bottom-left corner, and the bottom edge is constrained in the vertical direction to represent a membrane supported by a rigid substrate (or clamped support) that prevents vertical displacement. The top surface is traction-free, allowing it to deform out of plane (in the present 2D setting, in the y-direction). A vertical electric field is applied along the y-direction by prescribing the electric potential on the outer boundaries as in the bulk-composite calculations.

Figure 4.11 shows the membrane deformation at $E = 70$ V/mm for several values of the elastocapillary number χ. The top panel shows the reference configuration without an electric field. When the field is applied, the inclusions elongate along the field direction, generating local tractions on the surrounding matrix. Because the inclusions are arranged periodically in a thin membrane, these tractions lead to a spatially periodic displacement of the top surface, producing a wrinkled profile. As χ increases, the coupling between interfacial driving and matrix deformation becomes stronger and the wrinkling amplitude increases.

To quantify this response, we define the wrinkling amplitude Λ as the distance between the highest and lowest points on the top surface. Since Λ is a peak-to-trough measure, a single central unit cell contains one peak but two neighbouring troughs; we therefore compute Λ from the central three unit cells (and average) to capture a complete wavelength while minimising edge effects. Figure 4.12 plots Λ as a function of the applied electric field for different values of χ. The amplitude increases monotonically with field strength and is larger for higher χ, as a result of stronger inclusion elongation and weaker effective resistance of the composite. At $E = 70$ V/mm, the wrinkling amplitude reaches values of order 10 μm for the largest χ. This value is sufficient to

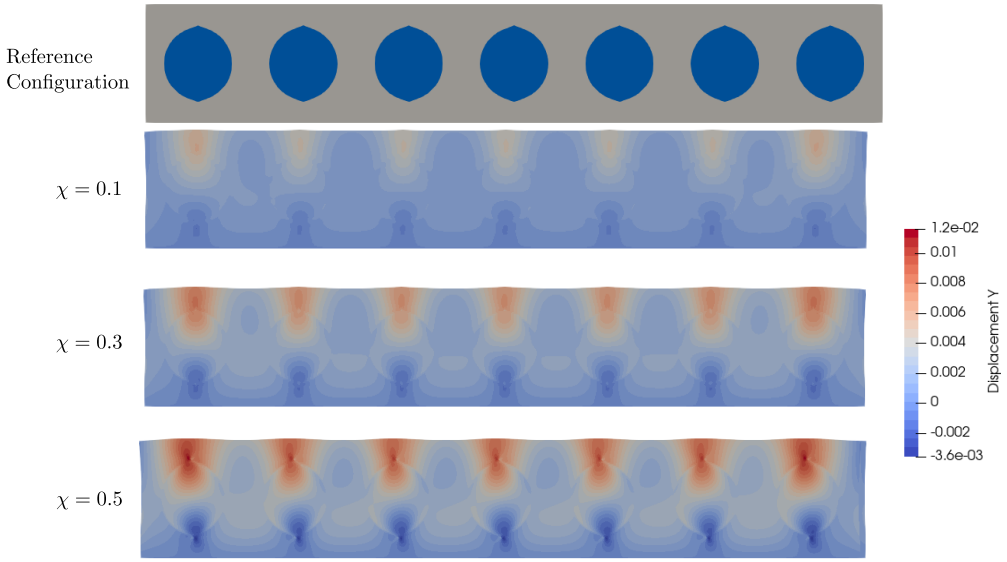

Figure 4.11: Deformation of a composite membrane under a vertically applied electric field ($E = 70\,\mathrm{V/mm}$). The top panel shows the reference configuration; the lower panels show the vertical displacement for different elastocapillary numbers χ. The colour scale indicates the vertical displacement u_y.

provide functionalities such as adhesion (Davis and Crosby, 2011) and wetting (Tokudome et al., 2012). The wrinkling wavelength is primarily set by the inclusion spacing and can therefore be tuned by adjusting the unit-cell size.

4.6 Conclusion

In this study, we developed a theoretical model that accounts for the coupling between electrostatic fields, surface anchoring, elasticity and director distortion. Based on this theory, we carried out numerical analyses of free-droplet problems and liquid-crystal inclusion problems using finite element simulations. We validated the model against experimental measurements of the elongation of liquid-crystal droplets under applied electric fields. In addition, we showed that, for liquid crystals with asymmetrically shaped molecules, flexoelectric effects are non-negligible and further promote droplet elongation, since flexoelectricity favours a more uniformly aligned director field.

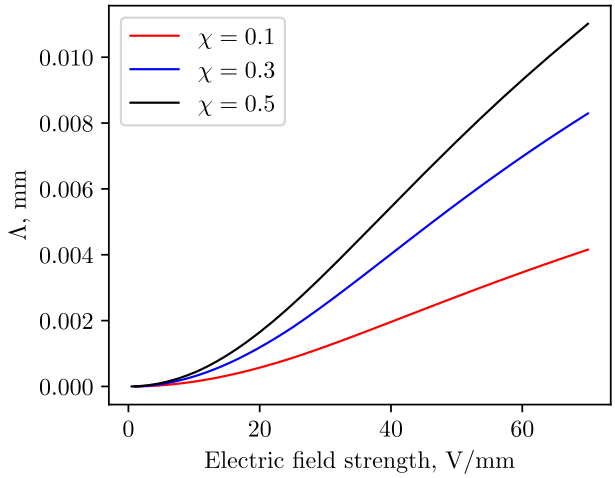

Figure 4.12: Maximum wrinkling amplitude Λ of the membrane as a function of the applied vertical electric field strength for different elastocapillary parameters χ.

We then used the model to illustrate the electro-mechanical response of liquid-crystal inclusions embedded in an elastic matrix through two case studies. The first case examined the response of the composite as a bulk material. Alignment of the director towards the electric field drives elongation or shortening of the inclusions in order to reduce the misalignment between the director and the interface. This shape change is resisted by the elasticity of the surrounding matrix, which is characterised by an elastocapillary parameter. In practice, to obtain a more sensitive actuator that produces larger deformations for a given field, a softer matrix is therefore desirable.

In the second case, we analysed a membrane consisting of a single layer of liquid-crystal inclusions, mimicking the response of a thin composite film. We showed that, upon application of an electric field of 70 V/mm, the deformation of the inclusions leads to surface wrinkling with amplitudes of order 4-10 μm, depending on the elastocapillary number. This reversible, electrically driven wrinkling points to a promising route for the design of functional surfaces with tunable topography.

5 | Chemo-mechanical modelling of polymerisation induced phase separation

This chapter investigates polymerisation-induced phase separation (PIPS) as a microstructure-formation mechanism for polymer-dispersed liquid crystals (PDLCs) and related liquid-crystal polymer composites, with emphasis on how reaction, diffusion, and mechanics jointly determine the evolving morphology. During polymerisation, an initially homogeneous mixture can be driven from a stable to an unstable thermodynamic state, triggering demixing and coarsening that sets the size, spacing, and connectivity of the emerging inclusions. As curing progresses, the formation of a percolated/entangled polymer network introduces elasticity that competes with segregation and can hinder or arrest ripening, thereby locking in a characteristic microstructural length scale and residual stress state that determines the overall response of the composite. The resulting morphology evolution is therefore controlled not only by the equilibrium free energy but also by the relative timescales of polymerisation and diffusion and by the strength of the emerging elastic resistance. These ideas can be summarised through key dimensionless groups, including the Damkohler number governing how rapidly the system is driven into instability and an elasticity ratio governing coarsening behaviour in the presence of network elasticity. Overall, the chapter provides a mechanistic process-to-microstructure link for composites such as PDLCs, establishing a foundation for defining physically meaningful reference states for subsequent liquid-crystal inclusion simulations and for clarifying the general role of elasticity in phase separations.

5.1 Introduction

In the previous chapters, we modelled the mechanical and electro-mechanical response of liquid crystal inclusions embedded in soft elastic matrices. In those simulations, the geometry and internal director configuration of the inclusions in the reference configuration were prescribed a priori and chosen to mimic droplets formed in a purely liquid environment. This assumption is convenient because it leads to a stress-free reference state for the matrix and simplifies the numerical implementation. However, it also hides the physical processes by which such microstructures arise in the first place. In many practical systems, including polymer-dispersed liquid crystals, liquid crystal droplets are generated in situ by polymerisation-induced phase separation (PIPS) from an initially homogeneous mixture of reactive species and liquid crystal (Kim et al., 1993; Serbutoviez et al., 1996; Hoppe et al., 2002; White et al., 2007; Zhu et al., 2014; Zakrzewski et al., 2023). A natural question is therefore how polymerisation kinetics, phase separation and the emergence of elasticity interact during PIPS, and how this chemo-mechanical coupling may influence the resulting microstructure. Addressing this question is not only important for understanding how droplets form, but also for defining a physically meaningful reference configuration for subsequent inclusion-response simulations: the phase-separation stage sets the characteristic length scales, connectivity, and residual stresses that later govern electro-mechanical actuation. In other words, a PIPS model provides the missing "microstructure formation" link between a homogeneous precursor mixture and the prescribed-inclusion geometries adopted in the previous chapters.

PIPS is not unique to liquid crystal composites. Similar mechanisms are found in a wide range of soft materials and are also observed in natural systems. Examples include the preparation of porous and macroporous hydrogels for drug delivery and tissue engineering (Guo et al., 2018; Dudaryeva et al., 2025; Müller et al., 2025), the fabrication of membranes and separation media with controlled pore structures (Taniguchi et al.,

2013; Dong et al., 2021; Yu et al., 2022; Kirkebæk et al., 2025), and the design of polymer electrolytes and structural energy-storage materials whose morphology is set during polymerisation (Schulze et al., 2014; Ihrner et al., 2017; Ling et al., 2023; Deshpande et al., 2024). In all of these systems, a reactive component polymerises within a multicomponent mixture, driving the solution out of its miscible region and triggering phase separation, while the forming polymer network progressively endows the material with elasticity. Understanding the coupling between reaction, phase separation and elasticity is therefore of broad relevance beyond any specific material class and provides a useful baseline for more specialised models of liquid crystal-containing systems.

From a thermodynamic viewpoint, phase separation in polymer solutions is often described using a Flory-Huggins mixing free energy, which balances the enthalpic interaction between components against the entropy of mixing. When control parameters such as temperature, composition or degree of polymerisation move the system into the unstable region of the phase diagram, composition fluctuations grow and the system demixes into coexisting phases (cf. Section 2.4). The kinetics of this process can be modelled by a Cahn-Hilliard-type equation (Cahn and Hilliard, 1958; Cahn, 1961) for a scalar composition or phase field, in which the chemical potential derives from the Flory-Huggins free energy augmented by a gradient (interfacial) term. This framework has been widely used to study liquid-liquid demixing in polymer blends and solutions (Chan and Rey, 1995; Barton et al., 1998; König et al., 2021). In particular, the same system has also been adopted to model polymerisation-induced phase separation problems (Chan and Rey, 1996, 1997; Oh and Rey, 2000; Kyu and Chiu, 2001; Vonka and Kosek, 2012). However, these models do not account for the resistance to droplet formation and coalescence arising from the surrounding elastic medium, which is essential to describe the system as elasticity is not a fixed background property in PIPS: the modulus emerges during polymerisation and can compete with phase separation on comparable time scales. As a result, the evolving network can alter the driving force for

demixing and introduce mechanical stresses that affect morphology changes. Capturing these effects requires a framework in which polymerisation kinetics, transport, and mechanics are treated in a single thermodynamically consistent model.

Recent studies have confirmed the effect of elastic energy in phase separation processes. Style et al. (Style et al., 2018) investigated the nucleation and growth of liquid droplets inside a cross-linked polymer network by saturating and swelling the network with fluid and decreasing the temperature to induce nucleation. They also showed that the size of liquid droplets in the phase-separated state can be tuned by changing the cross-link density of the polymer network. Subsequently, Kothari and Cohen (2020) used an energy-based approach to theoretically investigate the effect of the elastic properties of the matrix on nucleation-and-growth-type phase separation and showed that elasticity can postpone not only the formation of liquid inclusions, but also the coalescence of droplets due to Ostwald ripening, consistent with the experimental observations of Style et al. In addition to the suppression of phase separation, elasticity has also been found to promote the ripening of liquid droplets under certain conditions (Rosowski et al., 2020). These experimental and theoretical works confirm that elasticity plays an important role in liquid droplet formation and ripening when droplets are embedded in polymer networks, but the modelling frameworks considered so far are largely restricted to nucleation-and-growth-type phase separation, where there are either initial seeds for nucleation sites or initial finite size droplets in the reference configuration. Whether these findings still hold for spinodal-decomposition-type phase separation remains unclear, because the process begins from a homogeneous reference state and the morphology develops continuously rather than from pre-existing droplets.

A few very recent finite element formulations have begun to address chemo-mechanical coupling in phase separation. Soria et al. (Soria et al., 2025) proposed a Lagrangian theory for phase separation problems involving large deformations and solvent removal. This variational framework was implemented in a finite element code

and used to visualise the morphology of systems undergoing phase separation driven by mechanical loading and composition changes. In addition, Oudich et al. (Oudich et al., 2026) developed a phase field model describing chemo-mechanical coupling in elastic microphase separation triggered by spinodal decomposition.

These developments confirmed that chemo-mechanical coupling in phase separation is a rapidly emerging and active research area. However, existing models typically address either purely diffusive Cahn-Hilliard-type dynamics without elasticity, or elastic effects in mixtures without explicit polymerisation kinetics. In contrast, the present work combines a Flory-Huggins-Cahn-Hilliard phase field description with an explicit polymerisation-induced evolution of an elastic network. To the best of our knowledge, this proposed model provides one of the first continuum finite element frameworks to capture the coupled effects of PIPS and elasticity on phase separation morphologies.

In this chapter, we develop a minimal chemo-mechanical continuum model for a ternary system consisting of monomer, polymer and solvent. Monomer species polymerise into longer chains, and beyond a critical extent of reaction the polymer forms a physically cross-linked network that possesses composition-dependent elasticity. The total free-energy density is written as the sum of a Flory-Huggins-type mixing contribution, an interfacial contribution that penalises composition gradients, and an elastic contribution associated with the deformation of the polymer network. Mass conservation, mechanical equilibrium and thermodynamic consistency are enforced to derive a coupled set of evolution equations for the composition fields and the displacement field.

To obtain clear mechanistic insight and to enable systematic exploration of parameter space, we specialise this framework to a one-dimensional geometry and to an isotropic interfacial energy. The one-dimensional setting already captures the essential interplay between diffusion, reaction and elasticity along a confined direction, while remaining computationally affordable for extensive parametric studies. The use of a scalar phase field with isotropic surface tension allows us to focus on the generic fea-

tures of chemo-mechanical coupling during PIPS that are common to a broader class of polymerising soft materials. The liquid crystal-specific features considered in the previous chapters can then be viewed as additional layers of complexity to be coupled to this baseline framework in future work.

We emphasise that the present model does not attempt to predict the detailed shape and director configuration of individual liquid crystal droplets. Instead, it provides a first step towards linking the microstructure formation stage of PIPS to the inclusion problems studied earlier in the thesis, by quantifying how polymerisation kinetics and the emergence of elasticity influence the evolving composition profile and characteristic length scales of phase separation. In the final part of the chapter, we outline the corresponding multi-dimensional formulation and weak form, demonstrating that the same chemo-mechanical framework extends naturally to higher-dimensional geometries and could be used as the basis for future two- and three-dimensional simulations of phase separation in elastic media.

The chapter is organised as follows. Section 5.2 introduces the one-dimensional chemo-mechanical PIPS model and its governing equations. Section 5.4 describes the numerical implementation, including the weak form and time discretisation. Section 5.5 presents simulation results and parametric studies that illustrate the influence of elasticity and polymerisation on phase separation kinetics and morphology. Finally, in Section 5.6 we conclude the results in this chapter along with the relation to the liquid crystal inclusion problems considered in the previous chapters.

5.2 Theoretical framework

In this section, we outline the general chemo-mechanical continuum framework used to describe polymerisation-induced phase separation in a ternary mixture of monomer, polymer and solvent. We adopt a Lagrangian description based on a field of mark-

ers (Brassart et al., 2016) dispersed throughout the solution, following the ideas of Darken (Darken, 1948) and Stephenson (Stephenson, 1988) for diffusing and reacting mixtures. Each marker moves with the mixture and carries the local information on deformation and composition. We first present the kinematics and balance laws in a fully three-dimensional setting. We then specialise the formulation to a one-dimensional geometry, which may be interpreted as a long tube of unit-square cross section aligned with the X-axis. In this reduced setting, all fields depend only on the axial coordinate X and time t, while the deformation and stress state remain three-dimensional due to the lateral constraints imposed by the rigid side walls.

5.2.1 Kinematics

In a mixture undergoing diffusion and reaction, the number and identity of molecules contained in a small region of the body are not preserved in time. As a result, the classical notion of a material particle as a fixed collection of molecules becomes ambiguous. Following the approach of Darken (Darken, 1948) and Stephenson (Stephenson, 1988), we introduce a field of markers dispersed throughout the solution. These markers are imagined to be small enough to follow the motion of the mixture with fidelity, yet large enough that they do not participate in mixing or reaction themselves. In the present Lagrangian description, each marker is labelled by its position $\boldsymbol{X}$ in the reference configuration and carries information about the local deformation and composition; its current position is denoted by $\boldsymbol{x}(\boldsymbol{X}, t)$. The motion is thus described by the mapping

$$\boldsymbol{x} = \boldsymbol{\varphi}(\boldsymbol{X}, t), \tag{5.1}$$

and the deformation gradient is defined as

$$\boldsymbol{F}(\boldsymbol{X}, t) = \frac{\partial \boldsymbol{x}}{\partial \boldsymbol{X}}. \tag{5.2}$$

The local volumetric change is given by

$$\Omega = \frac{\mathrm{d}V}{\mathrm{d}V_0} = \det \boldsymbol{F}, \tag{5.3}$$

where V_0 and V denote, respectively, the reference and current volumes of a small region surrounding the marker.

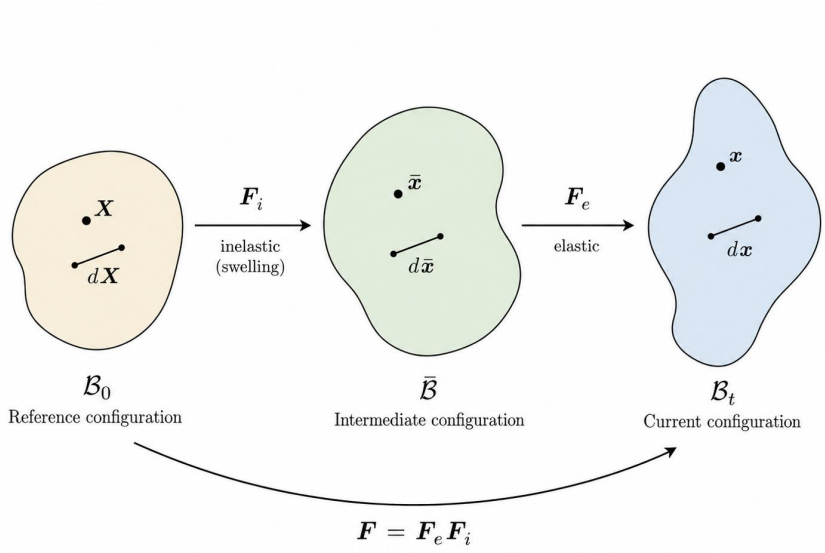

Figure 5.1: Schematic illustration of the multiplicative decomposition of the deformation gradient.

We decompose the deformation into elastic and inelastic parts (see Figure 5.1), where the former is associated with the distortion of the elastic polymer network and the latter with composition changes of the solution. The total deformation gradient is written in the multiplicative form

$$\boldsymbol{F} = \boldsymbol{F}_e\boldsymbol{F}_i, \tag{5.4}$$

where $\boldsymbol{F}_i$ denotes the inelastic deformation gradient associated with local swelling in-

duced by composition changes, and $\boldsymbol{F}_e$ denotes the elastic deformation gradient of the polymer network from the swollen intermediate configuration to the current configuration.

The corresponding volumetric change satisfies

$$\Omega = \Omega_e \, \Omega_i, \tag{5.5}$$

where $\Omega_e = \det \boldsymbol{F}_e$ and $\Omega_i = \det \boldsymbol{F}_i$ are the elastic and inelastic volume changes, respectively. In this study, we assume that all species, including the elastic network, are individually incompressible. As a consequence, the elastic response of the solution is isochoric, so that

$$\Omega_e = 1, \tag{5.6}$$

and hence

$$\Omega = \Omega_i. \tag{5.7}$$

In this formulation, $\boldsymbol{F}_i$ is not introduced as an independent internal variable with a separate phenomenological evolution law. Instead, it is determined by molecular incompressibility. Under the isotropic swelling assumption,

$$\boldsymbol{F}_i = \Omega_i^{1/3} \boldsymbol{I}. \tag{5.8}$$

Therefore, once the local composition is known, $\boldsymbol{F}_i$ is determined algebraically through the swelling ratio Ω_i. The time derivative of $\boldsymbol{F}_i$ is consequently inherited from the time dependence of Ω_i, rather than prescribed independently. In particular,

$$\dot{\boldsymbol{F}}_i \boldsymbol{F}_i^{-1} = \frac{1}{3} \frac{\dot{\Omega}_i}{\Omega_i} \boldsymbol{I}. \tag{5.9}$$

This point is important in the Coleman–Noll procedure. Since

$$\boldsymbol{F}_e = \boldsymbol{F}\boldsymbol{F}_i^{-1}, \tag{5.10}$$

its material time derivative is

$$\dot{\boldsymbol{F}}_e = \dot{\boldsymbol{F}}\boldsymbol{F}_i^{-1} - \boldsymbol{F}_e\dot{\boldsymbol{F}}_i\boldsymbol{F}_i^{-1}. \tag{5.11}$$

If $\boldsymbol{F}_i$ were treated as an independent internal variable, the dissipation inequality would introduce a thermodynamic force conjugate to $\dot{\boldsymbol{F}}_i$ and an additional evolution law would be required. In the present formulation, however, $\boldsymbol{F}_i$ is constrained by molecular incompressibility and its evolution follows from the mass balance equations and polymerisation kinetics.

For the composition, we define the nominal number concentrations of monomer, polymer and water per unit reference volume as $C_m(\boldsymbol{X}, t)$, $C_p(\boldsymbol{X}, t)$ and $C_w(\boldsymbol{X}, t)$, respectively. The corresponding nominal volume fractions per unit reference volume are

$$\Phi_m = v_m C_m, \qquad \Phi_p = v_p C_p, \qquad \Phi_w = v_w C_w, \tag{5.12}$$

where v_m, v_p and v_w are the molecular volumes of monomer, polymer and water. We assume that the molar volumes remain constant throughout deformation and diffusion, and that the molecular volumes of monomer and water are identical, $v_m = v_w = v$. In this chapter, we assume that the polymer molecules are monodisperse, that is, each polymer molecule consists of x_n monomers. Within each marker, the degree of polymerisation for all polymers are the same, while it can vary spatially in different markers. The molecular volume of polymer is $v_p = x_n v$, and we obtain

$$x_n = \frac{\Phi_p}{v C_p}. \tag{5.13}$$

The volumes of each species contained in V are

$$V_m = \Phi_m V_0, \qquad V_p = \Phi_p V_0, \qquad V_w = \Phi_w V_0, \tag{5.14}$$

and the total current volume is

$$V = V_m + V_p + V_w. \tag{5.15}$$

The inelastic volumetric change can then be written as

$$\Omega_i = \frac{V}{V_0} = \frac{V_m + V_p + V_w}{V_0} = \Phi_m + \Phi_p + \Phi_w. \tag{5.16}$$

The true volume fractions are related to the nominal ones by

$$\phi_i = \frac{\Phi_i}{\Omega}, \qquad i \in \{m, p, w\}, \tag{5.17}$$

and satisfy the local incompressibility constraint

$$\phi_m + \phi_p + \phi_w = 1. \tag{5.18}$$

Given our monodisperse assumption of the polymer, the number of polymer chains per unit reference volume is equal to the nominal concentration of initiators. In this study, we assume that the concentration of polymer chains is constant, so that

$$C_p = C_p^0 = \text{const.}, \tag{5.19}$$

where $C_p^0 = C_p|_{t=0}$ is the initial nominal number concentration of polymer chains. Combining this with Eqn. 5.13 allows us to express the degree of polymerisation in

terms of the polymer volume fraction as

$$x_n = \frac{\Phi_p}{C_p^0 v}. \tag{5.20}$$

5.2.2 Balance laws

Conservation of mass For any marker occupying a region $\mathcal{V}_0$ in the reference configuration, the rate of change of the total amount of each species within this region equals the net influx of that species through the boundary plus any sources inside the region. The conservation of mass can therefore be written as

$$\begin{aligned}
\frac{\mathrm{d}}{\mathrm{d}t}\int_{\mathcal{V}_0} C_m(\boldsymbol{X},t)\,\mathrm{d}V &= -\int_{\partial\mathcal{V}_0} \boldsymbol{J}_m\cdot\boldsymbol{N}\,\mathrm{d}S + \int_{\mathcal{V}_0} R_m\,\mathrm{d}V,\\
\frac{\mathrm{d}}{\mathrm{d}t}\int_{\mathcal{V}_0} C_w(\boldsymbol{X},t)\,\mathrm{d}V &= -\int_{\partial\mathcal{V}_0} \boldsymbol{J}_w\cdot\boldsymbol{N}\,\mathrm{d}S,\\
\frac{\mathrm{d}}{\mathrm{d}t}\int_{\mathcal{V}_0} \Phi_p(\boldsymbol{X},t)\,\mathrm{d}V &= \int_{\mathcal{V}_0} \tilde{R}_p\,\mathrm{d}V,
\end{aligned} \tag{5.21}$$

where $\boldsymbol{J}_i$ is the nominal flux vector of species i (number of molecules crossing a unit area per unit time, per unit reference volume), R_m is the number of monomers produced per unit reference volume and per unit time, and $\tilde{R}_p$ is the volumetric source term associated with the growth of the polymer phase. In Eqn. 5.21 we have assumed that water does not participate in reactions and that polymer chains cannot diffuse, so that $R_w = 0$ and $\boldsymbol{J}_p = \boldsymbol{0}$.

Applying the divergence theorem gives

$$\begin{aligned}
\int_{\mathcal{V}_0}\left(\frac{\partial C_m}{\partial t} + \mathrm{Div}\,\boldsymbol{J}_m - R_m\right)\mathrm{d}V = 0,\\
\int_{\mathcal{V}_0}\left(\frac{\partial C_w}{\partial t} + \mathrm{Div}\,\boldsymbol{J}_w\right)\mathrm{d}V = 0,\\
\int_{\mathcal{V}_0}\left(\frac{\partial \Phi_p}{\partial t} - \tilde{R}_p\right)\mathrm{d}V = 0.
\end{aligned} \tag{5.22}$$

Since these relations must hold for any arbitrary region $\mathcal{V}_0$, we obtain the local forms

$$\begin{aligned} \frac{\partial C_m}{\partial t} + \text{Div}\, \boldsymbol{J}_m &= R_m, \\ \frac{\partial C_w}{\partial t} + \text{Div}\, \boldsymbol{J}_w &= 0, \\ \frac{\partial \Phi_p}{\partial t} &= \tilde{R}_p. \end{aligned} \tag{5.23}$$

We describe the reaction behaviour by introducing the extent of reaction $p(\boldsymbol{X}, t)$, which represents the number of reactions per unit reference volume. The production rate of monomer can then be written as

$$R_m = -\dot{p}, \quad \tilde{R}_p = v\dot{p}. \tag{5.24}$$

Since there are no diffusive terms for polymers, the polymer volume fraction and the extent of reaction are algebraically coupled. Using the relation between the degree of polymerisation x_n and the polymer content (Eqn. 5.19 and 5.20), we also have

$$\dot{x}_n = \frac{\dot{p}}{C_p^0}. \tag{5.25}$$

Balance of linear and angular momentum We work in the reference configuration and neglect inertia. For a marker occupying a region $\mathcal{V}_0$ and subjected to a field of surface tractions $\boldsymbol{T}(\boldsymbol{X}, t)$ and body forces $\boldsymbol{B}(\boldsymbol{X}, t)$, the balance of linear momentum reads

$$\text{Div}\, \boldsymbol{P} + \boldsymbol{B} = \boldsymbol{0} \quad \text{in } \mathcal{V}_0, \tag{5.26}$$

where $\boldsymbol{P}$ is the first Piola-Kirchhoff stress tensor. The nominal traction on a surface with unit outward normal $\boldsymbol{N}$ in the reference configuration is

$$\boldsymbol{T} = \boldsymbol{P}\,\boldsymbol{N}. \tag{5.27}$$

The balance of angular momentum implies that the couple resulting from stresses vanishes. In the present formulation, this is expressed by

$$\boldsymbol{P}\,\boldsymbol{F}^T = \boldsymbol{F}\,\boldsymbol{P}^T, \tag{5.28}$$

which in turn ensures the symmetry of the associated Cauchy stress tensor $\boldsymbol{\sigma}$. The relation between $\boldsymbol{P}$ and $\boldsymbol{\sigma}$ is

$$\boldsymbol{P} = \Omega\,\boldsymbol{\sigma}\,\boldsymbol{F}^{-T}, \qquad \boldsymbol{\sigma} = \Omega^{-1}\,\boldsymbol{P}\,\boldsymbol{F}^T. \tag{5.29}$$

5.2.3 Free energy imbalance

We now formulate the second law of thermodynamics. Under isothermal conditions, the rate of change of the free energy stored in an arbitrary volume $\mathcal{V}_0$ of the reference configuration is bounded by the external power input. In nominal form, this inequality reads

$$\begin{aligned}\frac{\mathrm{d}}{\mathrm{d}t}\int_{\mathcal{V}_0}\Psi\,\mathrm{d}V \leq \int_{\mathcal{V}_0}\boldsymbol{B}\cdot\boldsymbol{v}\,\mathrm{d}V + \int_{\partial\mathcal{V}_0}\boldsymbol{T}\cdot\boldsymbol{v}\,\mathrm{d}S \\ - \int_{\partial\mathcal{V}_0}\mu_m\,\boldsymbol{J}_m\cdot\boldsymbol{N}\,\mathrm{d}S - \int_{\partial\mathcal{V}_0}\mu_w\,\boldsymbol{J}_w\cdot\boldsymbol{N}\,\mathrm{d}S \\ + \int_{\mathcal{V}_0}\Pi\left(\dot{\Omega} - v\,\dot{C}_w - v\,\dot{C}_m - v\,\dot{p}\right)\,\mathrm{d}V,\end{aligned} \tag{5.30}$$

where Ψ is the free energy per unit reference volume, μ_i is the chemical potential of species i, $\boldsymbol{v}(\boldsymbol{X},t) = \dot{\boldsymbol{\varphi}}(\boldsymbol{X},t)$ is the material velocity, $\boldsymbol{B}$ is the body force per unit reference volume, and $\boldsymbol{T}$ is the nominal traction. The first and second terms on the right-hand side represent the external mechanical power due to body forces and surface tractions, respectively. The third and fourth terms correspond to the chemical power associated with diffusion of monomer and water through the boundary. The last term

enforces the incompressibility constraint (cf. Eqn. 5.16)

$$\Omega = v\,C_m + v\,C_w + \Phi_p \;=\; v\,C_m + v\,C_w + v\,p, \tag{5.31}$$

through the Lagrange multiplier Π.

Applying the divergence theorem to the mechanical and chemical flux terms and using the transport theorem, we obtain

$$\begin{aligned}\int_{\mathcal{V}_0} \dot{\Psi}\,\mathrm{d}V \leq \int_{\mathcal{V}_0} (\boldsymbol{B} + \operatorname{Div}\boldsymbol{P})\cdot\boldsymbol{v}\,\mathrm{d}V \\ + \int_{\mathcal{V}_0} \left(\boldsymbol{P} : \dot{\boldsymbol{F}} - \mu_m \operatorname{Div}\boldsymbol{J}_m - \boldsymbol{J}_m\cdot\operatorname{Grad}\mu_m\right)\,\mathrm{d}V \\ + \int_{\mathcal{V}_0} \left(-\mu_w \operatorname{Div}\boldsymbol{J}_w - \boldsymbol{J}_w\cdot\operatorname{Grad}\mu_w\right)\,\mathrm{d}V \\ + \int_{\mathcal{V}_0} \Pi\left(\dot{\Omega} - v\,\dot{C}_w - v\,\dot{C}_m - v\,\dot{p}\right)\,\mathrm{d}V.\end{aligned} \tag{5.32}$$

Using the local balance of linear momentum (Eqn. 5.26) and the conservation of mass (Eqn. 5.23), the inequality can be rewritten in local form as

$$\begin{aligned}\dot{\Psi} \leq \boldsymbol{P} : \dot{\boldsymbol{F}} + \mu_m\,\dot{C}_m + \mu_w\,\dot{C}_w - \mu_m\,R_m - \boldsymbol{J}_m\cdot\operatorname{Grad}\mu_m - \boldsymbol{J}_w\cdot\operatorname{Grad}\mu_w \\ + \Pi\left(\dot{\Omega} - v\,\dot{C}_w - v\,\dot{C}_m - v\,\dot{p}\right).\end{aligned} \tag{5.33}$$

In our system, the free energy per unit reference volume Ψ is taken as a function of the deformation gradient, the local composition fields, and the gradient of the water concentration,

$$\Psi = \Psi(\boldsymbol{F},\, C_m,\, C_w,\, p,\, \operatorname{Grad} C_w)\,. \tag{5.34}$$

Here the gradient term accounts for the interfacial energy between water-poor and -rich

regions. The material time derivative of Ψ is

$$\dot{\Psi} = \frac{\partial \Psi}{\partial \boldsymbol{F}} : \dot{\boldsymbol{F}} + \frac{\partial \Psi}{\partial C_m}\,\dot{C}_m + \frac{\partial \Psi}{\partial C_w}\,\dot{C}_w + \frac{\partial \Psi}{\partial p}\,\dot{p} + \frac{\partial \Psi}{\partial (\operatorname{Grad} C_w)} \cdot \operatorname{Grad} \dot{C}_w. \tag{5.35}$$

For convenience, we introduce the microstress

$$\boldsymbol{\xi}_w := \frac{\partial \Psi}{\partial (\operatorname{Grad} C_w)}. \tag{5.36}$$

Using the product rule $\boldsymbol{a} \cdot \operatorname{Grad} b = \operatorname{Div}(\boldsymbol{a}\, b) - (\operatorname{Div} \boldsymbol{a})\, b$, we rewrite

$$\boldsymbol{\xi}_w \cdot \operatorname{Grad} \dot{C}_w = \operatorname{Div}(\boldsymbol{\xi}_w\, \dot{C}_w) - (\operatorname{Div} \boldsymbol{\xi}_w)\, \dot{C}_w, \tag{5.37}$$

and therefore

$$\dot{\Psi} = \frac{\partial \Psi}{\partial \boldsymbol{F}} : \dot{\boldsymbol{F}} + \frac{\partial \Psi}{\partial C_m}\,\dot{C}_m + \left(\frac{\partial \Psi}{\partial C_w} - \operatorname{Div} \boldsymbol{\xi}_w \right) \dot{C}_w + \frac{\partial \Psi}{\partial p}\,\dot{p} + \operatorname{Div}\left(\boldsymbol{\xi}_w\, \dot{C}_w \right). \tag{5.38}$$

Substituting this into inequality 5.33 gives

$$\begin{aligned} &\left(\boldsymbol{P} - \frac{\partial \Psi}{\partial \boldsymbol{F}} + \Omega\, \Pi\, \boldsymbol{F}^{-T} \right) : \dot{\boldsymbol{F}} + \left(\mu_m - \frac{\partial \Psi}{\partial C_m} - v\, \Pi \right) \dot{C}_m \\ &+ \left(\mu_w - \frac{\partial \Psi}{\partial C_w} + \operatorname{Div} \boldsymbol{\xi}_w - v\, \Pi \right) \dot{C}_w - \mu_m R_m - \left(\frac{\partial \Psi}{\partial p} + v\, \Pi \right) \dot{p} \\ &\quad - \operatorname{Div}\left(\boldsymbol{\xi}_w\, \dot{C}_w \right) - \boldsymbol{J}_m \cdot \operatorname{Grad} \mu_m - \boldsymbol{J}_w \cdot \operatorname{Grad} \mu_w \;\geq\; 0. \end{aligned} \tag{5.39}$$

The divergence term $\operatorname{Div}(\boldsymbol{\xi}_w\, \dot{C}_w)$ is not a new bulk constitutive assumption, but the surface power associated with the gradient contribution. This can be shown by integrating the local inequality over an arbitrary part $\mathcal{V}_0$ and using the divergence theorem, it contributes the boundary term

$$\int_{\mathcal{V}_0} \operatorname{Div}(\boldsymbol{\xi}_w\, \dot{C}_w)\, \mathrm{d}V = \int_{\partial \mathcal{V}_0} (\boldsymbol{\xi}_w \cdot \boldsymbol{N})\, \dot{C}_w\, \mathrm{d}A, \tag{5.40}$$

where $\boldsymbol{\xi}_w \cdot \boldsymbol{N}$ plays the role of a microtraction conjugate to $\dot{C}_w$. There are several ways of treating this term in the literature, Gurtin (1996) proposed a balance law for this microtraction such that this boundary term vanishes in the absence of any other body force conjugated with $\dot{C}_w$. Soria et al. (2025) assumed that there exists an "extra entropy flux" (denoted by W in their formulation) is associated with the flux of additional fields of C_w, and this extra entropy flux is taken exactly as $W = \boldsymbol{\xi}_w \dot{C}_w$, which cancelled the contribution of this term in the inequality. Here we adopt the balance theory in Gurtin (1996) and assume a microtraction free boundary condition and omit the boundary contribution.

We neglect viscoelasticity of the polymer network and therefore require that the dissipation due to elastic deformation vanishes. This yields the constitutive relation

$$\boldsymbol{P} = \frac{\partial \Psi}{\partial \boldsymbol{F}} - \Omega \, \Pi \, \boldsymbol{F}^{-T}. \tag{5.41}$$

We also assume that the system is always at local chemical equilibrium with respect to changes in C_m and C_w, so that

$$\begin{aligned} \mu_m &= \frac{\partial \Psi}{\partial C_m} + v \, \Pi, \\ \mu_w &= \frac{\partial \Psi}{\partial C_w} - \operatorname{Div} \boldsymbol{\xi}_w + v \, \Pi. \end{aligned} \tag{5.42}$$

The Lagrange multiplier Π enforces molecular incompressibility and acts as a pressure-like contribution to the chemical potentials: $v\Pi$ is the work needed to accommodate one additional molecule under the local volume constraint. The term $-\operatorname{Div} \boldsymbol{\xi}_w$ is the capillarity contribution generated by the gradient part of the free energy, penalising spatial variations of C_w and providing the chemical driving force that smooths diffuse interfaces.

Dissipation associated with polymerisation. Using $R_m = -\dot{p}$, the contribution of the reaction to the dissipation inequality becomes

$$\mathcal{D}_r = \left(\mu_m - v\,\Pi - \frac{\partial \Psi}{\partial p}\right)\dot{p} \;\geq\; 0. \tag{5.43}$$

The quantity in brackets,

$$\mathcal{A} := \mu_m - v\,\Pi - \frac{\partial \Psi}{\partial p} \;=\; \frac{\partial \Psi}{\partial C_m} - \frac{\partial \Psi}{\partial p}, \tag{5.44}$$

is the thermodynamic driving force (affinity) for polymerisation. A reaction event locally decreases C_m and increases p (equivalently $\Phi_p = vp$), and $\mathcal{A}$ measures the corresponding change in free energy per unit extent of reaction. Admissible kinetics must satisfy $\mathcal{A}\,\dot{p} \geq 0$ for all states. In a general near-equilibrium setting, one may prescribe $\dot{p} = L(\mathcal{A})$ with $L(\mathcal{A})\,\mathcal{A} \geq 0$.

Dissipation due to diffusion. The remaining bulk dissipation is due to diffusion,

$$\mathcal{D}_d = -\boldsymbol{J}_m \cdot \operatorname{Grad}\mu_m - \boldsymbol{J}_w \cdot \operatorname{Grad}\mu_w \;\geq\; 0, \tag{5.45}$$

which shows that diffusion is driven by gradients of chemical potential.

5.2.4 Free energy

We define the free energy of the system per unit reference volume, Ψ as

$$\Psi(\boldsymbol{F}, C_m, C_w, p, \operatorname{Grad} C_w) = \Psi_{el}(\boldsymbol{F}, p) + \Psi_{mix}(\boldsymbol{F}, C_m, C_w, p) + \Psi_{int}(\boldsymbol{F}, \operatorname{Grad} C_w), \tag{5.46}$$

where Ψ_{el}, Ψ_{mix} and Ψ_{int} represent the elastic, mixing and interfacial contributions to the free energy, respectively.

Elastic energy During PIPS, monomers are incorporated into polymer chains that grow from initiator sites, so that both the polymer content and the chain length increase with time. At early times the chains are short and the mixture behaves essentially as a viscous solution with negligible elastic resistance. Once the chains become sufficiently long, they form physical entanglements. On time scales shorter than disentanglement, these entanglements act as temporary cross-links and give rise to a rubber-like (neo-Hookean) elastic response. We therefore model the elastic contribution to the free energy per unit reference volume as

$$\Psi_{el}(\boldsymbol{F}, p; C_p^0) = \Omega \, \frac{G(\phi_p, x_n)}{2} \left(I_1^e - 3\right), \tag{5.47}$$

where

$$I_1^e = \mathrm{tr}\left(\boldsymbol{F}_e^T \boldsymbol{F}_e\right) \tag{5.48}$$

is the first invariant of the elastic left Cauchy-Green tensor, ϕ_p is the true polymer volume fraction, and $G(\phi_p, x_n)$ is the shear modulus of the entangled network in the current configuration. To specify $G(\phi_p, x_n)$, we adopt the classical entanglement-network description of semi-dilute polymer solutions (Doi and Edwards, 1988; Colby and Rubinstein, 1990; Rubinstein and Colby, 2003).

The elastic response of an entangled polymer melt (i.e. at polymer volume fraction $\phi_p = 1$, with no solvent present) exhibits a rubbery plateau in linear viscoelasticity: over an intermediate range of frequencies, the storage modulus $G'(\omega)$ becomes approximately frequency-independent because the deformation is resisted primarily by topological entanglements rather than by the flow. We denote this plateau value by $G^{\infty}(1)$, where the argument (1) indicates evaluation in the pure polymer state ($\phi_p = 1$) and the superscript "∞" is conventional notation for the plateau modulus rather than a literal limit.

In the entanglement picture, $G^{\infty}(1)$ is proportional to the number density of entan-

glement strands and can be written as

$$G^{\infty}(1) = \frac{\rho\, k_B T N_A}{M_e(1)} = \frac{\rho\, RT}{M_e(1)}, \tag{5.49}$$

where ρ is the mass density of the pure polymer melt, N_A is Avogadro's number, and $R = k_B N_A$ is the gas constant. Here $M_e(1)$ is the molar mass of polymer contained in one entanglement strand in pure polymer. Introducing the monomer molar mass M_0, we write

$$M_e(1) = x_e(1)\, M_0, \tag{5.50}$$

where $x_e(1)$ is the number of monomers between entanglements in the melt. For polymer solutions ($\phi_p < 1$, i.e. when solvent is present), dilution reduces the density of entanglement strands and therefore lowers the plateau modulus. In the semi-dilute regime (where polymer chains can meat each other but the system is still solvent-rich), a widely used scaling law expresses this concentration dependence as (Rubinstein and Colby, 2003)

$$G^{\infty}(\phi_p) \approx G^{\infty}(1)\, \phi_p^{2.3}. \tag{5.51}$$

It is often convenient to reformulate the same concentration dependence in terms of an effective entanglement strand length. Interpreting $G^{\infty}(\phi_p)$ through the melt relation 5.49 but with a concentration-dependent strand molar mass $M_e(\phi_p)$, and using the approximation $\rho(\phi_p) \simeq \rho\phi_p$ (polymer mass per unit current volume), we obtain

$$\frac{\rho\phi_p RT}{M_e(\phi_p)} \sim \frac{\rho RT}{M_e(1)}\, \phi_p^{2.3} \qquad \Rightarrow \qquad M_e(\phi_p) \sim M_e(1)\, \phi_p^{-1.3}, \tag{5.52}$$

since $M_e(\phi_p) = x_e(\phi_p) M_0$,

$$x_e(\phi_p) = x_e(1)\, \phi_p^{-1.3}. \tag{5.53}$$

The plateau modulus is physically meaningful only when the polymer chains are

long enough to contain at least one entanglement strand, i.e. when $x_n \gtrsim x_e(\phi_p)$. To capture this onset of elasticity during polymerisation, we introduce a smooth gating function that depends on the ratio $x_n/x_e(\phi_p)$:

$$g_x = \frac{1}{1 + \exp\left[-\dfrac{x_n/x_e(\phi_p) - 1}{\eta_x}\right]}, \tag{5.54}$$

where η_x controls the smoothness of the transition. When $x_n < x_e(\phi_p)$ the chains are too short to form an entangled network and $g_x \to 0$; when $x_n \gg x_e(\phi_p)$ the network response is governed by the entanglement strand length and $g_x \to 1$.

In the present model we multiplicatively combine Eqn. 5.51 and 5.54 to express the shear modulus as

$$G(\phi_p, x_n) = G^{\infty}(1)\, g_x\left(\frac{x_n}{x_e(\phi_p)}\right) \phi_p^{2.3}, \tag{5.55}$$

where ϕ_p and x_n can be calculated base on p and C_p^0 through Eqn. 5.20 and 5.25. In the present model, the monomer volume v and the intial polymer number concentration C_p^0 are fixed by the chemistry and the chosen initial composition. The density of the melt ρ can be easily measured. The plateau modulus of the melt can be measured from rheological tests on the polymer melt. The relation between the degree of polymerisation of the entanglement strand and the plateau modulus is given by Eqn. 5.49. Consequently, the only quantity that is not directly prescribed by the intial conditions is the entanglement length $x_e(1)$, which we can calculate through the measured or chosen value of G^{∞} using Eqns. 5.49 and 5.50.

In the illustrative parameter set used below, we adopt the inverse viewpoint: we choose a representative entanglement length $x_e(1) = 20$, together with $\rho = 1000\ \mathrm{kg\,m^{-3}}$, $M_0 = 50\ \mathrm{g\,mol^{-1}}$ and $T = 300\ \mathrm{K}$. The implied melt plateau modulus is

$$G^{\infty}(1) = \frac{\rho R T}{x_e(1) M_0} \approx 2.5 \times 10^6\ \mathrm{Pa}, \tag{5.56}$$

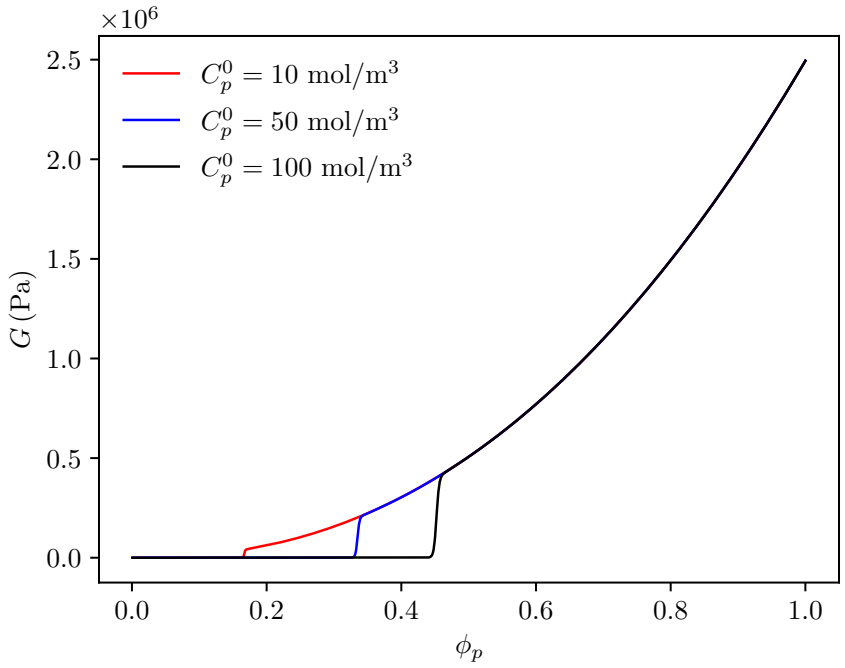

Figure 5.2: Evolution of the shear modulus with increasing true polymer volume fraction for different initial chain (initiator) concentrations C_p^0.

which lies within the range typically observed for soft entangled polymer networks (Rubinstein and Colby, 2003). Figure 5.2 illustrates how the shear modulus develops as polymerisation proceeds for different initial chain number densities C_p^0. In this illustrative test, we consider a two-species system where the mixture consists only monomer and polymer molecules. For each polymer volume fraction data point, we calculate the degree of polymerisation from Eqn. 5.20. At low ϕ_p, the modulus remains essentially zero because the chains are too short to form entanglements ($g_x \simeq 0$). As ϕ_p increases and x_n becomes comparable to $x_e(\phi_p)$, the modulus rises sharply. Increasing C_p^0 delays the onset of elasticity to larger ϕ_p because a higher chain number density yields shorter chains at fixed polymer content. At high ϕ_p the curves collapse onto the same $\phi_p^{2.3}$ trend, showing that once the network is well entangled the stiffness is controlled primarily by polymer concentration and chemistry, rather than by C_p^0.

Mixing energy We adopt a Flory-Huggins-type mixing free energy for the ternary system (cf. Section 2.4). We write

$$\begin{aligned}\Psi_{mix}(\boldsymbol{F}, C_m, C_w, p) &= \Omega\,\psi_{mix}(\phi_m, \phi_w, \phi_p, x_n) \;+\; \mu_0\, C_w \\ &= \mu_0\, C_w \;+\; \frac{\Omega k_B T}{v}\Big(\phi_m \ln \phi_m + \frac{\phi_p}{x_n}\ln \phi_p + \phi_w \ln \phi_w \\ &\qquad + \chi_{mp}\phi_m\phi_p + \chi_{mw}\phi_m\phi_w + \chi_{pw}\phi_p\phi_w\Big),\end{aligned} \tag{5.57}$$

where χ_{ij} $(i, j = m, p, w,\ i \neq j)$ denotes the Flory-Huggins interaction parameter between species i and j, and x_n is the (local) degree of polymerisation. μ_0 is the chemical potential of pure water, included as a reference level. With this choice, in the pure-water limit ($\phi_w = 1$) the mixing contribution vanishes and $\Psi_{mix} \to \mu_0 C_w$. In the present ternary system we neglect monomer-polymer interactions ($\chi_{mp} = 0$) and assume that monomer and polymer interact identically with water ($\chi_{mw} = \chi_{pw} = \chi$). Substituting 5.17 into 5.57 gives the nominal form

$$\Psi_{mix} = \frac{k_B T}{v}\left[\Phi_m \ln\left(\frac{\Phi_m}{\Omega}\right) + \frac{\Phi_p}{x_n}\ln\left(\frac{\Phi_p}{\Omega}\right) + \Phi_w \ln\left(\frac{\Phi_w}{\Omega}\right) + \chi\,\frac{\Phi_w}{\Omega}\,(\Phi_m + \Phi_p)\right], \tag{5.58}$$

where $x_n(X, t)$ is treated as a known local field determined by the polymerisation kinetics and the initial chain number concentration (see Eqn. 5.20).

Interfacial energy In addition to the bulk mixing contribution, phase separation between water and the organic components (monomer + polymer) gives rise to an interfacial energy cost. We choose the nominal water concentration C_w as the order parameter and penalise its spatial gradients through

$$\Psi_{int} = \kappa\,|\mathrm{Grad}\, C_w|^2, \tag{5.59}$$

where κ is an interfacial parameter. Smaller values of κ correspond to narrower diffuse interfaces, whereas larger values of κ favour smoother composition profiles.

5.2.5 Kinetic models

Diffusion We distinguish between the true fluxes in the current configuration and the nominal fluxes in the reference configuration. Let $\boldsymbol{j}_m$ and $\boldsymbol{j}_w$ denote the fluxes of monomer and water per unit current area. We assume that diffusion in the current configuration is driven by gradients of the chemical potentials,

$$\boldsymbol{j}_m = -M_m \operatorname{grad} \mu_m, \qquad \boldsymbol{j}_w = -M_w \operatorname{grad} \mu_w, \tag{5.60}$$

where $M_m > 0$ and $M_w > 0$ are scalar mobilities and $\operatorname{grad}(\cdot)$ denotes the spatial gradient.

In the material description, the balance laws are written in terms of the nominal fluxes $\boldsymbol{J}_m$ and $\boldsymbol{J}_w$, defined per unit reference area. These are related to the spatial fluxes by

$$\boldsymbol{J}_i = \Omega\, \boldsymbol{F}^{-1} \boldsymbol{j}_i, \qquad i \in \{m, w\}, \tag{5.61}$$

and the gradients are related by

$$\operatorname{grad}(\cdot) = \boldsymbol{F}^{-T} \operatorname{Grad}(\cdot). \tag{5.62}$$

Combining these relations, we obtain the constitutive laws for the nominal fluxes,

$$\begin{aligned} \boldsymbol{J}_m &= -\Omega M_m\, \boldsymbol{F}^{-1} \boldsymbol{F}^{-T} \operatorname{Grad} \mu_m, \\ \boldsymbol{J}_w &= -\Omega M_w\, \boldsymbol{F}^{-1} \boldsymbol{F}^{-T} \operatorname{Grad} \mu_w. \end{aligned} \tag{5.63}$$

Thus, diffusion is isotropic in the current configuration but appears with an effective mobility tensor $\Omega M_i\, \boldsymbol{F}^{-1} \boldsymbol{F}^{-T}$ in the reference configuration, reflecting the geometric

distortion introduced by the deformation. Substituting these expressions into the dissipation inequality 5.45 yields

$$\mathcal{D}_d = \Omega M_m \left(\text{Grad}\,\mu_m\right)^T \boldsymbol{F}^{-1}\boldsymbol{F}^{-T}\text{Grad}\,\mu_m + \Omega M_w \left(\text{Grad}\,\mu_w\right)^T \boldsymbol{F}^{-1}\boldsymbol{F}^{-T}\text{Grad}\,\mu_w \;\geq\; 0, \tag{5.64}$$

which is guaranteed because $\boldsymbol{F}^{-1}\boldsymbol{F}^{-T}$ is positive definite and $M_m, M_w > 0$.

Reaction In the present work, we adopt a simple kinetic model that is commonly used for irreversible, monomer-limited polymerisation (Chan and Rey, 1995), namely

$$\begin{cases} \dot{p} = k\, C_m, \quad k > 0, & \text{if } \mathcal{A} > 0, \\ p = 0, & \text{otherwise.} \end{cases} \tag{5.65}$$

In addition, we assume that the system starts from a solution of monomer and water only, i.e. $p|_{t=0} = 0$. As a result, combining the relations Eqn. 5.23 and 5.24, the polymer volume fraction can be written as

$$\Phi_p = vp. \tag{5.66}$$

5.3 One-dimensional governing equations and constitutive relations

We specialise the general framework to the one-dimensional tube geometry used in the numerical examples. The reference domain is the interval $X \in (0, L)$. The tube has a unit-square cross section; the lateral walls are rigid and frictionless, so that all fields depend only on X and t and there is no transverse deformation. Accordingly, the deformation gradient takes the diagonal form $\boldsymbol{F} = \text{diag}(\lambda, 1, 1)$. From the definition of

deformation gradient (Eqn. 5.2), the axial stretch writes

$$\lambda(X,t) = 1 + \frac{\partial u}{\partial X}, \qquad \Omega(X,t) = \det \boldsymbol{F} = \lambda(X,t). \tag{5.67}$$

Conservation of mass Specialising from Eqn. 5.23, the monomer and water balances in the reference configuration are

$$\begin{aligned} \frac{\partial C_m}{\partial t} + \frac{\partial J_m}{\partial X} &= -\dot{p}, \\ \frac{\partial C_w}{\partial t} + \frac{\partial J_w}{\partial X} &= 0, \end{aligned} \tag{5.68}$$

with Eqn. 5.65 as the local kinetic law for polymerisation. The nominal fluxes write as

$$J_m = -M_m\,\lambda^{-1}\,\frac{\partial \mu_m}{\partial X}, \qquad J_w = -M_w\,\lambda^{-1}\,\frac{\partial \mu_w}{\partial X}. \tag{5.69}$$

Balance of linear momentum and incompressibility constraint Molecular incompressibility reduces in 1D to the local algebraic relation

$$\lambda = \Phi_m + \Phi_w + \Phi_p = vC_m + vC_w + vp, \tag{5.70}$$

Hence λ is determined pointwise by the composition fields and the extent of reaction. Mechanical equilibrium in the tube implies $\partial_X P_{11} = 0$. With a traction-free end at $X = L$, $P_{11}(L,t) = 0$, we obtain $P_{11} = 0$. Using the constitutive relation $\boldsymbol{P} = \partial\Psi/\partial\boldsymbol{F} - \Omega\,\Pi\,\boldsymbol{F}^{-T}$ and the diagonal form of $\boldsymbol{F}$, the condition $P_{11} = 0$ yields the local identification

$$\Pi = \frac{\partial \Psi}{\partial \lambda}, \tag{5.71}$$

so that the Lagrange multiplier Π is also eliminated from the PDE system.

Chemical potentials (mixed Cahn-Hilliard form). The free energy per unit reference volume has the one-dimensional dependence

$$\Psi = \Psi(\lambda,\, C_m,\, C_w,\, p,\, \partial_X C_w)\,, \tag{5.72}$$

where the gradient term represents the interfacial contribution. The chemical potentials follow from the thermodynamic framework as

$$\mu_m = \frac{\partial \Psi}{\partial C_m} + v\,\Pi, \tag{5.73}$$

and

$$\mu_w = \frac{\partial \Psi}{\partial C_w} + v\,\Pi - \frac{\partial}{\partial X}\left(\frac{\partial \Psi}{\partial(\partial_X C_w)}\right), \tag{5.74}$$

with Π given locally by Eqn. 5.71 and λ by Eqn. 5.70. Introducing μ_m and μ_w as additional unknowns yields a mixed formulation that avoids fourth-order derivatives in the transport equations.

Boundary conditions. Unless stated otherwise, we impose impermeable (no-flux) conditions for monomer and water at the boundaries of the one-dimensional reference domain $X \in (0, L)$, i.e. $J_m = 0$ and $J_w = 0$ at $X = 0$ and $X = L$. In addition, the gradient contribution in the free energy introduces the microstress $\xi_w = \partial\Psi/\partial(\partial_X C_w)$ (cf. Eqn. 5.36), and we apply the associated natural boundary condition (vanishing microtraction)

$$\xi_w = 0 \qquad \text{at } X = 0, L. \tag{5.75}$$

To mimic a sample in contact with an external water bath, we extend the closed-system formulation to an open system by allowing solvent exchange across a selected boundary (take the right boundary here for example). All bulk equations and constitutive relations remain unchanged; only the water-transport boundary condition at $X = L$ is modi-

fied. Rather than prescribing $\mu_w = \mu_w^{\text{bath}}$ strictly, which can generate a thin boundary layer when μ_w contains logarithmic Flory-Huggins terms and thereby lead to numerical difficulties, we adopt the Robin exchange condition

$$J_w = h\big(\mu_w - \mu_w^{\text{bath}}\big) \qquad \text{at } X = L, \tag{5.76}$$

with coefficient $h > 0$, while retaining $J_w = 0$ at $X = 0$. In the limit $h \to \infty$, Eqn. 5.76 approaches the Dirichlet condition $\mu_w = \mu_w^{\text{bath}}$ at $X = L$.

The bath chemical potential μ_w^{bath} is an externally prescribed boundary value. To represent a homogeneous pure-water reservoir, we choose μ_w^{bath} to be consistent with the Flory-Huggins free energy convention adopted in Eqn. 5.57. With the added reference term $\mu_0 C_w$, the chemical potential of water in a homogeneous pure-water state ($\phi_w = 1$) reduces to the reference value μ_0.We set $\mu_0 = 0$ so that $\mu_w^{\text{bath}} = 0$ in all simulations. We use the same value $h = 10\,\text{mol}^2\text{J}^{-1}\text{m}^{-2}\text{s}^{-1}$ in all open-system simulations.

5.4 Time discretisation and weak formulation

In this section we seek a numerical solution of the one-dimensional PIPS model on $X \in (0, L)$. For clarity, we first summarise the governing equations in strong form and list the constitutive relations required to close the system.

The transport problem consists of the conservation of monomer and water

$$\begin{aligned} \frac{\partial C_m}{\partial t} + \frac{\partial J_m}{\partial X} &= -\dot{p}, \\ \frac{\partial C_w}{\partial t} + \frac{\partial J_w}{\partial X} &= 0, \end{aligned} \tag{5.77}$$

with nominal fluxes J_m and J_w defined in Eqn. 5.69. Polymerisation is modelled locally through the kinetic law

$$\dot{p} = k\, C_m, \tag{5.78}$$

so that $p(X,t)$ evolves pointwise without spatial fluxes.

To avoid fourth-order derivatives associated with the gradient contribution in the free energy, we adopt a mixed formulation in which the chemical potentials μ_m and μ_w are treated as additional unknown fields and constrained by their constitutive definitions,

$$\begin{aligned} \mu_m &= \frac{\partial \Psi}{\partial C_m} + v\,\Pi, \\ \mu_w &= \frac{\partial \Psi}{\partial C_w} + v\,\Pi - \frac{\partial}{\partial X}\left(\frac{\partial \Psi}{\partial (\partial_X C_w)}\right), \end{aligned} \tag{5.79}$$

where the free energy density $\Psi(\lambda, C_m, C_w, p, \partial_X C_w)$ is given in Section 5.2.4 by Eqns. 5.47, 5.57, and 5.59. We will further discuss the advantages of using this mixed formulation later in Section 5.4.2. The stretch λ (with $\Omega = \lambda$) and the Lagrange multiplier Π enforcing molecular incompressibility are determined pointwise from the constraint and the local constitutive relation

$$\lambda = vC_m + vC_w + vp, \qquad \Pi = \frac{\partial \Psi}{\partial \lambda}, \tag{5.80}$$

see Eqn. 5.71. We next discretise Eqns. 5.77-5.80 in time and derive the corresponding weak form used in the finite element implementation.

5.4.1 Time discretisation

We discretise the one-dimensional system Eqns. 5.77-5.80 in time. Let $t^{n+1} = t^n + \Delta t$. For any quantity a we define the mid-point value

$$a^{\text{mid}} := \tfrac{1}{2}\left(a^{n+1} + a^n\right). \tag{5.81}$$

We evaluate the fluxes and reaction source at the mid-point using Crank-Nicholson method, which offers a higher order accuracy in time than using backward Euler

method (LeVeque, 2007). The monomer and water balances are discretised as

$$\frac{C_m^{n+1} - C_m^n}{\Delta t} + \frac{\partial J_m^{\text{mid}}}{\partial X} = -\, k\, C_m^{\text{mid}}, \tag{5.82}$$

$$\frac{C_w^{n+1} - C_w^n}{\Delta t} + \frac{\partial J_w^{\text{mid}}}{\partial X} = 0, \tag{5.83}$$

with mid-point fluxes

$$J_m^{\text{mid}} = -M_m\, (\lambda^{\text{mid}})^{-1}\, \frac{\partial \mu_m^{\text{mid}}}{\partial X}, \qquad J_w^{\text{mid}} = -M_w\, (\lambda^{\text{mid}})^{-1}\, \frac{\partial \mu_w^{\text{mid}}}{\partial X}. \tag{5.84}$$

The chemical potentials are enforced at t^{n+1} through

$$\mu_m^{n+1} = \frac{\partial \Psi}{\partial C_m}\Big|_{n+1} + v\, \Pi^{n+1}, \tag{5.85}$$

$$\mu_w^{n+1} = \frac{\partial \Psi}{\partial C_w}\Big|_{n+1} + v\, \Pi^{n+1} - \frac{\partial}{\partial X}\left(\frac{\partial \Psi}{\partial (\partial_X C_w)}\Big|_{n+1}\right). \tag{5.86}$$

The extent of reaction is advanced algebraically with the mid-point reaction term to ensure consistency with the conservation equations,

$$p^{n+1} = p^n + \Delta t\, k\, C_m^{\text{mid}}. \tag{5.87}$$

5.4.2 Weak formulation

At each time step we solve for the four fields (C_m^{n+1}, C_w^{n+1}, μ_m^{n+1}, μ_w^{n+1}) in a coupled system. Keeping both the concentrations and chemical potentials as primary (nodal) unknowns gives a mixed Cahn-Hilliard-type formulation: eliminating μ would result in a fourth-order equation in C_w requiring C^1-continuous approximations, whereas the mixed form produces only second-order spatial operators that can be discretised with standard C^0 finite elements (such as Lagrange elements) (Gurtin, 1996; Soria et al.,

2025).

We introduce test functions $\hat{C}_m, \hat{C}_w, \hat{\mu}_m, \hat{\mu}_w$. Starting from the time-discretised strong forms in Section 5.4.1, we obtain the weak form by multiplying the PDEs (Eqns 5.82, 5.83, 5.85, 5.86) by the corresponding test functions and integrating over $(0, L)$:

$$\begin{aligned}
\int_0^L \left(\frac{C_m^{n+1} - C_m^n}{\Delta t} + \frac{\partial J_m^{\text{mid}}}{\partial X} + k\, C_m^{\text{mid}} \right) \hat{C}_m \, \mathrm{d}X = 0, \\
\int_0^L \left(\frac{C_w^{n+1} - C_w^n}{\Delta t} + \frac{\partial J_w^{\text{mid}}}{\partial X} \right) \hat{C}_w \, \mathrm{d}X = 0, \\
\int_0^L \left(\mu_m^{n+1} - \left.\frac{\partial \Psi}{\partial C_m}\right|_{n+1} - v\, \Pi^{n+1} \right) \hat{\mu}_m \, \mathrm{d}X = 0, \\
\int_0^L \left(\mu_w^{n+1} - \left.\frac{\partial \Psi}{\partial C_w}\right|_{n+1} - v\, \Pi^{n+1} + \frac{\partial}{\partial X} \left(\left.\frac{\partial \Psi}{\partial (\partial_X C_w)}\right|_{n+1} \right) \right) \hat{\mu}_w \, \mathrm{d}X = 0.
\end{aligned} \tag{5.88}$$

Integrating by parts gives

$$\begin{aligned}
\int_0^L \frac{C_m^{n+1} - C_m^n}{\Delta t} \hat{C}_m \, \mathrm{d}X - \int_0^L J_m^{\text{mid}} \frac{\partial \hat{C}_m}{\partial X} \, \mathrm{d}X + \left[J_m^{\text{mid}} \hat{C}_m \right]_0^L + \int_0^L k\, C_m^{\text{mid}} \hat{C}_m \, \mathrm{d}X = 0, \\
\int_0^L \frac{C_w^{n+1} - C_w^n}{\Delta t} \hat{C}_w \, \mathrm{d}X - \int_0^L J_w^{\text{mid}} \frac{\partial \hat{C}_w}{\partial X} \, \mathrm{d}X + \left[J_w^{\text{mid}} \hat{C}_w \right]_0^L = 0, \\
\int_0^L \left(\mu_m^{n+1} - \left.\frac{\partial \Psi}{\partial C_m}\right|_{n+1} - v\, \Pi^{n+1} \right) \hat{\mu}_m \, \mathrm{d}X = 0, \\
\int_0^L \left(\mu_w^{n+1} - \left.\frac{\partial \Psi}{\partial C_w}\right|_{n+1} - v\, \Pi^{n+1} \right) \hat{\mu}_w \, \mathrm{d}X \\
- \int_0^L \left.\frac{\partial \Psi}{\partial (\partial_X C_w)}\right|_{n+1} \frac{\partial \hat{\mu}_w}{\partial X} \, \mathrm{d}X + \left[\left.\frac{\partial \Psi}{\partial (\partial_X C_w)}\right|_{n+1} \hat{\mu}_w \right]_0^L = 0.
\end{aligned} \tag{5.89}$$

Imposing the boundary conditions stated in Section 5.3 (Eqn. 5.75) gives

$$\begin{aligned} \left[J_m^{\text{mid}} \hat{C}_m\right]_0^L &= 0, \\ \left[\left.\frac{\partial \Psi}{\partial(\partial_X C_w)}\right|_{n+1} \hat{\mu}_w\right]_0^L &= 0, \end{aligned} \tag{5.90}$$

and for the water flux term (Eqn. 5.76),

$$\begin{aligned} &\left[J_w^{\text{mid}} \hat{C}_w\right]_0^L = 0 \qquad \text{closed system,} \\ &\left[J_w^{\text{mid}} \hat{C}_w\right]_0^L = h\left(\mu_w^{\text{mid}} - \mu_w^{\text{bath}}\right) \hat{C}_w\Big|_{X=L} \qquad \text{open system, with } J_w = 0 \text{ at } X = 0. \end{aligned} \tag{5.91}$$

Substituting these into Eqn. 5.89:

$$\begin{aligned} \int_0^L \frac{C_m^{n+1} - C_m^n}{\Delta t} \hat{C}_m \,\mathrm{d}X - \int_0^L J_m^{\text{mid}} \frac{\partial \hat{C}_m}{\partial X} \,\mathrm{d}X + \int_0^L k\, C_m^{\text{mid}} \hat{C}_m \,\mathrm{d}X &= 0, \\ \int_0^L \frac{C_w^{n+1} - C_w^n}{\Delta t} \hat{C}_w \,\mathrm{d}X - \int_0^L J_w^{\text{mid}} \frac{\partial \hat{C}_w}{\partial X} \,\mathrm{d}X + h\left(\mu_w^{\text{mid}} - \mu_w^{\text{bath}}\right) \hat{C}_w\Big|_{X=L} &= 0, \\ \int_0^L \left(\mu_m^{n+1} - \left.\frac{\partial \Psi}{\partial C_m}\right|_{n+1} - v\,\Pi^{n+1}\right) \hat{\mu}_m \,\mathrm{d}X &= 0, \\ \int_0^L \left(\mu_w^{n+1} - \left.\frac{\partial \Psi}{\partial C_w}\right|_{n+1} - v\,\Pi^{n+1}\right) \hat{\mu}_w \,\mathrm{d}X - \int_0^L \left.\frac{\partial \Psi}{\partial(\partial_X C_w)}\right|_{n+1} \frac{\partial \hat{\mu}_w}{\partial X} \,\mathrm{d}X &= 0. \end{aligned} \tag{5.92}$$

This reduces to the weak form for closed systems when $h = 0$. Finally, inserting the time-discretised form for the nominal fluxes (Eqn. 5.84), the fully coupled weak prob-

lem is: find $(C_m^{n+1}, C_w^{n+1}, \mu_m^{n+1}, \mu_w^{n+1})$ such that for all $(\hat{C}_m, \hat{C}_w, \hat{\mu}_m, \hat{\mu}_w)$,

$$\begin{aligned}
\int_0^L \frac{C_m^{n+1} - C_m^n}{\Delta t}\,\hat{C}_m\,\mathrm{d}X + \int_0^L M_m(\lambda^{\mathrm{mid}})^{-1}\frac{\partial \mu_m^{\mathrm{mid}}}{\partial X}\frac{\partial \hat{C}_m}{\partial X}\,\mathrm{d}X + \int_0^L k\,C_m^{\mathrm{mid}}\,\hat{C}_m\,\mathrm{d}X = 0,\\
\int_0^L \frac{C_w^{n+1} - C_w^n}{\Delta t}\,\hat{C}_w\,\mathrm{d}X + \int_0^L M_w(\lambda^{\mathrm{mid}})^{-1}\frac{\partial \mu_w^{\mathrm{mid}}}{\partial X}\frac{\partial \hat{C}_w}{\partial X}\,\mathrm{d}X = 0,\\
\int_0^L \left(\mu_m^{n+1} - \left.\frac{\partial \Psi}{\partial C_m}\right|_{n+1} - v\,\Pi^{n+1}\right)\hat{\mu}_m\,\mathrm{d}X = 0,\\
\int_0^L \left(\mu_w^{n+1} - \left.\frac{\partial \Psi}{\partial C_w}\right|_{n+1} - v\,\Pi^{n+1}\right)\hat{\mu}_w\,\mathrm{d}X + \int_0^L \left.\frac{\partial \Psi}{\partial(\partial_X C_w)}\right|_{n+1}\frac{\partial \hat{\mu}_w}{\partial X}\,\mathrm{d}X = 0.
\end{aligned} \tag{5.93}$$

5.5 One-dimensional finite element example

We now present numerical results for the one-dimensional finite element model introduced above. The governing equations are discretised on the unit interval $L = 1, \mathrm{m}$. In this section, we first introduce the practical details of numerical implementation using `FEniCSx` software (Alnæs et al., 2015) in Section 5.5.1. In Section 5.5.2, we introduce the dimensionless parameters that are relevant to the problem. In Section 5.5.3 and Section 5.5.4, we show numerical results of closed and open systems, respectively.

5.5.1 Numerical implementation

The one-dimensional reference domain $\mathcal{B}_0$ with $L = 0.1\mathrm{m}$ is discretised by a uniform mesh of $N_e = 100$ intervals. We adopt an adaptive time stepping scheme where the initial time step is $\Delta t = 10^{-6}\mathrm{s}$ and the maximum allowed time step is $\Delta t = 0.01\mathrm{s}$. The time step is increased by 1.2 if the previous time step uses iterations fewer than 5, and shrink by 0.5 if the previous step is not converged. Representative simulations were repeated on refined meshes ($N_e = 200, 400$) and reduced time steps. The solution is considered converged as changes in key outputs, such as the polymer volume-

fraction profile $\phi_p(X,t)$ at selected times, are negligible under further refinement. Since we adopt a mixed formulation for the Cahn-Hilliard equation, such that all fields only require first spatial derivatives and are approximated in the same C^0-conforming first-order Lagrange function space (CG-1). To trigger the phase separation in the system, we prescribe a compositional noise for water concentration at $t = 0\,\mathrm{s}$ with an amplitude of 1% of the initial water concentration.

5.5.2 Dimensionless parameters

To interpret the coupling between elasticity, mixing and reaction-diffusion, we introduce two dimensionless groups that will be used throughout the remainder of this chapter. For clarity, Table 5.1 summarises the material and numerical parameters used in the simulations and indicates which quantities are held fixed across all runs and which are varied to change the dimensionless groups.

We define the characteristic mixing energy density

$$E^* = \frac{RT}{v}. \tag{5.94}$$

The elasticity ratio is then

$$r_e = \frac{G^\infty(1)}{E^*}, \tag{5.95}$$

which measures the strength of the polymer network elasticity relative to the thermodynamic driving force for demixing. In the parametric studies reported below, r_e is varied by changing the plateau modulus scale $G^\infty(1)$ while keeping T and v fixed.

To characterise the competition between diffusion and polymerisation, we define a reference diffusivity by introducing a reference chemical-potential scale RT and a reference concentration C_{ref},

$$D_{\mathrm{ref}} = \frac{M\,RT}{C_{\mathrm{ref}}}. \tag{5.96}$$

Table 5.1: Material and numerical parameters used in the simulations of Chapter 5. Unless stated otherwise, parameters are held fixed at the values listed here. The parameters varied in the r_e and Da sweeps are $G^{\infty}(1)$ and k, respectively.

Symbol	Meaning	Value
L	domain length	$1\,\mathrm{m}$
T	absolute temperature	$300\ \mathrm{K}$
R	gas constant	$8.3145\ \mathrm{J\,mol^{-1}\,K^{-1}}$
k_B	Boltzmann constant	$1.38064852 \times 10^{-23}\ \mathrm{J\,K^{-1}}$
v	monomer molar volume	$5 \times 10^{-4}\,\mathrm{m^3/mol}$
C_m^0	initial monomer concentration ($= C_{\mathrm{ref}}$)	$1000\,\mathrm{mol/m^3}$
C_w^0	initial water concentration	$1000\,\mathrm{mol/m^3}$
M_m	monomer mobility	$0.005\,\mathrm{mol^2 J^{-1} m^{-1} s^{-1}}$
M_w	water mobility	$0.005\,\mathrm{mol^2 J^{-1} m^{-1} s^{-1}}$
κ	gradient coefficient	$10^{-4}\,\mathrm{Jm^5 mol^{-2}}$
χ	Flory-Huggins interaction parameter(s)	1.5
$G^{\infty}(1)$	plateau modulus scale (varied to set r_e)	Dependent on r_e
k	reaction rate constant (varied to set Da)	Dependent on Da
h	exchange coefficient (open system)	$10\ \mathrm{mol^2\ J^{-1}\ m^{-2}\ s^{-1}}$
μ_w^{bath}	bath chemical potential	0

The associated characteristic times are

$$t_{\mathrm{diff}} = \frac{L^2}{D_{\mathrm{ref}}}, \qquad t_{\mathrm{react}} = \frac{1}{k}, \tag{5.97}$$

and the Damkohler number is

$$\mathrm{Da} = \frac{t_{\mathrm{diff}}}{t_{\mathrm{react}}} = \frac{kL^2}{D_{\mathrm{ref}}} = \frac{kL^2\,C_{\mathrm{ref}}}{M\,RT}. \tag{5.98}$$

We choose $C_{\mathrm{ref}} = C_m^0$ unless stated otherwise. In the parametric study, Da is varied by changing the reaction rate constant k while keeping $L(= 1\mathrm{m})$, M, T and C_{ref} fixed.

The dimensionless groups r_e and Da will be used in the next sections to organise the parameter space and to compare morphologies and timescales across simulations on a common basis.

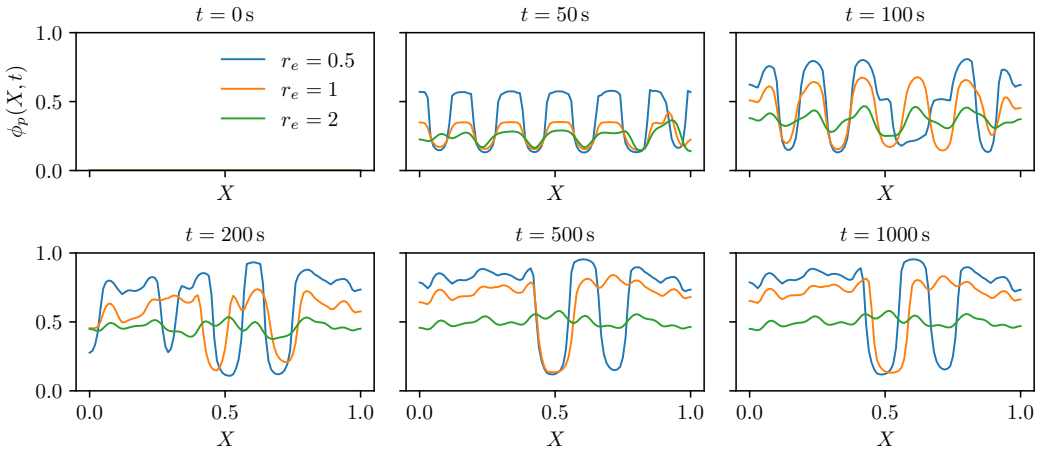

Figure 5.3: Profiles of the true polymer volume fraction $\phi_p(X,t)$ across the domain at different times for $r_e = 0.5$, 1, and 2.

5.5.3 PIPS in a closed system

Effect of elasticity We first analyse the effect of elasticity on the PIPS process with $\mathrm{Da} = 1$ in a closed system. The initial monomer and water concentrations are $C_m = C_w = 1000\ \mathrm{mol\,m^{-3}}$. The molar volumes of monomer and water are $v_m = v_w = v = 5 \times 10^{-4}\ \mathrm{m^3\,mol^{-1}}$. The initial number concentration of polymer chains is $C_p^0 = 10\ \mathrm{mol\,m^{-3}}$. The gradient-energy coefficient is $\kappa = 10^{-4}\ \mathrm{Jm^5mol^{-2}}$, and the interaction parameter between polymer/monomer and water is $\chi = 1.5$. Figure 5.3 shows the profiles of the true polymer volume fraction ϕ_p at selected times for systems with $r_e = 0.5$, 1, and 2. As polymerisation proceeds (e.g. $t = 50\,\mathrm{s}$), the reaction changes the local thermodynamics and small composition fluctuations are amplified once the system becomes unstable. At this stage, the characteristic wavelength is nearly identical for all r_e. By $t \approx 200\,\mathrm{s}$, the solutions enter a coarsening regime consistent with Ostwald ripening. At later times ($t \approx 350\,\mathrm{s}$-$1000\,\mathrm{s}$), the system approaches a quasi-equilibrium state and the profiles vary only weakly.

To further quantify the evolving morphology, we track the interface number $N_{\mathrm{int}}(t)$ and the phase contrast $\Delta\phi_p(t) = \phi_p^{\mathrm{rich}}(t) - \phi_p^{\mathrm{poor}}(t)$. The interface number is estimated

by counting the number of crossings of $\phi_p(X,t)$ with its spatial mean. To obtain representative "rich" and "poor" values that are insensitive to the diffuse interfacial width, we define $\phi_p^{\mathrm{rich}}(t)$ as the spatial mean of the upper tail of the ϕ_p distribution (here the top 5% of grid values), and $\phi_p^{\mathrm{poor}}(t)$ as the mean of the lower tail (bottom 5%). Figure 5.4 shows the temporal evolution of these metrics. The stepwise decrease of $N_{\mathrm{int}}(t)$ reflects discrete ripening events in which a narrow domain collapses and a pair of interfaces is removed. During phase separation, reducing interfacial area lowers the gradient-energy contribution, which results in eliminating of interfaces. When elasticity is coupled to composition through the local volume change λ and an composition dependent modulus, the chemical potential acquires an additional mechanical contribution. Physically, converting a small domain into its neighbours requires not only redistributing material but also accommodating the associated local swelling, i.e. the domain interiors and interfacial regions have different λ, so interface motion modifies the displacement field and the associated elastic energy. Increasing r_e strengthens this chemo-mechanical feedback, so the available chemical potential to drop to drive interface motion is reduced: diffusion that would increase segregation or eliminate a domain is opposed by an elastic penalty associated with swelling or shrinking. As a result, interface migration becomes slower and the domain-elimination events occur less frequently within the simulated time window, leaving a finer morphology (larger N_{int}) at late times even though the interfacial energy alone would favour further coarsening.

The phase-contrast curves show that $\Delta\phi_p(t)$ increases rapidly after the onset of instability, which is due to the formation and sharpening of polymer-rich and polymer-poor domains. For $r_e = 0.5$ and 1, the contrast grows monotonically and then reach equilibrium at later times. The stiffest case ($r_e = 2$) differs at later times because strong elasticity restricts the solvent redistribution required to further deepen segregation. For a large modulus, the swelling driven water uptake (or expulsion) is strongly resisted because it would introduce more excessive elastic energy. Consequently, the composi-

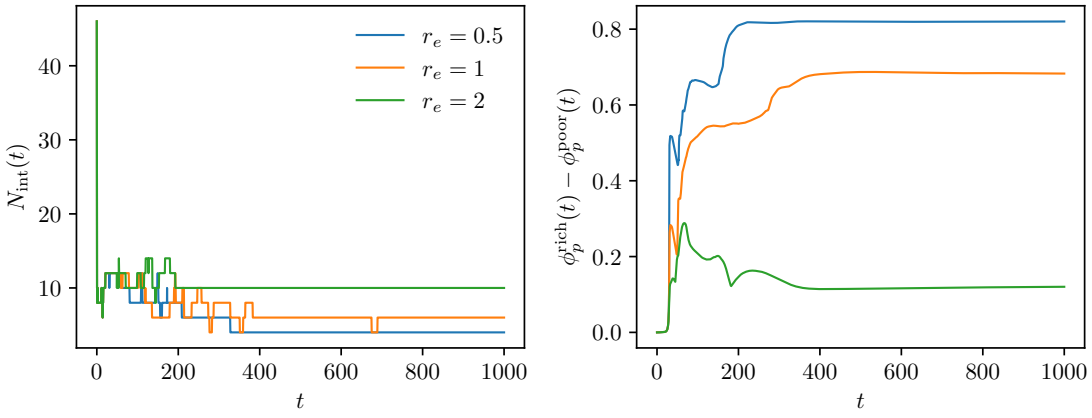

(a) (b)

Figure 5.4: Evolution of (a) the number of interfaces $N_{\text{int}}(t)$ and (b) the phase contrast $\phi_p^{\text{rich}}(t) - \phi_p^{\text{poor}}(t)$ for $\text{Da} = 1$.

tion in polymer-rich regions changes only weakly once the initial pattern has formed, while polymerisation continues throughout the domain and gradually increases $\phi_p^{\text{poor}}(t)$ in the polymer-poor regions. As $\phi_p^{\text{poor}}(t)$ rises under this mechanical constraint, the difference $\Delta\phi_p(t) = \phi_p^{\text{rich}}(t) - \phi_p^{\text{poor}}(t)$ decreases, producing the observed non-monotonic evolution for $r_e = 2$.

It can also be seen that the onset times of the phase separation across the three cases are similar. In this model the onset is primarily controlled by the polymerisation-driven change in the mixing energy, whereas the elastic modulus remains small at early conversion due to the weak entanglement. Elasticity therefore has only a weak influence on the time at which fluctuations begin to grow, but it strongly affects the subsequent growth rate and coarsening kinetics once appreciable segregation and deformation mismatch have developed and elastic modulus is large enough.

These trends can be explained by inspecting the energetic evolution during PIPS. Figure 5.5 shows the mixing, interfacial, and elastic energy contributions as functions of time. The mixing energy first decreases and then increases. The initial decrease is associated with the diffusion-driven smoothing of the prescribed compositional noise,

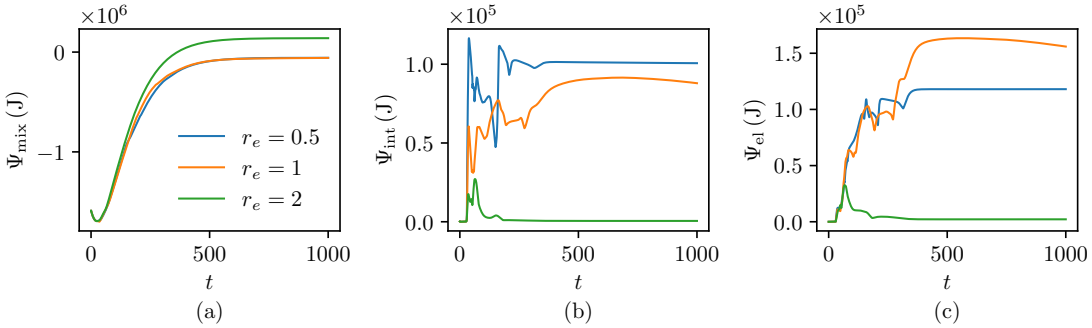

Figure 5.5: Evolution of (a) mixing energy, (b) interfacial energy, and (c) elastic energy for different r_e at $\mathrm{Da} = 1$.

whereas the later increase is due to continued polymerisation, which reduces the entropy of mixing. The interfacial energy increases rapidly at early times as interfaces are created, and then gradually reaches a plateau as coarsening reduces interfacial area. Larger r_e suppresses phase separation and yields a smaller interfacial-energy contribution at long times. The elastic energy initially increases with a similar trend across cases and then reaches different equilibrium values. Notably, the equilibrium value of Ψ_{el} is not monotonic in r_e. This arises from competing effects: increasing r_e raises the energetic penalty per unit deformation, while simultaneously suppressing the composition-driven deformation itself. In this parametric study, $r_e = 1$ corresponds to an intermediate regime where the system still develops appreciable strains, yet the stiffness is sufficiently large that these strains contribute significant elastic energy.

Effect of Damkohler number We next investigate the role of reaction-diffusion competition by sweeping the Damkohler number Da at fixed elasticity ($r_e = 1$), while keeping all other parameters identical to the previous section. Figure 5.6 shows snapshots of $\phi_p(X, t)$ for $\mathrm{Da} = 0.5$, 1, and 2 at selected times. By $t \approx 50$ s, polymerisation has modified the thermodynamic driving force sufficiently that composition fluctuations begin to grow. For $\mathrm{Da} = 2$, the profile is already more irregular by this time, indicating an earlier onset of the phase separation process. From $t \approx 200$ s onwards, the morphology

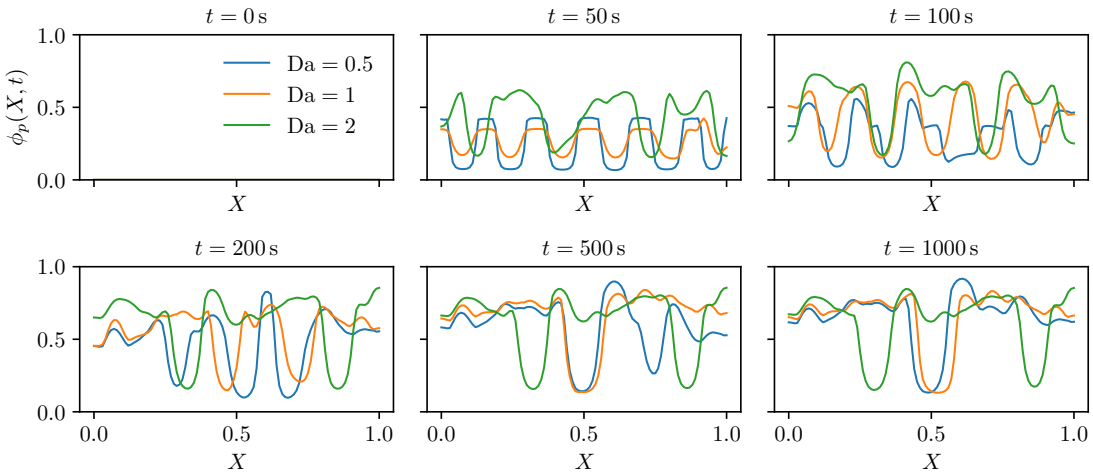

Figure 5.6: Profiles of the true polymer volume fraction $\phi_p(X,t)$ across the domain at different times for $\mathrm{Da} = 0.5$, 1, and 2.

evolves through coarsening: the pattern becomes less regular and changes mainly via domain elimination events. At later times ($t \approx 500$-1000 s), these elimination events become less frequent and the morphology changes only weakly over time.

We quantify these trends using the same morphological metrics as shown in Figure 5.7. In Figure 5.7(a), the onset of interface elimination occurs earlier for larger Da as a result of faster polymerisation relative to diffusion. By the end of the simulation, the interface number becomes essentially identical across all three cases, suggesting that within the explored range Da mainly affects the transient kinetics rather than the final morphology at fixed elasticity. Figure 5.7(b) shows that the phase contrast rises rapidly from near zero once phase separation begins, and reaches similar equilibrium values. Larger Da results in a slightly smaller equilibrium value for the phase contrast.

Figure 5.8 shows the evolution of the mixing, interfacial, and elastic energy contributions for different Da. The mixing contribution increases monotonically and approaches a plateau, reflecting the progressive loss of mixing entropy during polymerisation. Larger Da leads to an earlier rise because polymerisation proceeds faster relative to diffusion. The interfacial energy increases rapidly at early times as interfaces form,

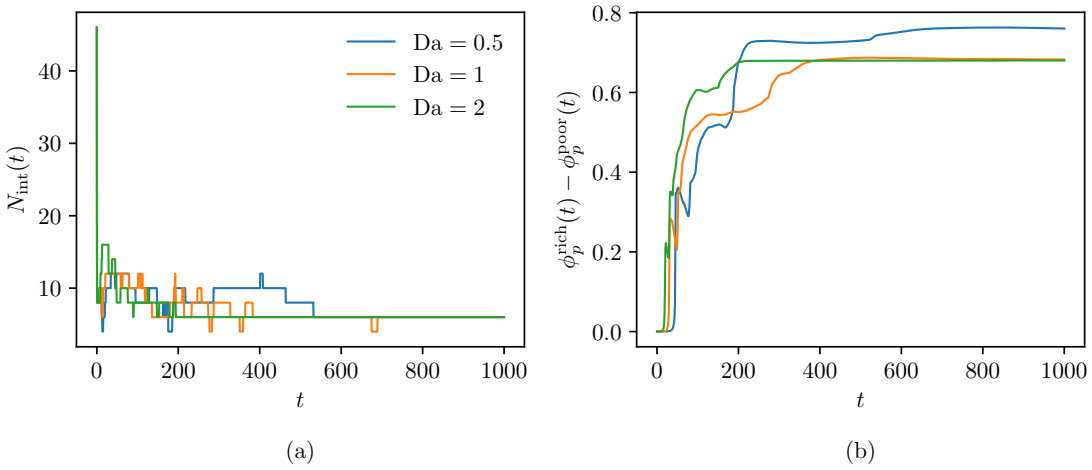

Figure 5.7: Evolution of (a) the number of interfaces $N_{\text{int}}(t)$ and (b) the phase contrast $\phi_p^{\text{rich}}(t) - \phi_p^{\text{poor}}(t)$ for $r_e = 1$.

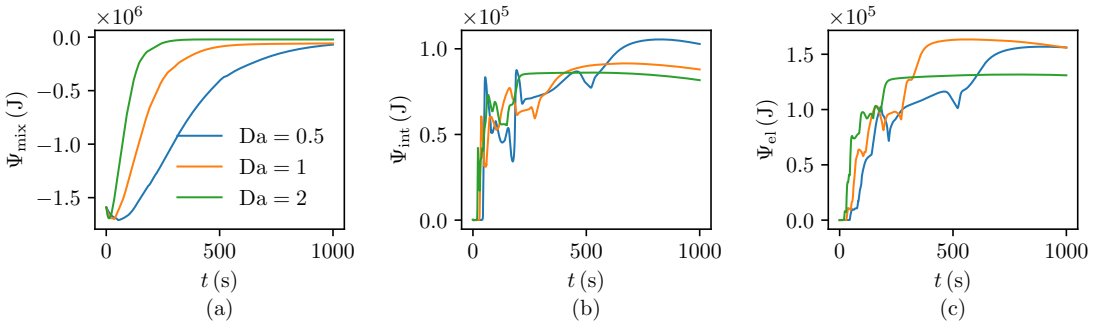

Figure 5.8: Evolution of (a) mixing energy, (b) interfacial energy, and (c) elastic energy for different Da at $r_e = 1$.

representing interface rearrangements and elimination events, and then saturates to a equilibrium value. Finally, the elastic energy in larger Da cases reach equilibrium earlier.

The Da and r_e parametric studies are used here to separate kinetic effects from mechanical control of the equilibrium morphology. In the present one-dimensional simulations, both $N_{\mathrm{int}}(t)$ and $\Delta\phi_p(t)$ approach approximately constant values by the end of the simulation, which we interpret as an equilibrium state. Larger Da triggers earlier growth of composition fluctuations and earlier interface elimination events, but the interface number and overall morphology become similar across the cases considered as the system approaches equilibrium. This indicates that, once the system has entered the two-phase regime, the equilibrium morphology is only weakly sensitive to the quench rate within the explored range. By contrast, varying r_e produces persistent differences up to equilibrium. Increasing r_e reduces the attainable phase contrast $\Delta\phi_p$ by penalising composition driven swelling, while simultaneously hindering interface rearrangements and slowing domain elimination, thereby preserving a finer morphology at equilibrium. Taken together, the figures show that Da mainly controls when phase separation and coarsening occur, whereas r_e controls the equilibrium balance between microstructure fineness and segregation amplitude. In the present parameter range, an intermediate $r_e = 1$ provides the most favourable compromise between retaining multiple domains and sustaining a meaningful contrast.

5.5.4 PIPS in an open system (water reservoir)

To mimic a sample in contact with an external water bath, we extend the closed-system formulation to an open system by allowing solvent exchange across the right boundary via the reservoir condition introduced earlier with Eqn. 5.76. In this subsection, we consider $\mathrm{Da} = 1$ and vary the elasticity ratio r_e.

Figure 5.9 shows the evolution of the true polymer volume fraction $\phi_p(X, t)$ for

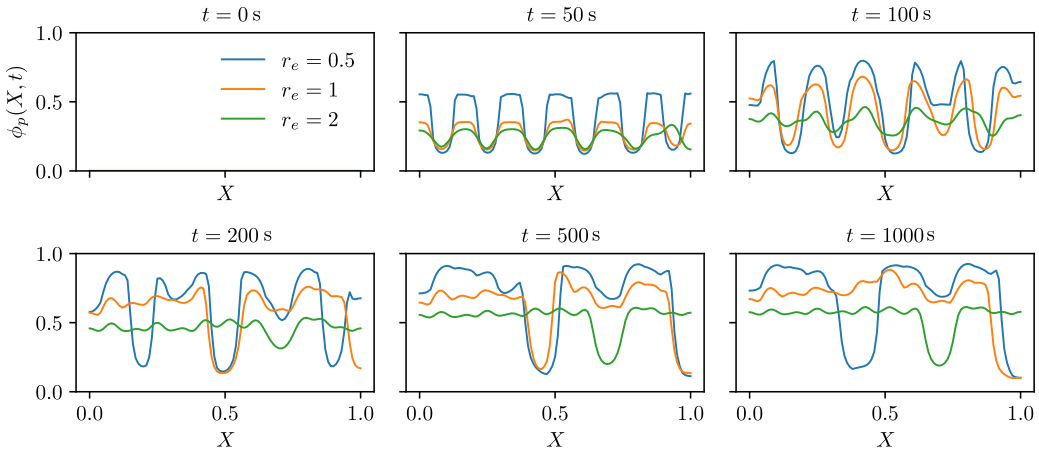

Figure 5.9: Profiles of the true polymer volume fraction $\phi_p(X,t)$ across the domain at different times for $r_e = 0.5$, 1, and 2 under the water-reservoir boundary condition (Da $= 1$).

$r_e = 0.5$, 1, and 2 under the water-reservoir boundary condition. By $t \approx 50$ s, phase separation is already evident. The early-stage amplitude depends strongly on elasticity: smaller r_e produces a larger contrast between polymer-rich and polymer-poor regions. By $t \approx 100$ s, the profiles become less regular as domains interact and some local features begin to merge or disappear.

From $t \approx 200$ s onward, the morphology evolves through discrete interface-elimination events. In the stiffest case ($r_e = 2$), small amplitude oscillations are progressively absorbed and the profile evolves toward a small number of broad regions. A distinctive feature of the open system is the emergence of a persistent boundary influence at late times: fixing the water chemical potential at the reservoir boundary drives solvent exchange, which alters the local swelling behaviour and therefore the true volume fractions. This leads to increasingly tilted long-time profiles ($t \approx 500$-1000 s), with a polymer-poor region preferentially developing close to the reservoir side. Increasing r_e still suppresses the peak-to-trough contrast by penalising swelling mismatch, and in addition it reduces the strength of the reservoir-induced asymmetry, where the polymer-poor region remains farther away from the right boundary.

The corresponding morphological metrics are shown in Figure 5.10. Compared with the closed system (Figure 5.3), the dependence of the equilibrium interface number on elasticity is reversed: in the open system, $N_{\mathrm{int}}(t)$ decreases with increasing r_e, so the stiffest network approaches a morphology with fewer interfaces. This behaviour reflects the fact that the reservoir breaks mass conservation, imposing a sustained solvent-exchange and swelling bias near the boundary. Under strong elasticity, repeatedly accommodating swelling mismatch across many alternating domains becomes energetically costly, so the system lowers its total free energy by forming fewer macroscopic regions. Figure 5.10(b) shows that the phase contrast rises rapidly after onset and then approaches a plateau. Increasing r_e reduces the attainable contrast, due to the mechanical penalty for swelling mismatch. Notably, the reservoir elevates the equilibrium contrast in the stiffest case ($r_e = 2$) compared with the closed system (from ~ 0.1 to ~ 0.3), indicating that solvent exchange can enhance the effective driving force for demixing even when elasticity suppresses segregation in the closed setting. Once this contrast is enforced by the bath, a stiffer network can lower its energetic cost primarily by reducing the number of interfaces, consistent with the observed decrease of equilibrium N_{int} with r_e.

Finally, Figure 5.11 directly compares $\phi_p(X, t)$ between the open and closed systems for $r_e = 0.5$ and 2. At early times ($t \approx$ 50-100 s), the profiles are similar, indicating that the initial wavelength selection is governed mainly by the thermodynamic instability created by polymerisation induced mixing energy changes. At later times, the closed system remains approximately spatially symmetric and coarsens without a preferred location, whereas the open system develops a pronounced boundary bias due to solvent exchange. This bias is strongest in the softer case ($r_e = 0.5$), where the reservoir drives substantial reorganisation and boundary-biased segregation, and it is weaker for $r_e = 2$, where elastic resistance limits swelling-driven redistribution.

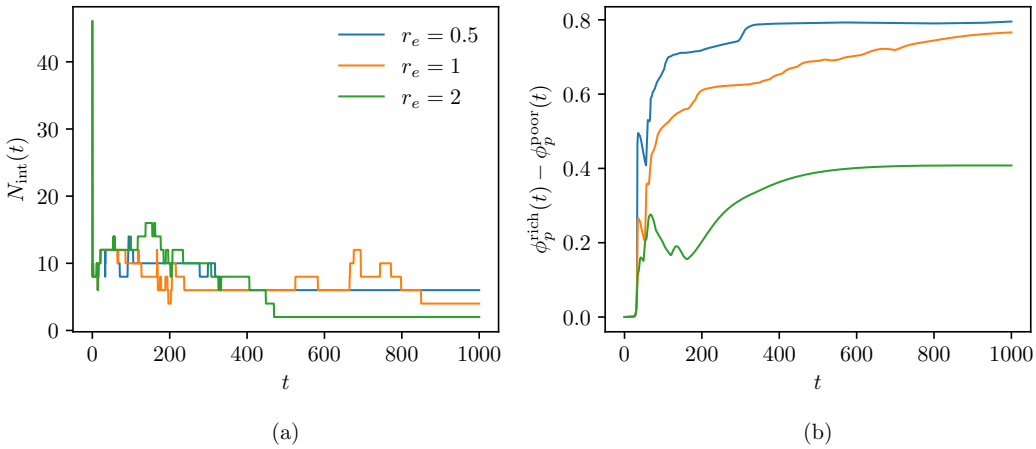

(a) (b)

Figure 5.10: Evolution of (a) the number of interfaces $N_{\text{int}}(t)$ and (b) the phase contrast $\phi_p^{\text{rich}}(t) - \phi_p^{\text{poor}}(t)$ for $r_e = 0.5$, 1, and 2 under the water-reservoir boundary condition ($\text{Da} = 1$).

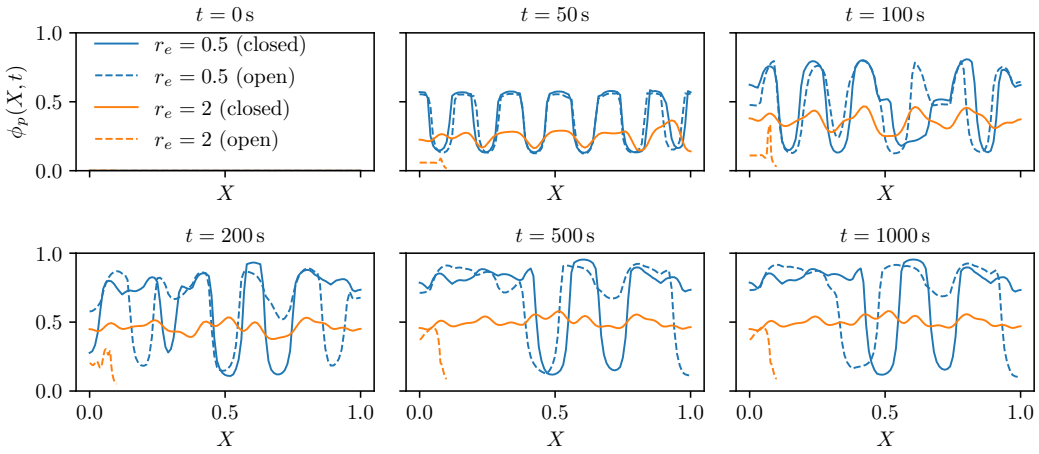

Figure 5.11: Comparison of $\phi_p(X,t)$ profiles between the open (water-reservoir) and closed systems for $r_e = 0.5$ and 2 at $\text{Da} = 1$. Solid lines denote the closed system and dashed lines denote the open system.

5.6 Conclusion

In this chapter we developed a thermodynamically consistent chemo-mechanical continuum framework for polymerisation-induced phase separation (PIPS) in a ternary monomer-polymer-solvent mixture. Polymerisation, diffusion-driven demixing, and the emergence of elasticity were treated within a single free-energy formulation, in which the nominal free energy comprises a Flory-Huggins mixing term, a Cahn-Hilliard-type gradient penalty, and an elastic contribution associated with an evolving polymer network. Rather than prescribing elasticity a priori, the shear modulus was allowed to develop dynamically as a function of composition and chain growth through a smooth entanglement "gate". This provides a physically meaningful bridge between an initially homogeneous precursor mixture and the mechanically stressed, phase-separated microstructures that motivate the prescribed-inclusion simulations of earlier chapters.

Specialising the general three-dimensional theory to a one-dimensional tube geometry enabled a clear interpretation of the multiphysics coupling and an efficient finite element implementation. In this reduced setting we performed systematic parametric studies and characterised morphology using two simple measures: the interface count $N_{\mathrm{int}}(t)$ and the phase-contrast amplitude $\Delta\phi_p(t)$. Two dimensionless parameters were introduced to interpret the results: the elasticity ratio r_e, measuring mechanical penalty relative to the mixing-energy scale, and the Damkohler number Da, measuring the relative rate of polymerisation and diffusive relaxation. In the closed system, increasing r_e hindered interface rearrangements and slowed the discrete domain-elimination events associated with coarsening, leading to a finer morphology at the expense of reduced phase contrast. By contrast, varying Da primarily shifted the timing of pattern development: larger Da promoted earlier phase separation, while the equilibrium interface count and overall morphology at fixed elasticity were only weakly affected within the range considered.

Introducing solvent exchange through a water-reservoir boundary condition altered the equilibrium behaviour. The reservoir breaks global mass conservation and imposes a sustained chemical-potential bias, which is reflected in asymmetric equilibrium profiles. In this open system the dependence of the equilibrium interface count on elasticity is reversed: for larger r_e the system lowers its total energetic cost by eliminating interfaces and forming fewer, broader regions, rather than maintaining many weakly segregated domains. Although larger r_e continues to suppress segregation by penalising swelling mismatch, the reservoir can elevate the equilibrium phase contrast, and the stiffest cases therefore reduce interfacial area more aggressively, leading to smaller equilibrium N_{int}. This demonstrates that the equilibrium outcome is a coupled consequence of mechanics, thermodynamics, and boundary-mediated mass exchange.

Finally, while the present one-dimensional model does not resolve the detailed shapes or director configurations of liquid crystal droplets, it establishes the missing microstructure-formation link absent from the prescribed-inclusion studies of earlier chapters. In particular, it provides a route to define physically meaningful reference configurations for subsequent electromechanical actuation simulations, including the characteristic length scale, connectivity, and residual-stress state inherited from formation. The general weak form outlined in this chapter extends naturally to two and three dimensions, where future work can address morphology and coarsening in realistic geometries, anisotropic interfacial effects, and liquid-crystal-specific thermodynamics.

6 | Conclusion

6.1 Overview

In this thesis, we developed theoretical and numerical models to describe the response of liquid crystal inclusions embedded in soft matrices. This response arises from a multiphysics interplay between the liquid-crystal orientational tensor field, the mechanical deformation of the surrounding elastic matrix, the interfacial energy at the inclusion-matrix boundary, and (when present) externally applied electric fields. To isolate and quantify the roles of these coupled mechanisms, we employed variational formulations, from which the governing equations follow naturally and the associated driving forces admit clear physical interpretations. Building on these formulations, we implemented corresponding numerical models to validate the theory and to elucidate the coupled behaviour through systematic parametric studies.

In Chapter 3, we examined the mechanical response of liquid crystal inclusions in soft matrices. We developed a continuum theory that couples the liquid-crystal order-parameter field, anisotropic surface tension, and matrix elasticity, and implemented it in the open-source finite element framework `FEniCSx` in both axisymmetric and three dimensional cases. The simulations confirm that, analogous to simple liquid inclusions, liquid crystal inclusions can reinforce the effective stiffness of the composite in the regime of a large elastocapillary number. This reinforcement is enhanced by stronger anchoring, which increases the inclusion aspect ratio in the reference configuration and strengthens shape-induced load transfer. For a fixed anchoring strength, the reinforcement effect weakens as the dimensionless inclusion volume decreases. In contrast, the response of the order-parameter field is mediated primarily through interface deformation and is therefore more sensitive to external loading when the elastocapillary number is small. In this regime, the director field undergoes more pronounced reorientation for larger dimensionless inclusion volumes and weaker anchoring strengths, consistent with

reduced interfacial constraints and greater compliance of the inclusion-matrix boundary.

In Chapter 4, we investigated the electromechanical response of liquid crystal inclusions. Building on the same variational modelling framework, we incorporated electric-field coupling and implemented the resulting governing equations in a finite element code. We first validated the model against experimental measurements of liquid crystal droplet elongation under applied electric fields. We further showed that for liquid crystals with asymmetrically shaped molecules, flexoelectricity (i.e. spontaneous polarisation induced by director gradients) can have non-negligible effects on the equilibrium droplet shape and can promote additional droplet elongation. The validated model was then used to analyse liquid crystal inclusions embedded in an elastic matrix through two case studies. In the first case, we examined the composite response as an effective bulk material. Electric-field-induced director alignment drives inclusion elongation or shortening, depending on the orientation of the applied field, to reduce misalignment between the director and the inclusion-matrix interface. This shape change is resisted by the elasticity of the surrounding matrix, which is characterised by the elastocapillary number. The simulations confirm that, for a given field strength, a softer matrix produces a larger inclusion deformation and therefore yields a more sensitive actuator. In the second case, we modelled a thin composite membrane consisting of a single layer of liquid crystal inclusions to represent a thin film architecture. Under an applied electric field, inclusion deformation generates surface wrinkling with amplitudes on the order of several microns, depending on the elastocapillary number. This electrically driven wrinkling provides a promising route for designing functional surfaces with tunable surface topography. In such systems, the electric field acts as an external control parameter that changes the internal director configuration and the associated stresses. These stresses can then drive mechanical deformations at the free surface or, leading to the formation of wrinkles. Since the amplitude, wavelength, and orientation of the wrinkles depend on the strength of the electric field, the elasticity of the surrounding matrix, and the

anchoring conditions at the interface, the resulting surface morphology can in principle be adjusted by appropriate material design. This provides a mechanism for creating adaptive surfaces whose roughness, optical response, wettability, adhesion, or frictional properties can be controlled by an applied voltage.

In Chapter 5, we established a thermodynamically consistent chemo-mechanical framework for polymerisation-induced phase separation (PIPS) in a ternary monomer-polymer-solvent mixture, taking into account polymerisation kinetics and the emergence of elasticity within a single free-energy formulation. We specialised the theory to one-dimensional finite-element simulations and interpreted the results using two morphology measures: the interface count $N_{\mathrm{int}}(t)$ and the phase-contrast amplitude $\Delta\phi_p(t)$. From parametric studies in the elasticity ratio r_e and the Damköhler number Da, we showed that Da controls how rapidly the system is driven into instability, while r_e governs the subsequent coarsening-contrast trade-off. Stiffer networks tend to suppress segregation while hindering ripening. Introducing a water-reservoir boundary condition further showed that boundary-mediated mass exchange can qualitatively alter long-time outcomes, strengthening segregation but favouring fewer, broader domains in stiff systems. Overall, the chapter provides the missing microstructure-formation link needed to define physically meaningful reference states, including length scale, connectivity, and residual stress. It also points to natural extensions of the framework to 2D-3D geometries and liquid-crystal-specific physics in future work.

6.2 Future work

The models developed in this thesis provide a unified variational foundation for describing electromechanical liquid crystal inclusions and chemo-mechanical microstructure formation during PIPS. Several directions can further enhance predictive capability and strengthen the link to fabrication and device performance. The overarching goal of fu-

ture work is to develop an end-to-end framework that connects processing conditions, evolving microstructure, and field-driven functionality within a thermodynamically consistent setting.

A direct extension of Chapter 5 is to carry the chemo-mechanical PIPS framework to two and three dimensions. Higher-dimensional simulations are essential for capturing connectivity changes, droplet topology, and coalescence pathways that cannot be represented in 1D. In particular, 2D-3D computations would enable quantitative predictions of characteristic length scales, domain-size distributions, and connectivity metrics, and would allow systematic investigation of how elasticity activation near gelation arrests coarsening in realistic morphologies. A practical next step is to retain the same free-energy structure and extend the current 1D implementation to 2D and 3D, with attention to numerical robustness. This includes adopting adaptive time stepping based on residual and energy decay. In addition, it will be important to explore alternative elasticity-activation laws around gelation, for example by comparing smooth sigmoid activation, percolation-inspired thresholds, and conversion-dependent modulus laws, and by testing their impact on arrest length scales and residual stress patterns. The 1D measures $N_{\mathrm{int}}(t)$ and $\Delta\phi_p(t)$ provide clear physical interpretation and are convenient for parameter sweeps, but more descriptors are necessary in 2D-3D. Future work will therefore introduce more parameters of morphology metrics, including correlation lengths extracted from structure factors, domain-size distributions, interfacial area density, percolation and connectivity measures. These metrics would allow direct comparison between coarsening laws in the pre-gelation/entanglement regime and arrested morphologies post-gelation/entanglement, and would provide a clearer bridge to experimental observables such as droplet size histograms and connectivity of LC-rich domains.

With 2D-3D numerical methods in place, a key next step is to connect microstructure formation to the liquid crystal inclusion problems described in Chapter 3 and Chapter 4.

Within the present modelling philosophy, this can be achieved by embedding liquid-crystal-specific physics into the phase-separation framework, for example by introducing an order parameter in the liquid-crystal-rich domains, anisotropic surface energies at the evolving polymer-liquid-crystal interface, and electrostatic couplings that act during or after phase separation. This would yield a process-to-function pathway in which curing conditions (e.g. Da, boundary exchange, and gelation threshold) determine inclusion morphology, which then controls field-driven deformation and functional surface response. An important modelling objective is to define physically meaningful reference configurations for subsequent actuation calculations, including the distribution of inclusion shapes, the residual stress state, and the length scale set by arrested coarsening.

The current work assumes a single LC phase and neglects the isotropic-nematic transition. Incorporating phase-transition physics into the present framework is a natural extension, particularly for systems in which temperature or composition changes can trigger nematic ordering. Practically, this can be achieved by coupling the phase-field composition variables to a Landau-de Gennes LC free energy and allowing the LC order parameter to vary depending on local thermodynamic state. Such an extension would enable investigation of co-evolving phase separation and ordering kinetics, including the possibility of order-driven interface instabilities and defect-mediated coarsening. Beyond PDLCs, this direction is also relevant for modelling complex soft and biological systems where active or passive liquid-crystalline ordering is coupled to mechanics and composition (Tarafder et al., 2020).

In addition, many soft matrices relevant to PDLC fabrication and hydrogel-like systems exhibit pronounced viscoelastic behaviour. Incorporating viscoelasticity into the matrix and liquid crystal response would enable the model to describe time-dependent stress relaxation during coarsening and under electric-field actuation, and to distinguish between transient and quasi-equilibrium deformation modes. Liquid crystals are also intrinsically dissipative materials (Sonnet and Virga, 2012), and time-dependent switch-

ing is a key functionality metric for LC devices (Luo et al., 2012). Therefore, an important future direction is to augment the present variational formulation with a dissipation potential consistent with Ericksen-Leslie-type theories and Landau-de Gennes theories (Leslie, 1979; Sonnet and Virga, 2012; Zhang et al., 2019b). This would allow prediction of switching times, hysteresis under cyclic loading, and rate-dependent shape changes in inclusions and membranes, thereby extending the current equilibrium-focused studies to dynamic device operation.

The water-reservoir boundary condition studied in Chapter 5 demonstrates that boundary-mediated mass exchange can qualitatively alter long-time microstructure. Future work should broaden this aspect by considering additional open-system mechanisms such as spatially varying mobility, concentration-dependent diffusivity, and non-uniform polymerisation rates that mimic curing gradients (e.g. realistic systems in photo-polymerisation). These effects can generate spatially heterogeneous gelation times and therefore spatially heterogeneous stiffness, which may strongly bias morphology selection and residual stress. Extending the framework to include such heterogeneities would provide a direction to study how processing protocols and boundary conditions can be used as controls for microstructure engineering.

While this thesis focused on morphology, mechanics, and electromechanical deformation, the ultimate application of liquid-crystal composites is often defined by optical performance. A natural next step is to link predicted inclusion shapes and director fields to optical scattering or homogenised electro-optical models, for example by extracting effective refractive-index distributions and computing transmittance, haze, or switching thresholds. For membrane architectures, coupling computed topography to contact, adhesion, or wetting models would quantify how electrically driven wrinkling translates into functional surface behaviour. These additions would allow the framework to predict not only deformation but also application-relevant metrics, thereby enabling more direct design decisions guided by measurable performance targets.

Finally, the numerical framework developed here enables systematic design studies. In particular, inclusion geometry, spacing, and boundary constraints can be optimised to maximise actuation sensitivity or to programme surface-mode shapes in thin films. In future work, this can be pursued through parametric studies guided by non-dimensional groups (e.g. elastocapillary number, anchoring strength, and field strength), as well as through optimisation methods that target specific objectives such as maximum wrinkle amplitude, prescribed wavelength selection, or minimal required voltage. These informations can be useful to identify robust design methods for tunable, field-responsive soft composites.

Bibliography

J. H. Adler, A. S. Andrei, and T. J. Atherton. Nonlinear methods for shape optimization problems in liquid crystal tactoids. *arXiv*, 2023.

H. Alghamdi and A. H. M. Almawgani. Smart and efficient energy saving system using PDLC glass. In *2019 Smart City Symposium Prague (SCSP)*, pages 1–5. IEEE, 2019.

M. S. Alnæs, J. Blechta, J. Hake, A. Johansson, B. Kehlet, A. Logg, C. Richardson, J. Ring, M. E. Rognes, and G. N. Wells. The FEniCS project version 1.5. *Archive of Numerical Software*, 3, 2015.

D. Andrienko. Introduction to liquid crystals. *Journal of Molecular Liquids*, 267:520–541, October 2018.

D. Andrienko and M. P. Allen. Theory and simulation of the nematic zenithal anchoring coefficient. *Physical Review E*, 65(2):021704, 2002.

O. A. Aphonin, Y. V. Panina, A. B. Pravdin, and D. A. Yakovlev. Optical properties of stretched polymer dispersed liquid crystal films. *Liquid Crystals*, 15(3):395–407, 1993.

M. Bagnani, G. Nyström, C. De Michele, and R. Mezzenga. Amyloid fibrils length controls shape and structure of nematic and cholesteric tactoids. *ACS Nano*, 13(1): 591–600, 2019.

Y. Bai and L. Brassart. Mechanics of liquid crystal inclusions in soft matrices. *Journal of the Mechanics and Physics of Solids*, 197:106070, 2025.

N. Balenko, V. Shibaev, and A. Bobrovsky. Mechanosensitive polymer-dispersed cholesteric liquid crystal composites based on various polymer matrices. *Polymer*, 281:126119, 2023.

N. V. Balenko, V. P. Shibaev, and A. Y. Bobrovsky. Mechano-optical response of novel polymer composites based on elastic polyurethane matrix filled with low-molar-mass cholesteric droplets. *Macromolecular Materials and Engineering*, 306(10):2100262, October 2021.

F. Ballarin. Multiphenicsx: an easy prototyping of multiphysics problems on conforming meshes, 2024. URL https://multiphenics.github.io/. Accessed: February 10, 2024.

M. Baratta, G. De Filpo, A. Tursi, A. I. Mashin, and F. P. Nicoletta. Polymer Dispersed Liquid Crystals with elongated droplets as novel pressure sensors. *Liquid Crystals*, 49(5):657–665, 2022.

G. Barbero, I. Dozov, J.-F. Palierne, and G. Durand. Order electricity and surface orientation in nematic liquid crystals. *Physical Review Letters*, 56(19):2056, 1986.

B. F. Barton, P. D. Graham, and A. J. McHugh. Dynamics of spinodal decomposition in polymer solutions near a glass transition. *Macromolecules*, 31(5):1672–1679, 1998.

M. A. Bates. Computer simulation studies of nematic liquid crystal tactoids. *Chemical Physics Letters*, 368(1–2):87–93, 2003.

F. C. Bawden, N. W. Pirie, J. D. Bernal, and I. Fankuchen. Liquid crystalline substances from virus-infected plants. *Nature*, 138(3503):1051–1052, 1936.

M. J. Bertocchi, D. C. Ratchford, R. Casalini, J. H. Wynne, and J. G. Lundin. Electrospun polymer fibers containing a liquid crystal core: insights into semiflexible confinement. *The Journal of Physical Chemistry C*, 122(29):16964–16971, 2018.

F. Bloisi, P. Terrecuso, and L. Vicari. Polarized light scattering in a novel polymer dispersed liquid-crystal geometry. *Journal of the Optical Society of America A*, 14 (3):662–668, 1997.

D. Boffi, F. Brezzi, and M. Fortin. *Mixed Finite Element Methods and Applications*, volume 44. Springer, 2013.

M. Born. *Ueber anisotrope Flüssigkeiten: Versuch einer Theorie der flüssigen Kristalle und des elektrischen Kerr-Effekts in Flüssigkeiten*. 1916.

B. J. Boyd, D. V. Whittaker, S.-M. Khoo, and G. Davey. Lyotropic liquid crystalline phases formed from glycerate surfactants as sustained release drug delivery systems. *International Journal of Pharmaceutics*, 309(1–2):218–226, 2006.

L. Brassart, Q. Liu, and Z. Suo. Shear, dilation, and swap: Mixing in the limit of fast diffusion. *Journal of the Mechanics and Physics of Solids*, 96:48–64, 2016.

J. W. Cahn. On spinodal decomposition. *Acta Metallurgica*, 9(9):795–801, 1961.

J. W. Cahn and J. E. Hilliard. Free energy of a nonuniform system. I. interfacial free energy. *The Journal of Chemical Physics*, 28(2):258–267, 1958.

C. Casagrande, P. Fabre, M. A. Guedeau, and M. Veyssie. Observation of anisotropic droplets in nematic-nematic phase separation. *Europhysics Letters*, 3(1):73, 1987.

E. P. Chan, E. J. Smith, R. C. Hayward, and A. J. Crosby. Surface wrinkles for smart adhesion. *Advanced Materials*, 20(4):711–716, 2008.

P. K. Chan and A. D. Rey. Computational analysis of spinodal decomposition dynamics in polymer solutions. *Macromolecular Theory and Simulations*, 4(5):873–899, 1995.

P. K. Chan and A. D. Rey. Polymerization-induced phase separation. 1. droplet size selection mechanism. *Macromolecules*, 29(27):8934–8941, 1996.

P. K. Chan and A. D. Rey. Polymerization-induced phase separation. 2. morphological analysis. *Macromolecules*, 30(7):2135–2143, 1997.

X. Chen, E. Korblova, D. Dong, X. Wei, R. Shao, L. Radzihovsky, M. A. Glaser, J. E. Maclennan, D. Bedrov, D. M. Walba, et al. First-principles experimental demonstration of ferroelectricity in a thermotropic nematic liquid crystal: Polar domains and striking electro-optics. *Proceedings of the National Academy of Sciences of the United States of America*, 117(25):14021–14031, 2020.

Z. Cheng, T. Wang, X. Li, Y. Zhang, and H. Yu. NIR–Vis–UV light-responsive actuator films of polymer-dispersed liquid crystal/graphene oxide nanocomposites. *ACS Applied Materials & Interfaces*, 7(49):27494–27501, 2015.

R. H. Colby and M. Rubinstein. Two-parameter scaling for polymers in θ solvents. *Macromolecules*, 23(10):2753–2757, 1990.

S. J. Cox, V. Y. Reshetnyak, and T. J. Sluckin. Effective medium theory of light scattering in polymer dispersed liquid crystal films. *Journal of Physics D: Applied Physics*, 31(14):1611, 1998.

L. S. Darken. Diffusion, mobility and their interrelation through free energy in binary metallic systems. *Transactions of the American Institute of Mining and Metallurgical Engineers*, 175:184–201, 1948.

C. S. Davis and A. J. Crosby. Mechanics of wrinkled surface adhesion. *Soft Matter*, 7 (11):5373–5381, 2011.

P.-G. de Gennes and J. Prost. *The Physics of Liquid Crystals*. International Series of Monographs on Physics. Oxford University Press, Oxford, 1993.

P. S. de Laplace. *Traité de Mécanique Céleste: Supplément au dixième livre du Traité de Mécanique Céleste sur l'action capillaire*, volume 6. Duprat, 1808.

A. DeBenedictis and T. J. Atherton. Shape minimisation problems in liquid crystals. *Liquid Crystals*, 43(13–15):2352–2362, 2016.

J. Deng, W. Liang, S. Rhodes, and J. Fang. Influence of polymer networks on the sensor properties of hydrogel dispersed liquid crystal droplets. *Colloids and Surfaces A: Physicochemical and Engineering Aspects*, 570:438–443, 2019.

S. Deshpande, V. Vidyaprakash, S. Oka, S. S. Dasari, K.-W. Liu, C. Wang, J. L. Lutkenhaus, and M. J. Green. Low-temperature structural battery electrolytes produced by polymerization-induced phase separation. *ACS Applied Polymer Materials*, 6(11): 6323–6333, 2024.

A. E. Diegel and S. W. Walker. A finite element method for a phase field model of nematic liquid crystal droplets. *arXiv*, 2017.

J. W. Doane, N. A. Vaz, B.-G. Wu, and S. Žumer. Field controlled light scattering from nematic microdroplets. *Applied Physics Letters*, 48(4):269–271, 1986.

M. Doi. *Soft Matter Physics*. Oxford University Press, 2013.

M. Doi and S. F. Edwards. *The Theory of Polymer Dynamics*, volume 73. Oxford University Press, 1988.

Z. Dong, H. Cui, H. Zhang, F. Wang, X. Zhan, F. Mayer, B. Nestler, M. Wegener, and P. A. Levkin. 3D printing of inherently nanoporous polymers via polymerization-induced phase separation. *Nature Communications*, 12(1):247, 2021.

I. Dozov, D. N. Stoenescu, S. Lamarque-Forget, P. Martinot-Lagarde, and E. Polossat. Planar degenerated anchoring of liquid crystals obtained by surface memory passivation. *Applied Physics Letters*, 77(25):4124–4126, 2000.

P. S. Drzaic. *Liquid Crystal Dispersions*. World Scientific, 1995.

H. L. Duan, J. Wang, Z. P. Huang, and B. L. Karihaloo. Eshelby formalism for nano-inhomogeneities. *Proceedings of the Royal Society A: Mathematical, Physical and Engineering Sciences*, 461(2062):3335–3353, 2005a.

H. L. Duan, J.-X. Wang, Z. P. Huang, and B. L. Karihaloo. Size-dependent effective elastic constants of solids containing nano-inhomogeneities with interface stress. *Journal of the Mechanics and Physics of Solids*, 53(7):1574–1596, 2005b.

O. Y. Dudaryeva, L. Cousin, L. Krajnovic, G. Gröbli, V. Sapkota, L. Ritter, D. Deshmukh, Y. Cui, R. W. Style, R. Levato, et al. Tunable bicontinuous macroporous cell culture scaffolds via kinetically controlled phase separation. *Advanced Materials*, 37 (7):2410452, 2025.

G. Durand. Order electricity in liquid crystals. *Physica A: Statistical Mechanics and its Applications*, 163(1):94–100, 1990.

J. L. Ericksen. Conservation laws for liquid crystals. *Transactions of the Society of Rheology*, 5:23, 1961.

J. L. Ericksen. Hydrostatic theory of liquid crystals. *Archive for Rational Mechanics and Analysis*, 9:371–378, 1962.

J. L. Ericksen. Inequalities in liquid crystal theory. *The Physics of Fluids*, 9(6):1205–1207, 1966.

D. Filip, I. Costa, J. L. Figueirinhas, and M. H. Godinho. Strain-induced matrix and droplets anisotropic deformation in liquid crystalline cellulose dispersed liquid crystal films. *Composite Interfaces*, 13:477–486, 2006.

P. J. Flory. Thermodynamics of high polymer solutions. *The Journal of Chemical Physics*, 10(1):51–61, 1942.

J.-B. Fournier and P. Galatola. Modeling planar degenerate wetting and anchoring in nematic liquid crystals. *Europhysics Letters*, 72(3):403, 2005.

F. C. Frank. Liquid crystals. on the theory of liquid crystals. *Discussions of the Faraday Society*, 25, 1958.

B. J. Frisken and P. Palffy-Muhoray. Freedericksz transitions in nematic liquid crystals: The effects of an in-plane electric field. *Physical Review A*, 40(10):6099, 1989.

A. A. F. Froyen and A. P. H. J. Schenning. A multifunctional structural coloured electronic skin monitoring body motion and temperature. *Soft Matter*, 19(3):361–365, 2023.

A. Gangal, P. Singh, S. Manori, R. K. Shukla, et al. Nematic lyotropic liquid crystalline ordering in rhizome powder of curcuma species and water mixtures: rheological properties and antioxidant applications. *Soft Matter*, 21(22):4420–4433, 2025.

C. Geuzaine and J.-F. Remacle. Gmsh: A 3-D finite element mesh generator with built-in pre- and post-processing facilities. *International Journal for Numerical Methods in Engineering*, 79(11):1309–1331, 2009.

V. Ghorapade and W.-C. Wang. Electro-hydrodynamic programming reshapes liquid crystal dynamics in free-form director fields. *Scientific Reports*, 14(1):4226, 2024.

A. Ghosh. Investigation of vacuum-integrated switchable polymer dispersed liquid crystal glazing for smart window application for less energy-hungry building. *Energy*, 265:126396, 2023.

K. Ghosh and O. Lopez-Pamies. Elastomers filled with liquid inclusions: Theory, numerical implementation, and some basic results. *Journal of the Mechanics and Physics of Solids*, 166:104930, 2022.

J. W. Gibbs. On the equilibrium of heterogeneous substances. *American Journal of Science*, 3(96):441–458, 1878.

Y. Guan, D. M. Agra-Kooijman, S. Fu, A. Jákli, and J. L. West. Responsive liquid-crystal-clad fibers for advanced textiles and wearable sensors. *Advanced Materials*, 31(29):1902168, July 2019.

S. Guo, G. Kang, D. T. Phan, M. N. Hsu, Y. C. Por, and C. H. Chen. Polymerization-induced phase separation formation of structured hydrogel particles via microfluidics for scar therapeutics. *Scientific Reports*, 8(1):2245, 2018.

M. E. Gurtin. *An Introduction to Continuum Mechanics*, volume 158. Academic Press, 1982.

M. E. Gurtin. Generalized Ginzburg–Landau and Cahn–Hilliard equations based on a microforce balance. *Physica D: Nonlinear Phenomena*, 92(3–4):178–192, 1996. doi: 10.1016/0167-2789(96)00025-0.

M. E. Gurtin and A. I. Murdoch. A continuum theory of elastic material surfaces. *Archive for Rational Mechanics and Analysis*, 57(4):291–323, 1975.

G. B. Hadjichristov. Ion-conducting composites of polymers and nematic liquid crystals. *ACS Omega*, 8(11):9684–9701, 2023.

H. Hakemi. Polymer dispersed liquid crystal (pdlc) industrial technology and development in europe. *Molecular Crystals and Liquid Crystals*, 684(1):7–14, 2019.

Z. He, W. Shen, P. Yu, Y. Zhao, Z. Zeng, Z. Liang, Z. Chen, H. Zhang, H. Zhang, Z. Miao, and D. Wang. Viewing-angle-switching film based on polymer dispersed liquid crystals for smart anti-peeping liquid crystal display. *Liquid Crystals*, 49(1): 59–65, 2022.

A. Hemaida, A. Ghosh, S. Sundaram, and T. K. Mallick. Evaluation of thermal performance for a smart switchable adaptive polymer dispersed liquid crystal (PDLC) glazing. *Solar Energy*, 195:185–193, 2020.

D. L. Henann and K. Bertoldi. Modeling of elasto-capillary phenomena. *Soft Matter*, 10(5):709–717, 2014.

G. A. Holzapfel. *Nonlinear Solid Mechanics: A Continuum Approach for Engineering Science*. Kluwer Academic Publishers, Dordrecht, 2002.

C. E. Hoppe, M. J. Galante, P. A. Oyanguren, and R. J. J. Williams. Polymer-dispersed liquid crystals with co-continuous structures generated by polymerization-induced phase separation of EBBA-epoxy solutions. *Macromolecules*, 35(16):6324–6331, 2002.

H. Hou, J. Yin, and X. Jiang. Smart patterned surface with dynamic wrinkles. *Accounts of Chemical Research*, 52(4):1025–1035, 2019.

Y. Huang, E.-L. Hsiang, M.-Y. Deng, and S.-T. Wu. Mini-LED, micro-LED and OLED displays: present status and future perspectives. *Light: Science & Applications*, 9(1): 105, 2020.

M. L. Huggins. Some properties of solutions of long-chain compounds. *The Journal of Physical Chemistry*, 46(1):151–158, 1942.

N. Ihrner, W. Johannisson, F. Sieland, D. Zenkert, and M. Johansson. Structural lithium ion battery electrolytes via reaction induced phase-separation. *Journal of Materials Chemistry A*, 5(48):25652–25659, 2017.

V. Jamali, N. Behabtu, B. Senyuk, J. A. Lee, I. I. Smalyukh, P. van der Schoot, and M. Pasquali. Experimental realization of crossover in shape and director field of nematic tactoids. *Physical Review E*, 91(4):042507, 2015.

A. Javili and P. Steinmann. A finite element framework for continua with boundary energies. part i: The two-dimensional case. *Computer Methods in Applied Mechanics and Engineering*, 198(27–29):2198–2208, 2009.

A. Javili and P. Steinmann. A finite element framework for continua with boundary en-

ergies. part ii: The three-dimensional case. *Computer Methods in Applied Mechanics and Engineering*, 199(9–12):755–765, 2010.

W. Kamal, M. Li, J.-D. Lin, E. Parry, Y. Jin, S. J. Elston, A. A. Castrejón-Pita, and S. M. Morris. Spatially patterned polymer dispersed liquid crystals for image-integrated smart windows. *Advanced Optical Materials*, 10(3):2101748, 2022.

A. V. Kaznacheev, M. M. Bogdanov, and S. A. Taraskin. The nature of prolate shape of tactoids in lyotropic inorganic liquid crystals. *Journal of Experimental and Theoretical Physics*, 95(1):57–63, 2002.

J. R. Kelly and P. Palffy-Muhoray. The optical response of polymer dispersed liquid crystals. *Molecular Crystals and Liquid Crystals*, 243(1):11–29, 1994.

M. Khalid, K. Shanks, A. Ghosh, A. Tahir, S. Sundaram, and T. K. Mallick. Temperature regulation of concentrating photovoltaic window using argon gas and polymer dispersed liquid crystal films. *Renewable Energy*, 164:96–108, 2021.

M. Khan, S. Liu, L. Qi, C. Ma, S. Munir, L. Yu, and Q. Hu. Liquid crystal-based sensors for the detection of biomarkers at the aqueous/LC interface. *TrAC Trends in Analytical Chemistry*, 144, November 2021.

J. Y. Kim, C. H. Cho, P. Palffy-Muhoray, and T. Kyu. Polymerization-induced phase separation in a liquid-crystal-polymer mixture. *Physical Review Letters*, 71(14):2232, 1993.

Y.-K. Kim, B. Senyuk, and O. D. Lavrentovich. Molecular reorientation of a nematic liquid crystal by thermal expansion. *Nature Communications*, 3(1):1133, 2012.

B. S. Kirkebæk, A. Ali, and C. A. Quist-Jensen. Masked stereolithography and polymerization induced phase separation for 3D printing of membranes. *Scientific Reports*, 15(1):18776, 2025.

R. Koizumi, D. Golovaty, A. Alqarni, B.-X. Li, P. J. Sternberg, and O. D. Lavrentovich. Topological transformations of a nematic drop. *Science Advances*, 9(27):eadf3385, 2023.

B. König, O. J. J. Ronsin, and J. Harting. Two-dimensional cahn–hilliard simulations for coarsening kinetics of spinodal decomposition in binary mixtures. *Physical Chemistry Chemical Physics*, 23(43):24823–24833, 2021.

M. Kothari and T. Cohen. Effect of elasticity on phase separation in heterogeneous systems. *Journal of the Mechanics and Physics of Solids*, 145:104153, 2020.

S. Krichen, L. Liu, and P. Sharma. Liquid inclusions in soft materials: Capillary effect, mechanical stiffening and enhanced electromechanical response. *Journal of the Mechanics and Physics of Solids*, 127:332–357, 2019.

T. Kyu and H.-W. Chiu. Morphology development during polymerization-induced phase separation in a polymer dispersed liquid crystal. *Polymer*, 42(21):9173–9185, 2001.

Y.-T. Lai, J.-C. Kuo, and Y.-J. Yang. A novel gas sensor using polymer-dispersed liquid crystal doped with carbon nanotubes. *Sensors and Actuators A: Physical*, 215:83–88, 2014.

O. D. Lavrentovich. Ferroelectric nematic liquid crystal, a century in waiting. *Proceedings of the National Academy of Sciences of the United States of America*, 117(26): 14629–14631, 2020.

K. Y. Lee and D. R. Paul. A model for composites containing three-dimensional ellipsoidal inclusions. *Polymer*, 46(21):9064–9080, 2005.

F. M. Leslie. Theory of flow phenomena in liquid crystals. In *Advances in Liquid Crystals*, volume 4, pages 1–81. Elsevier, 1979.

R. J. LeVeque. *Finite difference methods for ordinary and partial differential equations: steady-state and time-dependent problems*. Society for Industrial and Applied Mathematics (SIAM), Philadelphia, PA, 2007.

H. Lin, H. Ding, and J. R. Kelly. The mechanism of switching a PDLC film. *Molecular Crystals and Liquid Crystals*, 262(1):99–109, 1995.

C. Ling, T. Naren, X. Liu, J. Yang, P. Xiao, W. Wei, X. Ji, G.-C. Kuang, and L. Chen. In-situ polymerization induced phase separation to develop high-performance self-healable polymeric electrolytes for lithium metal battery. *Materials Today Energy*, 36:101372, 2023.

J. Liu, R. Cheng, K. Heimann, Z. Wang, J. Wang, and F. Liu. Temperature-sensitive lyotropic liquid crystals as systems for transdermal drug delivery. *Journal of Molecular Liquids*, 326:115310, 2021.

K. Liu, S. Tang, L. Zhu, W. Wen, M. Liu, H. Li, C. Zhou, and B. Luo. Bio-inspired liquid crystal gel with adjustable viscoelasticity to modulate cell behaviors and fate. *Composites Part B: Engineering*, 234, 2022.

N. Liu, Q. Sun, Z. Yang, L. Shan, Z. Wang, and H. Li. Wrinkled interfaces: taking advantage of anisotropic wrinkling to periodically pattern polymer surfaces. *Advanced Science*, 10(12):2207210, 2023.

N. A. Lockwood, J. C. Mohr, L. Ji, C. J. Murphy, S. P. Palecek, J. J. de Pablo, and N. L. Abbott. Thermotropic liquid crystals as substrates for imaging the reorganization of matrigel by human embryonic stem cells. *Advanced Functional Materials*, 16(5): 618–624, 2006.

J. C. Loudet, A. Choudhury, M. Qiu, and J. J. Feng. Particle trapped at the isotropic-nematic liquid crystal interface: Elastocapillary phenomena and drag forces. *Physical Review E*, 105(4):1–15, 2022.

Y. Lu, X. Wang, D. Yang, Z. Zhong, H. Gao, X. Du, Y. Zhao, Z. He, H. Cao, Z. Yang, et al. PDLC flexible films with multiple fluorescence and voltage modulated modes and intelligent coding for applications in anti-counterfeiting and transparent displays. *Chemical Engineering Journal*, 496:153742, 2024a.

Y. Lu, D. Yang, H. Gao, X. Du, Y. Zhao, D. Wang, Z. He, Z. Miao, H. Cao, Z. Yang, et al. Enhanced electro-optical properties of polymer-dispersed liquid crystals co-doped with fluorescent molecules and nanoparticles for multifunctional applications. *Chemical Engineering Journal*, page 149654, 2024b.

C. Luo, A. Majumdar, and R. Erban. Multistability in planar liquid crystal wells. *Physical Review E*, 85(6):061702, 2012.

H. Ma, Q. Kang, T. Wang, and L. Yu. A liquid crystals-based sensing platform for detection of α-amylase coupled with destruction of host-guest interaction. *Colloids and Surfaces B: Biointerfaces*, 173:616–622, January 2019.

W. Maier and A. Saupe. A simple molecular statistical theory of the nematic crystalline-liquid phase. *Zeitschrift für Naturforschung A*, 14:882–889, 1959.

D. Manaila-Maximean. Confined liquid crystals-polymer dispersed liquid crystal films. *UPB Scientific Bulletin, Series A: Applied Mathematics and Physics*, 83(1):271–278, 2021.

E. Mema, L. Kondic, and L. J. Cummings. Effects of flexoelectricity and weak anchoring on a fréedericksz transition cell. *Physical Review E*, 95(1):012701, 2017.

W. Meng, Y. Gao, X. Hu, L. Tan, L. Li, G. Zhou, H. Yang, J. Wang, and L. Jiang. Photothermal dual passively driven liquid crystal smart window. *ACS Applied Materials & Interfaces*, 14(24):28301–28309, 2022.

L. Metselaar, I. Dozov, K. Antonova, E. Belamie, P. Davidson, J. M. Yeomans, and A. Doostmohammadi. Electric-field-induced shape transition of nematic tactoids. *Physical Review E*, 96(2):022706, 2017.

R. B. Meyer. Piezoelectric effects in liquid crystals. *Physical Review Letters*, 22(18): 918, 1969.

D. S. Miller, X. Wang, and N. L. Abbott. Design of functional materials based on liquid crystalline droplets. *Chemistry of Materials*, 26(1):496–506, 2014.

R. Moldovan and M. R. Puică. Concentration dependence in the landau–de gennes theory for nematic lyotropic liquid crystals. *Physics Letters A*, 286(2–3):205–209, 2001.

N. J. Mottram and C. J. P. Newton. Introduction to Q-tensor theory. *arXiv*, 2014.

M. Z. Müller, M. Bernero, C. Xie, W. Qiu, E. Oggianu, L. Rabut, T. C. T. Michaels, R. W. Style, R. Müller, and X.-H. Qin. Cell-guiding microporous hydrogels by photopolymerization-induced phase separation. *Nature Communications*, 16(1): 4923, 2025.

A. Novikov and D. Makarov. Untwisting of a soft ferrocholesteric liquid crystal by shear flow and magnetic field. In *Journal of Physics: Conference Series*, volume 1389, page 12053. IOP Publishing, 2019.

R. W. Ogden. *Elements of the Theory of Finite Elasticity*. Cambridge University Press, 2001.

J. Oh and A. D. Rey. Theory and simulation of polymerization-induced phase separation in polymeric media. *Macromolecular Theory and Simulations*, 9(8):641–660, 2000.

S. W. Oh, S. M. Ji, C. H. Han, and T. H. Yoon. A cholesteric liquid crystal smart window with a low operating voltage. *Dyes and Pigments*, 197, 2022.

M. Oh-e and D. Y. Zheng. Newly discovered dimensional effects of electrodes on liquid crystal THz phase shifters enable novel switching between in-plane and out-of-plane. *Scientific Reports*, 12(1), 2022.

L. Onsager. The effects of shape on the interaction of colloidal particles. *Annals of the New York Academy of Sciences*, 51(4):627–659, 1949.

C. W. Oseen. The theory of liquid crystals. *Transactions of the Faraday Society*, 29: 883–899, 1933.

H. Oudich, P. Carrara, and L. De Lorenzis. Phase-field modeling of elastic microphase separation. *Journal of the Mechanics and Physics of Solids*, 206:106380, 2026.

S. Pagidi, K. S. Pasupuleti, M. Reddeppa, S. Ahn, Y. Kim, J.-H. Kim, M.-D. Kim, S. H. Lee, and M. Y. Jeon. Resistive type NO2 gas sensing in polymer-dispersed liquid crystals with functionalized-carbon nanotubes dopant at room temperature. *Sensors and Actuators B: Chemical*, 370:132482, 2022.

A. H. Pesch and C. Vetter. A control-oriented model for polymer-dispersed liquid crystal films as an actuator for natural light control. *Actuators*, 14:167, 2025.

N. Popov, L. W. Honaker, M. Popova, N. Usol'tseva, E. K. Mann, A. Jákli, and P. Popov. Thermotropic liquid crystal-assisted chemical and biological sensors. *Materials*, 11 (1):20, 2017.

T. Porenta, M. Ravnik, and S. Žumer. Effect of flexoelectricity and order electricity on defect cores in nematic droplets. *Soft Matter*, 7(1):132–136, 2011.

P. Prinsen and P. van der Schoot. Shape and director-field transformation of tactoids. *Physical Review E*, 68(2):11, 2003.

P. Prinsen and P. van der Schoot. Continuous director-field transformation of nematic tactoids. *The European Physical Journal E*, 13:35–41, 2004.

O. O. Ramdane, P. Auroy, S. Forget, E. Raspaud, P. Martinot-Lagarde, and I. Dozov. Memory-free conic anchoring of liquid crystals on a solid substrate. *Physical Review Letters*, 84(17):3871, 2000.

A. Rapini and M. Papoular. Distortion d'une lamelle nématique sous champ magnétique: conditions d'ancrage aux parois. *Le Journal de Physique Colloques*, 30(C4): C4–54, November 1969.

H. Ren, Y.-H. Fan, Y.-H. Lin, and S.-T. Wu. Tunable-focus microlens arrays using nanosized polymer-dispersed liquid crystal droplets. *Optics Communications*, 247 (1–3):101–106, 2005.

C. Robinson. Liquid-crystalline structures in solutions of a polypeptide. *Transactions of the Faraday Society*, 52:571–592, 1956.

K. A. Rosowski, T. Sai, E. Vidal-Henriquez, D. Zwicker, R. W. Style, and E. R. Dufresne. Elastic ripening and inhibition of liquid–liquid phase separation. *Nature Physics*, 16(4):422–425, 2020.

M. Rubinstein and R. H. Colby. *Polymer Physics*. Oxford University Press, 2003.

V. Y. Rudyak, A. V. Emelyanenko, and V. A. Loiko. Structure transitions in oblate nematic droplets. *Physical Review E*, 88(5):052501, 2013.

M. Safdari, R. Zandi, and P. van der Schoot. Effect of electric fields on the director field and shape of nematic tactoids. *Physical Review E*, 103(6):062703, January 2021.

J. Sang, J. Zhang, H. Feng, J. Sun, J. Shang, Y. Zhang, S. Zhao, K. Neyts, and V. Chigrinov. Flexible and transferable silver nanowire liquid crystal polymer film obtained via photo-alignment programming. *Advanced Optical Materials*, 10(16):2200950, 2022.

M. Schadt. Liquid crystal materials and liquid crystal displays. *Annual Review of Materials Science*, 27(1):305–379, 1997.

C. D. Schimming and J. Viñals. Equilibrium morphology of tactoids in elastically anisotropic nematics. *Soft Matter*, 18(41):8024–8033, 2022.

M. W. Schulze, L. D. McIntosh, M. A. Hillmyer, and T. P. Lodge. High-modulus, high-conductivity nanostructured polymer electrolyte membranes via polymerization-induced phase separation. *Nano Letters*, 14(1):122–126, 2014.

C. Serbutoviez, J. G. Kloosterboer, H. M. J. Boots, and F. J. Touwslager. Polymerization-induced phase separation. 2. morphology of polymer-dispersed liquid crystal thin films. *Macromolecules*, 29(24):7690–7698, 1996.

R. Shadkami and P. K. Chan. Computational analysis on the performance of elongated liquid crystal biosensors. *Micromachines*, 14(10):1831, 2023.

D. Sharma, A. J. Middya, N. Singh, S. Singhal, and A. Dan. Microscale liquid crystal droplet-embedded hydrogel film for ultrasensitive optical detection of bacterial endotoxins. *Small*, page 2503766, 2025.

P. Sharma, S. Ganti, and N. Bhate. Effect of surfaces on the size-dependent elastic state of nano-inhomogeneities. *Applied Physics Letters*, 82(4):535–537, 2003.

M. Skarabot, N. J. Mottram, S. Kaur, C. T. Imrie, E. Forsyth, J. M. D. Storey, R. Mazur, W. Piecek, and L. Komitov. Flexoelectric polarization in a nematic liquid crystal enhanced by dopants with different molecular shape polarities. *ACS Omega*, 7(11): 9785–9795, 2022.

M. Song, J. Seo, H. Kim, and Y. Kim. Ultrasensitive multi-functional flexible sensors based on organic field-effect transistors with polymer-dispersed liquid crystal sensing layers. *Scientific Reports*, 7(1):1–11, 2017.

A. M. Sonnet and E. G. Virga. *Dissipative Ordered Fluids: Theories for Liquid Crystals*, volume 100. Springer Science & Business Media, 2012.

A. G. Soria, A. Stracuzzi, and A. E. Ehret. A consistent lagrangian theory for phase separation in chemoelastic polymeric media at large deformations. *Journal of the Mechanics and Physics of Solids*, page 106256, 2025.

P. Steinmann. On boundary potential energies in deformational and configurational mechanics. *Journal of the Mechanics and Physics of Solids*, 56(3):772–800, 2008.

J. Stelzer, L. Longa, and H.-R. Trebin. Homeotropic surface anchoring of a gay-berne nematic liquid crystal. *Physical Review E*, 55(6):7085, 1997.

G. B. Stephenson. Deformation during interdiffusion. *Acta Metallurgica*, 36(11):2663–2683, 1988.

I. W. Stewart. *The Static and Dynamic Continuum Theory of Liquid Crystals: A Mathematical Introduction*. Routledge, Oxon, 2021. ISBN 978-0-7484-0896-2 (pbk.). Originally published: 2004.

R. W. Style, C. Hyland, R. Boltyanskiy, J. S. Wettlaufer, and E. R. Dufresne. Surface tension and contact with soft elastic solids. *Nature Communications*, 4(1):2728, 2013.

R. W. Style, R. Boltyanskiy, B. Allen, K. E. Jensen, H. P. Foote, J. S. Wettlaufer, and E. R. Dufresne. Stiffening solids with liquid inclusions. *Nature Physics*, 11(1):82–87, 2015a.

R. W. Style, J. S. Wettlaufer, and E. R. Dufresne. Surface tension and the mechanics of liquid inclusions in compliant solids. *Soft Matter*, 11(4):672–679, 2015b.

R. W. Style, T. Sai, Nicoló Fanelli, M. Ijavi, K. Smith-Mannschott, Q. Xu, L. A. Wilen, and E. R. Dufresne. Liquid-liquid phase separation in an elastic network. *Physical Review X*, 8, 2018.

I. Taniguchi, S. Duan, T. Kai, S. Kazama, and H. Jinnai. Effect of the phase-separated structure on CO2 separation performance of the poly(amidoamine) dendrimer immobilized in a poly(ethylene glycol) network. *Journal of Materials Chemistry A*, 1(46): 14514–14523, 2013.

A. K. Tarafder, A. von Kügelgen, A. J. Mellul, U. Schulze, D. G. A. L. Aarts, and T. A. M. Bharat. Phage liquid crystalline droplets form occlusive sheaths that encapsulate and protect infectious rod-shaped bacteria. *Proceedings of the National Academy of Sciences of the United States of America*, 117(9):4724–4731, 2020.

M. M. Tefelska, T. R. Woliński, S. Ertman, K. Mileńko, R. Laczkowski, A. Siarkowska, and A. W. Domański. Electric field sensing with photonic liquid crystal fibers based on micro-electrodes systems. *Journal of Lightwave Technology*, 33(12):2405–2411, 2015.

R. Teixeira de Souza, M. M. A. de Jesus, J. C. Dias, and L. R. Evangelista. Reorientation effect and electrical current in a weakly anchored nematic cell. *Physical Review E*, 80(4):041702, 2009.

B. Tjipto-Margo and D. E. Sullivan. Molecular interactions and interface properties of nematic liquid crystals. *The Journal of Chemical Physics*, 88(10):6620–6630, 1988.

Y. Tokudome, K. Suzuki, T. Kitanaga, and M. Takahashi. Hierarchical nested wrinkles on silica-polymer hybrid films: stimuli-responsive micro periodic surface architectures. *Scientific Reports*, 2(1):683, 2012.

M. Tsige, M. P. Mahajan, C. Rosenblatt, and P. L. Taylor. Nematic order in nanoscopic liquid crystal droplets. *Physical Review E*, 60(1):638, 1999.

D. Vanzo, M. Ricci, R. Berardi, and C. Zannoni. Shape, chirality and internal order of freely suspended nematic nanodroplets. *Soft Matter*, 8(47):11790–11800, 2012.

E. G. Virga. *Variational Theories for Liquid Crystals*. CRC Press, 2019.

M. Vonka and J. Kosek. Modelling the morphology evolution of polymer materials undergoing phase separation. *Chemical Engineering Journal*, 207:895–905, 2012.

H. Wang, T. Peng, H. Wu, J. Chen, M. Chen, L. Mei, F. Li, W. Wang, C. Wu, and X. Pan. In situ biomimetic lyotropic liquid crystal gel for full-thickness cartilage defect regeneration. *Journal of Controlled Release*, 338:623–632, 2021.

Y. Wang and D. L. Henann. Finite-element modeling of soft solids with liquid inclusions. *Extreme Mechanics Letters*, 9:147–157, 2016.

M. Warenghem, N. Isaert, and P. Bernard. Orientation of nematics on metallic liquid surface. *Journal of Optics*, 15(3):133, 1984.

P. Wei, L. Li, L. Wang, J. Yan, N. Zeng, L. Li, N. Sun, L. Bai, H. Li, and Y. Zhang. Synthesis and properties of high performance biobased liquid crystal copolyesters toward load-bearing bone repair application. *European Polymer Journal*, 173, 2022.

T. J. White, L. V. Natarajan, T. J. Bunning, and C. A. Guymon. Contribution of monomer functionality and additives to polymerization kinetics and liquid crystal phase separation in acrylate-based polymer-dispersed liquid crystals (PDLCs). *Liquid Crystals*, 34(12):1377–1385, 2007.

E. Willman, L. Seddon, M. Osman, A. Bulak, R. James, S. E. Day, and F. A. Fernandez. Liquid crystal alignment induced by micron-scale patterned surfaces. *Physical Review E*, 89(5):052501, 2014.

B.-G. Wu, J. H. Erdmann, and J. W. Doane. Response times and voltages for PDLC light shutters. *Liquid Crystals*, 5(5):1453–1465, 1989.

K. Wu, J. Sun, F. Meng, M. Fan, X. Kong, M. Cai, T. Zhao, C. Yang, Y. Xin, J. Xing, et al. Highly flexible and electrically controlled grating enabled by polymer dispersed liquid crystal. *Journal of Molecular Liquids*, 353:118664, 2022.

Y. Wu, W. Yu, and C. Zhou. A study on interfacial tension between flexible polymer and liquid crystal. *Journal of Colloid and Interface Science*, 298(2):889–898, 2006.

G. Wulff. Xxv. zur frage der geschwindigkeit des wachsthums und der auflösung der krystallflächen. *Zeitschrift für Kristallographie*, 34(1–6):449–530, 1901.

Y.-Y. Xiao, Z.-C. Jiang, J.-B. Hou, X.-S. Chen, and Y. Zhao. Electrically driven liquid crystal network actuators. *Soft Matter*, 18:4850, 2022.

Y.-C. Yang, M.-H. Lee, J.-E. Kim, H. Y. Park, and J.-C. Lee. Theoretical study on the homeotropic-transient planar transition of cholesteric liquid crystals. *Japanese Journal of Applied Physics*, 40(2R):649, 2001.

T. Young. An essay on the cohesion of fluids. *Philosophical Transactions of the Royal Society of London*, (95):65–87, 1805.

B. Yu, Z. Huang, D. Fang, S. Yu, T. Fu, Y. Tang, and Z. Li. Biomimetic porous fluoropolymer films with brilliant whiteness by using polymerization-induced phase separation. *Advanced Materials Interfaces*, 9(1):2101485, 2022.

H. Yu, C. Dong, W. Zhou, T. Kobayashi, and H. Yang. Wrinkled liquid-crystalline microparticle-enhanced photoresponse of PDLC-like films by coupling with mechanical stretching. *Small*, 7(21):3039–3045, 2011.

L. Yu, Z. Cheng, Z. Dong, Y. Zhang, and H. Yu. Photomechanical response of polymer-dispersed liquid crystals/graphene oxide nanocomposites. *Journal of Materials Chemistry C*, 2(40):8501–8506, 2014.

L. Zakrzewski, Y. Kim, Y. Song, C. Y. Ryu, C. Bae, and C. R. Picu. Interplay of photopolymerization and phase separation kinetics and the resulting structure-property relationship of photocurable resins. *Polymer*, 280:126032, 2023.

C. Zhang, H. Wang, S. Guan, Z. Guo, X. Zheng, Y. Fan, Y. Wang, T. Qu, Y. Zhao, A. Chen, et al. Self-powered optical switch based on triboelectrification-triggered liquid crystal alignment for wireless sensing. *Advanced Functional Materials*, 29 (13):1808633, 2019a.

G. Zhang, A. Zhu, S. Wang, Q. Chen, B. Liu, J. Zhou, and Z. Wu. Stabilizing liquid crystal droplets with hydrogel films and its application in monitoring adenosine triphosphate. *Colloids and Surfaces A: Physicochemical and Engineering Aspects*, 654:130122, 2022.

H.-L. Zhang, H. Deng, H. Ren, M.-Y. He, D.-H. Li, and Q.-H. Wang. See-through 2D/3D compatible integral imaging display system using lens-array holographic optical element and polymer dispersed liquid crystal. *Optics Communications*, 456: 124615, 2020.

P. Zhang, X. Tong, Y. Gao, Z. Qian, R. Ren, C. Bian, J. Wang, and G. Cai. A sensing and stretchable polymer-dispersed liquid crystal device based on spiderweb-inspired silver nanowires-micromesh transparent electrode. *Advanced Functional Materials*, 33(41):2303270, 2023.

Y. Zhang, C. Xuan, Y. Jiang, and Y. Huo. Continuum mechanical modeling of liquid crystal elastomers as dissipative ordered solids. *Journal of the Mechanics and Physics of Solids*, 126:285–303, 2019b.

Z. Zhang, X. He, L. Zhang, J. Xu, B. Yuan, C. Chen, C. Zou, Q. Wang, Y. Gao, M. Yu, et al. A novel low-voltage fast-response electrically controlled dimming film based

on fluorinated PDLC for smart window applications. *Chemical Engineering Journal*, 479:147668, 2024.

J. Zhu and Q. Liu. The osmocapillary effect on a rough gel surface. *Journal of the Mechanics and Physics of Solids*, 170:105124, 2023.

Z. Zhu, G. Song, J. Liu, P. G. Whitten, L. Liu, and H. Wang. Liquid crystalline behavior of graphene oxide in the formation and deformation of tough nanocomposite hydrogels. *Langmuir*, 30(48):14648–14657, 2014.

H. Zocher. Über freiwillige strukturbildung in solen. *Zeitschrift für Anorganische und Allgemeine Chemie*, 147:91, 1925.